Influence of Purge Flow Swirl and Passage Discrete Hole Injection Angle on Turbine Blade Endwall Cooling

A DISSERTATION
SUBMITTED TO THE FACULTY OF THE
UNIVERSITY OF MINNESOTA
BY

Matthew Edward Stinson

IN PARTIAL FULFILLMENT OF THE REQUIREMENTS
FOR THE DEGREE OF
DOCTOR OF PHILOSOPHY

Dr. Richard J. Goldstein, Advisor
Dr. Terrence W. Simon, Co-advisor

August 2019

Acknowledgments

I want to thank Dr. Richard Goldstein for his support throughout my research, for his thoughtful advice and suggestions, and his kind encouragement during the difficult phases of my work. I am thankful for the freedom he gave me in my research and my time as a graduate student, which allowed for greater exploration and learning.

I am also thankful to Dr. Terry Simon for his suggestions and advice during my work. The breadth and depth of his knowledge were beneficial for my research and general studies in the thermal/fluid sciences.

My graduate work would not have been enjoyable without my fellow research group members: Dr. Kalyanjit Ghosh, Dr. Dan Keene, Rajat Mittal, Rishabh Srivastava, Matthew Taliaferro, and Matteo Angelino. They helped me with my research through many interesting technical discussions.

I want to thank the ME research machine shop for their helpful, friendly, and knowledgeable staff. I would especially like to thank Mike Jensen, for his contributions during the design phase of my research, and Pat Nelsen, for his many great suggestions and his assistance in setting up the experimental apparatus.

This research was made possible, in part, by financial support from IHI Corporation.

Dedication

This work is dedicated to my wife, Kelsey, for her support and encouragement during the challenges of graduate school. This work is also dedicated to my parents, Joel and Elizabeth, for teaching me to work hard for things that I aspire to achieve.

Abstract

Gas turbine blade endwall cooling presents a significant challenge due to the complex secondary flow structures within blade passages. Purge flow coolant, which passes through the gap between the stator and rotor, and discrete cooling holes, which are positioned strategically within the coolant passage, are often utilized together to provide complete cooling coverage on the blade endwall surface. The relative motion between the stator and rotor surfaces gives the purge flow a degree of swirl. Discrete injection holes are usually angled in close alignment with the near-wall flow direction, but this is often not achievable due to manufacturing constraints. The effects of purge flow swirl and discrete hole injection angle are not well documented but are expected to influence the endwall cooling significantly. Therefore, it is the focus of this work to investigate the influence of purge flow swirl and passage discrete hole injection angle on endwall cooling.

An experimental study is performed to investigate these endwall cooling phenomena using the naphthalene sublimation technique in a linear cascade composed of five high-pressure turbine blades. Detailed measurements for the endwall Sherwood number and film cooling effectiveness are made over a range of blowing rates, purge flow swirl angles, and discrete hole injection angles. The work is split into four complementary experimental cases. In the first case, a 45° straight injection slot is used to investigate the effect of purge flow blowing rate and swirl angle on endwall cooling. The purge flow swirl is simulated using turning vanes within the slot. In the second case, a more realistically shaped slot, featuring a gradual ramp leading to the endwall, is used to investigate the effect of purge flow blowing rate and swirl angle on endwall cooling. The purge flow swirl is again simulated with turning vanes, which are now located immediately upstream of the ramp. In the third case, 15 discrete endwall cooling holes are positioned along the endwall to investigate the effect of discrete hole injection blowing rate and discrete hole injection angle on endwall cooling. Two endwall plates

are utilized: one that angles the discrete holes in alignment with the local near-wall flow direction and a second that angles the discrete holes 90° relative to the first, representing a near worse case misalignment effect. In the fourth and last case, the combined cooling sources from the realistic slot and the 15 discrete holes are studied together. This case investigates the interactions between the two coolant sources.

The secondary flows in the blade passage limited the axial penetration of the purge flow coolant by sweeping the coolant toward the suction side of the blade passage. At high purge flow blowing rates, the effect of increasing the swirl angle led to significantly reduced axial penetration and thus overall reduced film cooling effectiveness levels. However, for low blowing rates, the effect of the swirl angle was weak. These results indicate that the blowing rate strongly influences to what degree the coolant follows its initial trajectory exiting the cooling slot, which is tied strongly to the swirl angle. Therefore, for low blowing rates, the coolant flow path is nearly unaffected by its swirl angle, whereas, at high blowing rates, the coolant flow path is closely aligned with its swirl angle. The purge flow results indicate that for realistic levels of purge flow blowing and swirl inadequate endwall cooling coverage will result, so supplementary coolant sources, like discrete cooling holes, must be utilized to provide complete endwall cooling coverage. The discrete hole injection angle misalignment effect led to multiple penalties: the Sherwood number was moderately enhanced, and the film cooling effectiveness was moderately reduced. This result indicates that the discrete hole injection angle misalignment effect promotes significant mixing and should be actively avoided where possible. The findings from this work demonstrate that the purge flow swirl and the discrete hole injection angle effects significantly influence endwall cooling and should not be neglected when designing endwall cooling schemes.

Table of Contents

List of Tables

List of Figures

Nomenclature

English Letter Symbols

AR	area ratio	1
C	discharge coefficient	1
C	chord length	m
C_{ax}	axial chord length	m
C_p	blade pressure coefficient, $(p - p_{\mathrm{in}}) \,/\, \left(\frac{1}{2}\rho V_{\mathrm{in}}^2\right)$	1
c_p	specific heat at constant pressure	J/(kg K)
c_v	specific heat at constant volume	J/(kg K)
D	pipe diameter	m
d	internal orifice diameter	m
D_{naph}	binary diffusion coefficient for naphthalene in air	m^2/s
DR	coolant density ratio, $\rho_{\mathrm{c}}/\rho_\infty$	1
E_{hw}	hot-wire voltage	V
E_{LVDT}	LVDT voltage	V
E_{PT}	pressure transducer voltage	V
E_{TC}	thermocouple voltage	V
F	heat/mass analogy factor, Nu/Sh	1
g	local acceleration due to gravity	$\mathrm{m/s}^2$
h	heat transfer coefficient	$\mathrm{W/(m^2\,K)}$
h_{m}	mass transfer coefficient, $\dot{m}'' / \left(\rho_{\mathrm{v,w}} - \rho_{\mathrm{v,iw}}\right)$	m/s
h'_{m}	mass transfer coefficient, $\dot{m}'' / \left(\rho_{\mathrm{v,w}} - \rho_{\mathrm{v},\infty}\right)$	m/s
K	acceleration parameter, $K = \frac{\nu}{V^2}\frac{\mathrm{d}V}{\mathrm{d}s}$	1
k	thermal conductivity	W/(m K)
k	turbulent kinetic energy, $\frac{1}{2}\left(\overline{u'^2} + \overline{v'^2} + \overline{w'^2}\right)$	J/kg
$\dot{m}$	mass flow rate	kg/s
MFR_{h}	discrete hole mass flow ratio, $15\dot{m}_{\mathrm{h}}/\dot{m}_{\mathrm{in}}$	1
MFR_{s}	slot mass flow ratio, $\dot{m}_{\mathrm{s}}/\dot{m}_{\mathrm{in}}$	1
M_{h}	discrete hole blowing ratio, $(\rho_{\mathrm{h}} V_{\mathrm{h}})/(\rho_{\mathrm{in}} V_{\mathrm{in}} \frac{1+AR}{2})$	1
M	molar mass	kg/mol
$\dot{m}''$	mass flux	$\mathrm{kg/(s\,m^2)}$
M_{s}	slot blowing ratio, $(\rho_{\mathrm{s}} V_{\mathrm{s,ax}})/(\rho_{\mathrm{in}} V_{\mathrm{in}})$	1

n	number of experimental replications performed	1
$NHFR$	net heat flux reduction, $1 - q''_{\mathrm{w}}/q''_{\mathrm{w},M0}$	1
$\overline{NHFR}$	pitchwise-averaged net heat flux reduction	1
$\overline{\overline{NHFR}}$	area-averaged net heat flux reduction	1
Nu	Nusselt number, hC/k	1
p	pressure	Pa
Pr	Prandtl number, $c_p\mu/k$	1
q''	heat flux	$\mathrm{W/m^2}$
R	resistance	Ω
Re	blade Reynolds number based on cascade outlet velocity, $\rho V_{\mathrm{out}} C/\mu$	1
R	specific gas constant, $\overline{R}/M$	$\mathrm{J/(kg\,K)}$
$\overline{R}$	universal gas constant	$\mathrm{J/(mol\,K)}$
s	distance measured along a streamline	m
Sc	Schmidt number, ν/D_{naph}	1
Sh	Sherwood number, $h_{\mathrm{m}}C/D_{\mathrm{naph}}$	1
Sh'	Sherwood number, $h'_{\mathrm{m}}C/D_{\mathrm{naph}}$	1
$\overline{Sh}$	pitchwise-averaged Sherwood number	1
$\overline{\overline{Sh}}$	area-averaged Sherwood number	1
s_{p}	distance measured along the pressure surface of a blade	m
s_{s}	distance measured along the suction surface of a blade	m
St	Stanton number, $h/\left(\rho V_\infty c_p\right)$	1
St_{m}	mass Stanton number, h_{m}/V_∞	1
T	temperature	°C
t	time	s
Tu	turbulence intensity, v_{RMS}/V	1
u	velocity component in the x-direction	m/s
U_x	expanded uncertainty of variable x	$[x]$
$\overline{u}$	time-averaged velocity component in the x-direction	m/s
u'	fluctuating velocity component in the x-direction	m/s
u^+	streamwise velocity in wall coordinates, $\overline{u}/u_\tau$	1
u_τ	friction velocity, $\sqrt{\tau_{\mathrm{w}}/\rho}$	m/s
V	mean velocity, $\sqrt{\overline{u}^2 + \overline{v}^2 + \overline{w}^2}$	m/s
v	velocity component in the y-direction	m/s
$\overline{v}$	time-averaged velocity component in the y-direction	m/s
v'	fluctuating velocity component in the y-direction	m/s
v_{RMS}	root mean square of the turbulent velocity fluctuations, $\sqrt{\frac{\overline{u'^2}+\overline{v'^2}+\overline{w'^2}}{3}}$	m/s
w	velocity component in the z-direction	m/s
$\overline{w}$	time-averaged velocity component in the z-direction	m/s
w'	fluctuating velocity component in the z-direction	m/s
x	a spatial coordinate in the cartesian coordinate system	m

Y	expansibility factor	1
y	a spatial coordinate in the cartesian coordinate system	m
y^+	wall-normal distance in wall coordinates, yu_τ/ν	1
z	a spatial coordinate in the cartesian coordinate system	m

Greek Letter Symbols

β_1	blade inlet angle	$^\circ$
β_2	blade outlet angle	$^\circ$
γ	ratio of specific heats, c_p/c_v	1
δ	boundary layer thickness at $u = u_\infty$	m
δ_1	displacement thickness	m
δ_2	momentum thickness	m
δ_{99}	boundary layer thickness at $u = 0.99u_\infty$	m
Δp	pressure differential	Pa
ε	turbulent kinetic energy dissipation	$\mathrm{m}^2/\mathrm{s}^3$
η	Kolmogorov length scale	m
η_{aw}	adiabatic wall film cooling effectiveness, $(T_{\mathrm{aw}} - T_\infty)/(T_{\mathrm{c}} - T_\infty)$	1
η_{iw}	impermeable wall film cooling effectiveness, $(\rho_{\mathrm{v,iw}} - \rho_{\mathrm{v},\infty})/(\rho_{\mathrm{v,c}} - \rho_{\mathrm{v},\infty})$	1
$\overline{\eta}_{\mathrm{iw}}$	pitchwise-averaged impermeable wall film cooling effectiveness	1
$\overline{\overline{\eta}}_{\mathrm{iw}}$	area-averaged impermeable wall film cooling effectiveness	1
θ	swirl angle, $\tan^{-1}(V_{\mathrm{s,tan}}/V_{\mathrm{s,ax}})$	$^\circ$
μ	dynamic viscosity	$\mathrm{kg}/(\mathrm{m\,s})$
ν	kinematic viscosity, μ/ρ	m^2/s
ρ	density	kg/m^3
τ_w	wall shear stress	Pa
ϕ	non-dimensional coolant vapor density, $(\rho_{\mathrm{v,c}} - \rho_{\mathrm{v},\infty}) / (\rho_{\mathrm{v,w}} - \rho_{\mathrm{v},\infty})$	1

Subscripts

∞	evaluated in the freestream at the outer edge of the boundary layer
0	corresponding to the pure air injection experiment
1	corresponding to the naphthalene-saturated injection experiment
ax	axial direction
c	coolant
out	evaluated at the cascade outlet conditions
h	discrete hole coolant
in	evaluated at the cascade inlet conditions
M0	corresponding to $M = 0$ conditions (no coolant injection)
naph	naphthalene
ref	reference
s	slot coolant
s	solid

tan	tangential direction
v	vapor
w	wall

Chapter 1

Introduction

1.1 Gas Turbines

Gas turbine usage is widespread for propulsion and power generation. The basic operation of a gas turbine is explained briefly. Ambient air passes through a compressor to increase its pressure. Heat is then added to the high-pressure air in a combustion chamber. The hot, high-pressure air is then expanded through a turbine, which powers the compressor. Excess power from the turbine can then be used to produce shaft work for power generation. Alternatively, a nozzle is located downstream of the turbine to generate thrust for propulsion. Figure 1.1 shows a schematic of a gas turbine engine.

With energy demands increasing and non-renewable energy sources decreasing, there is a natural demand and push for highly efficient and highly reliable gas turbine engines. Classical thermodynamics reveals that higher turbine inlet temperatures are required to increase the turbine power output and to increase the energy efficiency of the turbine. In practice, thermodynamic considerations are not the only driving factors: material requirements and other design constraints must be considered. While laboratory ideas such as ceramic materials have been proposed for their very high failure temperatures, in practice these are not currently mechanically robust enough for turbomachinery. Instead, turbine blades are cast out of superalloys, which have excellent mechanical characteristics. Modern turbine inlet temperatures have risen to levels at or even above the failure temperature of the advanced superalloys. This result is only possible with a careful design of the turbine cooling system: typically a combination of internal and external cooling is used on the surfaces that need protection. High-pressure cooling air is readily available for use as cooling fluid by

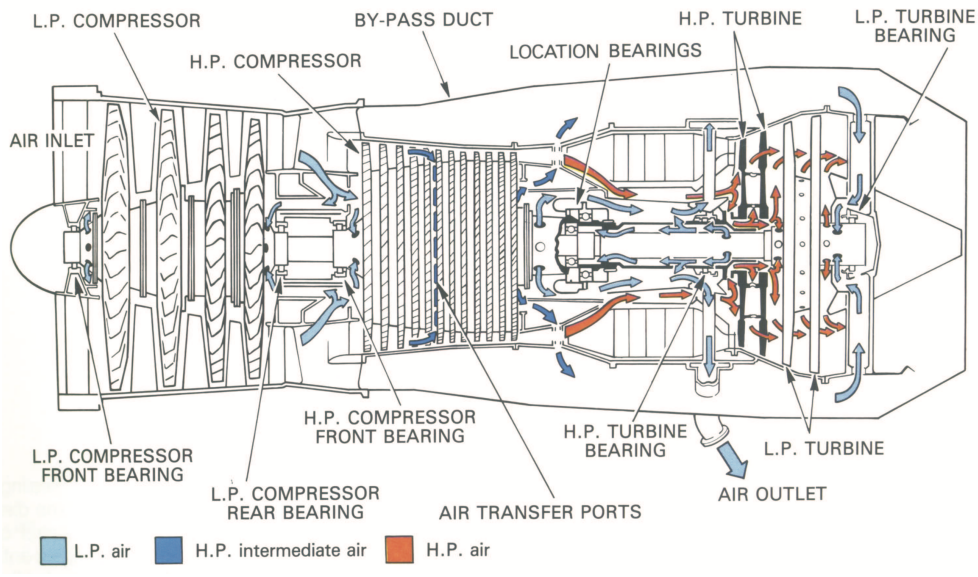

Figure 1.1: Gas Turbine Engine (Rolls Royce, 1986)

taking compressor exit air and bypassing the combustion chamber. This cooling air is routed to key cooling locations. Figures 1.1 and 1.2 illustrate typical coolant routing in a gas turbine.

A primary external cooling method that has gained widespread usage in gas turbines is film cooling. In film cooling, coolant air is discharged through the surface and provides a protective film of coolant between the hot working fluid and the turbine passage surfaces that are to be protected. Film cooling techniques are used on nozzle guide vanes, rotor blades, and on the vane and blade endwall surfaces as pictured in Fig. 1.3. They are especially critical in the first few turbine stages where the working gas is at its highest temperature. The temperature profile exiting the combustor (upstream of the turbine) is approximately parabolic, and thus the highest thermal loads are found on the stator vane and the rotor blade surfaces. Therefore, much of the first turbine film cooling studies have focused their efforts on these surfaces. More recently, this temperature profile has flattened due to combustor redesigns intended to reduce emissions and increase combustor exit temperatures (Simon and Piggush, 2008). Due to these advances, an increased heat load is occurring on the turbine endwall, and much research effort is currently devoted to endwall film cooling. Endwall region cooling presents a challenging problem due to the complex secondary flow structures in the blade passages. A depiction of secondary endwall flow patterns

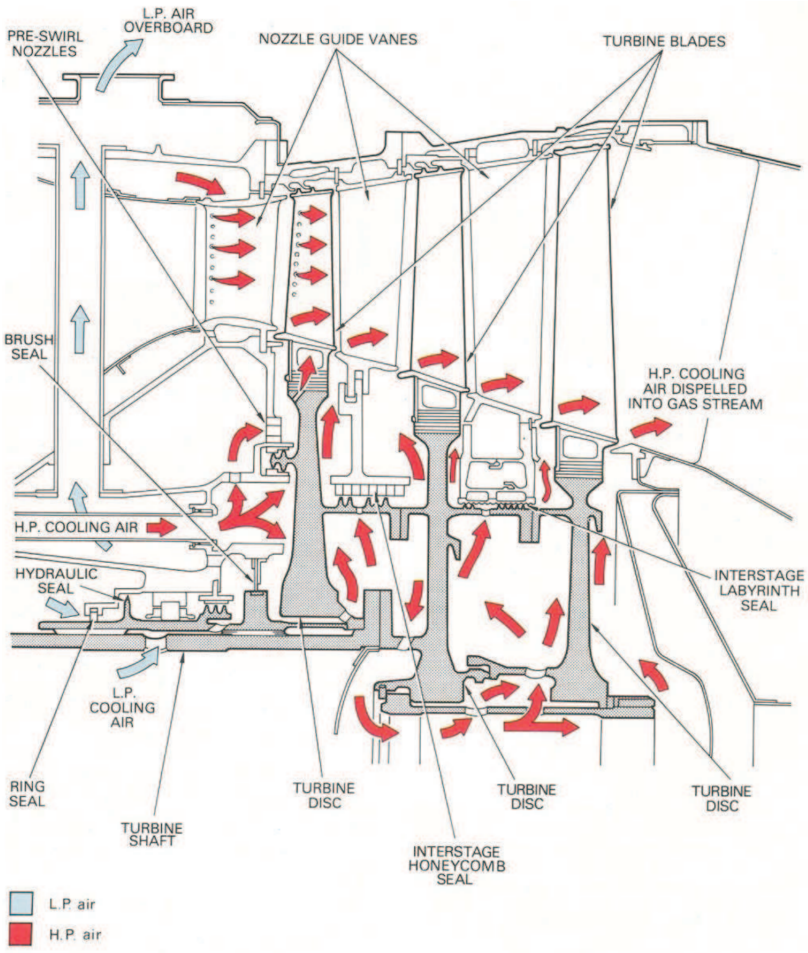

Figure 1.2: Wheelspace Coolant Flow Paths (Rolls Royce, 1986)

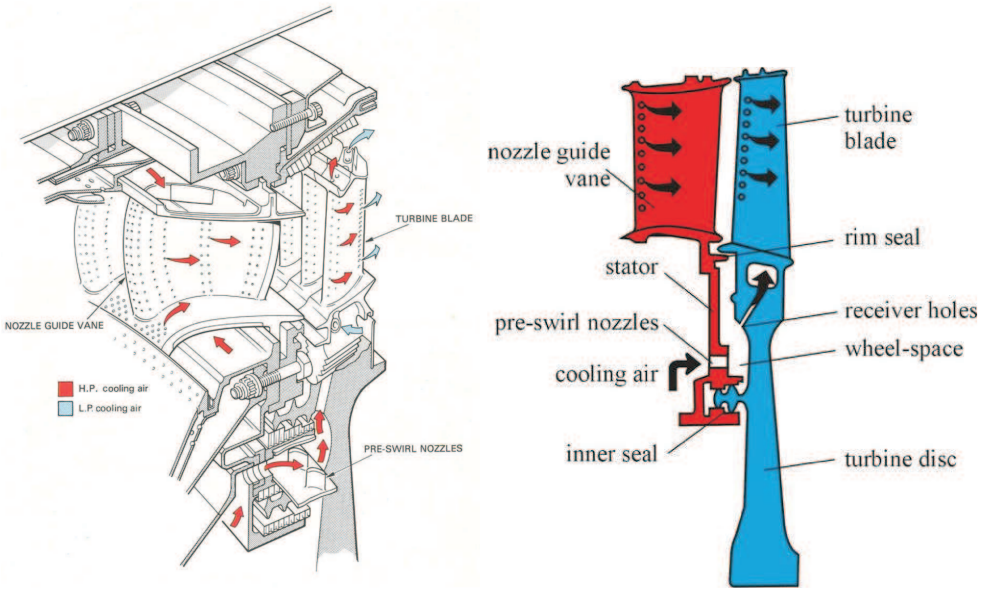

Figure 1.3: Passage Film Cooling (Rolls Royce, 1986)

in a turbine passage is shown in Fig. 1.4. It is found to be particularly challenging to cool near the leading edge stagnation point of the endwall and throughout the passage on the endwall surface near the pressure side. This latter difficulty is due to the secondary flows, which sweep coolant from the pressure side to the suction side along the endwall and promote mixing via the vortex flows within the passage. The primary means of cooling the endwall is achieved using an arrangement of discrete film cooling holes placed strategically on the endwall surface. Another cooling source for the endwall is the purge flow coolant injected between the rotor and stator sections of the turbine. The purge flow is primarily used to purge the wheelspace of hot gas or to prevent ingestion of hot gas into the gap which could damage turbine disk components However, if the purge flow is appropriately utilized, additional discrete film cooling holes on the endwall surface might be eliminated or reduced. These endwall cooling paths are both shown in Fig. 1.3.

In a gas turbine engine, the relative motion between the stator and rotor endwall surfaces leads to the purge flow having a swirling flow behavior (azimuthal flow component in a gas turbine) both in the stator and rotor reference frames. This swirling flow is directed towards the suction side of the blade, meaning the pressure side of the endwall may be particularly challenging to cool with purge flow coolant

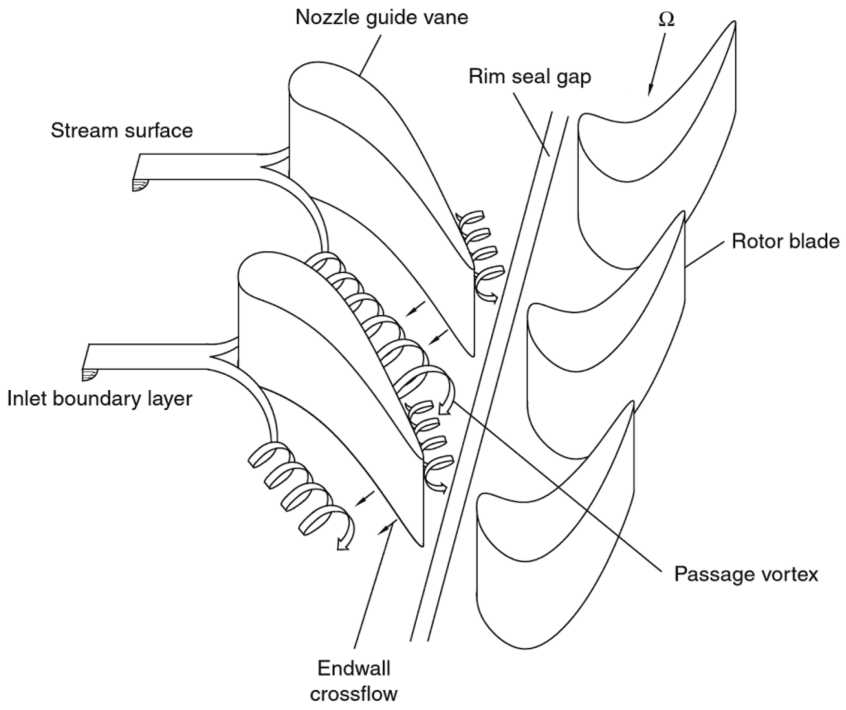

Figure 1.4: Nozzle Vane and Rotor Blade Endwall Flows (Childs, 2010)

alone. When designing the endwall cooling scheme in a turbine blade passage, it is critical to account for this relative coolant swirl behavior properly. Without accounting for this effect, there is a risk of inadequate film cooling coverage on the endwall surface. Furthermore, due to the difficulty in cooling the endwall with purge flow alone, discrete holes are usually positioned throughout the passage and especially on the pressure side to achieve adequate endwall cooling.

1.2 Objectives

The goal of this research is to experimentally investigate the influence of purge flow swirl and passage discrete hole injection angle on blade passage endwall film cooling using the naphthalene sublimation technique. The research aims to investigate cooling performance over a range of experimental conditions, including varying purge flow rate, varying purge flow swirl angle, and varying rim seal geometry (simplified and realistic geometries). Additionally, the effect of discrete hole film cooling is evaluated both with and without the purge flow coolant injection. The discrete hole blowing rates are

varied along with their injection angle to understand the effect of discrete hole injection direction on film cooling. The work is split into four different distinct experimental configurations: (1) purge flow coolant injection with straight slot geometry, (2) purge flow coolant injection with realistic slot geometry, (3) discrete hole coolant injection, and (4) combined purge flow coolant injection (realistic slot) with discrete hole coolant injection.

This thesis is organized to explain the experimental methods and significant results related to the stated objectives. Chapter 2 includes a literature review of the work in the area of passage flow structures, endwall heat transfer, and endwall film cooling. Chapter 3 outlines the experimental facilities used in this work. Chapter 4 details the experimental techniques used to accomplish the stated objectives, including the experimental procedures involved in making mass flow and film cooling measurements. Chapter 5 details the qualification of the wind tunnel facility and characterizes the test section flow. Chapter 6 presents the results and discusses the detailed results achieved in this work. Chapter 7 summarizes and concludes the key findings made in this work and suggests potential future work in this area.

Chapter 2

Background

Turbine endwall flow, heat transfer, and film cooling have received significant attention from researchers due to their importance in gas turbine engine operation and due to their inherent complexities, which warrant significant study. A background is given in this chapter that summarizes the various studies and work done in this field. Typically, these studies will simplify the vast majority of the complex phenomena and only focus on the specific aspect under study. Early work in this field has been done primarily in linear cascades. Currently, much of the more recent work has been transitioning to rotational rigs, which can capture some physics not present in linear cascades. The first section of this chapter discusses flow structure work in a turbine passage. The second section discusses heat transfer work on the turbine endwall. The third section discusses film cooling work on the turbine endwall. The present work is then discussed as it relates to previous studies and works in the field.

2.1 Flow Structures in a Turbine Passage

The flow within a turbine passage is a very complicated fluid mechanics problem. Practically, it is challenging to perform detailed experimental work in an operating engine. Instead, much of the work has been done in linear cascades within wind tunnels. The primary flow within a linear cascade is two dimensional, which follows the contour of the blades. However, the presence of the endwall in a cascade gives rise to the complex secondary flow, which leads to three-dimensional flow. The main secondary flow structures within the turbine passage include the endwall crossflow and various vortex flow systems. The endwall crossflow is a boundary layer flow along

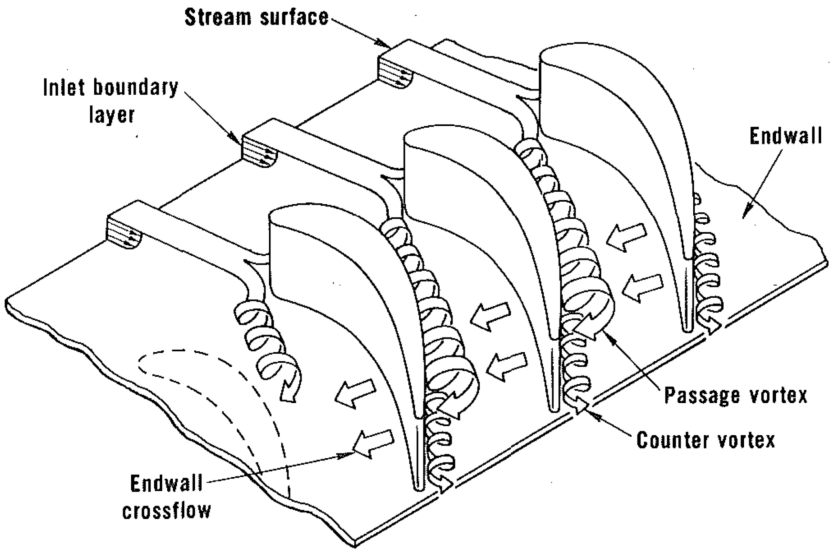

Figure 2.1: Secondary Flows in Turbine Cascade (Langston, 1980)

the endwall that travels from the pressure side to the suction side of the passage, which occurs because the fluid in that region is not moving fast enough to balance the pressure gradient. The vortex flows are found to be very complex and strongly dependent on geometry and other flow conditions.

Langston (1980) was an early pioneer in understanding these phenomena and made flow measurements to gain insight into this complex flow. He found that the approach flow splits at the leading edge of the blade and forms a horseshoe vortex. One leg of this vortex is on the pressure side of the blade, and the other leg is on the suction side of the blade in the next passage. The pressure side leg travels through the passage from the pressure side of the passage to the suction side. This vortex is known as the passage vortex for this reason. The passage vortex meets up with the suction side vortex that remains near the junction of the blade and the endwall. An illustration of these two vortices and the secondary passage flow is presented in Fig. 2.1.

In addition to the horseshoe vortexes starting from the leading edge, other smaller corner vortexes are found both on the pressure and suction sides of the passage. There is also an induced vortex starting from where the passage vortex reaches the suction side of the blade. These vortex systems are described and experimentally confirmed by Wang et al. (1995), who also found that the passage vortex lifts away from the endwall surface after reaching the suction side of the blade. An illustration showing

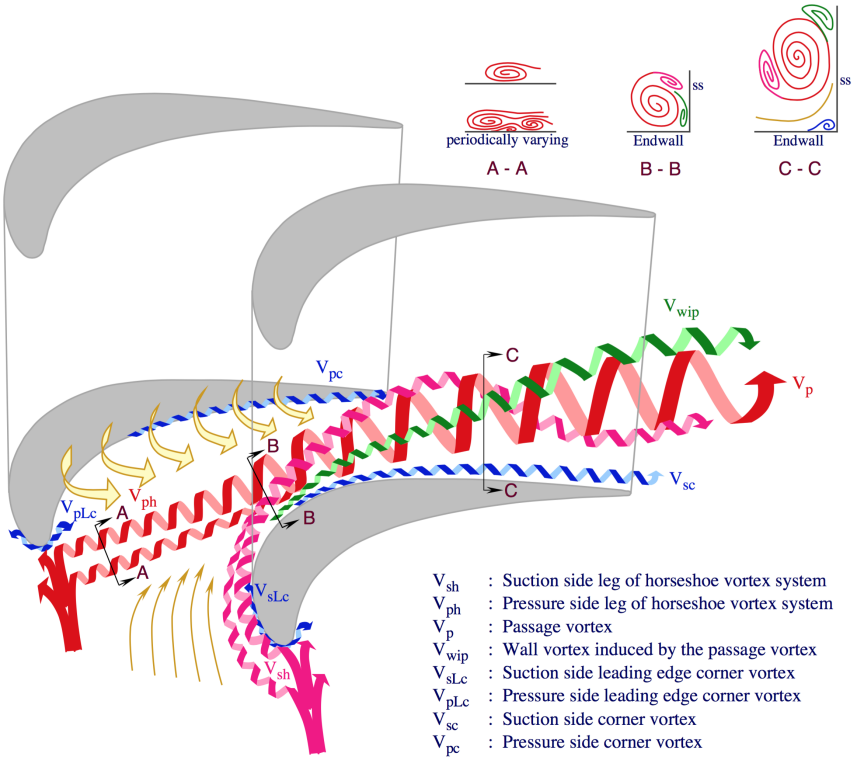

Figure 2.2: Secondary Flows in Turbine Cascade (Wang et al., 1995)

the vortex systems and their interaction is presented in Fig. 2.2.

From an aerodynamic perspective, these secondary flow structures are found to lead to increased energy dissipation, which leads to decreased turbine work and lower turbine efficiencies (Denton, 1993).

2.2 Endwall Heat Transfer

The previously discussed secondary flows near the endwall exhibit a strong influence on endwall heat transfer. Blair (1974) was first to measure heat transfer and film cooling effectiveness on the endwall surface. He found variations in heat transfer due to the secondary flows present in the passage and extreme variations in the film cooling effectiveness due to the coolant air being swept towards the suction wall. Specifically, he found that the presence of the horseshoe vortex significantly enhanced leading edge heat transfer. Graziani et al. (1980) performed a detailed study on endwall heat transfer, which supported Blair's work: increased heat transfer rates were observed at

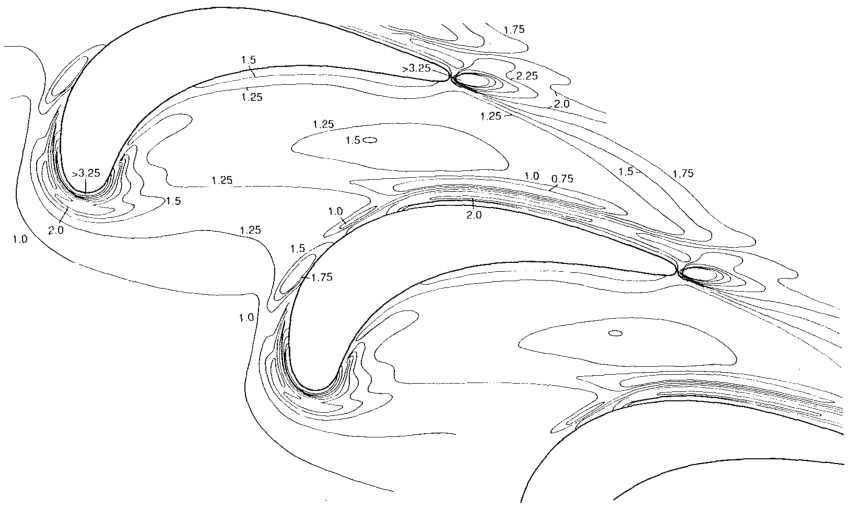

Figure 2.3: Endwall Mass Transfer (Goldstein and Spores, 1988)

the leading edge. Also, he documented increased heat transfer due to the secondary flow on the suction side of the endwall and negligible heat transfer increase due to the secondary flow on the pressure side of the endwall. Goldstein and Spores (1988) made high-resolution mass transfer measurements using the naphthalene sublimation technique and identified two regions with high mass transfer rates: at the leading edge of the endwall surface where the horseshoe vortex forms and on the endwall surface near the trailing edge of the suction side. A contour of these results is presented in Fig. 2.3.

In most of the previously described work, low or moderate levels of freestream turbulence were present at the passage entrance. However, in gas turbine engines, very high levels of turbulence intensity are expected due to many wake generating objects: so it is essential to consider and understand. Radomsky and Thole (2000) determined that increased turbulence intensity increased the heat transfer coefficient throughout the passage, but has a minimal effect near the leading edge and near the trailing edge of the suction side as the local vortexes dominate the heat transfer behavior. Lee et al. (2004) showed that higher freestream turbulence enhanced heat/mass transfer in the central passage area and led to more uniform heat transfer overall.

Blade geometry, including blade fillets, are expected to play a role in passage heat transfer. Han and Goldstein (2006) ran experiments investigating the effects of leading edge fillets and verified that the passage vortex was weakened, leading to decreased

heat transfer rates while the corner vortex was strengthened, leading to enhanced heat transfer rates.

2.3 Endwall Film Cooling

Endwall film cooling attempts to cool the endwall utilizing cooling slots and holes. The endwall secondary flows previously described tended to enhance heat transfer and to push coolant towards the suction side of the passage making cooling the endwall difficult. The following studies give insight into this difficulty. Granser and Schulenberg (1990) reported similar results as Blair, which showed that the highest values for the film cooling effectiveness were found on the suction side of the endwall since the coolant is swept in that direction. Roy et al. (2000) used a slot upstream of the passage which decreased the heat transfer at the leading edge, but a significant portion of the passage did not receive enough coolant. L. J. Zhang and Jaiswal (2001) varied the blowing rate both for an upstream slot and an upstream row of discrete holes and confirmed that it had a substantial positive effect on the film cooling effectiveness. L. Zhang and Moon (2003) also studied the effect of a backward-facing step in combination with the upstream row of discrete holes and found that the film cooling effectiveness in the passage was decreased. Burd and Simon (2000b) and Oke, Simon, Burd, et al. (2000) studied the effects of upstream slot injection. They found that low blowing rates led to inadequate film cooling coverage in the passage and that with high blowing rates the passage vortex was disrupted and better coverage was seen throughout the passage. Nicklas (2001) reported that discrete film cooling holes near the leading edge increased the strength of the leading edge vortex. Thole and Knost (2005) performed a combined study on endwall film cooling with both upstream slot injection and discrete film cooling holes on the endwall. The discrete film cooling holes were found to be necessary to cool the endwall thoroughly. A contour of those results is highlighted in Fig. 2.4. Overall, these results tend to show that the pressure side of the endwall is quite challenging to cool, so increased coolant rates and dedicated cooling holes in that area are likely required to provide complete endwall coverage.

While film cooling works to decrease the adiabatic wall recovery temperature or the driving temperature difference, it often also works to enhance heat transfer coefficients, so one must be careful to consider the effect of both. As a specific example of this,

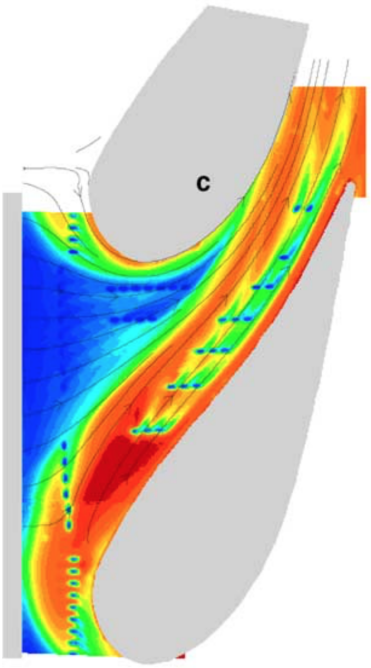

Figure 2.4: Endwall Film Cooling (Thole and Knost, 2005)

Schmidt et al. (1996) and Sen et al. (1996) measured the effect of compound angles for a row of discrete cooling holes and found that both the film cooling effectiveness and the heat transfer coefficient increased when the injected flow direction was misaligned with the main flow. As these are two competing effects, they recommend evaluating the net heat flux reduction to determine the net benefit, if any.

Slot cooling studies traditionally inject the flow in the axial direction: neglecting any swirl effect due to the rotation of the turbine blade. However, the effect of slot cooling swirl (or the coolant injection direction itself) is expected to be a significant effect, potentially as significant as slot coolant rates in determining cooling effectiveness. Therefore, coolant injection swirl may need to be considered when considering cooling endwalls within blade passages. Limited work is available in the literature which considers this effect. Recently, an aerothermal study by Ong et al. (2012) investigated the effect of swirl angle of an upstream slot in a blade passage. They found that adjusting the coolant swirl angle can have a significant effect on axial penetration of the coolant into the passage and the interaction with the secondary flows, which in turn affects the stage efficiencies. Barigozzi et al. (2014) studied the aerothermal

effects of purge flow swirl and found an endwall cooling reduction and aerodynamic efficiency enhancement for realistic swirl levels (compared to neglecting swirl). Stinson et al. (2014) studied coolant swirl from a 45° purge flow slot and found that increased swirl significantly reduced endwall film cooling effectiveness when combined with high blowing rates, while at low blowing rates the effect of the swirl was negligible. Li et al. (2016) found a similar effect, but with a minor enhancement effect due to swirl at low blowing rates. K. Zhang et al. (2019) found that the effect of slot purge flow swirl in the presence of a slashface gap flow was negligible, but with the exception that there was a weak film cooling enhancement effect near the leading edge suction side.

2.4 Relation to Present Work

In recent literature, much attention has been devoted to film cooling on the turbine endwall using upstream injected slot flow to simulate purge flow. Typically in these studies, the flow is injected in the axial direction without any swirl component. However, in the case of cooling the endwall within a rotor blade passage, there is significant swirl level present between the injected flow and the main flow which is expected to have a significant effect on the coolant's ability to cool the endwall. For this reason, the consideration of coolant swirl on endwall film cooling is a core element of this work. Additionally, while discrete holes are typically injected in alignment with the local endwall flow velocity in an ideal design, it may not always be practical due to manufacturing constraints, so the effect of discrete hole injection direction is evaluated in this work. In summary, this work aims to build on much of the previous work by investigating the effects of both purge flow swirl and passage discrete hole injection angle, in addition to typical considerations like coolant flow rates. This work should give insight and a greater understanding of the effects and importance of coolant flow direction and how it affects endwall cooling strategies, particularly in blade passages.

Chapter 3

Experimental Facilities

The experiments for this work were performed in a wind tunnel facility in the Heat Transfer Laboratory at the University of Minnesota. A description of the wind tunnel facility and its injection system is presented in the following sections.

3.1 Wind Tunnel

A 22.4 kW blower draws air at room temperature through an inlet filter. The blower exit passes through a diffuser and a heat exchanger before entering three settling chambers separated by a honeycomb and screens. Air then passes through a square contraction nozzle with an area ratio of 6.25 and an exit cross-section of 45.7 cm $\times$ 45.7 cm. The flow exits the contraction with a low turbulence intensity level and a high degree of flow uniformity. The mainstream velocity level is controlled by a variable torque system that keeps the blower rotating at a constant frequency selected by the operator. The resolution for the blower controller is 0.1 hz. A schematic diagram of the wind tunnel is shown in Fig. 3.1. The wind tunnel's contraction exit passes through a dividing wall between adjacent rooms, one room before the test section and the other at the tunnel's outlet. It is helpful to keep the tunnel's inlet and outlet in separate rooms so that the outlet air does not feed back into the inlet. Weather sealing is used to minimize any airflow between the two rooms. The room on the inlet side of the tunnel has three doors to the building's main hallway, each with louvers. Meanwhile, the room on the outlet side of the tunnel has doors to the main building hallway with no louvers and with weather sealing to minimize airflow. Additionally, the room on the outlet side has venting windows to the outdoors that are opened when the wind

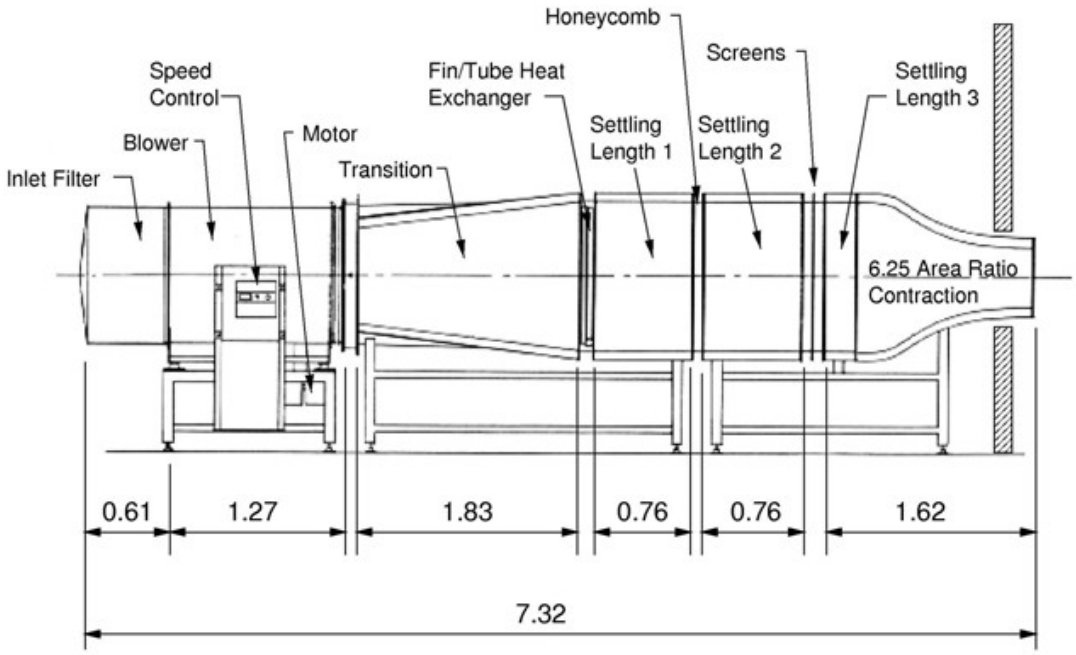

Figure 3.1: Tunnel Schematic (dimensions in m)

tunnel is in use. With this arrangement, inlet air is drawn from the building and discharged out of the building with no air feedback. This setup helps to maintain temperature stability since the building air acts as a large thermal reservoir, and, most importantly, maintains fresh air inlet conditions (naphthalene-free).

3.1.1 Test Section

The test section is connected to the exit of the contraction nozzle and consists of a straight square duct section, a linear cascade section, and two tailboards that make up the outlet of the tunnel (see Fig. 3.2). The straight section's top wall features a slot at the entrance for inserting turbulence generating grids. Additionally, various slots are positioned upstream of the linear cascade section for insertion of instruments. The test section is designed with inside and outside bleed paths to help balance the airflow between the four blade passages. Ultimately, the bleed paths were found to be unneeded and were taped into closed positions. Downstream of the square duct section is the linear cascade, which feeds into the tailboard outlet section. The tailboard outlet section discharges to the room and is then vented through the windows outside

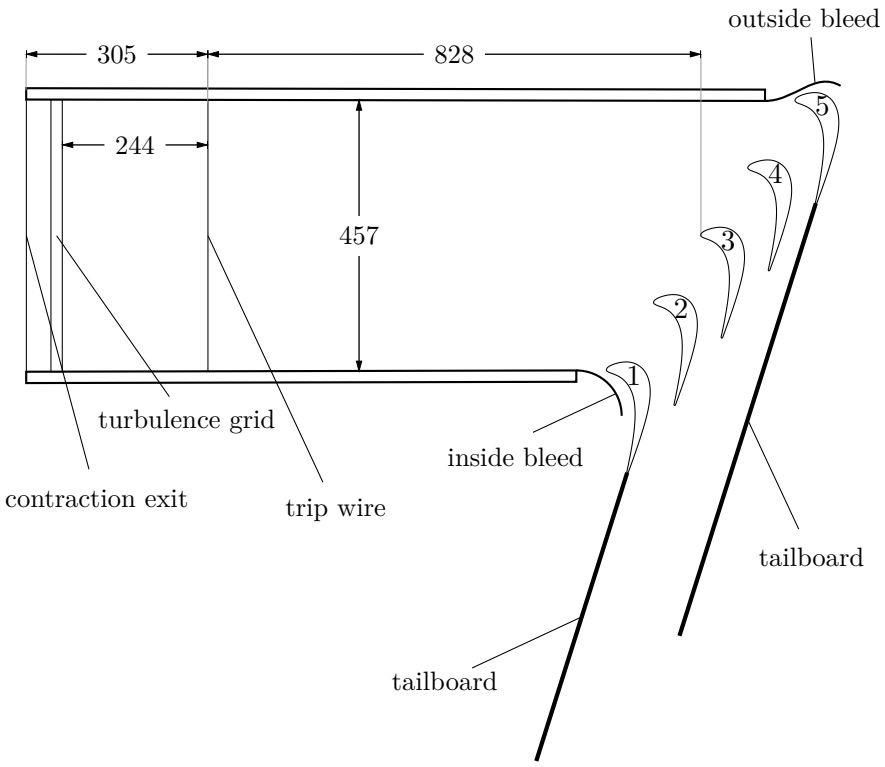

Figure 3.2: Wind Tunnel Test Section (top-down view, dimensions in mm)

Table 3.1: Turbulence Grid Geometry

Mesh Size, M (mm)	Orifice (mm)	Mesh Bar Width (mm)	Solidity, S
38.1	25.4	12.7	0.333

of the building.

In the experiments performed, an effort was made to obtain moderate levels of turbulence ($Tu \approx 5\,\%$). A wake-generating grid comprised of vertical aluminum bars with a rectangular cross-section was used to achieve this. The aluminum bars are rectangular with sharp edges. The grid's geometry is detailed in Table 3.1. Vertical bars were specifically chosen for the grid to minimize any boundary layer overshoot on the bottom wall of the test section. Furthermore, a 1.4 mm tripwire was installed 244 mm downstream from the turbulence grid to help promote boundary layer uniformity along the bottom wall.

Table 3.2: Cascade Geometry

Number of blades	5
Chord length of blades, C	184.15 mm
Axial chord length of blades, C_{ax}	129.64 mm
Blade pitch of cascade, P	138.11 mm
Cascade height, H	457.20 mm
Aspect ratio (span/chord), H/C	2.48
Solidity (pitch/chord), P/C	0.75
Blade inlet angle, β_1	35°
Blade outlet angle, β_2	72.5°
Inlet/outlet area ratio of cascade, AR	2.724
Inlet contraction area ratio	6.25
Fillet radius	6 mm

3.1.2 Linear Cascade

The blades in the present study are large-scale incompressible flow models of a high-pressure turbine rotor blade. The geometrical parameters of the turbine cascade are summarized in Table 3.2. Figure 3.3 illustrates the coordinate systems and the nomenclature used for the cascade.

The linear cascade consists of five blades made of aluminum. The two outer blades are fixed to the bottom and the top walls of the test section and act as sidewalls to the flow. The three central blades are removable and are fixed in place by screws at the top and bottom walls of the tunnel during experiments. The blades were manufactured with a fillet on the bottom endwall to simulate the weld bead from manufacturing. The bottom wall of the linear cascade section has a cutout to insert mass transfer plates. The mass transfer plates serve as the mass transfer surface for endwall mass transfer measurements. Additional details for this plate and the mass transfer technique are discussed in Chapter 4.

3.2 Injection Systems

The injection systems described in this section were designed to facilitate studying the effect of coolant swirl, coolant flow rates, and injection geometry on endwall heat transfer and film cooling. Multiple inlet slots with different geometry and varying

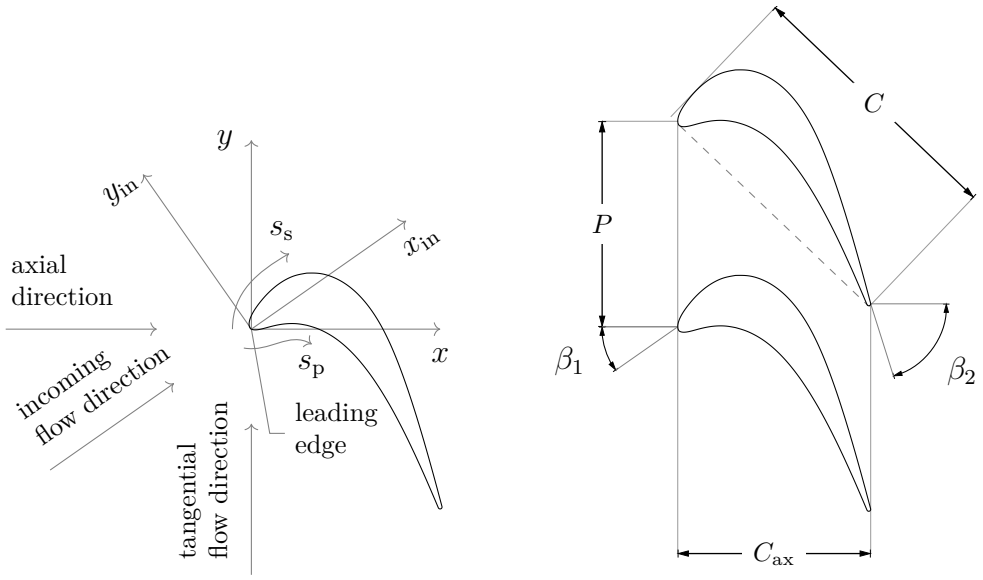

(a) Coordinate Systems (b) Nomenclature

Figure 3.3: Cascade Geometry Diagram

swirl vane angles were built for this study. Additionally, multiple controllable coolant flow paths were built to control the purge flow and discrete hole flow.

3.2.1 Injection Parameters

For the purge flow injection, the coolant's relative flow rate is captured with the slot blowing ratio M_s, defined as:

$$M_s = \frac{\rho_s V_{s,ax}}{\rho_{in} V_{in}} \tag{3.1}$$

The numerator in Eq. (3.1) is found by measuring the total slot mass flow rate divided by the slot injection area. Furthermore, the swirl angle θ for the purge flow is defined as:

$$\theta = \tan^{-1}\left(\frac{V_{s,tan}}{V_{s,ax}}\right) \tag{3.2}$$

where the swirl flow is aligned with the tangential direction in the blade coordinate system (y direction in Fig. 3.3), but directed in the negative direction (toward the suction surface).

For the discrete hole injection, the coolant's relative flow rate is captured with the

blowing ratio M_{h}, defined as:

$$M_{\mathrm{h}} = \frac{\rho_{\mathrm{h}} V_{\mathrm{h}}}{\rho_{\mathrm{in}} V_{\mathrm{in}} \frac{1+AR}{2}} \tag{3.3}$$

The numerator in Eq. (3.3) is found by measuring the total discrete hole mass flow rate divided by the total discrete hole injection area for the 15 holes: $(15A_{\mathrm{hole}})$, where A_{hole} is the area corresponding to the hole diameter of 2.413 mm. The $(1 + AR)/2$ factor in Eq. (3.3) is included since the denominator represents the average mainstream velocity between the passage inlet and outlet, which experiences acceleration throughout the passage. Note that the definition is as if the mass flow rate from each hole is equal. However, in practice, this will not be the case since the holes furthest downstream will receive the most mass flow rate compared to holes most upstream since the downstream holes are exposed to the lowest freestream pressure.

Auxiliary Injection Flow Parameters

While the blowing ratios and swirl angle were the primary design parameters used in this work, there are some additional quantities often of interest. The slot mass flow ratio is defined as:

$$MFR_{\mathrm{s}} = \frac{\dot{m}_{\mathrm{s}}}{\dot{m}_{\mathrm{in}}} \tag{3.4}$$

where both quantities are normalized per unit pitch. The mass flow ratio is proportional to the blowing ratio for a given geometry. For the straight slot case in this work, $MFR_{\mathrm{s}} = 0.010\,57 M_{\mathrm{s}}$. For the realistic slot case in this work, $MFR_{\mathrm{s}} = 0.026\,43 M_{\mathrm{s}}$. Similarly, for the discrete hole injection, the discrete hole mass flow ratio is defined as:

$$MFR_{\mathrm{h}} = \frac{15\dot{m}_{\mathrm{h}}}{\dot{m}_{\mathrm{in}}} \tag{3.5}$$

where the factor of 15 is due to the 15 discrete holes per passage. For the geometry in this work, $MFR_{\mathrm{h}} = 0.002\,444 M_{\mathrm{h}}$.

The coolant density ratio is defined as:

$$DR = \frac{\rho_{\mathrm{c}}}{\rho_{\infty}} \tag{3.6}$$

In this work, the density ratio for the slot and discrete hole flows were near unity

Table 3.3: Straight Slot Turning Vane Geometry

Vane Angle (°)	Pitch (mm)	Thickness (mm)	Width, W (mm)	Length, L (mm)
30	9.9	0.25	$4/\cos 45° = 5.7$	$18/(\cos 45° \cos 30°) = 29.4$
60	9.9	0.25	$4/\cos 45° = 5.7$	$18/(\cos 45° \cos 60°) = 50.9$

since the pressure at the injection point was assumed to equal to the freestream, the temperature was controlled to be equal to the freestream, and the effect of naphthalene on the density is negligible since it is a trace substance.

3.2.2 Purge Flow Injection Slots

In this work, two different purge flow injection slot geometries were used. First, a simplified geometry referred to as the straight slot geometry was used to study the primary effects of interest without introducing the effect of a more sophisticated coolant injection geometry on the results. Later, a slot geometry with geometric features more in common with injection slots seen in the application was used, which is referred to as the realistic slot geometry.

Straight Slot

The straight geometry slot was installed upstream of the turbine blades to provide the simulated purge flow injection. The wind tunnel test section was modified to accommodate the straight slot, as shown in Fig. 3.4. The straight slot is a 4 mm wide rectangular duct angled at 45° relative to the endwall, with additional details shown in Fig. 3.4.

In this work, the effect of the coolant's blowing ratio and swirl direction was studied. Three interchangeable straight slots were built with turning vanes embedded within the slot to set the coolant swirl angle. The different straight slots were made to produce the following three swirl angles: 0°, 30°, and 60°. Note that the 0° slot was built without turning vanes rather than with 0° vanes. The turning vanes themselves are in the shape of parallelograms with width W and length L. The detailed dimensions for the turning vanes are given in Table 3.3. A photo of one of the straight slots with turning vanes in place is shown in Fig. 3.5.

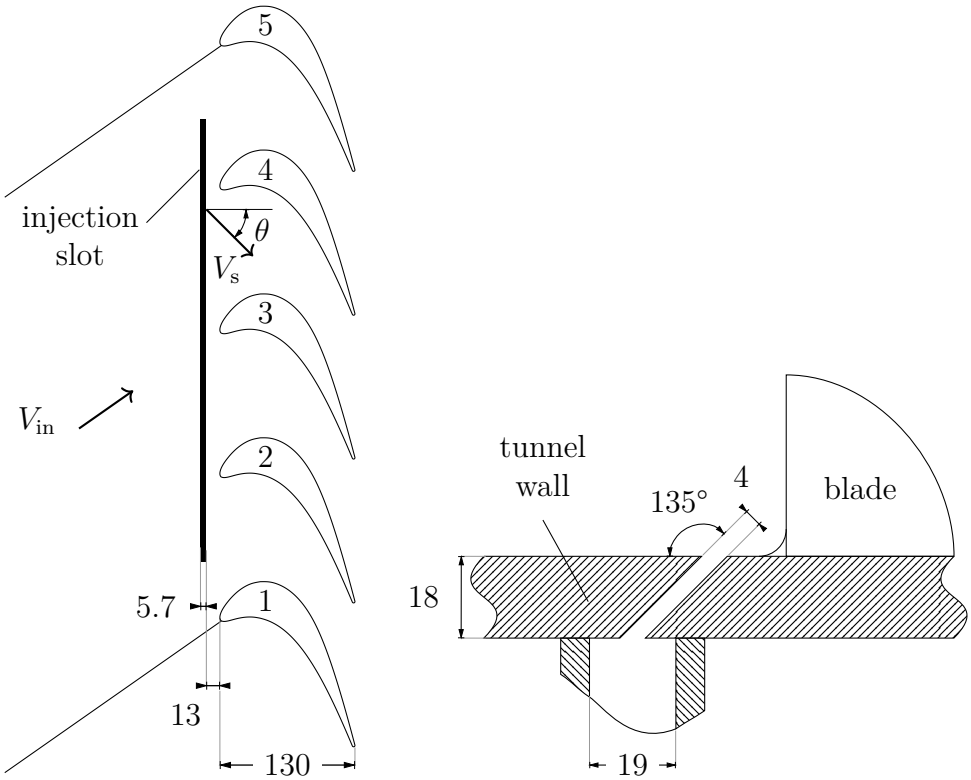

Figure 3.4: Straight Slot Dimensions (dimensions in mm)

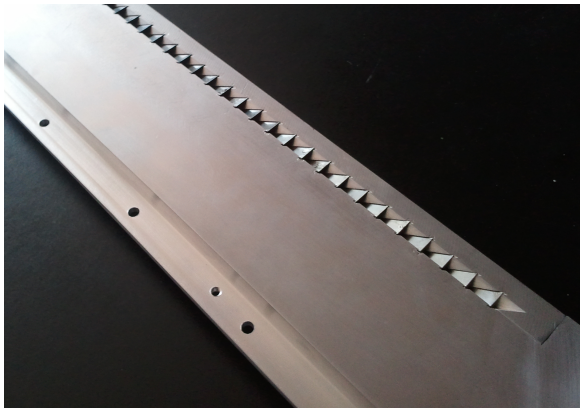

Figure 3.5: Straight Slot Insert with Turning Vanes

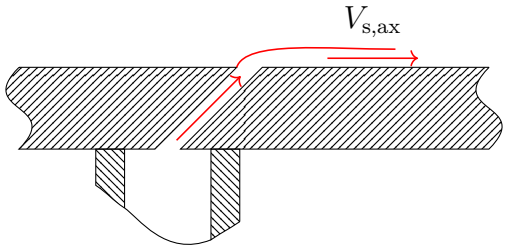

Figure 3.6: Injection Slot Flow Direction ($V_{s,tan}$ is going out of the page)

For calculating the blowing ratio and the swirl angle, the axial coolant velocity is taken as if the coolant turns 45° and follows the endwall. By doing this, the axial velocity is equivalent to the in-slot axial velocity direction. This velocity equivalency idea is illustrated in Fig. 3.6.

Realistic Slot

Compared with the straight slot, the realistic slot has a more gradual and natural ramp path for the injection flow to travel. This ramp shape is designed to minimize the chance of flow separation leading up to the endwall surface, plus to minimize mixing of the coolant with the main flow. The slot is also enlarged to 10 mm as compared to the 4 mm straight slot. To compensate for the larger flow area, the blowing ratio used for the realistic slot was roughly four-tenths that of the straight slot, resulting in roughly the same amount of coolant (per unit pitch). These features should lead to improved endwall cooling (if all else is equal). The details of the changes to the test section geometry and of the slot itself are shown in Fig. 3.7.

Like the straight slot, multiple versions of the realistic slot were manufactured to study the effect of the swirl angle. The different realistic slots were made to produce the following three swirl angles: 0°, 22.5°, and 45°. The turning vanes are rectangular, and the details are given in Table 3.4. The turning vanes are positioned immediately upstream of the ramp instead of within the ramp for the straight slot. Note that the 0° slot was built without turning vanes rather than with 0° vanes.

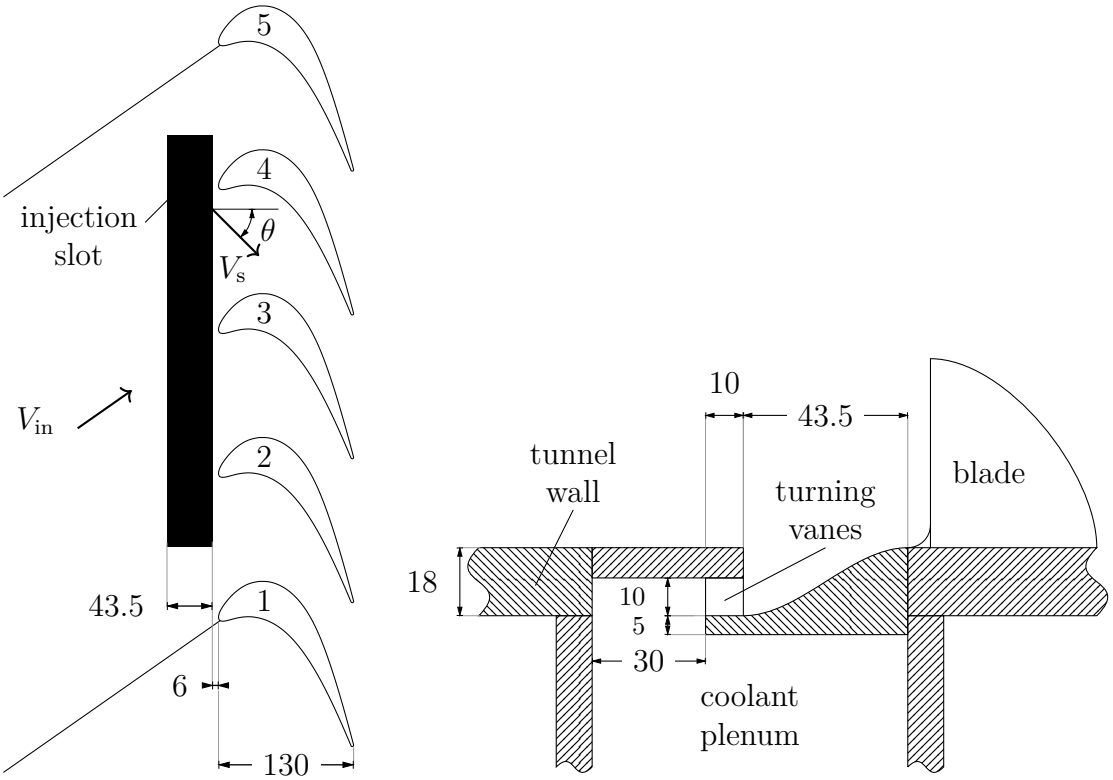

Figure 3.7: Realistic Injection Slot Dimensions (dimensions in mm)

Table 3.4: Realistic Slot Turning Vane Geometry

Vane Angle (°)	Pitch (mm)	Thickness (mm)	Width, W (mm)	Length, L (mm)
22.5	5	0.51	10	$10/\cos 22.5° = 10.8$
45	5	0.51	10	$10/\cos 45° = 14.1$

3.2.3 Discrete Hole Injection

In this study, two different discrete film cooling hole geometries were used. In the first geometry, the holes were chosen so that their flow was roughly aligned with the endwall boundary layer flow direction. This choice was intended to minimize mixing at the outlet of the injection hole while maximizing endwall cooling downstream of the injection hole. In the second geometry, the injection holes were rotated 90° relative to the first geometry. Two separate mass transfer plates were manufactured to accommodate these two different hole flow directions. Each mass transfer plate is equipped with 15 discrete holes. The 15 holes are made up of 5 rows at varying axial positions, with each axial position having 3 holes. The hole exit locations for the two plates are matching; however, the angle of the injection holes differ by the previously stated 90°. There are a few minor exceptions to this due to manufacturing constraints. The specific positions of the 15 holes and their rotation in the cascade geometry coordinate system (normalized by the axial chord length) are listed in Table 3.5. The purpose of using the two different plates was to study the effect of the discrete hole injection direction and to measure the sensitivity of the injection angle on the endwall heat transfer and film cooling. The discrete hole injection locations are shown in Figs. 3.8 and 3.9. The injection hole is designed with a laidback fan-shaped geometry design, with geometry details shown in Fig. 3.10. This design helps to maximize downstream and film cooling coverage area with minimum mixing with the main flow. The injection hole diameter is 2.413 mm, and the total slot length is 13.285 mm, leading to $L/D \approx 5.5$. Ideally, an $L/D \gtrsim 10$ was desired to achieve fully developed flow, but due to design and manufacturing constraints for the mass transfer plates, this was not achievable. However, the achieved value of L/D was considered acceptable. Additionally, due to the difficulty of manufacturing the discrete injection holes into the mass transfer plate, the injection holes were manufactured as individual inserts and installed into the mass transfer plate.

3.2.4 Air Plenum Designs

Two separate plenums supplied by the building high-pressure air line provide the flow for the upstream injection slot and the discrete injection holes. The two plenums were metered with orifice meters (discussed further in Chapter 4). The plenum

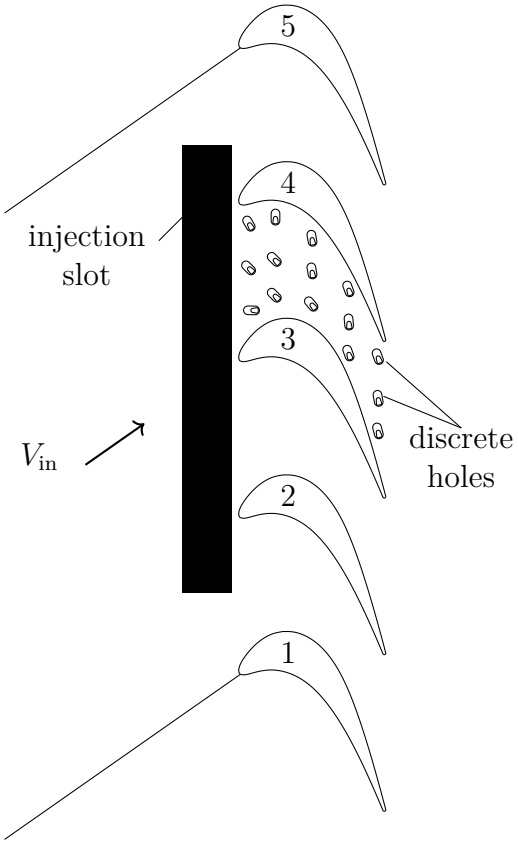

Figure 3.8: Location of Discrete Injection Holes

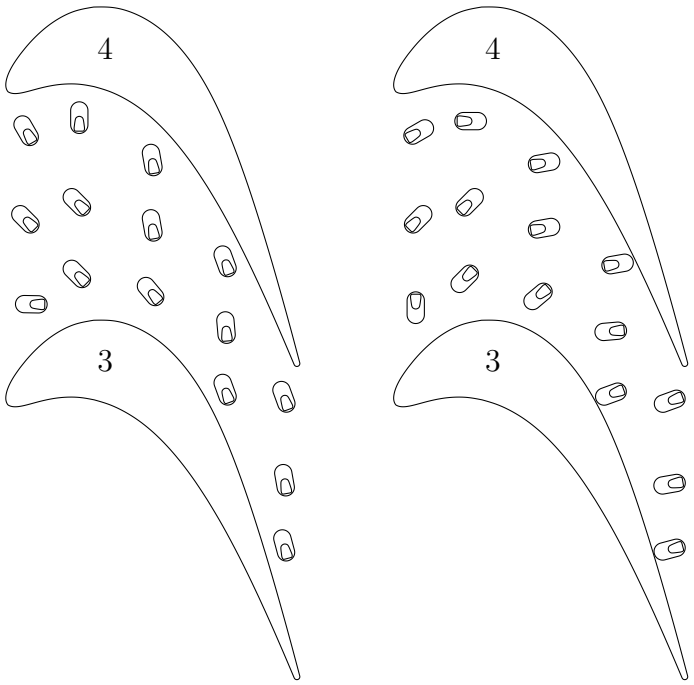

(a) 0° Plate (b) 90° Plate

Figure 3.9: Discrete Hole Locations (zoom-in)

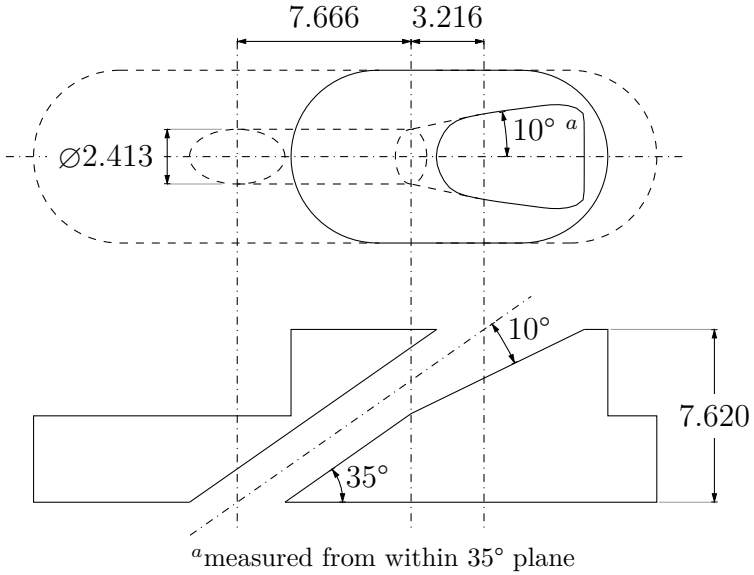

Figure 3.10: Laidback Fan-shaped Hole Geometry (dimensions in mm)

Table 3.5: Discrete Hole Exit Locations

Hole Num.	θ_0	θ_{90}	x/C_{ax}	y/C_{ax}
1	$-60°$	$-150°$	0.075	0.901
2	$-90°$	$-180°$	0.25	0.943
3	$-80°$	$-170°$	0.5	0.800
4	$-70°$	$-170°$	0.75	0.455
5	$-70°$	$20°$	0.95	-0.005
6	$-45°$	$-135°$	0.075	0.601
7	$-45°$	$-135°$	0.25	0.659
8	$-80°$	$-170°$	0.5	0.577
9	$-85°$	$5°$	0.75	0.229
10	$-80°$	$10°$	0.95	-0.290
11	$-1°$	$90°$	0.075^a	0.321
12	$-45°$	$45°$	0.25	0.415
13	$-50°$	$40°$	0.5	0.355
14	$-70°$	$20°$	0.75	0.019
15	$-75°$	$15°$	0.95	-0.511

[a] equal to 0.099 for the 0° plate

temperatures were controlled upstream with tape heaters to match the main flow tunnel temperature. The tape heaters were controlled via a variable AC transformer to supply the appropriate level of heating. Both the leading edge plenum and the discrete hole plenum are capable of supplying naphthalene-saturated air and naphthalene-free air. The saturation process was accomplished by routing the naphthalene through two separate layers of naphthalene. The layers were separated by screens to ensure no naphthalene powder (in solid phase) was carried with the air. The thickness of the first layer was experimentally set to a level that was sufficient for full saturation, so, ideally, the second layer of naphthalene was not needed. However, the second layer was still utilized for two purposes: (1) to act as a backup if the first layer did not fully saturate the air in the case of the naphthalene unfavorably redistributing itself, and (2) to act as a visual test to determine if the flow was saturated. The way this worked was that after each experiment, the naphthalene was topped off in preparation for the next experiment, and if the naphthalene beds were designed and functioning correctly, then naphthalene top-off would be needed in the first layer only, while the second layer's thickness would be unchanged. If this was found to be the case, it meant no

or minimal additional saturation happened in the second layer, and thus the air was saturated or nearly saturated with naphthalene. Note that the naphthalene powder layers were used only in the experiments where the injected air was saturated with naphthalene vapor, and they were removed for the cases when the injected air was naphthalene-free.

Upstream Slot Plenum

The upstream slot plenum was constructed from plexiglass and was positioned underneath the test section. The plenum sat on a platform that could be raised or lowered. The top wall of the plenum had weather sealing, and it was raised against the tunnel wall to create a seal, only allowing the plenum air to exit via the slot. In the plenum, air enters at the bottom and then passes through the naphthalene powder layer (if applicable) followed by a mesh layer, which provides flow uniformity and prevents naphthalene dust from passing. The upstream slot plenum is pictured in Fig. 3.11.

Discrete Hole Plenum

The discrete hole plenum was 3D printed from ABS plastic and was designed to conform to the shape of the bottom of the discrete hole mass transfer plate. The plenum was secured to the bottom of the mass transfer plate with screws, and it had weather sealing around its perimeter for an air-tight seal. Additionally, the ABS plastic was sealed with acetone to make the part air-tight. The 3D printed part is pictured in Fig. 3.12. Upstream of the discrete hole plenum is a dedicated saturation chamber for the discrete hole injection flow path. The saturation chamber is constructed from plexiglass and contains two naphthalene layers. Wire mesh and perforated sheets surround the naphthalene layers. The saturation chamber is pictured in Fig. 3.13.

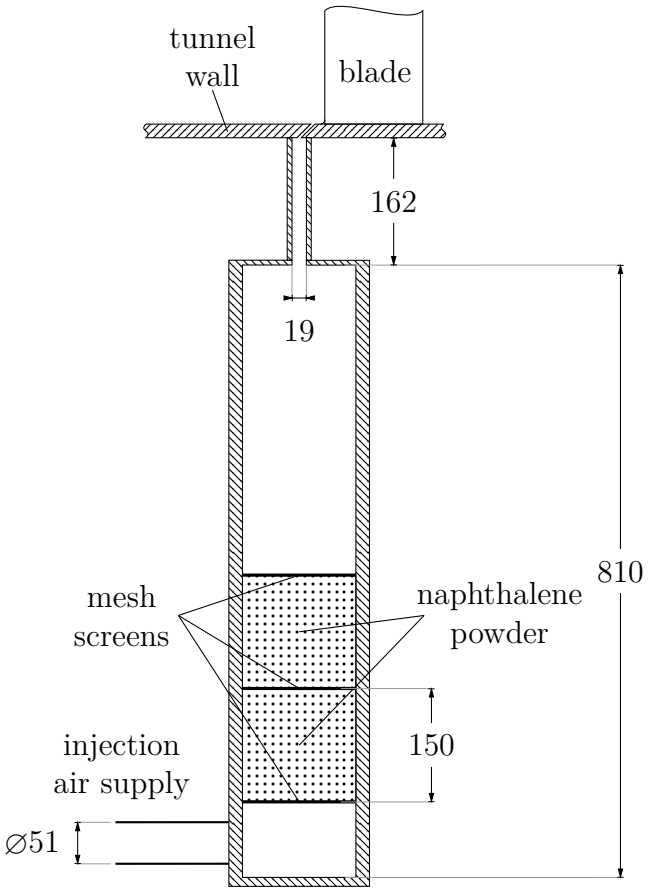

Figure 3.11: Slot Injection Plenum (dimensions in mm)

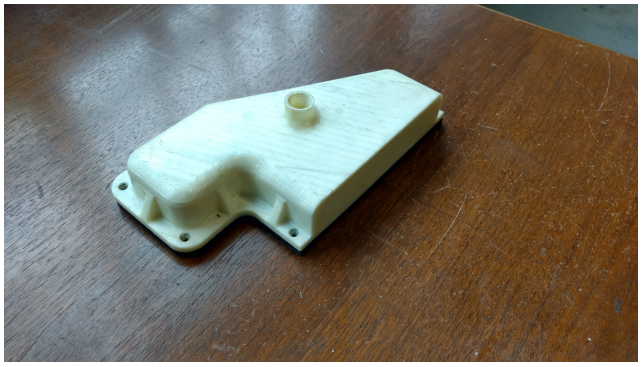

Figure 3.12: Discrete Hole Plenum

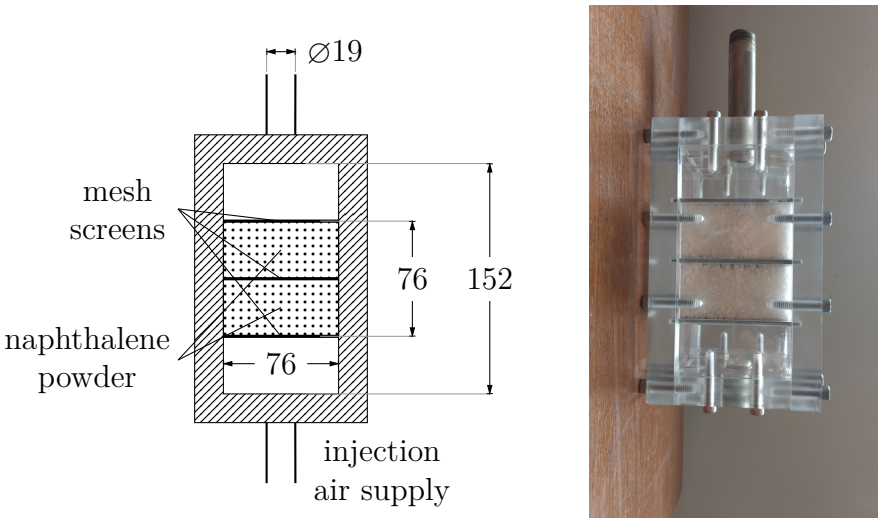

(a) Drawing (dimensions in mm) (b) Photo

Figure 3.13: Discrete Hole Saturation Chamber

Chapter 4

Experimental Technique

In this work, various air flow measurements and naphthalene mass transfer measurements were made. Primary measurements, including pressure, temperature, displacement, and time, were required to process the main results of interest. In the following sections, the measurement equipment, the measurement techniques, and any required calibrations for the measurements are described.

Linux workstations were utilized for data acquisition purposes. Digital signals were sent and received through an IEEE-4888 (GPIB) interface. Multimeters were the primary source of measurement data. A high-speed Agilent 34411A multimeter was used for hot-wire measurements, and a Keithley 2000 multimeter was used for all other measurements. A Keithley 7001 multiplexer was used in conjunction with the Keithley multimeter to select the desired measurement channels.

4.1 Pressure Measurements

4.1.1 Atmospheric Pressure Measurements

The atmospheric pressure was measured using a Setra Model 470 digital pressure transducer. The device works using the SETRACERAM™ capacitive sensor. The manufacturer's short term accuracy is specified as 0.02 % of the full-scale reading, and long term drift is expected to be 0.05 % of the full-scale reading based on the calibration schedule for the instrument. The expanded relative uncertainty level is estimated to be 0.05 % of the full-scale reading, calculated from the root of the sum of squares of the short term accuracy and the long term drift. The full-scale is 110 kPa

Figure 4.1: Setra Model 470 Digital Pressure Transducer

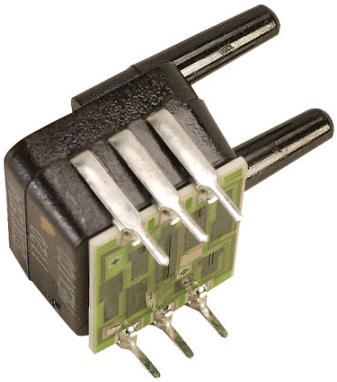

Figure 4.2: OMEGA PXSDX Pressure Sensors

while in barometric pressure range mode, leading to an absolute expanded uncertainty of 60 Pa. The pressure transducer broadcasts its reading over a pressure server and can be accessed by calling the `pressure` command on an Enet managed Linux computer in the Mechanical Engineering building at the University of Minnesota.

4.1.2 Differential Pressure Measurements

Differential pressure measurements are primarily made using OMEGA PXSDX pressure transducers (Fig. 4.2) that produce voltage differences roughly proportional to pressure differences. The readings are used for measuring static pressures inside the wind tunnel (relative to the atmosphere) and for dynamic pressure differences made with pitot-static tubes and orifice plates. Six different pressure transducers were used

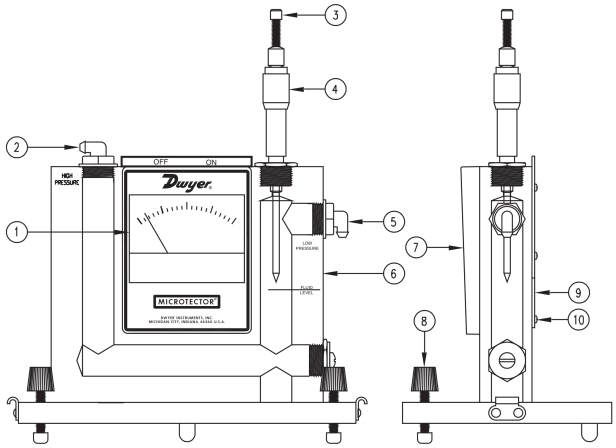

Figure 4.3: Dwyer Microtector Water Manometer

in this work with various pressure differential ranges to accommodate the required measurements as needed. The pressure transducers were soldered onto a prototype board and are powered using a low variance, low noise, constant voltage power source from OMEGA.

Water manometers were also used for calibration purposes: calibrating the pressure transducers and for calibrating the hot-wire. For pressure differentials below 50 mmH2O, measurements were made using a Dwyer Model 1430 Microtector®, shown in Fig. 4.3. The water manometer indicates half of the pressure differential in millimeters of water. By performing manometer height readings to the nearest 0.005 mm at both the zero pressure differential level and with a pressure differential to be measured, the pressure differential can be measured with an expanded uncertainty level of 0.0082 mmH2O or 0.080 Pa. For pressure differentials above 50 mmH2O, measurements were made using glass U-tube manometers with a scale behind the glass that can be read to the nearest 0.5 mm. With both sides of the manometer being read and contributing to the uncertainty, the expanded uncertainty is 0.41 mmH2O or 4.0 Pa.

The general expression for making pressure differential readings within a gas using U-tube manometers filled with a single liquid is as follows:

$$\Delta p = (\rho_{\mathrm{l}} - \rho_{\mathrm{g}})gh \tag{4.1}$$

where the ρ_l is the liquid density and ρ_g is the gas density. The equation implicitly assumes the gas density is the same on either side of the manometer. A first-order correction for this assumption is done by setting ρ_g to the average gas density on either side of the manometer; this average density can be solved for iteratively since one side is typically known and the other is a function of the pressure differential reading.

4.1.3 Pressure Transducer Calibration

The Omega PXSDX miniature temperature-compensated pressure sensors were calibrated against the U-tube water manometers. The pressure differentials were set by flowing air through an orifice and simultaneously making pressure differential readings using orifice taps routed to both the water manometer and pressure transducers. A series of pressure levels were chosen and executed in a random order for calibration purposes. After the data were collected, curve fits were found in the following form:

$$\Delta p = a + bE_{\mathrm{PT}} \tag{4.2}$$

where a and b are fitting parameters and E_{PT} is the voltage output by the pressure transducer. Parameter a is expected to drift with ambient temperature and with time, while parameter b is expected to remain relatively constant. In practice, the pressure transducers are used by first zeroing the pressure difference and making a voltage measurement, designated as $E_{\mathrm{PT},0}$. Then, for a nonzero pressure difference measurement, the pressure differential is found equal to $\Delta p = b\,(E_{\mathrm{PT}} - E_{\mathrm{PT},0})$.

The pressure transducer calibrations are summarized in Table 4.1 and plotted in Figs. 4.4 to 4.9. The key output from the calibration is the coefficient b, and the expanded combined uncertainty for the coefficient is also reported.

4.2 Temperature Measurements

In this work, temperature measurements were made with E-type thermocouples. The thermocouples used an ice bath as a reference, and their open-circuit voltages were measured using a multimeter. A spool of 30 gauge "Special Limits of Error (SLE)" thermocouple wire was purchased from Omega for use. Omega reports that the limits

Table 4.1: Pressure Transducer Calibration Summary

Pressure Transducer	Max Pressure kPa	Slope, b kPa/mV	U_b kPa/mV	Data Points
1 PXSDX-005DV	34.5	0.5810	0.0027	10
2 PXSDX-001DV	6.9	0.3796	0.0018	7
3 PXSDX-005WCDV	1.2	0.061 19	0.000 39	7
4 PXSDX-001DV	6.9	0.3838	0.0029	7
5 PXSDX-001DV	6.9	0.3805	0.0022	7
6 PXSDX-001DV	6.9	0.3826	0.0017	7

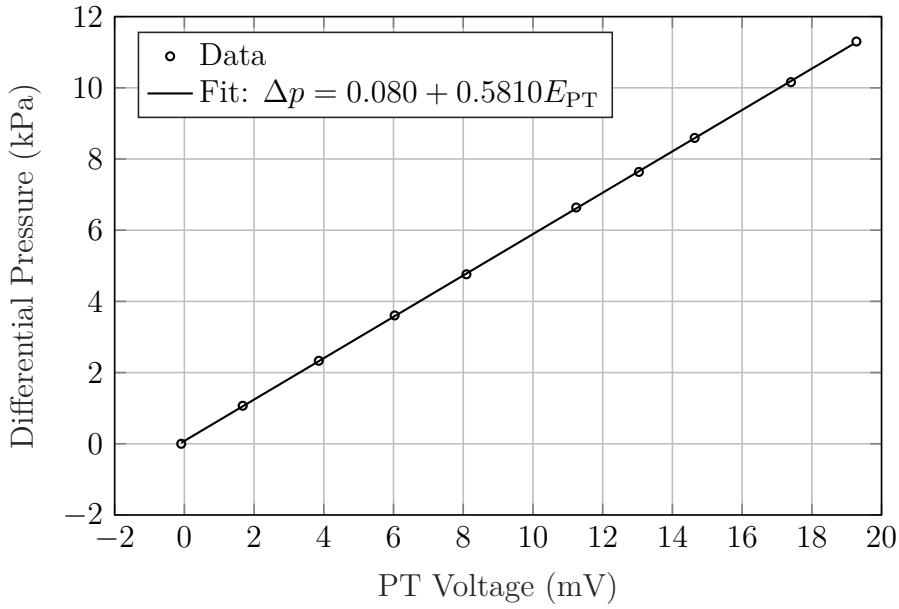

Figure 4.4: Pressure Transducer 1 Calibration

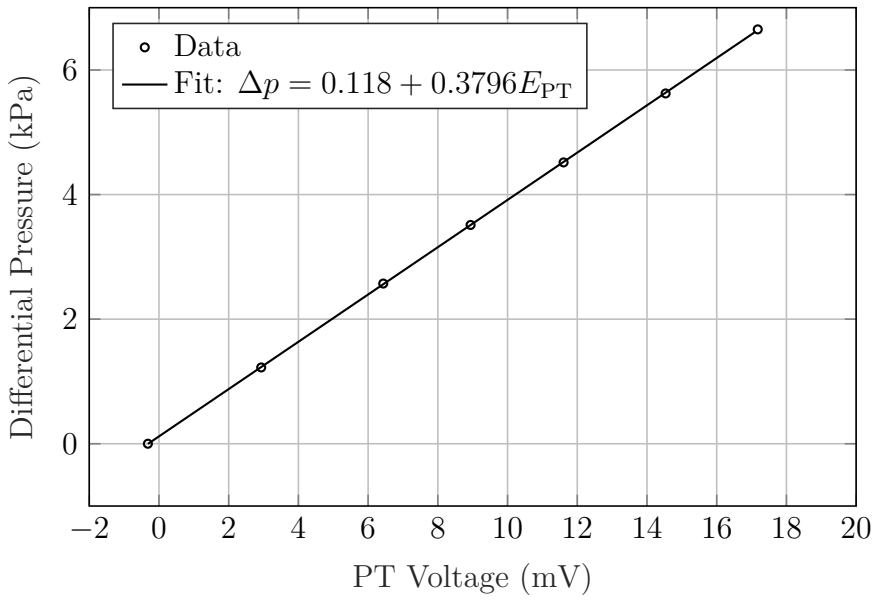

Figure 4.5: Pressure Transducer 2 Calibration

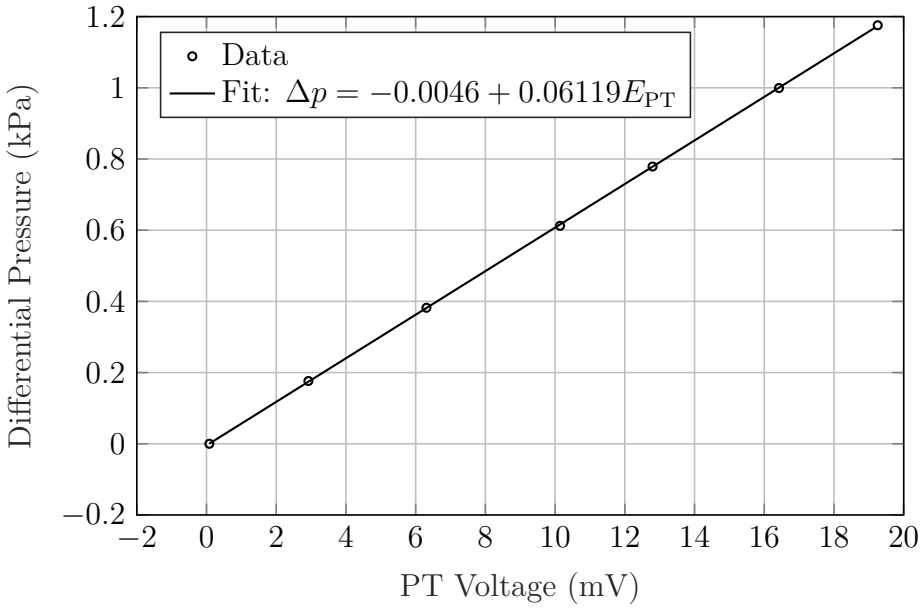

Figure 4.6: Pressure Transducer 3 Calibration

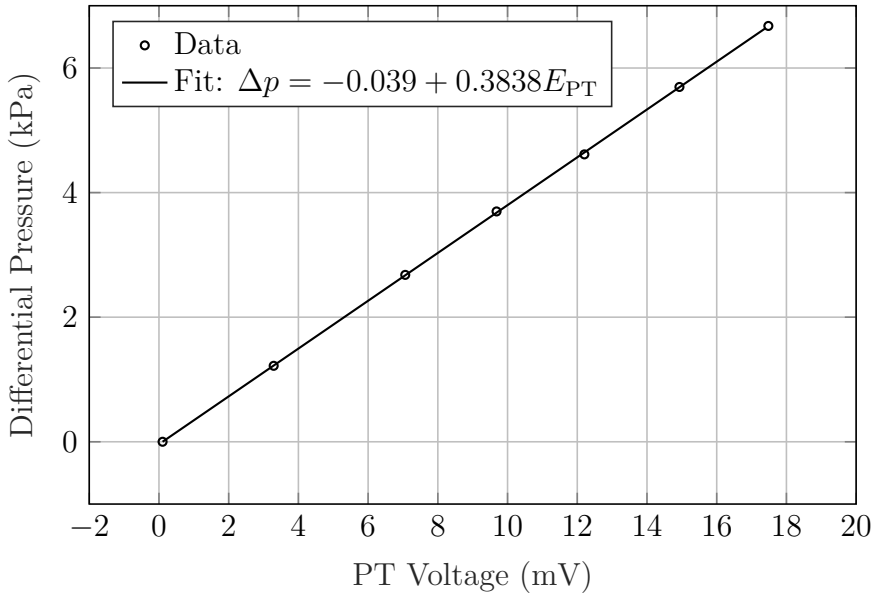

Figure 4.7: Pressure Transducer 4 Calibration

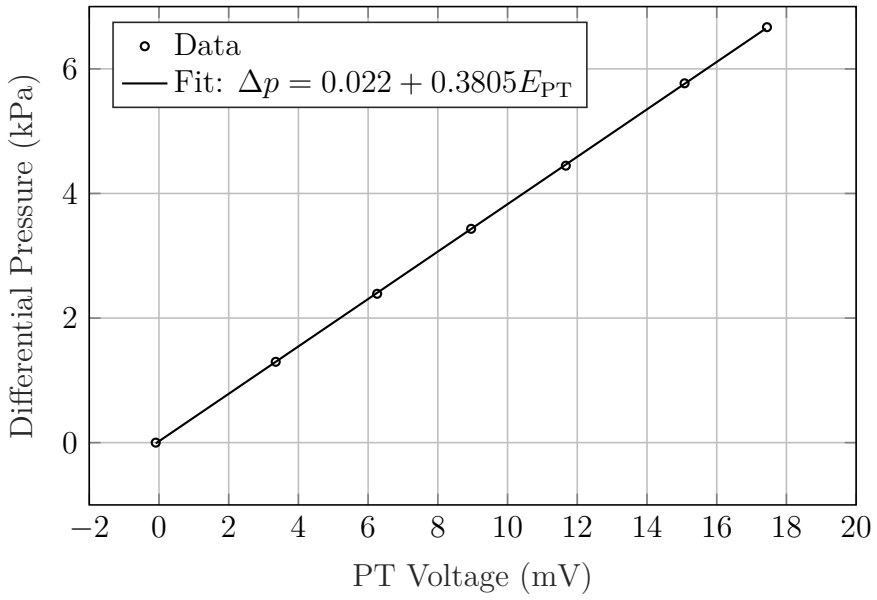

Figure 4.8: Pressure Transducer 5 Calibration

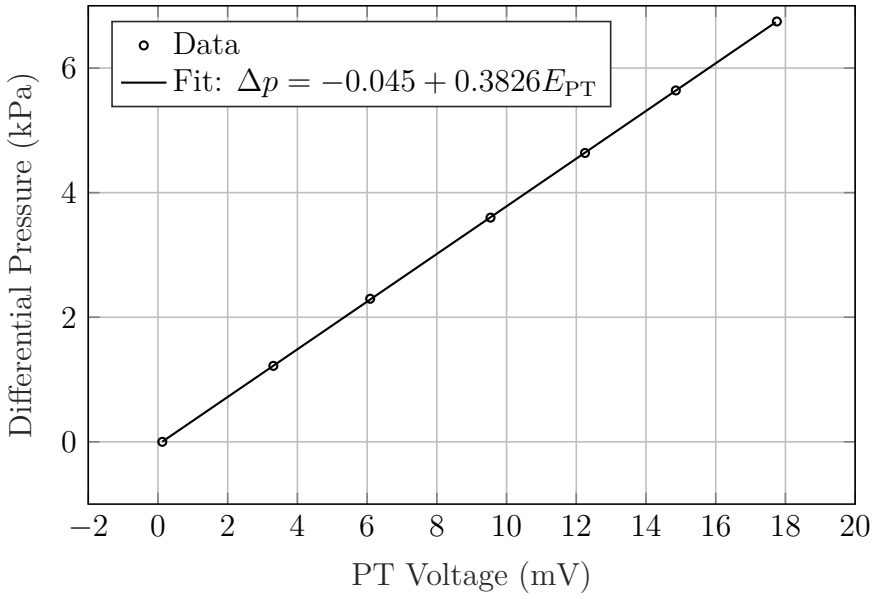

Figure 4.9: Pressure Transducer 6 Calibration

of error for the "special limits of error" wire is the greater of 1 °C or 0.4 %. This level of error was determined to be too large for use in this work: primarily because naphthalene transport properties are sensitive to temperature and the considerable temperature uncertainty would lead to large mass (heat) transfer uncertainties. The thermocouples are calibrated against a standard platinum resistance thermometer (SPRT) in the calibration facility within the heat transfer laboratory at the University of Minnesota in order to overcome this issue.

4.2.1 SPRT Calibration

A Rosemount 162CE SPRT (Fig. 4.10) was used in the calibration facility for calibrating thermocouples. The unit was initially calibrated by the manufacturer in 1982 on the International Practical Temperature Scale of 1968 (IPTS-68). The old SPRT calibration must first be converted to the International Temperature Scale of 1990 (ITS-90) to use it for calibration. The procedure for this conversion is explained in the ITS-90 primary and supplementary material (Bedford et al., 1996; Preston-Thomas, 1990a,b). The result from that process is a calibration valid from 0 °C up to the freezing point of Zinc (419.527 °C). The conversion process technically adds some uncertainty to the resulting SPRT calibration, but it is negligible compared with other

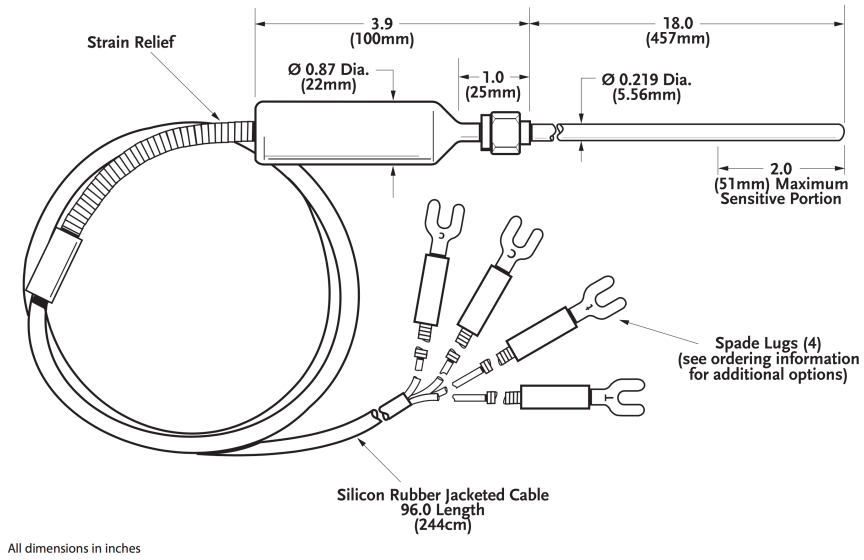

Figure 4.10: Rosemount 162CE SPRT

uncertainties, as detailed later, so it can safely be ignored. Temperatures from the SPRT are determined in terms of the ratio of its resistance R at a temperature and the resistance R at the triple point of water (273.16 K):

$$W(T) = R(T)/R(273.16\,\mathrm{K}) \tag{4.3}$$

Once W is known, the reference function, W_r, can be calculated from the deviation function as defined below:

$$\begin{aligned} W(T) - W_\mathrm{r}(T) = a\,(W(T)-1) + b\,(W(T)-1)^2 \\ +c\,(W(T)-1)^3 + d\,(W(T) - W(660.323\,^\circ\mathrm{C}))^2 \end{aligned} \tag{4.4}$$

where a, b, c, and d are all found via calibration. When an SPRT is calibrated up to the freezing point of silver (961.78 °C), coefficients a, b, c, and d are all fit. However, in this case, the SPRT is only calibrated up to the freezing point of zinc, so $c = d = 0$. The complete calibration can then be described by a, b, and $R(273.16\,\mathrm{K})$ as detailed in Table 4.2. After the reference function, W_r, is calculated, the temperature in degrees

Table 4.2: 1982 SPRT Calibration - Converted to ITS-90

$R(273.16\,\mathrm{K})$	a	b	c, d
25.562 17	$-6.382\,279 \times 10^{-5}$	$-1.350\,632 \times 10^{-5}$	0

Table 4.3: Inverse Reference Function Constants

d_0	439.932 854
d_1	472.418 020
d_2	37.684 494
d_3	7.472 018
d_4	2.920 828
d_5	0.005 184
d_6	−0.963 864
d_7	−0.188 732
d_8	0.191 203
d_9	0.049 025

Celsius can be calculated with the inverse reference function:

$$T = \sum_{i=0}^{9} d_i \left[\frac{W_\mathrm{r}(T) - 2.64}{1.64} \right]^i \tag{4.5}$$

where the values for the constants d_i are given in Table 4.3.

After the original 1982 calibration was converted to the ITS-90 scale, the resistance at the triple point of water was measured since it is expected to exhibit some drift over time. The triple point of water was measured using a water triple point cell (Fig. 4.11). The procedure for its use involves filling the thermometer well with a small amount of ethanol as a thermal contact fluid followed by dropping in dry ice to form the ice sheath around the thermometer well. After the ice sheath gains sufficient size, the well is filled with ethanol and the ice sheath is detached from the thermometer well by using a sharp twisting motion. The triple point cell can then be used for calibration and measurement purposes.

The SPRT is equipped with four wires to perform a high-accuracy 4-wire resistance measurement. Additionally, a standard 10 Ω resistor and a standard 100 Ω resistor were maintained in a resistor oil bath and were used to correct for and minimize the

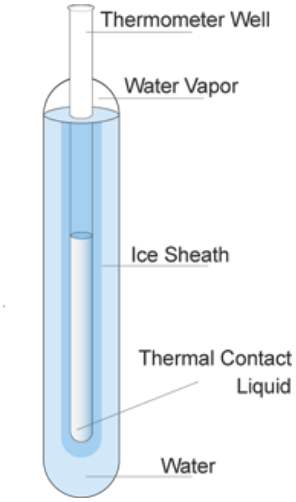

Figure 4.11: Water Triple Point Cell

effect of any multimeter systematic error. If it is assumed the multimeter's systematic error is of the nature that can be explained by an offset and slope correction, the resistance correction can be made in the following way:

$$R_{\text{true}} = R_{\text{true,10}} + \frac{(R_{\text{true,100}} - R_{\text{true,10}})}{(R_{\text{meas,100}} - R_{\text{meas,10}})} (R_{\text{meas}} - R_{\text{meas,10}}) \tag{4.6}$$

where $R_{\text{true,10}}$ and $R_{\text{true,100}}$ are the known true values of the standard resistors, $R_{\text{meas,10}}$ and $R_{\text{meas,100}}$ are the measured values of the standard resistors, and R_{meas} and R_{true} are the measured and true values of the resistance measurement. The true values for the standard resistors are nearly constant but have known functions of temperature; therefore, the oil bath temperature was measured, and the temperature correction was made. With the described approach taken, the resistance of the SPRT can be measured, and its value was found to be equal to $25.563\,89\,\Omega$, which is a drift of $0.001\,72\,\Omega$ relative to the 1982 manufacture calibration value. If this drift had been significant relative to accuracy requirements, then it would have been recommended to undergo a complete recalibration. However, the drift was relatively small, so the original calibration could still safely be used with small modifications. Additionally, if there is evidence that the change in the triple point of water resistance is accelerating over time, it would be suggested to replace the SPRT. In this case, there was no evidence that the water triple point resistance was accelerating over time based on the periodic recordings

for the SPRT triple point resistance since the original calibration. Long term drift in the SPRT's resistance can be explained by two primary phenomena (D. R. White et al., 2007): (1) impurities and high-energy defects, and (2) permanent dimensional changes caused by plastic deformation, volatilization of platinum, and changes due to oxidation. The first type leads to resistance changes that can be well approximated by Matthiessen's rule. The second type leads to changes in resistance at the triple point of water, but not to the general $W(T)$ relationship, so no explicit correction is needed besides accounting for the latest resistance at the triple point of water. If all of the drift were from the first type, Matthiessen's rule would predict the drift in the resistance ratio as the following:

$$\Delta W_{\text{drift}}(T) = W(T) - W_{\text{ideal}}(T) \approx \frac{\Delta R(273.16\,\text{K})}{R(273.16\,\text{K})}\,(1 - W(T)) \tag{4.7}$$

where $\Delta R(273.16\,\text{K})$ is the change in the resistance of the SPRT at water triple point since the 1982 calibration. Since it is generally unknown which types of drift are present, the best course of action is to assume half the drift is from each type, which implies a correction and a correction uncertainty:

$$W_{\text{corrected}}(T) = W(T) - \Delta W_{\text{drift}}(T)/2 \tag{4.8}$$

$$u_{W_{\text{corrected}}(T)} = \sqrt{\Delta W^2_{\text{drift}}(T)/12} \tag{4.9}$$

where the corrected resistance ratio, $W_{\text{corrected}}(T)$, is used in Eq. (4.4) rather than the uncorrected resistance ratio directly.

There are two elemental systematic uncertainty sources for the SPRT calibration: the uncertainty from the initial calibration and the uncertainty related to the long term drift in the SPRT calibration. The estimate for the uncertainty from the initial calibration comes from the recommendation by D. R. White et al. (2007) and the uncertainty due to long term drift (Eq. (4.9)) can be propagated to the temperature reading uncertainty. The combined standard uncertainty from these two effects is shown in Fig. 4.12.

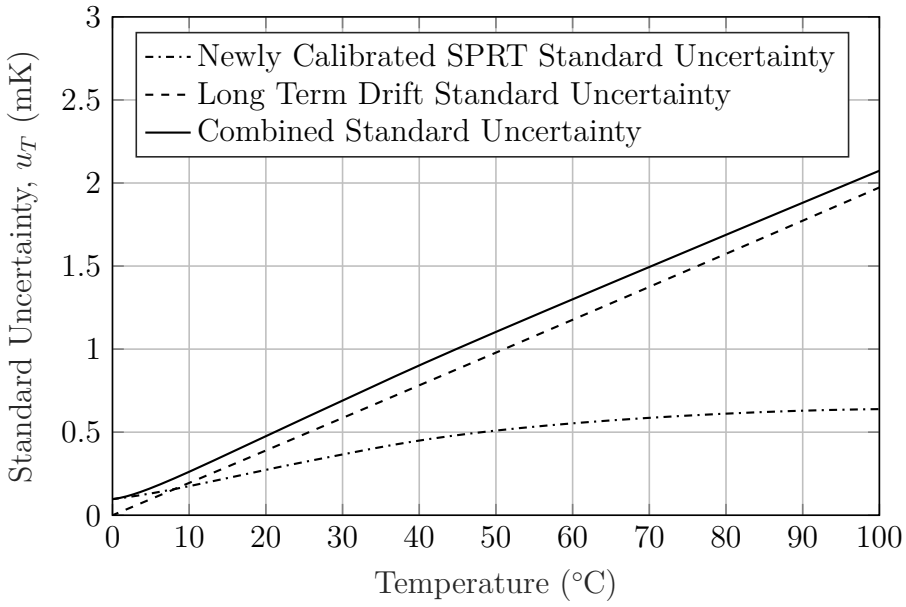

Figure 4.12: SPRT Standard Uncertainty

4.2.2 Thermocouple Calibration

Five bare wire E-type thermocouples were constructed for calibration purposes against the SPRT in the calibration facility (Fig. 4.13). The calibration was performed by submerging the five thermocouples and the SPRT into the calibration water bath and making measurements at different levels for the bath temperature. The bath temperature can be varied via electrical resistance heaters and a refrigeration loop for chilling the water. The refrigeration capacity can be manually controlled via a throttling valve; however, the valve was set to the fully open position during the calibration. The electrical resistance heaters have multiple levels of power output, and the lowest heater power output level that can counteract the refrigeration capacity was chosen for a given water bath set point. The resistance heaters were then controlled via a thermostat that operates in an on-off fashion. The bath was maintained at a nearly uniform temperature by running a bath stirrer throughout the calibration.

Eight different temperature levels were chosen for calibration in the range of 10 °C to 55 °C, and they were executed in random order. After the calibration data were taken, a curve fit regression was performed, which accounts for random error in the voltage reading and random error in the temperature reading (Fig. 4.14). The curve

Figure 4.13: Rosemount Temperature Calibration Facility

fit takes the form of a polynomial, which is most typically used for thermocouples. The intercept was chosen to be zero since it must be for an ice point reference. A third-order polynomial was chosen with an intercept equal to zero by considering both the Akaike information criterion (Pan, 2001) and using leave-one-out cross-validation methods (Kohavi et al., 1995), which both recommended the third-order polynomial when the intercept was zero. The 95 % confidence interval for the calibration was also generated, which accounts for random errors and systematic errors (Fig. 4.15). Generally, the expanded uncertainty level for the calibration is on the order of 0.01 K around room temperature. There are two minimums observed in the confidence interval result: one near the center of the dataset and the other at 0 mV, which must be equal to zero given the zero intercept model. This result indicates the fit may be safely used down to 0 °C even though the lowest measured point was near 10 °C.

4.3 Mass Flow Rate Measurements

Mass flow measurements for film cooling injection were measured using orifice plates. In the experimental facility, two different orifice plate systems were installed: one plate for measuring the injected mass flow rate to the upstream slot and the other for measuring the injected mass flow rate to the discrete hole injection sites. The orifice plate measurement systems are designed to conform to the ASME guide for fluid flow measurements: *Measurement of Fluid Flow in Pipes Using Orifice, Nozzle, and Venturi* (2007). High-level details for the two orifice plate systems are shown in

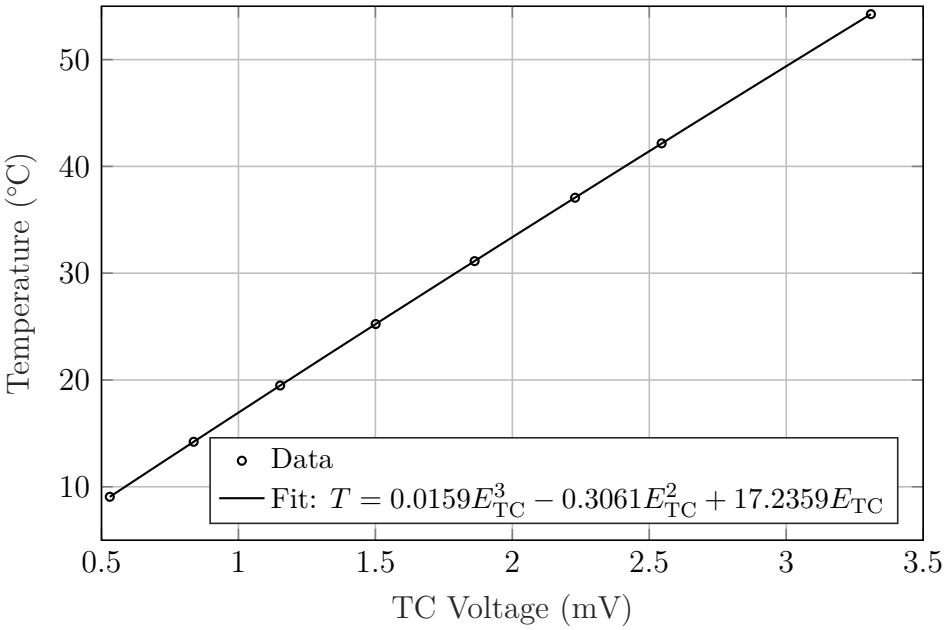

Figure 4.14: Thermocouple Calibration

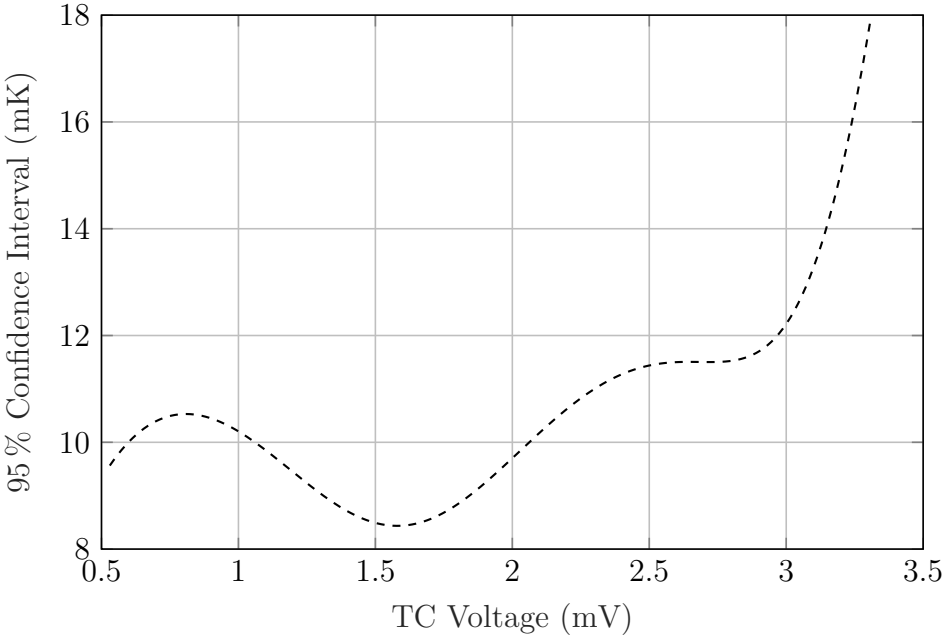

Figure 4.15: Thermocouple Calibration Confidence Interval

Table 4.4: Orifice Plate Descriptions

Orifice Plate	D m	β	Flow Conditioner	Tap Type
1 — Upstream Slot	0.052 725	0.5925	Tube Bundle	Flange
2 — Discrete Holes	0.052 501 8	0.290 276	Zanker Plate	Flange

Table 4.4. The following general equation can be used to relate the pressure drop over the orifice to the mass flow rate:

$$\dot{m} = \frac{C}{\sqrt{1-\beta^4}} Y \frac{\pi}{4} d^2 \sqrt{2\Delta p \rho_1} \tag{4.10}$$

where C is the discharge coefficient, Y is the expansibility factor, Δp is the pressure drop between the orifice taps, ρ_1 is the density upstream of the orifice, $\beta = d/D$, d is the internal orifice diameter, and D is the internal pipe diameter. The upstream density is calculated using the upstream absolute pressure and temperature. The temperature was measured downstream and was assumed to be equal to the upstream temperature due to low-velocity differences and pressure differences between the upstream and downstream locations in this idealized isenthalpic device. The temperature can also be controlled with tape heaters installed upstream of the orifice. These heaters were used to heat the injected air up to the main flow air temperature in the wind tunnel. The injection temperature tended to be cooler than the tunnel temperature (had this step not been taken), so it was appropriate only to use heating to equalize the temperatures. The discharge coefficient C represents the ratio between the actual flow rate and the ideal flow rate for incompressible flow. The effect is primarily due to the vena contracta effect and is a function of Reynolds number and geometry. The following relation for the discharge coefficient is specified in the ASME guide for use

with orifice plates:

$$
\begin{aligned}
C = {} & 0.5961 + 0.0261\beta^2 - 0.216\beta^8 + 0.000521\left(\frac{1\times10^6\beta}{Re_D}\right)^{0.7} \\
& + (0.0188 + 0.0063A)\beta^{3.5}\left(\frac{1\times10^6}{Re_D}\right)^{0.3} + (0.043 + 0.080\exp(-10L_1) \\
& - 0.123\exp(-7L_1))(1 - 0.11A)\frac{\beta^4}{1-\beta^4} - 0.031(M_2' - 0.8M_2'^{1.1})\beta^{1.3} \\
& + 0.011(0.75 - \beta)\left(2.8 - \frac{D}{25.4\,\mathrm{mm}}\right)
\end{aligned}
\tag{4.11}
$$

where the final term is included only when $D < 71.12\,\mathrm{mm}$, Re_D is the pipe Reynolds number, $M_2' = 2L_2'/(1-\beta)$, $A = (19\,000\beta/Re_D)^{0.8}$, $L_1 = l_1/D$, and $L_2' = l_2'/D$. The variable l_1 is the distance of the upstream tap from the upstream orifice face, and l_2' is the distance of the downstream tap from the downstream orifice face. For flange taps, $l_1 = l_2' = 25.4\,\mathrm{mm}$. The relative expanded uncertainty in the discharge coefficient was found to be 0.6 % for the first-orifice plate and 0.8 % for the second orifice plate following the uncertainty estimation procedure in the ASME guide. The discharge coefficient correlation is valid when the flow upstream of the orifice plate is approximately fully developed. Care was taken to achieve this state by installing appropriate flow conditioners, which help to produce a fully-developed velocity distribution and a low-swirl state, which is also characteristic of a fully-developed flow. Two different styled flow conditioners were used: a tube bundle (Fig. 4.16) and a Zanker plate (Fig. 4.17). The specific details for the flow conditioner designs are given in the ASME guide. The expansibility factor Y takes into account the compressibility of the fluid when working with gases. An empirical formula for calculating the expansibility factor is specified in the ASME guide:

$$
Y = 1 - \left(0.351 + 0.256\beta^4 + 0.93\beta^8\right)\left(1 - \left(\frac{p_2}{p_1}\right)^{\frac{1}{\gamma}}\right) \tag{4.12}
$$

where p_1 is the pressure reading at the upstream tap, p_2 is the pressure reading at the downstream tap, and γ is the ratio of specific heats. This relation is valid only for $p_2/p_1 \geq 0.8$, which was the case in this work. The relative expanded uncertainty in the expansibility factor is $3.5\frac{\Delta p}{\gamma p_1}\%$.

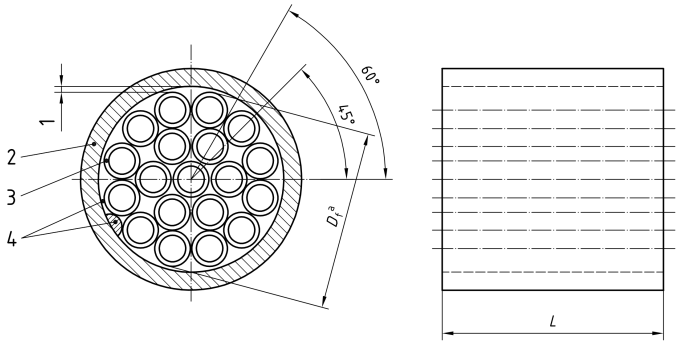

Figure 4.16: Tube Bundle Flow Conditioner

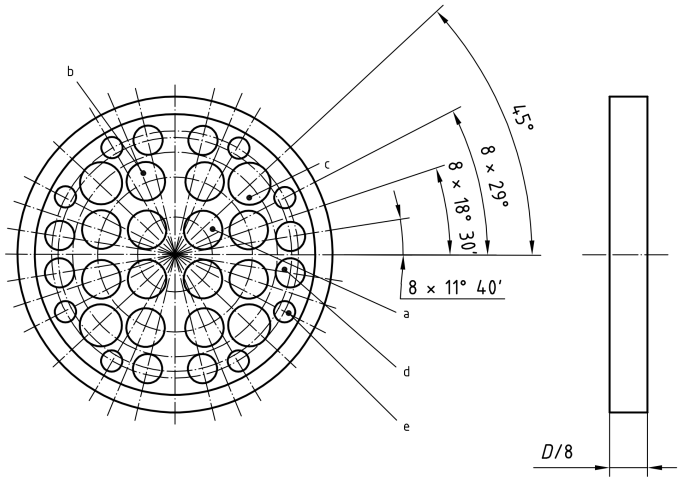

Figure 4.17: Zanker Plate Flow Conditioner

Figure 4.18: TSI Alnor Telescoping Pitot Probe

4.4 Air Velocity Measurements

Air velocity measurements within the wind tunnel were made with a pitot-static probe for calculating the mean tunnel velocity and hot-wires for measuring the turbulent boundary layer and the tunnel's turbulence intensity level.

4.4.1 Pitot-Static Velocity Measurement

The telescoping TSI pitot-static probe (Fig. 4.18) makes indirect velocity measurements by measuring the pressure difference between the pitot pressure and the static pressure. The probe is designed to be minimally sensitive to pitch and yaw within several degrees of 0°. The velocity predicted by the probe can be derived using the Bernoulli equation, which can be arranged to relate the pressure differential measured to the flow velocity:

$$V = \sqrt{\frac{2\Delta p}{\rho}} \tag{4.13}$$

which requires steady and incompressible flow conditions. In this experiment, the turbulence levels were moderate, so the steady flow assumption was violated. However, since the level of the turbulence intensity was approximately constant at the probe

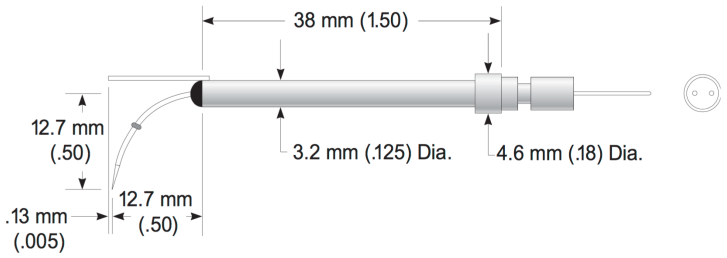

Figure 4.19: TSI Model 1218-T1.5 Standard Boundary Layer Probe

measurement location, the velocity can be corrected using the following approach:

$$V_{\text{corrected}} = \sqrt{\frac{V^2}{1 + Tu^2}} \tag{4.14}$$

where Tu is the turbulence intensity level. The correction can be derived by rearranging Eq. (4.13) for Δp and time-averaging the velocity term. Additionally, since this is a gas flow, there are small differences in gas density between the static and pitot pressure locations. A first-order correction for this effect was applied by averaging the static density and the pitot density. This correction was considered appropriate here, rather than using a compressible formulation, because of the low Mach numbers in the experiments.

4.4.2 Hot-wire Measurement

The tunnel turbulence intensity and boundary layer velocity profiles were measured using a hot-wire anemometer. The measurement equipment includes a TSI IFA-100 and a TSI model 1218-T1.5 boundary layer hot-wire probe (Fig. 4.19). The hot-wire is effectively a small, heated cylinder in crossflow that operates in such a way that its temperature, T_{wire}, is held constant at 250 °C, as controlled by the IFA-100. The power input to the wire will be equal to the power dissipated via heat and can be related to the heat transfer coefficient in the following way:

$$q = hA_{\text{wire}} \left(T_{\text{wire}} - T_{\infty}\right) = \frac{E_{\text{hw}}^2}{R_{\text{wire}}} \tag{4.15}$$

where h is the heat transfer coefficient, E_{hw} is the hot-wire voltage, R_{wire} is the wire resistance, and A_{wire} is the wire surface area. Furthermore, the heat flow rate can be related to the flow perpendicular to the wire: increased velocity leads to an increased heat flow rate. This relationship can be generalized using convective heat transfer theory, which describes the relationship with the following non-dimensional variables:

$$Nu = f(Re, Pr) \tag{4.16}$$

where the Reynolds number, Re, and the Nusselt number, Nu, for a cylinder with diameter D are given below:

$$Nu_D = \frac{hD}{k} \tag{4.17}$$

$$Re_D = \frac{\rho V D}{\mu} \tag{4.18}$$

where k and μ are the thermal conductivity and dynamic viscosity of the air, respectively. The Prandtl number, Pr, is a function of only fluid properties: only dependent on gas temperature for an ideal gas. Typically, the effect of fluid properties that vary with temperature are ignored or "baked-in" to hot-wire calibrations, so the effect of Prandtl number was also ignored here. The most notable exception would be the case when the hot-wire is used to make measurements over wide temperature ranges. Very often, the following formulation is used for hot-wires, which was also adopted here:

$$Nu = A + BRe^m \tag{4.19}$$

where m is usually between 0.4 to 0.5, or fixed to 0.5 in the case of "King's Law." Coefficients A, B, and optionally m are found via calibration. Equation (4.19) can be put in an expanded form with dimensional variables by combining with Eqs. (4.15), (4.17) and (4.18), which results in:

$$\frac{E_{\text{hw}}^2 D}{R_{\text{wire}} A_{\text{wire}} \left(T_{\text{wire}} - T_\infty\right) k} = A + B \left(\frac{pVD}{R_{\text{air}} T \mu} \right)^m \tag{4.20}$$

Then, by removing the constant terms and the fluid properties that vary only with temperature, the following simplified form remains:

$$\frac{E_{\text{hw}}^2}{T_{\text{wire}} - T_\infty} = A + B\,(pV)^m \tag{4.21}$$

which captures the primary relationship between the instantaneous hot-wire voltage and instantaneous flow velocity, with the key secondary corrections for the driving temperature difference and the gas pressure also captured. Note that in the case of liquid hot-wire measurements (not used in this work), the pressure term should not be included. Finally, the following substitutions are made to display the calibration in the two primary variables:

$$E_{\text{hw,ref}} = E_{\text{hw}} \sqrt{\frac{T_{\text{wire}} - T_{\text{ref}}}{T_{\text{wire}} - T_\infty}} \tag{4.22}$$

$$V_{\text{ref}} = V \frac{p}{p_{\text{ref}}} \tag{4.23}$$

where $p_{\text{ref}} = 101\,325\,\text{Pa}$ and $T_{\text{ref}} = 25\,^\circ\text{C}$. The resulting final reported form for the hot-wire calibration is

$$E_{\text{hw,ref}}^2 = A + B V_{\text{ref}}^m \tag{4.24}$$

4.4.3 Hot-wire Calibration

The hot-wire was calibrated in the jet facility developed by Wilson (1970). The facility produces a uniform jet with low turbulence intensity at a calibrated velocity. It was used to calibrate the hot-wire velocity to voltage relationship over the range of 5 m/s to 30 m/s.

The jet facility is equipped with a resistance temperature detector (RTD) and a pressure tap to determine the temperature and pressure conditions within the flow channel of the device. A four-wire resistance measurement was made to measure the resistance of the RTD, and the pressure measurements were made using the Dwyer Model 1430 Microtector®. Meanwhile, the hot-wire voltage measurements were made on the high-speed Agilent 34411A multimeter.

The data reduction equations to calculate the jet nozzle velocity, U_{n}, and are

described in Eqs. (4.25) to (4.31):

$$D_{\mathrm{ch}} = 25.564\,\mathrm{mm}, d = 8.128\,\mathrm{mm} \tag{4.25}$$

$$C_{\mathrm{n}} = 1.000 \pm 0.002 \tag{4.26}$$

$$Y = \sqrt{\frac{1}{1 - \left(\frac{p_{\mathrm{atm}}}{p_{\mathrm{ch}}}\right)^{\frac{2}{\gamma}} \left(\frac{d}{D_{\mathrm{ch}}}\right)^4} \left(\frac{\frac{\gamma-1}{\gamma}\left(1 - \left(\frac{p_{\mathrm{atm}}}{p_{\mathrm{ch}}}\right)^{\frac{\gamma}{\gamma-1}}\right)}{1 - \frac{p_{\mathrm{atm}}}{p_{\mathrm{ch}}}} \right)} \tag{4.27}$$

$$\rho_{\mathrm{ch}} = \frac{p_{\mathrm{ch}}}{R_{\mathrm{air}} T_{\mathrm{ch}}} \tag{4.28}$$

$$U_{\mathrm{n}} = C_{\mathrm{n}} Y \sqrt{\frac{2\left(p_{\mathrm{ch}} - p_{\mathrm{atm}}\right)}{\rho_{\mathrm{ch}}}} \tag{4.29}$$

$$T_{\mathrm{ch}} = \frac{R_{\mathrm{RTD}}/R_0 - 1}{A} \tag{4.30}$$

$$R_0 = 200\,\Omega, A = 0.003\,864 \tag{4.31}$$

For the hot-wire, 50 000 voltage measurements were made at 50 kHz from the signal coming from the IFA-100. The IFA-100 applies a voltage gain and offset, so the measured voltage needs to be corrected to the true hot-wire voltage using the following formula:

$$E_{\mathrm{hw}} = \frac{E_{\mathrm{IFA100}}}{\mathrm{IFA100}_{\mathrm{gain}}} + \mathrm{IFA100}_{\mathrm{offset}} \tag{4.32}$$

where $\mathrm{IFA100}_{\mathrm{gain}} = 10$ and $\mathrm{IFA100}_{\mathrm{offset}} = 1\,\mathrm{V}$ which were chosen using the suggested procedure from the IFA-100 manual. Note that all the other settings for the IFA-100 were followed from the manual's instructions.

The nozzle flow facility is supplied with compressed dry air from the building. A flow valve is used to control the nozzle velocity level. Ten target pressure differentials over the hot-wire velocity calibration range were chosen and executed in random order. Since the observed level of uncertainty in the voltage reading was higher than desired, particularly at lower flow rates, repeat measurements were made. In total, 28 readings were made for the calibration. The random uncertainty for pressure readings was negligible, so a least-squares regression was performed which assumed there was error only in the voltage reading. The results for the calibration are detailed

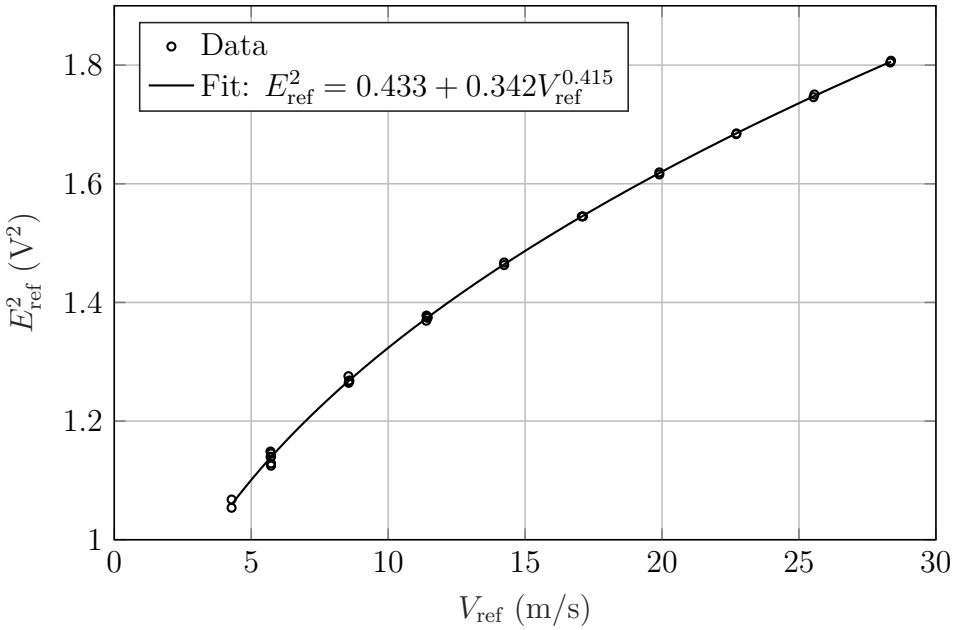

Figure 4.20: Hot-wire Calibration

in Fig. 4.20 with the confidence interval for the squared voltage in Fig. 4.21. Note that the exponent m was within the expected range for hot-wire calibrations, providing some additional validation for the calibration.

4.5 Mass Transfer Measurements

Mass transfer information was obtained using the naphthalene sublimation technique. The naphthalene sublimation technique has been used extensively in the Heat Transfer Laboratory at the University of Minnesota. The technique does not suffer from many of the issues that direct heat transfer measurements suffer, such as conduction and radiation errors and difficulties prescribing boundary conditions. Also, the measurement technique is very accurate and provides high spatial resolution.

Mass transfer measurements were performed on the turbine endwall in order to obtain a local non-dimensional mass transfer coefficient, the Sherwood number. Then, if desired, the non-dimensional heat transfer coefficient, the Nusselt number, can be found by applying the heat/mass transfer analogy. Mass transfer measurements were also used to deduce the film cooling effectiveness.

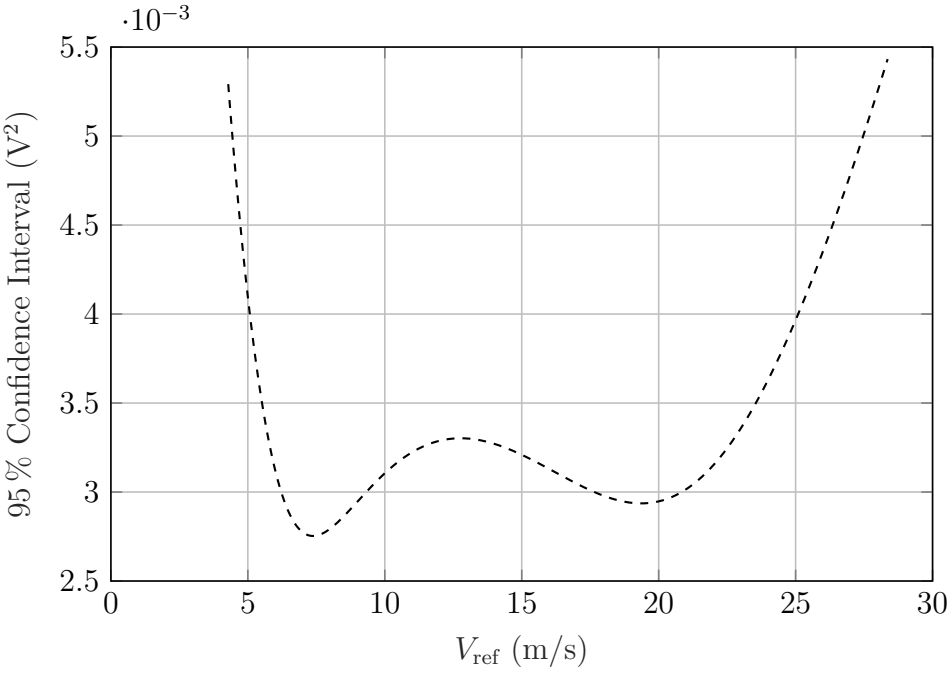

Figure 4.21: Hot-wire Calibration Confidence Interval

4.5.1 Heat/Mass Transfer Analogy Theory

The heat/mass transfer analogy is a principle that allows heat transfer behavior to be understood from mass transfer behavior and vice versa. The analogy is demonstrated by comparing the heat and mass transport equations under a specific set of assumptions and analogous flow conditions.

The general energy transport equation can be shown to be

$$\rho c_p \frac{DT}{Dt} = \nabla \cdot k\nabla T + \frac{Dp}{Dt} + \mu\Phi + \dot{q}''' \tag{4.33}$$

for constant specific heat and negligible Dufour effect (mass diffusion induced heat transfer). From left to right, the terms in the energy transport equation represent, from a Lagrangian perspective, (1) the energy storage, (2) the energy added via conduction, (3) the reversible conversion from mechanical work to thermal energy, (4) the irreversible conversion from mechanical work to thermal energy, and (5) the energy generated. Similarly, the general species transport equation can be shown to

be

$$\frac{D\rho_{\mathrm{A}}}{Dt} = \nabla \cdot D_{\mathrm{AB}} \nabla \rho_{\mathrm{A}} + \dot{m}'''_{\mathrm{A}} \tag{4.34}$$

for negligible Soret effect (heat diffusion induced mass transfer). Here, from left to the right, the terms in the species transport equation represent, from a Lagrangian perspective, (1) the species mass storage, (2) the species mass added via mass diffusion, and (3) the species mass added via chemical reactions.

Equations (4.33) and (4.34) can be restated in non-dimensional form for the case of steady-state, time-averaged, two-dimensional turbulent boundary layer flow, now from a Euclidean perspective, with the additional assumptions of low-speed flow (energy equation), no heat generation (energy equation), and no chemical reactions (mass equation), as applicable in this work:

$$\overline{u^*}\frac{\partial \theta}{\partial x^*} + \overline{v^*}\frac{\partial \theta}{\partial y^*} = \frac{1}{RePr}\frac{\partial}{\partial y^*}\left(\left(1 + \frac{\varepsilon_{\mathrm{M}}}{\nu}\frac{Pr}{Pr_{\mathrm{t}}}\right)\frac{\partial \theta}{\partial y^*}\right) \tag{4.35}$$

$$\overline{u^*}\frac{\partial \phi}{\partial x^*} + \overline{v^*}\frac{\partial \phi}{\partial y^*} = \frac{1}{ReSc}\frac{\partial}{\partial y^*}\left(\left(1 + \frac{\varepsilon_{\mathrm{M}}}{\nu}\frac{Sc}{Sc_{\mathrm{t}}}\right)\frac{\partial \phi}{\partial y^*}\right) \tag{4.36}$$

where $\theta = \left(\overline{T} - T_{\mathrm{w}}\right) / \left(T_{\infty} - T_{\mathrm{w}}\right)$, $\phi = \left(\overline{\rho_{\mathrm{A}}} - \rho_{\mathrm{A,w}}\right) / \left(\rho_{\mathrm{A},\infty} - \rho_{\mathrm{A,w}}\right)$, $Pr_{\mathrm{t}} = \varepsilon_{\mathrm{M}}/\varepsilon_{\mathrm{H}}$, $Sc_{\mathrm{t}} = \varepsilon_{\mathrm{M}}/\varepsilon_{\rho}$, $\varepsilon_{\mathrm{M}} = -\overline{u'v'}/\frac{\partial \overline{u}}{\partial y}$, $\varepsilon_{\mathrm{H}} = -\overline{T'v'}/\frac{\partial \overline{T}}{\partial y}$, and $\varepsilon_{\rho} = -\overline{\rho'_{\mathrm{A}}v'}/\frac{\partial \overline{\rho_{\mathrm{A}}}}{\partial y}$. By inspecting Eqs. (4.35) and (4.36), the analogy between heat and mass transfer is now readily apparent: for the case when $Pr = Sc$ coupled with analogous boundary conditions, the non-dimensional heat and mass transfer coefficients will be equal: $Nu = Sh$. For the case when $Pr \neq Sc$, the behavior is still analogous, but the dependency on Prandtl and Schmidt numbers must be accounted for when applying the analogy. The ratio between the non-dimensional heat and mass transfer coefficients is called the analogy factor F:

$$F = Nu/Sh \tag{4.37}$$

As an example, the solutions for the thermal boundary layer flows are often in the following form: $Nu = cRe^m Pr^n$. To convert to the equivalent mass transfer solution, replace Nu with Sh and Pr with Sc to get the following: $Sh = cRe^m Sc^n$. This case leads to an analogy factor equal to

$$F = (Pr/Sc)^n \tag{4.38}$$

which is a typical result for most boundary layer scenarios. Values for n can be found in the literature for various flow situations and is typically near 1/3.

In addition to determining the relationship between heat and mass transfer coefficients, the heat/mass analogy can also be used to understand the relationship between the film cooling effectiveness determined from heat versus mass transfer measurements. From analyzing the boundary layer equations or making dimensional analysis arguments, it can again be determined as long as $Pr = Sc$ and other flow-related parameters are the same, the film cooling effectiveness measured in the heat or mass transfer domain will be equal: $\eta_{\text{aw}} = \eta_{\text{iw}}$. However, there is a question as to what happens when this is not the case. For laminar boundary layer film cooling, it is evident that as the Prandtl number increases, the film cooling effectiveness increases due to the decreasing importance of advection, which works to decrease the film cooling effect. However, for a turbulent boundary layer, this effect is minimized due to dominant effect of turbulent mixing (Goldstein, 1971), in which case the turbulent boundary layer thicknesses, whether the momentum, heat, or mass boundary layer, are each nearly the same. By analyzing with the turbulent flow conservation equations (Eqs. (4.35) and (4.36)), the turbulent diffusion term dominates the molecular diffusion since $\varepsilon_{\text{M}} \gg \nu$ in turbulent flow, and the effect of Prandtl or Schmidt numbers becomes damped. However, the effect of the turbulent Prandtl or turbulent Schmidt numbers now become significant, which themselves depend on the Prandtl and Schmidt numbers and other flow conditions. For Prandtl numbers in the range corresponding from air to water (0.7 to 8) and for typical Reynolds numbers, the turbulent Prandtl number nearly collapses to a single curve (Kays, 2012) throughout the turbulent boundary layer. Therefore, the ratio between the turbulent Prandtl and turbulent Schmidt numbers in most practical flows and situations can be considered to be equal to unity, demonstrated consistently in the literature (Eckert and Drake Jr, 1987; Hinze, 1987; F. M. White, 1988). The Schmidt number is near 2.28 for the naphthalene mass transfer experiments in this work. Therefore, following the above argument, it can be claimed that the heat/mass analogy for film cooling effectiveness is nearly independent of Prandtl or Schmidt numbers for turbulent flow, so long as the Prandtl and Schmidt numbers are typical in value, say from approximately 0.5 to 10, as applicable in this work.

Figure 4.22: Assembled Mass Transfer Plate During the Casting Process

4.5.2 Mass Transfer Measurement Procedure

The experimental procedure begins with the preparation of the naphthalene coated endwall mass transfer plate. Naphthalene is applied through a casting procedure. The mass transfer plate, together with a flat aluminum shear plate, acts as a mold for the naphthalene. The shear plate has a polished mirror-like surface to produce a very smooth naphthalene surface. Before casting, the shear plate is cleaned with alcohol and cotton swabs.

To begin the casting process, the assembled mass transfer plate with the shear plate is warmed in a laboratory oven while the naphthalene powder is placed in a beaker and melted in a fume hood using a laboratory hot plate. The casting requires 175 ml of liquid naphthalene. The melted naphthalene is brought to approximately 190 °C. The assembled mass transfer plate is then removed from the oven and placed in the fume hood. Finally, a funnel is attached to the mass transfer plate, and the liquid naphthalene is poured into the mold. The assembled mass transfer plate is pictured after the naphthalene has been poured in Fig. 4.22.

After the naphthalene has been poured, the mold is allowed to cool for at least two hours. Then, the shear plate is removed from the mass transfer plate by using a mallet with horizontal strikes. An image of the finished cast surface is pictured in Fig. 4.23.

After inspecting the naphthalene cast for cracks and air pockets, an initial profile

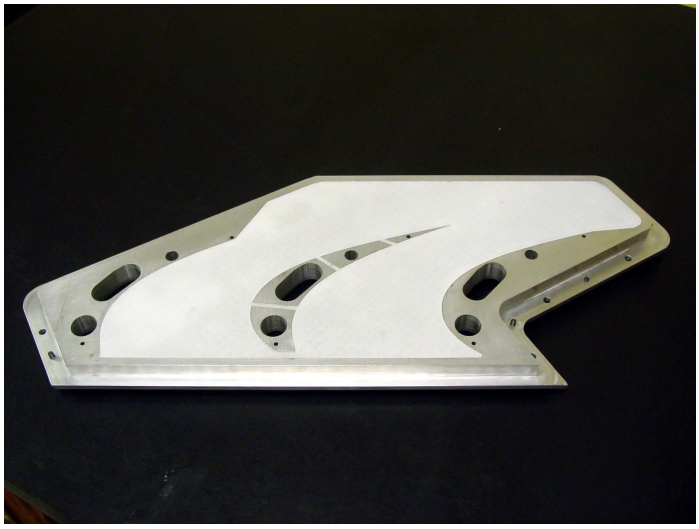

Figure 4.23: Finished Naphthalene Cast on the Turbine Endwall

of the naphthalene surface is taken using a Linear Variable Differential Transformer (LVDT). An LVDT probe is fixed on a 2-axis scanning table for measuring the endwall. A schematic diagram for the system is reported in Fig. 4.24. The LVDT probe is moved along the surface of the endwall using a system of translation slides (Unislides) and stepper motors. The motion controllers are connected to a Linux workstation through an IEEE-488 GPIB bus.

The data acquisition program is written in the C programming language. The system uses a multiplexer to send thermocouple and LVDT signals to a digital multimeter. Thermocouple measurements are made for the ambient temperature and thermocouples embedded into the naphthalene. The naphthalene profile is acquired relative to a reference point on the mass transfer plate.

Once the mass transfer plate has been secured on the scanning table, the time is recorded with a quartz timer (typical accuracy of 0.01 % (*Stopwatch and Timer Calibrations* 2009)), and the scanning begins. The scanning of the endwall surface takes approximately 60 minutes. The voltages read by the LVDT probes at each measured location are saved to a text file. For this mass transfer plate, 4060 measurements are made, which includes 3660 on the naphthalene surface. The temperatures are measured throughout the scan and are saved to a text file.

When the measurement process is complete, the mass transfer plate is removed from the scanning table and placed into an airtight container with naphthalene-saturated

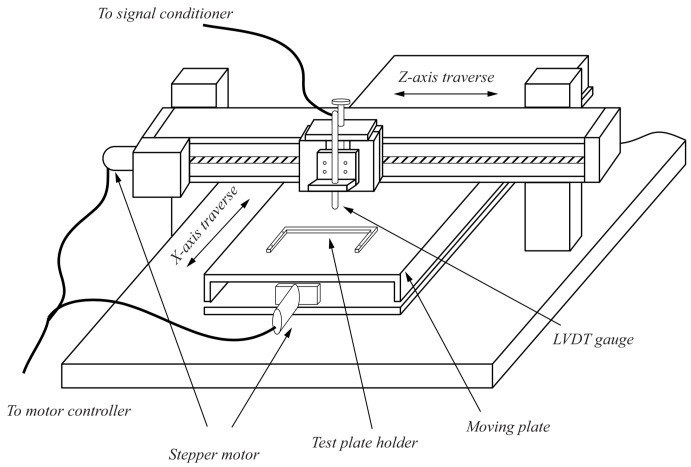

Figure 4.24: Schematic of Two-Axis Scanning Table

air, which minimizes further sublimation. The container holding the mass transfer plate is then transported from the scanning room to the wind tunnel room. The mass transfer plate is then removed from the container, and the plate is then mounted into the test section of the wind tunnel. This operation involves aligning several components and tightening of several screws. These steps take approximately 10 min. The wind tunnel is then turned on, and the injected air lines are opened. The start time for the experiment is recorded. During the run, various quantities are recorded including the atmospheric pressure, the dynamic pressure in the wind tunnel upstream of the turbine blades, the static temperature in the tunnel, and the temperature of the mass transfer plate. The experiment is run for approximately one hour. At the end of the experiment, the wind tunnel and the injected air lines are turned off, and the time is recorded. The mass transfer plate is removed from the wind tunnel and placed back into the airtight container. The mass transfer plate is brought back from the wind tunnel room to the scanning room. The plate is removed from the airtight container and then mounted on the scanning table for the final surface scan. The scan is started, and the time is recorded. The differences between the initial and the final scan are used to calculate the mass transfer during the experiment.

Two experiments are performed with the previously described procedure to determine both the mass transfer and the film cooling effectiveness: (1) with pure air injected through the film cooling locations and (2) with naphthalene-saturated air injected through the film cooling locations. From experiment (1) alone, the Sherwood number

is determined. The film cooling effectiveness is determined from the combined results of (1) and (2). Additionally, the net benefit from film cooling can be assessed with results (1) and (2), in conjunction with a third case (3) in which no film cooling is present.

4.5.3 Mass Transfer Data Processing

After the experiments have been performed, a grid of voltages representing the naphthalene layer height is processed. At each measurement location, the difference between voltages from the initial and final scans is linearly proportional to the sublimation depth at that location. The proportionality constant was found by calibrating the LVDT probe using a set of gauge blocks. The equation to find the depth δz is shown below:

$$\delta z \propto (E_{\mathrm{LVDT,f}} - E_{\mathrm{LVDT,i}}) = b\,(E_{\mathrm{LVDT,f}} - E_{\mathrm{LVDT,i}}) \tag{4.39}$$

where b is the proportionality constant found via calibration. The depth of naphthalene sublimed due to natural convection during the scanning, mounting, and moving of the mass transfer plate is estimated as $\delta z_{\mathrm{natural}}$, as explained in Section 4.5.6. The mass flux associated with forced convection can now be determined with the additional knowledge of the solid naphthalene density, ρ_{s}, and the experimental time, δt:

$$\dot{m}'' = \rho_{\mathrm{s}} \frac{\delta z - \delta z_{\mathrm{natural}}}{\delta t} \tag{4.40}$$

Then, the mass transfer coefficient, h'_{m}, and the non-dimensional mass transfer coefficient, Sh', can be calculated using the following definitions:

$$h'_{\mathrm{m}} = \frac{\dot{m}''}{\rho_{\mathrm{v,w}} - \rho_{\mathrm{v},\infty}} \tag{4.41}$$

$$Sh' = \frac{h'_{\mathrm{m}} C}{D_{\mathrm{naph}}} \tag{4.42}$$

where $\rho_{\mathrm{v,w}}$ is the naphthalene vapor density at the wall, $\rho_{\mathrm{v},\infty}$ is the naphthalene vapor density in the mainstream (equal to zero), C is the blade chord length, and D_{naph} is the binary diffusion coefficient for naphthalene in air. The prime symbols in h'_{m} and

Sh' are used to denote that this mass transfer coefficient definition is sensitive coolant vapor density. The non-dimensional coolant vapor density ϕ is defined as

$$\phi = \frac{\rho_{\mathrm{v,c}} - \rho_{\mathrm{v},\infty}}{\rho_{\mathrm{v,w}} - \rho_{\mathrm{v},\infty}} \tag{4.43}$$

where $\rho_{\mathrm{v,c}}$ is the naphthalene vapor density of the coolant. The naphthalene vapor density can be calculated using ideal gas law. For example, at the wall, it is calculated as

$$\rho_{\mathrm{v,w}} = \frac{p_{\mathrm{v,w}}}{R_{\mathrm{naph}} T_{\mathrm{w}}} \tag{4.44}$$

where the $p_{\mathrm{v,w}}$ is the saturated naphthalene vapor pressure at the wall, T_{w} is the wall temperature, and R_{naph} is the specific gas constant of naphthalene. Note that $p_{\mathrm{v,w}}$ is found using the saturation pressure of pure naphthalene evaluated at the wall temperature T_{w}. The properties for naphthalene, including the functions for the naphthalene vapor pressure and the binary diffusion coefficient for naphthalene in air, are presented by Goldstein and H. H. Cho (1995); example calculations are shown in Appendix A.

For the experiment with pure air injection, $\phi = 0$, and for the experiment with naphthalene-saturated air injection, $\phi = 1$. The mass transfer coefficient for the pure air injection experiment shall be denoted as $h'_{\mathrm{m},0}$, and the mass transfer coefficient for the naphthalene-saturated air injection experiment shall be denoted as $h'_{\mathrm{m},1}$. Similarly, the Sherwood numbers corresponding to the pure air injection and naphthalene-saturated injection experiments are now expressed as Sh'_0 and Sh'_1, respectively.

Since the proper mass transfer coefficient should be independent of the field vapor densities and only dependent on the flow itself, the true mass transfer coefficient and the non-dimensional mass transfer coefficient are defined as

$$h_{\mathrm{m}} = \frac{\dot{m}''}{\rho_{\mathrm{v,w}} - \rho_{\mathrm{v,iw}}} \tag{4.45}$$

$$Sh = \frac{h_{\mathrm{m}} C}{D_{\mathrm{naph}}} \tag{4.46}$$

where $\rho_{\mathrm{v,iw}}$ is the impermeable wall naphthalene vapor density: the wall vapor density that occurs when it is in equilibrium with the flow field. In other words, $\rho_{\mathrm{v,iw}}$ is the wall vapor density that must occur for the mass flux to be zero. Then, since $\rho_{\mathrm{v,c}}$

equals $\rho_{v,\infty}$ for the pure air injection experiment, $\rho_{v,iw}$ must also equal $\rho_{v,\infty}$ since there is only one field concentration present. Therefore, the mass transfer coefficient determined from the pure air injection experiment using Eq. (4.41) must be equal to the true mass transfer coefficient:

$$h_m = h'_{m,0} \tag{4.47}$$

$$Sh = Sh'_0 \tag{4.48}$$

The heat/mass analogy may be applied at this point using Eq. (4.38) with an appropriately chosen value for n. However, in this work, the results will be presented as Sherwood numbers directly without applying the analogy.

In addition to finding the heat or mass transfer coefficient, it is desirable to determine the film cooling effectiveness. The film cooling effectiveness, called the adiabatic wall film cooling effectiveness in the thermal domain, is defined as follows:

$$\eta_{aw} = \frac{T_{aw} - T_\infty}{T_c - T_\infty} \tag{4.49}$$

where T_∞ is the mainstream temperature, T_c is the temperature of the injected cooling air, and T_{aw} is the temperature that the wall assumes when adiabatic or in thermal equilibrium with the neighboring flow. The equivalent mass transfer film cooling effectiveness, called the impermeable wall film cooling effectiveness, is defined as follows:

$$\eta_{iw} = \frac{\rho_{v,iw} - \rho_{v,\infty}}{\rho_{v,c} - \rho_{v,\infty}} \tag{4.50}$$

The flow conditions for the pure air and the naphthalene-saturated injected experiments are the same; thus, the true Sherwood numbers from both experiments must also be equal. The flow conditions are specified by the Reynolds number, the turbulence intensity, the Schmidt number, the swirl angle, and the blowing ratio. After manipulating Eqs. (4.41) to (4.43), (4.45) and (4.46), the effectiveness can be shown to be equal to

$$\eta_{iw} = \frac{Sh'_0 - Sh'_1}{\phi_1 Sh'_0} \tag{4.51}$$

Note that ϕ_1 should be equal to 1 (by definition), but it may not precisely be due to minor differences in the injected temperature compared to the tunnel temperature.

Eckert (1984) discusses additional details on this indirect method for measuring the film cooling effectiveness and how it relates to a more direct measurement. Since $Sh = Sh'_0$ and $\phi_1 = 1$, the effectiveness can be said to simply equal

$$\eta_{\text{iw}} = \frac{Sh - Sh'_1}{Sh} \tag{4.52}$$

Ultimately, the heat transfer coefficient and the driving temperature difference contribute to the net heat flux that occurs on a turbine endwall. The quantity that takes both effects into account is called the Net Heat Flux Reduction ($NHFR$), defined as:

$$NHFR = 1 - \frac{q''_{\text{w}}}{q''_{\text{w},M0}} \tag{4.53}$$

where the $M0$ subscript denotes no blowing, so $q''_{\text{w},M0}$ is the heat flux that results without any film coolant. In the mass transfer domain, this can be shown to be equal to:

$$NHFR = 1 - \frac{Sh\,(1 - \eta_{\text{iw}}\phi)}{Sh_{M0}} \tag{4.54}$$

Instead of the value for ϕ taken from either the naphthalene-free or naphthalene-saturated conditions in this work, a value of $\phi = 1.6$ is taken, which is representative of the non-dimensional coolant temperature that occurs in typical turbine blade operations (Sen et al., 1996). An experiment was performed to measure Sh_{M0} where all of the flow conditions are the same except with $M = 0$. The experiment without film coolant was performed with a taped slot.

Since the above derivations require matching flow conditions, corrections can be applied to account for the inability to precisely match conditions in an experimental setting. The Schmidt number is not controlled since it depends on the ambient temperature, which may vary experiment to experiment. The Schmidt number has a weak dependence on the temperature, so it is nearly inconsequential. Nonetheless, a first-order correction can be applied for the Schmidt number by correcting to reference Schmidt number: $Sh'_{\text{corrected}} = Sh'\,(Sc_{\text{ref}}/Sc)^{1/3}$, which assumes that $Sh \propto Sc^{1/3}$. Here, Sc_{ref} is taken as 2.28, where 2.28 is a representative Schmidt number at room temperature. Additionally, while the main flow was controlled to target a specific Reynolds number, it was only able to be controlled within approximately 1 %, so a Reynolds number correction was applied as follows: $Sh'_{\text{corrected}} = Sh'\,(Re_{\text{ref}}/Re)^{0.65}$,

where the reference Reynolds number is the design Reynolds number value. The value of 0.65 in the exponent is deduced from experiments at significantly different Reynolds number, which is demonstrated in Chapter 6.

4.5.4 LVDT Calibration

The naphthalene surface was measured using a Linear Variable Differential Transformer (LVDT). The LVDT probe was held in a fixed position on the 2-axis scanning table while the mass transfer plate was traversed horizontally using a system of translation slides and stepper motors. The LVDT probe is spring-loaded, which allows it to extend and retract to follow the mass naphthalene surface contour. The LVDT's spring was selected so that its force was not high enough to dent the naphthalene surface.

The LVDT probe was calibrated using a set of gauge blocks of known thicknesses. The LVDT signal was measured over a range of $-12\,\mathrm{V}$ to $12\,\mathrm{V}$ and was expected to vary linearly versus displacement, so a curve fit in the following form was used:

$$E_{\mathrm{LVDT}} = a + bz \tag{4.55}$$

where a and b are fit during the LVDT calibration. The gauge blocks were set up in $0.002\,\mathrm{in}$ increments over a total range of $0.016\,\mathrm{in}$, leading to 9 measurements in total. The gauge block stacks were measured in random order during the LVDT calibration. During the calibration process, it was observed that the LVDT probe's voltage reading tends to have an initial reading that settles to a final reading after some time once a gauge block stack was placed under the LVDT probe. Roughly, it was observed that the voltage increased by about $0.06\,\mathrm{V}$ in $5\,\mathrm{min}$. Therefore, to calibrate the LVDT signal, two voltage readings were made: an initial reading measured within a second or so after the gauge block stack was placed under the LVDT probe and a settled reading at $5\,\mathrm{min}$ after the gauge block stack was placed under the LVDT probe.

Since the gauge blocks were not measured, there was no random error in the gauge block height, so the regression method used assumed all error was present in the voltage measurement signal only. The results of the calibration are summarized in Fig. 4.25 and Table 4.5. In Table 4.5, the slope b and the expanded uncertainty for b are reported. It is observed that the uncertainty for the initial fit value in b is higher than the settled value, which was expected since the change in the voltage signal was

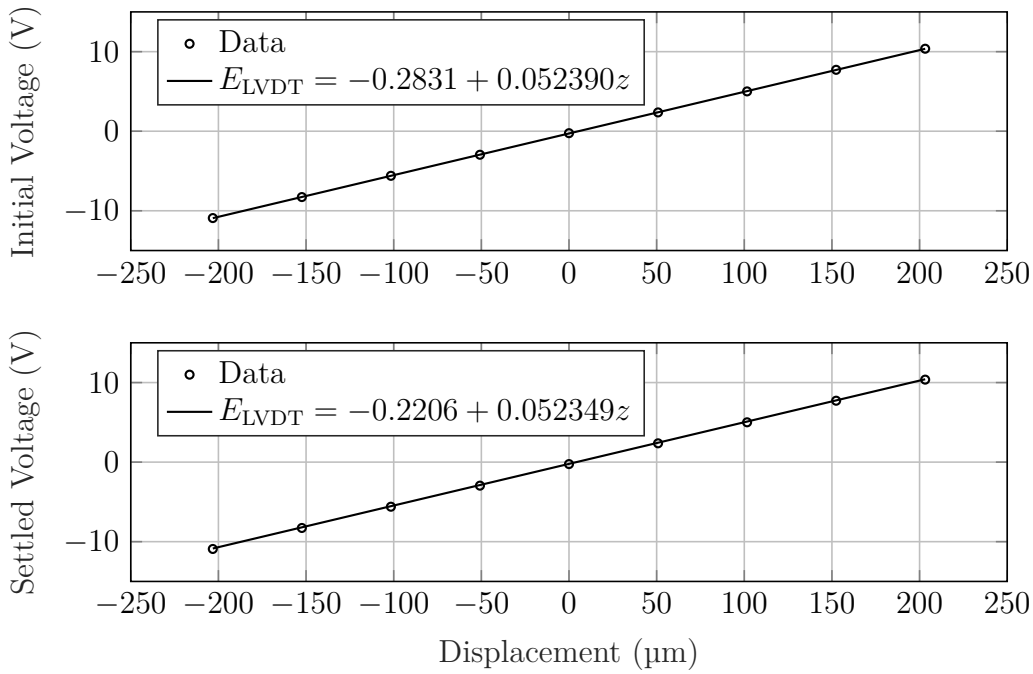

Figure 4.25: LVDT Calibration

Table 4.5: LVDT Calibration Summary

Calibration	Slope, b V/µm	U_b V/µm
Initial (Time = 0 min)	0.052 390	0.000 113
Settled (Time = 5 min)	0.052 349	0.000 088
Weighted Average	0.052 365	0.000 070

more rapid at 0 min compared to 5 min. The initial and settled values for slope b are within each other's confidence intervals, suggesting there is a true value for b that is independent of settling time. An inverse variance weighting was performed for a weighted average value for b, which is the value for b that is used in this work. Due to the nature of the settling voltage phenomena in the LVDT signal, it is beneficial to use consistent timing for each LVDT measurement when many LVDT measurements are being made in series.

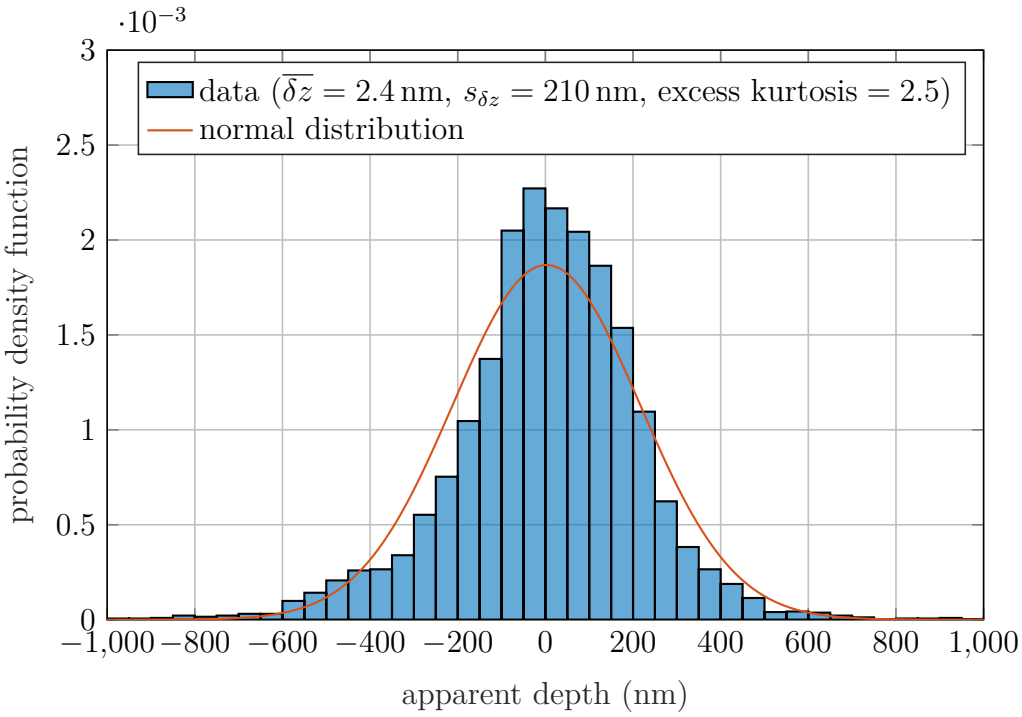

Figure 4.26: Mock Sublimation Test

4.5.5 Mock Sublimation Test

A mock sublimation test was performed to check the repeatability of the LVDT measurements on a passive surface. The passive surface used was a rectangular aluminum plate that was mounted and measured on the same XY table as the mass transfer plates. The results from this experiment verify the accuracy level of the mass transfer measurement method. The plate was measured five times with a reset between each set of measurements. The apparent depth difference between each scan combination was obtained, resulting in ten sets of depth differences, and 6480 data points in total. These points are shown on a histogram with comparison to a normal distribution in Fig. 4.26. The data nearly follow a normal distribution but does have some significant excess kurtosis, indicating that more outliers will occur compared to the expectation from a normal distribution corresponding to the measured sample mean and sample standard deviation. The mean depth from a typical mass transfer experiment in this work is near 80 µm, so the mean relative expanded confidence interval is nearly 0.5 %.

4.5.6 Natural Convection Correction

Naphthalene primarily sublimates while the mass transfer plate is in the test section with the wind tunnel turned on. However, unintended natural sublimation occurs during the scanning and installing of the mass transfer plate into the tunnel. The mass transfer plates with discrete holes were tested under natural convection conditions to determine the strength of this effect. First, the plates were cast and scanned as usual. Then, instead of starting an experiment in the wind tunnel, the plates were left on the scanning table for roughly 24 h before scanning again. The results were processed as Sherwood numbers and are shown in Fig. 4.27.

The Rayleigh number for natural convection was estimated for a horizontal plate for naphthalene diffusing into air assuming zero temperature difference. It was found to be approximately equal to 500 based on the characteristic length defined as the mass transfer surface area divided by its perimeter. Given the low Rayleigh number value, it is assumed the natural convection Sherwood number is negligibly dependent on the Rayleigh number and the uncontrolled convective room air currents may dominate. The air vents in the scanning room, where the natural convection primarily occurs, were closed to minimize this effect. In this situation, it is expected that a constant value correction for the Sherwood number should be applicable. Three natural convection scans were performed (one on the 0° plate and two on the 90° plate) and the Sherwood number was found to have consistent behavior across each. The Sherwood number was nearly equal to 10 across the entire mass transfer surface except at low and high axial positions, where it was enhanced. Therefore, the corrections to be applied when processing the experimental results were chosen to be functions of location axial position x, only.

The natural correction depth correction effect can be determined with Eqs. (4.56) to (4.58), and solving for $\delta z_{\text{natural}}$ given Sh_{natural} from Fig. 4.27.

$$\dot{m}''_{\text{natural}} = \rho_{\text{s}} \frac{\delta z_{\text{natural}}}{\delta t_{\text{natural}}} \tag{4.56}$$

$$h_{\text{m,natural}} = \frac{\dot{m}''_{\text{natural}}}{\rho_{\text{v,w}} - \rho_{\text{v},\infty}} \tag{4.57}$$

$$Sh_{\text{natural}} = \frac{h_{\text{m,natural}} C}{D_{\text{naph}}} \tag{4.58}$$

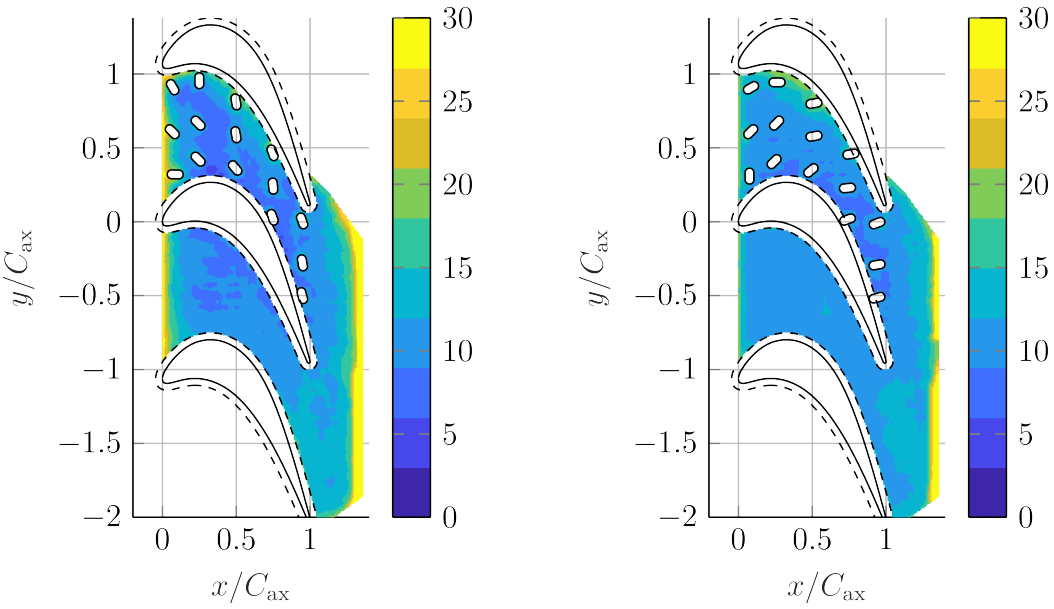

(a) Sh_{natural} Contour for 0° Plate

(b) Sh_{natural} Contour for 90° Plate

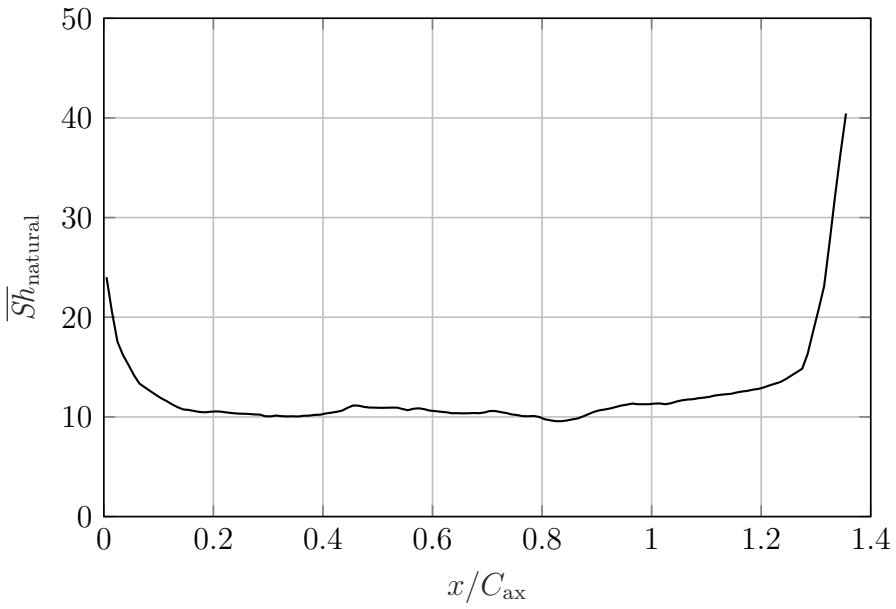

(c) Pitchwise-Averaged Natural Convection Sherwood Number

Figure 4.27: Natural Convection Sherwood Results

Chapter 5

Test Section Qualification

This chapter details the experimental and accompanying computational work performed to qualify the wind tunnel used in this work. The blade pressure distribution is reported along with the turbulent boundary layer and freestream turbulence measurements upstream of the blade passage section. The blade passage pressures and velocity fields were determined from a 2D CFD study. Additionally, estimates for the mass transfer and film cooling were be made from momentum integral theory.

5.1 Blade Pressure Distribution

Pressure distributions were obtained using an aluminum blade equipped with static pressure taps. The pressure tap holes are 0.7 mm in diameter. Internal to the blade, there are stainless steel tubes connected to flexible hoses that come out of a central opening in the blade. A figure of the blade and tap locations setup is shown in Fig. 5.1. The blade mounts in the tunnel and the flexible hoses exit on the bottom side of the test section. The flexible hoses connect to a multi-tube manometer (Fig. 5.2), which facilitate measuring many static pressures relative to the local atmospheric pressure level.

The blade can be placed in positions 2, 3, and 4 of the test section (see Fig. 3.2). This wind tunnel velocity can be controlled and set to the target blade Reynolds number. The blade Reynolds number is defined in this work based on the blade chord length C and the cascade exit velocity V_{ex}:

$$Re = \frac{\rho V_{\text{ex}} C}{\mu} \tag{5.1}$$

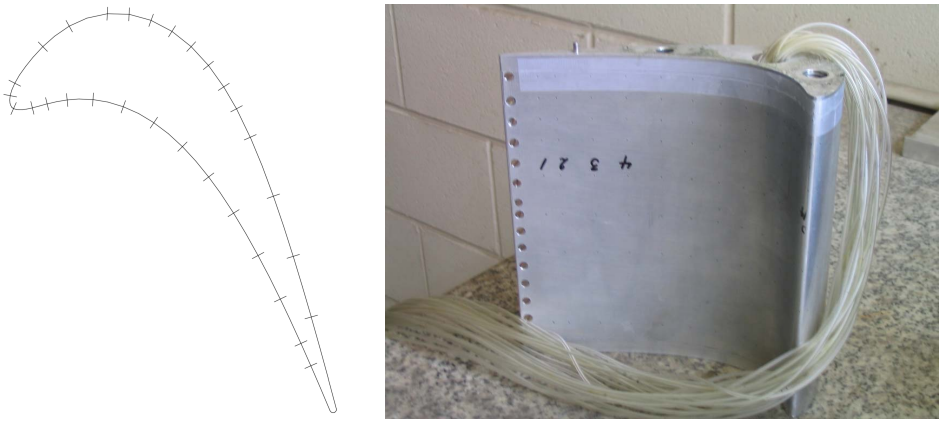

(a) Blade Tap Locations (b) Blade with Pressure Taps

Figure 5.1: Blade Pressure Tap Setup

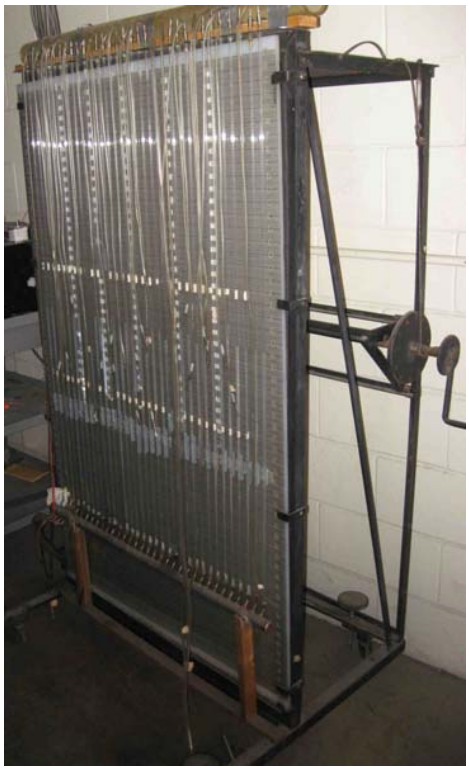

Figure 5.2: Multi-Tube Manometer

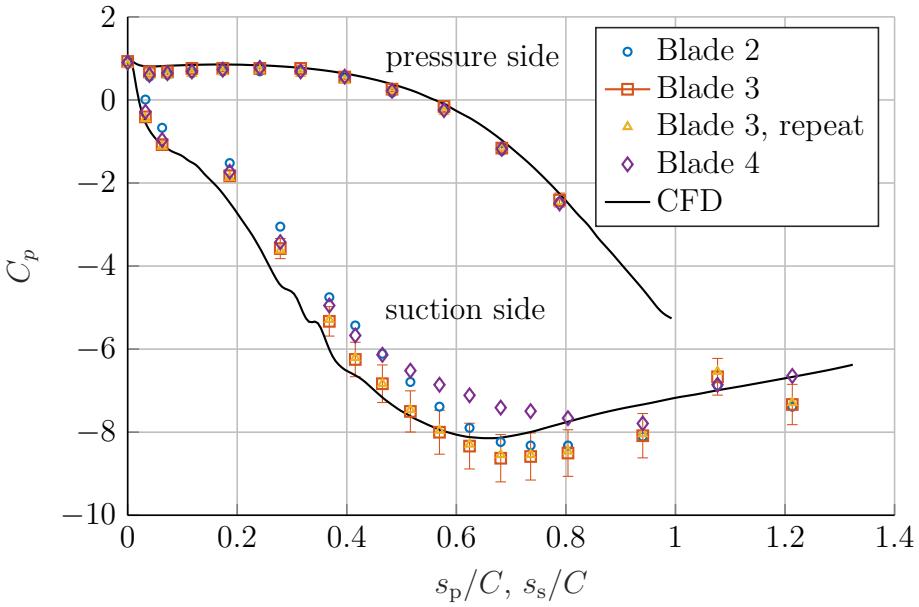

Figure 5.3: Static Pressure Measurement on the Blade Surface

During the blade pressure distribution experiment, the tunnel velocity was set so that the Reynolds number is 5.0×10^5, which is near the Reynolds number used during the mass transfer experiments. The tunnel was left on for 15 min so that the initial transients settle. The following measurements were then recorded: the array of blade static pressures (relative to atmosphere), the upstream tunnel static pressure (relative to atmosphere), the upstream dynamic pressure, the atmospheric pressure, and the upstream temperature. The measurements were processed to calculate the pressure distribution in terms of a pressure coefficient, C_p:

$$C_p = \frac{p - p_{\text{in}}}{\frac{1}{2}\rho V_{\text{in}}^2} \tag{5.2}$$

Note that the denominator of the pressure coefficient calculation was set equal to the dynamic pressure measurement that was made upstream of the blade passage. Additionally, the upstream pressure level, p_{in}, was set to the static pressure made upstream of the blade passage.

The results for these measurements are shown in Fig. 5.3 along with a computational fluid dynamics (CFD) result for the expected pressure coefficient distribution over the surface of the blade. The pressure results are displayed in the streamline coordinate

system. The results are separated onto the two sides of the blade (pressure side and suction side). An uncertainty analysis was performed, and it is observed that the relative uncertainty level is significant, especially on the suction side of the blade. Error bars (95 % confidence intervals) are shown for a single case in Fig. 5.3; however, they were similar in magnitude for each case so are not displayed to avoid cluttering the figure. It is observed that the most deviation between the results occurs in the region with the most significant measurement uncertainty (as indicated by the error bars). Additionally, it is found that the suction side of blade 4 exhibits the highest deviation from the group. However, no mass transfer measurements were made beyond the suction side of blade 4, and this outside passage may be influenced by the sidewalls, so it is not considered a cause for concern. Similarly, no mass transfer measurements were made beyond the pressure side of blade 2. It is observed that all of the results (at the three blade locations and the CFD results) agree very well on the pressure side of the blade; however, there are some systematic differences observed between the different cases occurring on the suction side. The differences are consistent among the three blade measurement cases and the CFD case, however, there is no significant indication of issues or imbalance between the blade passages.

A Reynolds number sensitivity study was performed by extending the CFD study to multiple Reynolds numbers. As indicated in Fig. 5.4, it is shown that for the studied Reynolds numbers, the pressure coefficient is found to be nearly Reynolds number independent, indicating that the normalized pressure field and velocity field do not depend on Reynolds number in this cascade. Additionally, this leads to the expectation that the film cooling effectiveness should also be Reynolds number independent in this experimental work in this high Reynolds number regime. The minimal effect that is found in Fig. 5.4 is that a larger Reynolds number leads to increased pressure coefficient, consistent with expectations: larger Reynolds numbers lead to thinner boundary layers, lower freestream velocities, and higher freestream pressures.

The CFD study used ANSYS CFX with the SST turbulence model and the Gamma Theta transition model enabled with incompressible air as the fluid. Intermediate levels (5 %) for freestream turbulence were set at the inlet conditions, and two velocities (10 m/s and 20 m/s) were selected to correspond to Reynolds number levels similar to experimental conditions in the wind tunnel. The CFD study included a single blade outline in the center and utilized the periodicity boundary condition to simulate

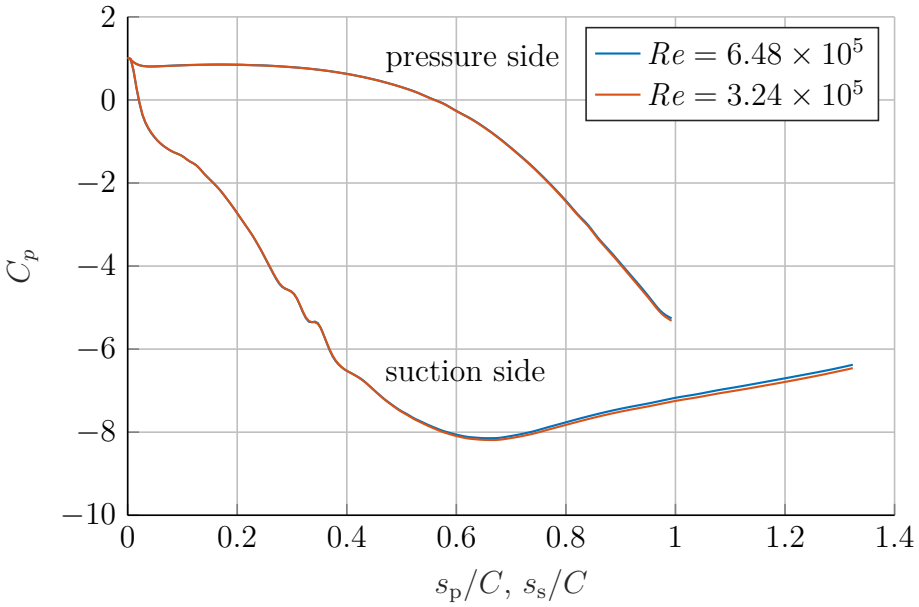

Figure 5.4: CFD Test for Reynolds Number Independence

a linear cascade. Only a single discretization volume was used in the wall-normal direction of the blade, and a symmetry boundary condition was enforced to capture the 2D effects only (no effect of the presence of the endwall). Mesh-independence and turbulence model independence (turning off the transitional model or switching to a k-epsilon or Spalart-Allmaras turbulence model) were performed. It was found that the effect of further discretizing the mesh into additional subvolumes was negligible on the final results, so the results were determined to be mesh independent. It was also found that the final results were minimally affected by the turbulence model. The final mesh and some of its settings and statistics are pictured in Fig. 5.5.

5.2 Field Pressure and Velocity

The CFD study also yielded results for the field pressure coefficient, the field speed, and the field velocity components, as pictured in Figs. 5.6 to 5.9. The results are displayed by stitching together two of the CFD results for better visualization of the whole flow field. Each of these results is expected to be nearly Reynolds number independent. Another output of interest for turbulent boundary layers is the acceleration parameter

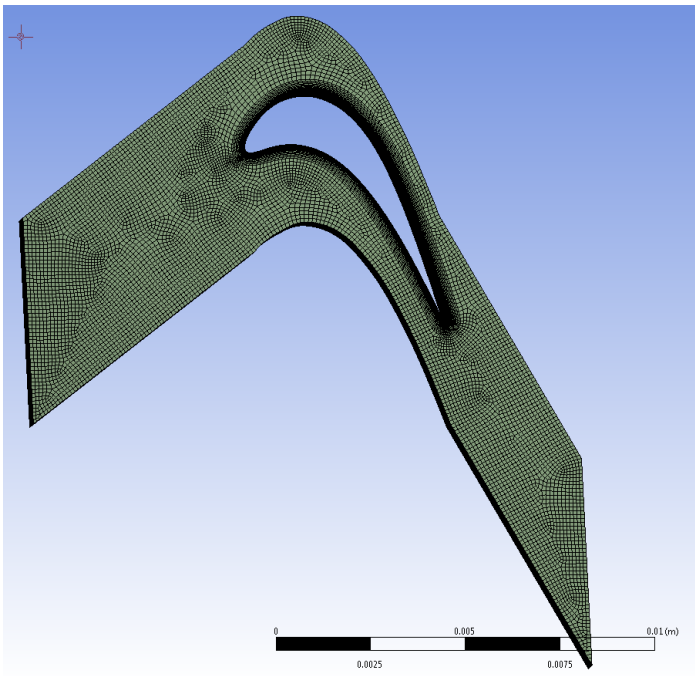

(a) CFD Mesh

Details of "Mesh"

Defaults	
Physics Preference	CFD
Solver Preference	CFX
Relevance	0
Sizing	
Use Advanced Size Function	On: Curvature
Relevance Center	Fine
Initial Size Seed	Active Assembly
Smoothing	High
Transition	Slow
Span Angle Center	Fine
Curvature Normal Angle	Default (18.0 °)
Min Size	1.e-006 m
Max Face Size	1.e-004 m
Max Size	2.e-004 m
Growth Rate	Default (1.20)
Minimum Edge Length	5.4389e-003 m
Inflation	
Use Automatic Inflation	None
Inflation Option	Smooth Transition
Transition Ratio	0.77
Maximum Layers	5
Growth Rate	1.2
Inflation Algorithm	Pre
View Advanced Options	No
Patch Conforming Options	
Triangle Surface Mesher	Program Controlled
Advanced	
Defeaturing	
Statistics	
Nodes	480274
Elements	453040
Mesh Metric	None

(b) Mesh Details

Figure 5.5: CFD Mesh Summary

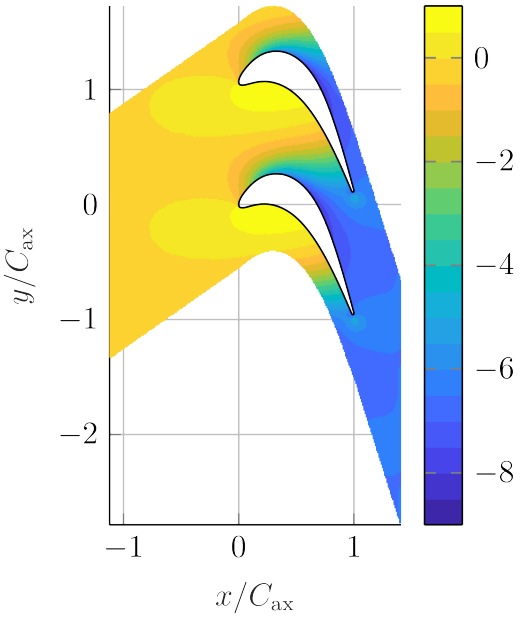

Figure 5.6: Pressure Coefficient Distribution (C_p)

K:

$$K = \frac{\nu}{V^2}\frac{\mathrm{d}V}{\mathrm{d}s} \tag{5.3}$$

where s is the distance measured along a streamline. Turbulent boundary layer heat and mass transfer are known to be inversely sensitive to high acceleration levels, which are expected to be significant in a blade passage. When the acceleration parameter $K \gtrsim 1 \times 10^{-6}$, the favorable pressure gradient causes the viscous sublayer to thicken, resulting in reduced heat transfer coefficients (Kays, 2012). Additionally, when $K \gtrsim 3.5 \times 10^{-6}$, relaminarization is expected to occur, in which the viscous sublayer completely engulfs the boundary layer. By non-dimensionalizing Eq. (5.3), K is revealed to be inversely proportional to Re. By analyzing the velocity component field with Matlab's `stream2` function, streamlines can be determined. Then, by numerically differentiating the speed field along the streamline, the acceleration parameter can be determined. The parameter was calculated here for $Re = 600\,000$ and is shown in Fig. 5.11, which demonstrates that that high acceleration occurs over a significant portion of the flow passage. Additionally, significant deceleration occurs near the stagnation point and in its vicinity on the pressure side of the passage.

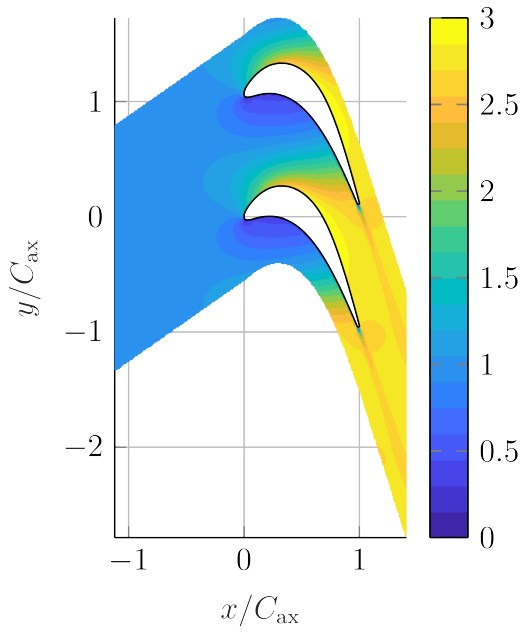

Figure 5.7: Normalized Speed Distribution (V/V_{in})

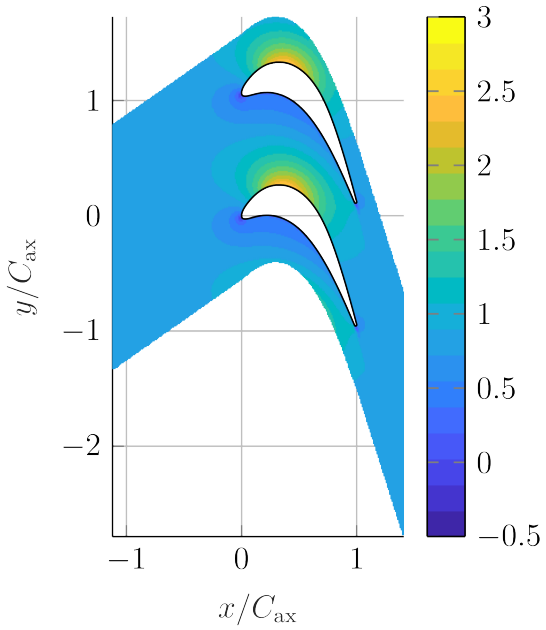

Figure 5.8: Normalized Velocity X-component Distribution (u/V_{in})

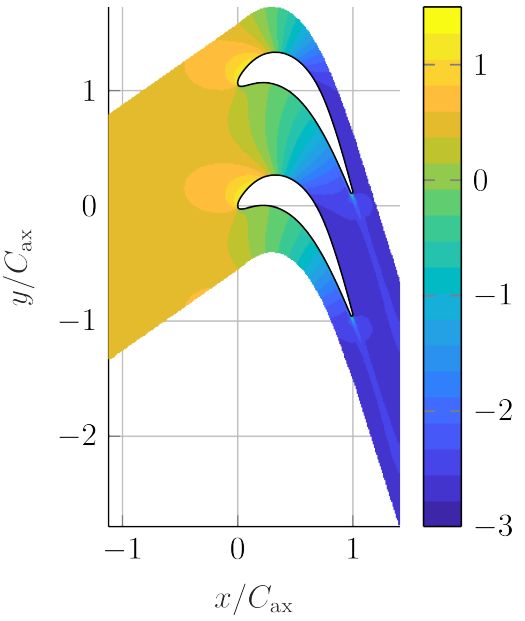

Figure 5.9: Normalized Velocity Y-component Distribution (v/V_{in})

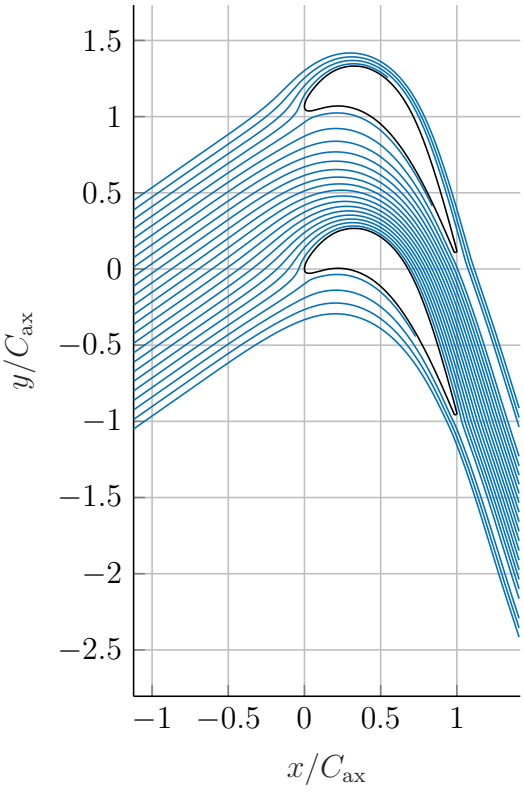

Figure 5.10: Cascade Streamlines

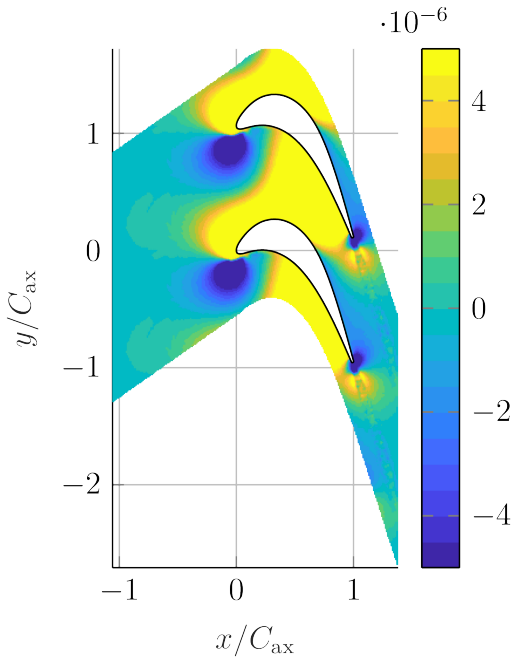

Figure 5.11: Acceleration Parameter K Distribution ($Re = 6 \times 10^5$)

5.2.1 Crossflow Velocity

The 2D CFD results will predict pressure levels reasonably well in the entire flow field (even near the walls); however, the velocities in the presence of walls will be different due to the no-slip boundary condition. Furthermore, since the streamlines are turning, there exist pressure gradients normal to the main flow streamlines, leading to crossflow within the boundary layer. A first-order analysis was performed to predict the crossflow effect. The crossflow profile is often approximated by two different profiles: the Mager profile (Mager, 1952) and the Johnston profile (Johnston, 1960). The Mager profile is defined as

$$w = u\left(1 - \frac{y}{\delta}\right)^2 \tan\beta_{\mathrm{w}} \tag{5.4}$$

which only has a single parameter β_{w}, which is the angle between the main flow streamlines and surface streamlines. The Johnston profile is triangular with an inner and outer region velocity profile. The inner viscous region has a profile defined as

$$w = u\tan\beta_{\mathrm{w}} \tag{5.5}$$

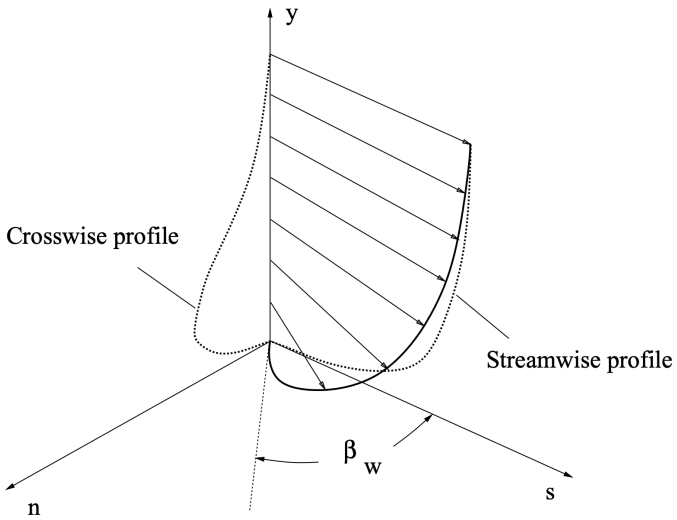

Figure 5.12: Crossflow Boundary Layer Profile (B. Mughal and Drela, 1993)

where this β_w parameter has the same meaning as in the Mager model. The outer near-inviscid region has a profile defined as

$$w = A\,(u_\infty - u) \tag{5.6}$$

where A is an additional crossflow parameter. A representative image of a boundary layer exhibiting crossflow, with β_w labeled, is shown in Fig. 5.12. In the outer, near-inviscid region of the boundary layer, the crossflow parameter A can be estimated by integrating along the main flow streamlines (Cumpsty, 1968):

$$A = u_\infty^2 \int_0^\alpha \frac{\mathrm{d}\alpha'}{u_\infty^2} \tag{5.7}$$

where α is the angle turned in the main flow streamlines. This approach does not handle cross-over (two-way crossflow) or crossflow decay and may tend to overestimate A since viscosity is not considered. Next, there is the issue of relating the crossflow parameter A to parameter β_w. For the Mager profile, the following simple relation is implied: $\beta_w = \tan^{-1}(A)$. More generally, as may be useful when using the Johnston profile, A can be related to angle β_w given the local skin friction and local boundary

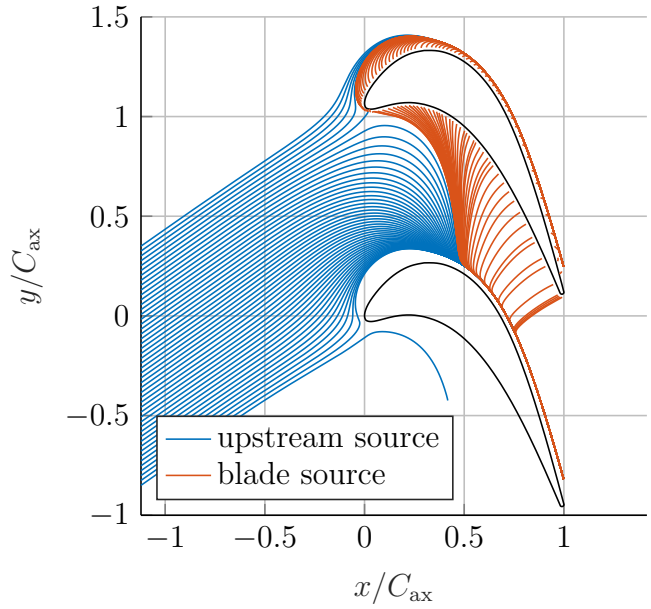

Figure 5.13: Endwall Surface Cascade Streamlines

layer Mach number in the main flow (Smith, 1972):

$$A = \tan\left(\beta_{\mathrm{w}}\right) \frac{\sqrt{C_{f_1} \cos\left(\beta_{\mathrm{w}}\right)\left(1 + 0.18 Ma_{\infty}^2\right)}}{0.10 - \sqrt{C_{f_1} \cos\left(\beta_{\mathrm{w}}\right)\left(1 + 0.18 Ma_{\infty}^2\right)}} \tag{5.8}$$

For typical values for C_{f_1}, Ma_{∞}, and β_{w} in a turbulent blade passage, the Mager profile result of $\beta_{\mathrm{w}} = \tan^{-1}(A)$ is reasonable. Therefore, to estimate the surface streamlines, this result, in combination with Eq. (5.7), was taken, which produces the surface streamlines shown in Fig. 5.13. The result reveals that a significant amount of crossflow is present within the passage, indicating the purge flow may struggle to provide significant endwall cooling.

A single endwall flow visualization run was performed for the realistic slot geometry for the following flow parameters: $M_{\mathrm{s}} = 0.430$, $Tu = 5\,\%$, $\theta = 22.5°$. The oil dot technique is used, in which a small amount of charcoal powder is mixed with SAE 20W motor oil, which is applied to contact paper on the bottom endwall using a laboratory micro-pipette. The endwall component is mounted into the test section, and the tunnel is run until the oil dots have stopped moving. Then the endwall section is removed from the tunnel and photographed. The resulting photo indicates

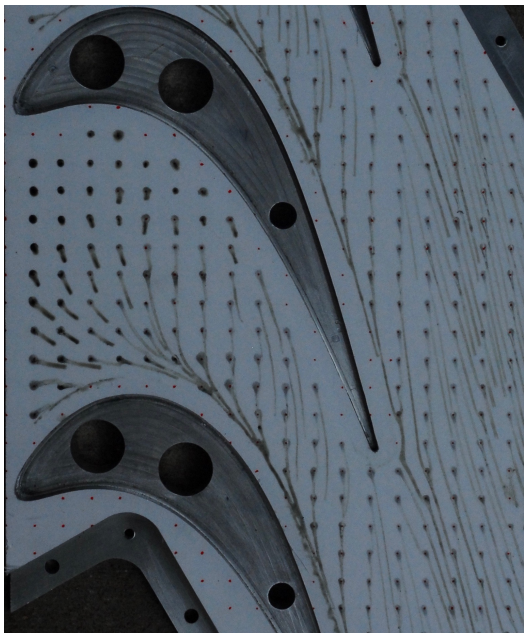

Figure 5.14: Endwall Flow Visualization

the surface flow direction and the magnitude of the local shear stress, or, roughly, the local flow speed. The results shown in Fig. 5.14 indicates a strong secondary crossflow effect is occurring. The crossflow appears to thoroughly sweep the entering endwall flow towards the suction side of the blade near $x/C_{\text{ax}} = 0.5$, which is in good agreement with Fig. 5.13. Note that the blade with a fillet around its perimeter was used and an oil trace around the fillet edge is observed in the photograph. Some locations on the endwall surface have nearly zero axial component. The locations of low and high velocities are in alignment with the 2D CFD predictions. While a detailed visualization study was not performed for all flow conditions, these results are in alignment with expectations and previous visualization studies performed in this facility (Papa, 2006). The strong secondary flow effect found here is expected to be reasonably consistent across all the cases except for the highest blowing ratios, in which the purge flow may overpower the crossflow effect.

5.3 Endwall Mass Transfer and Film Cooling

5.3.1 Mass Transfer

Since endwall mass transfer measurements are performed in this work, it is of interest to establish some theoretical baseline results for the endwall mass transfer. For this purpose, the freestream speed and streamlines can be used to generate boundary layer integral solutions. Using the approach described by Kays (2012), the mass Stanton number St_m can be computed for laminar and turbulent boundary layer flows, respectively, as follows:

$$St_\mathrm{m} = \frac{0.332\nu^{1/2}V_\infty^{1/2}Sc^{-2/3}}{\left(\int_0^s V_\infty^2\,\mathrm{d}s\right)^{1/2}} \tag{5.9}$$

$$St_\mathrm{m} = \frac{0.0296\nu^{1/5}Sc^{-2/3}}{\left(\int_0^s V_\infty\,\mathrm{d}s\right)^{1/5}} \tag{5.10}$$

where the mass Stanton number is defined as h_m/V_∞ here. Since the results in this work are processed as Sherwood numbers, Eqs. (5.9) and (5.10) are restated in the following form:

$$Sh = \frac{0.332Re^{1/2}Sc^{1/3}V_\infty^{*\,3/2}}{\left(\int_0^{s^*} V_\infty^{*\,2}\,\mathrm{d}s^*\right)^{1/2}} \tag{5.11}$$

$$Sh = \frac{0.0296Re^{4/5}Sc^{1/3}V_\infty^*}{\left(\int_0^{s^*} V_\infty^*\,\mathrm{d}s^*\right)^{1/5}} \tag{5.12}$$

where the $s^* = s/C$, $V_\infty^* = V_\infty/V_\mathrm{ex}$, and both Re and Sh are based on blade chord length C and cascade exit velocity V_ex used elsewhere in this work. Now, the non-dimensionalized velocity speed field (Fig. 5.7 renormalized with V_ex) can be evaluated and integrated along the non-dimensional streamlines (Fig. 5.10 renormalized with C) to determine the endwall mass transfer. The streamline integration is began starting at $x = 0$, at which point the resulting mass transfer coefficient is infinite. The results were processed and are shown in Fig. 5.15. While turbulent flow and boundary layers are present leading up to the cascade section, the high acceleration may lead to lower mass transfer levels; the laminar solution serves as a reasonable lower bound point of reference that may have some relevance in the case of relaminarization. Note that this analysis does not consider the effect of the purge flow injection. Generally, the

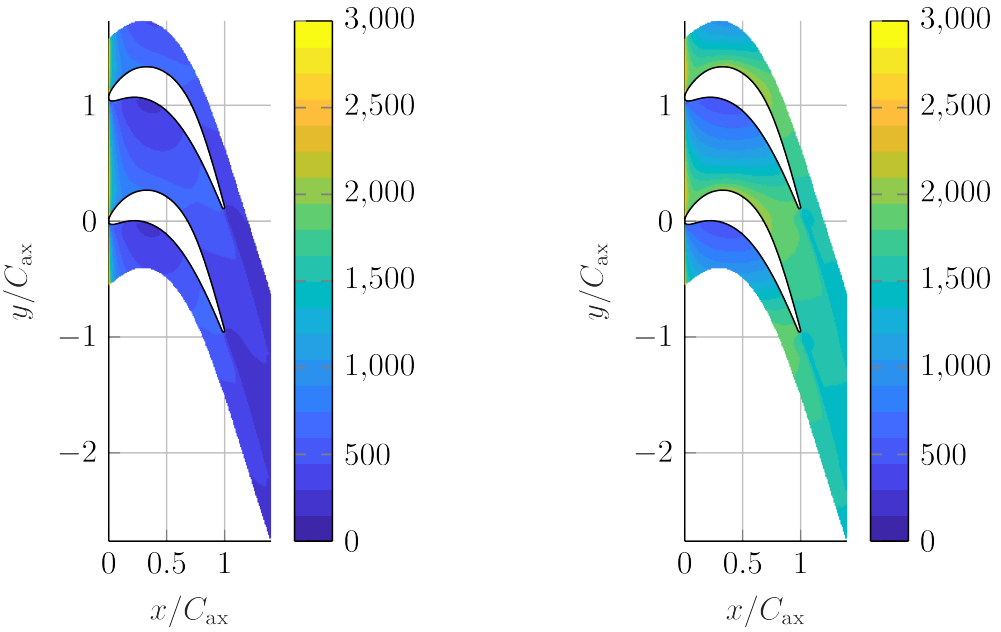

(a) Laminar

(b) Turbulent

Figure 5.15: Model Endwall Sherwood Number ($Re = 6 \times 10^5$, $Sc = 2.28$)

purge flow injection is expected to enhance mass transfer.

5.3.2 Film Cooling

Next, the endwall film cooling effectiveness on the endwall can also be predicted. Using the approaches described by Goldstein (1971) and Leontiev (1999), the film cooling effectiveness can be calculated from the following set of equations:

$$\eta_{\text{iw}} = \left(1 + 0.254\zeta\beta^{5/4}\right)^{-4/5} \tag{5.13}$$

$$\zeta = \frac{\Delta s^*}{MS}\left(\frac{\mu_{\text{s}}}{\mu_{\infty,0}} Re_S\right)^{-1/4} \tag{5.14}$$

$$\Delta s^* = \int_0^s \frac{\rho_\infty V_\infty \mu_{\infty,0}}{\rho_{\infty,0} V_{\infty,0} \mu_\infty}\,\mathrm{d}s \tag{5.15}$$

$$M = \frac{\rho_{\text{s}} V_{\text{s}}}{\rho_{\infty,0} V_{\infty,0}} \tag{5.16}$$

$$Re_S = \frac{\rho V_s S}{\mu} \tag{5.17}$$

$$\beta = 1 + 1.5 \times 10^{-4} Re_S \sin\alpha \tag{5.18}$$

where S is the slot injection width. The ζ term accounts for both the initial quantity of injected coolant and the downstream decay. The β term accounts for the increased mixing effect due to the slot injection angle α, which is measured relative to the surface (45° for the straight slot). Note that the '0' subscript denotes the freestream conditions at the slot exit. This formulation is especially applicable for slot flow aligned with the main flow, and accounts for variable freestream velocity (wedge flow), but it cannot account for crossflow effects. Since the injected flow is misaligned with the slot flow (even without swirl), an approximate idea was to assume that the injected coolant immediately turns and follows the main flow. Under such situations, $V_s = V_{s,ax}/\cos\gamma$, where γ is the angle formed between the main flow direction and the slot flow direction (without swirl). Also, note the blowing ratio M used here uses the local freestream velocity rather than the upstream inlet velocity (used elsewhere in this work). The results from this analysis are given for both the straight slot and the realistic slot in Figs. 5.16 and 5.17, respectively. It is found that the realistic slot has enhanced film cooling effectiveness compared to the straight slot. This is due to the decreased value for β (less mixing) at the cost of an increased value for ζ (slot farther upstream), leading to a net film cooling benefit.

The most significant shortcoming of this analysis is that the secondary flow effects are not accounted for: especially the crossflow. The crossflow leads to a significant sweeping effect of the coolant towards the suction side of the passage. For this reason, these results are expected to overestimate the effectiveness compared to the experiment significantly.

5.4 Discrete Hole Loss Coefficient and Flow Distribution

An experiment was performed to evaluate the discrete hole injection loss coefficient. The discrete hole plenum was supplied with high-pressure air with the mass flow rate measured via its upstream orifice plate. One of the 15 holes was used as a pressure tap

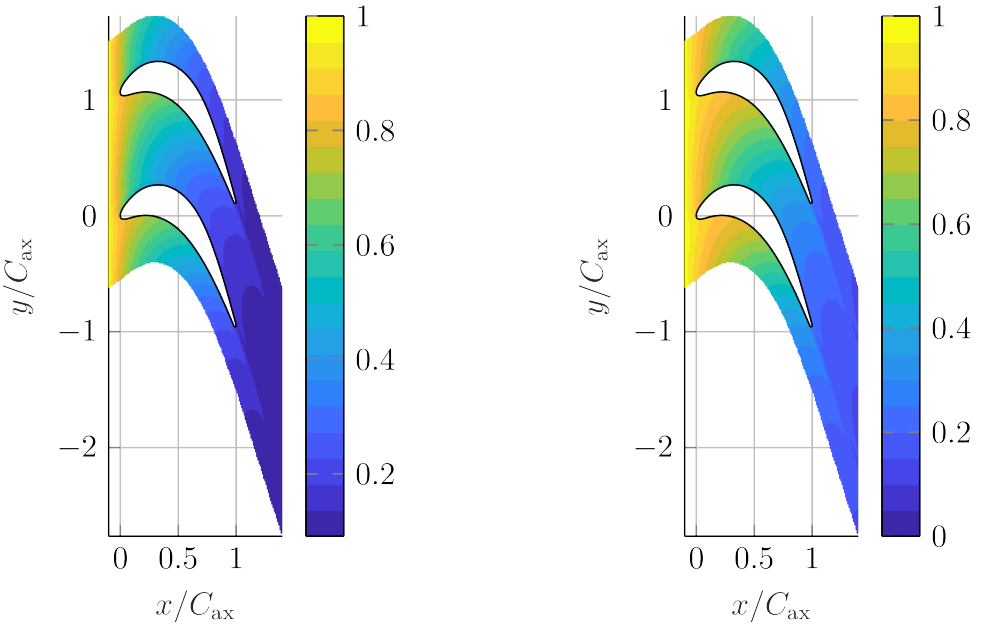

(a) $M_{\text{s}} = 0.5$

(b) $M_{\text{s}} = 1$

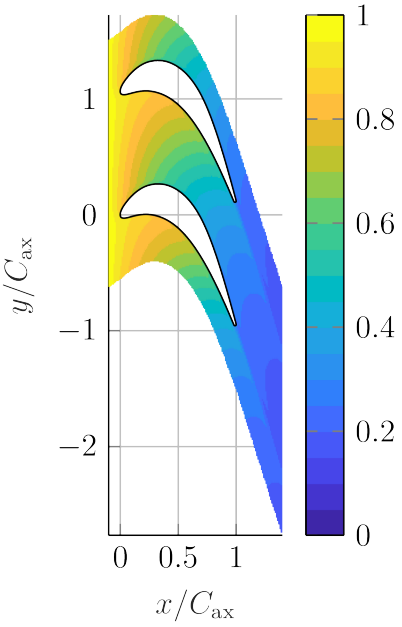

(c) $M_{\text{s}} = 1.5$

Figure 5.16: Model Endwall Effectiveness—Straight Slot ($Re = 6 \times 10^5$)

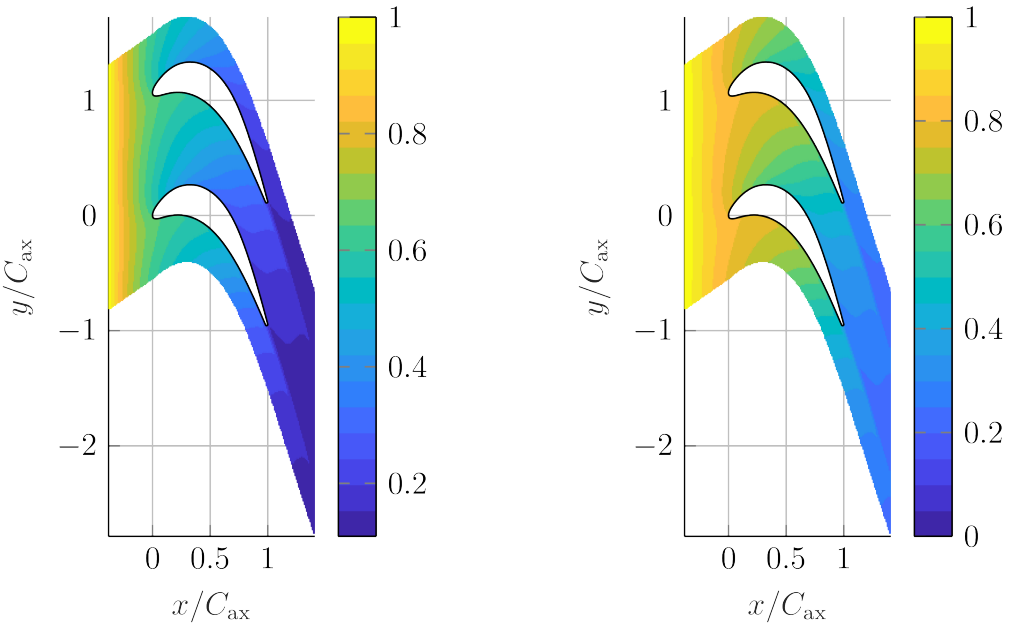

(a) $M_s = 0.215$ (b) $M_s = 0.430$

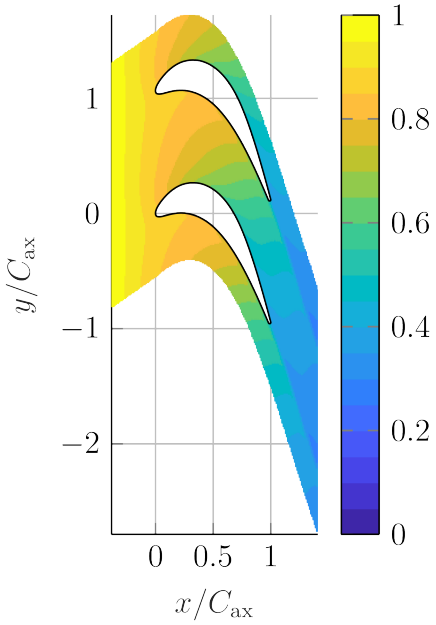

(c) $M_s = 0.645$

Figure 5.17: Model Endwall Effectiveness—Realistic Slot ($Re = 6 \times 10^5$)

to determine the plenum pressure while the other 14 holes discharged into a quiescent ambient. The room pressure and plenum temperature were also measured. From these measurements, a discrete hole loss coefficient can be determined by assuming the mass flow rate is equal among the 14 holes. The discrete hole injection pressure drop is stated as:

$$\Delta p_{\mathrm{h}} = K_{\mathrm{loss}} \frac{1}{2} \rho V_{\mathrm{h}}^2 \tag{5.19}$$

where V_{hole} is calculated at the injection hole throat area. A simple estimate for the loss coefficient is to model the pressure losses as sudden large contractions followed by sudden large expansions, leading to estimated loss coefficients of 1.5 (the sum of 0.5 and 1, respectively, for the contraction and expansion loss coefficients (*Flow of fluids through valves, fittings, and pipe* 1978)). The loss coefficient was experimentally found to be 1.55 over a broad range of flow rates, which is in alignment with the expected result.

Since the freestream pressure varies throughout the blade passage due to significant flow acceleration within, the injected mass flow will be more concentrated towards the downstream locations since the pressure is lowest. Considering the loss coefficient and the freestream pressure distribution presented in Section 5.2, the flow distribution for the 15 holes can be estimated. The plenum pressure level can be solved for iteratively until the total mass flow rate equals the prescribed mass flow rate for the given blowing ratio M_{h}. Then, the individual mass flow rates for each hole can be determined since all of the pressures are known for each discrete hole location. The results from this analysis are given in Fig. 5.18, where $\dot{m}_{\mathrm{h,ideal}} = \dot{m}_{\mathrm{h,total}}/15$. Note that the locations for the 15 holes are detailed in Table 3.5. It is expected that as the discrete hole flow rate increases (larger M_{h}), the discrete hole mass flow rates shall become more uniform since the discrete hole pressure drop will dominate relative to the passage pressure distribution effect. This is demonstrated in these results: the maldistribution for $M_{\mathrm{h}} = 0.75$ is quite significant, while the maldistribution for the higher blowing rates is minor.

5.5 Entrance Flow Measurements

Cascade entrance flow measurements were made at four measurement locations within the test section, as specified in Fig. 5.19. The calibrated boundary layer probe,

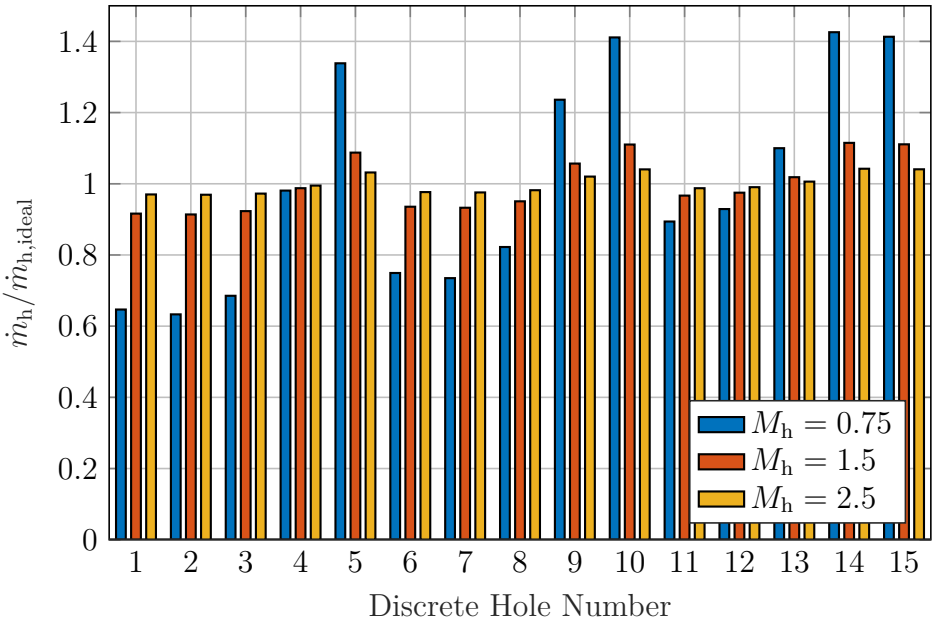

Figure 5.18: Discrete Hole Flow Distribution

discussed in Section 4.4.2, was used to make the measurements both within the boundary layer and within the freestream. For each hot-wire measurement location, 50 000 voltage measurements are made at 50 kHz, and the corresponding velocity measurement is calculated for each. The instantaneous velocity at a given point is described by u, v, and w velocity components, which can be decomposed into their time-averaged and fluctuating components:

$$\begin{aligned} u &= \overline{u} + u' \\ v &= \overline{v} + v' \\ w &= \overline{w} + w' \end{aligned} \tag{5.20}$$

The hot-wire probe is positioned so that it is orthogonal to the main flow direction, where it is primarily sensitive to the u and v velocity components. The probe is expected to be minimally sensitive to the w velocity component since the hot-wire aspect ratio, l/d, is significantly large. While the probe is directly sensitive to u and v velocity component, the effect of the fluctuating velocity component v', is negligible for turbulence intensities below 20 %, so the effect of the fluctuating component v' measurement can be safely neglected here (Constants, 1963). Therefore, mathemat-

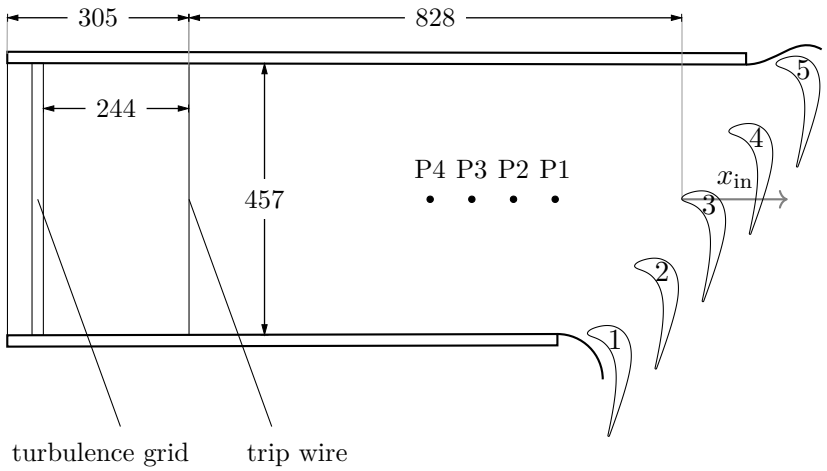

Figure 5.19: Boundary Layer Measurement Locations (dimensions in mm)

ically, the mean and standard deviation of the 50 000 measurements correspond to $\overline{u}$ and $\sqrt{\overline{u'^2}}$, respectively. The mean velocity and root-mean-square (RMS) of the turbulent velocity fluctuations are defined below:

$$V = \sqrt{\overline{u}^2 + \overline{v}^2 + \overline{w}^2} \tag{5.21}$$

$$v_{\text{RMS}} = \sqrt{\frac{\overline{u'^2} + \overline{v'^2} + \overline{w'^2}}{3}} \tag{5.22}$$

Then, since $\overline{v} = \overline{w} = 0$, the mean velocity $V = \overline{u}$. Additionally, under the assumption of isotropic turbulence, $v_{\text{RMS}} = \sqrt{\overline{u'^2}} = \sqrt{\overline{v'^2}} = \sqrt{\overline{w'^2}}$. The turbulence intensity is then calculated with the following equation once the RMS and mean velocity are known:

$$Tu = \frac{v_{\text{RMS}}}{V} \tag{5.23}$$

5.5.1 Boundary Layer Measurements

The boundary layer upstream of the entrance to the linear cascade was characterized and detailed in the following section. To measure the boundary layer at a given upstream position, the boundary layer probe was first positioned 66 mm away from the bottom wall in the wind tunnel on a linear slide. Since the probe is required to get very close to the wall to characterize the boundary layer fully, the wall-normal

position must be known precisely. Therefore, the precise probe position y_{true} is defined as equal to $y_{\text{approx}} + y_{\text{shift}}$, where y is the normal distance measured from the wall. Initially, the value for y_{shift} is set equal to 0 as an initial guess, and as velocity profile data is collected the estimate for y_{shift} is updated. As the probe's position moves close to the wall, enough data have then been collected such that y_{shift} is well known, and its estimate changes minimally with each additional measurement point. The distance the probe traverses from point to point is set equal to $\min(0.1y_{\text{true}}, 2\,\text{mm})$ where the mathematical function "min" returns the minimum of its two arguments.

The boundary layer results are processed and put into the u^+ and y^+ coordinate system, which is convenient for describing the turbulent boundary layer:

$$u^+ = \overline{u}/u_\tau \tag{5.24}$$

$$y^+ = yu_\tau/\nu \tag{5.25}$$

where ν is the kinematic viscosity and u_τ is the friction velocity, defined as

$$u_\tau = \sqrt{\tau_w/\rho} \tag{5.26}$$

where τ_w is the wall shear stress and ρ is the air density. Density and viscosities are known as functions of pressure and temperature. However, τ_w and therefore u_τ are initially unknown until deduced from the boundary layer measurements.

From turbulent boundary layer theory, the near-wall velocity profile called the viscous sublayer is found to be equal to

$$u^+ = y^+ \tag{5.27}$$

which is found by taking the boundary layer equations and assuming there is no eddy-transport nearest to the wall. Additionally, further from the wall beyond the viscous sublayer, there exists a region where the average velocity is proportional to the logarithm of the distance from the wall, called the log-law region:

$$u^+ = \frac{1}{\kappa} \ln y^+ + C^+ \tag{5.28}$$

This region is roughly applicable to within the inner 20 % of the boundary layer height,

called the inner layer. It has been found experimentally for a smooth wall that $C = 5.0$ and $\kappa = 0.41$ are accurate for use to represent the log-law region.

Between the viscous sublayer and the log-law region is the buffer layer. There is expected to be a smooth transition from the viscous sublayer to the log-law region, but there is no closed-form theoretical solution. However, many approximate semi-empirical solutions tend to work well in this layer. One such form is recommended by Musker (1979), which is designed to predict an equivalent solution to the viscous sublayer solution and the log-law solution when $y^+ \to 0$ and $y^+ \to \infty$, respectively:

$$\frac{\mathrm{d}u^+}{\mathrm{d}y^+} = \frac{\frac{y^{+2}}{\kappa} + \frac{1}{s}}{y^{+3} + \frac{y^{+2}}{\kappa} + \frac{1}{s}} \tag{5.29}$$

where s is a constant that corresponds to a set of values from the log-law solution: κ and C^+. By matching the solution of Eqs. (5.28) and (5.29) at a sufficiently large y^+, s is found using an iterative procedure to be equal to 0.001 093 (at four significant figures) for $C = 5.0$ and $\kappa = 0.41$. Then a closed-form solution for Eq. (5.29) can be found by integration. For the values s and κ used above, the following is found to directly relate u^+ to y^+ throughout the full inner layer of the turbulent boundary layer (the viscous sublayer, the buffer layer, and the log-law layer):

$$\begin{aligned} u^+ = {} & -5.42384 \tan^{-1}\left(0.488153 - 0.119737 y^+\right) - 0.8661 \ln\Big(y^{+2} - 8.15377 y^+ \\ & + 86.3713\Big) + 4.17122 \ln\left(y^+ + 10.5928\right) - 3.52006 \end{aligned} \tag{5.30}$$

In the processing of the velocity measurements, two particular quantities are estimated: $\overline{u}_\infty$ and δ_{99}. The quantity $\overline{u}_\infty$ is found by locating the widest dataset (starting furthest from the wall) such that a piecewise-constant velocity profile is appropriate. A piecewise-constant profile is determined to be appropriate when the 95 % confidence interval for the slope of a straight line fit contains zero. Then $\overline{u}_\infty$ is set to the mean of the velocity measurements in that dataset. After $\overline{u}_\infty$ is found, the dataset containing 4 points above and 4 points below $0.99\overline{u}_\infty$ is located. A straight line is fit against that dataset, and the y location at which $u = 0.99\overline{u}_\infty$ is solved for, which is defined as δ_{99}.

As boundary layer velocity measurements are collected, a best fit is performed for u_τ and y_{shift} in real-time against Eq. (5.30) using the dataset within the inner 10 % of the boundary layer, defined as the region where $y_{\text{true}} < 0.1\delta_{99}$. The final fit values

after all the data has been collected are considered the final estimates for u_τ and y_{shift}.

The boundary layer profiles at the four locations were processed according to the described methods and are shown in Fig. 5.20. The boundary layer profiles are shown in u^+ and y^+ coordinates, with comparisons to theoretical profiles. The boundary layer profiles are found to collapse to a universal curve that matches the theoretical expectations within the inner region for a turbulent boundary layer. The profiles diverge from the log-law in the outer region. Additionally, they separate from each other at the edge of the boundary layer, where it is found that position 4 exhibits the smallest freestream velocity, and position 1 exhibits the highest freestream velocity. This is consistent with expectations: for internal flow (wind tunnel) situations with a growing boundary layer, the freestream velocity should accelerate.

The normalized $\overline{u'^2}$ turbulent velocity profile is also plotted for the four measurement locations in Fig. 5.21. Again, the profiles are found to collapse onto a universal curve in the inner layer with the peak value occurring near $y^+ = 15$. Pope (2011) presents some direct numerical simulation results for channel flow that indicate a peak value of 7.5 for $\overline{u'^2}/u_\tau^2$ that occurs near $y^+ = 15$, which is in good agreement with the findings here. Additionally, it is suggested that the location of the peak value appears to be independent of the Reynolds number, but the actual peak value is Reynolds number dependent. At the edge of the boundary layer, it is found that the profiles diverge and the most downstream location (Position 1) is found to have the minimum $\overline{u'^2}$. This finding matches expected results for decaying turbulence downstream of a turbulent grid.

The boundary layer displacement thickness δ_1 and momentum thickness δ_2, defined below, can be found by performing numerical integration using the trapezoid rule.

$$\delta_1 = \int_0^\infty \left(1 - \frac{\overline{u}}{\overline{u}_\infty}\right) \mathrm{d}y \tag{5.31}$$

$$\delta_2 = \int_0^\infty \frac{\overline{u}}{\overline{u}_\infty}\left(1 - \frac{\overline{u}}{\overline{u}_\infty}\right) \mathrm{d}y \tag{5.32}$$

The shape factor is defined as

$$H = \delta_1/\delta_2 \tag{5.33}$$

which quantifies the "flatness" of the boundary layer profile. A shape factor of 2.6 is found for the laminar Blasius boundary layer, and the shape factor is typically near

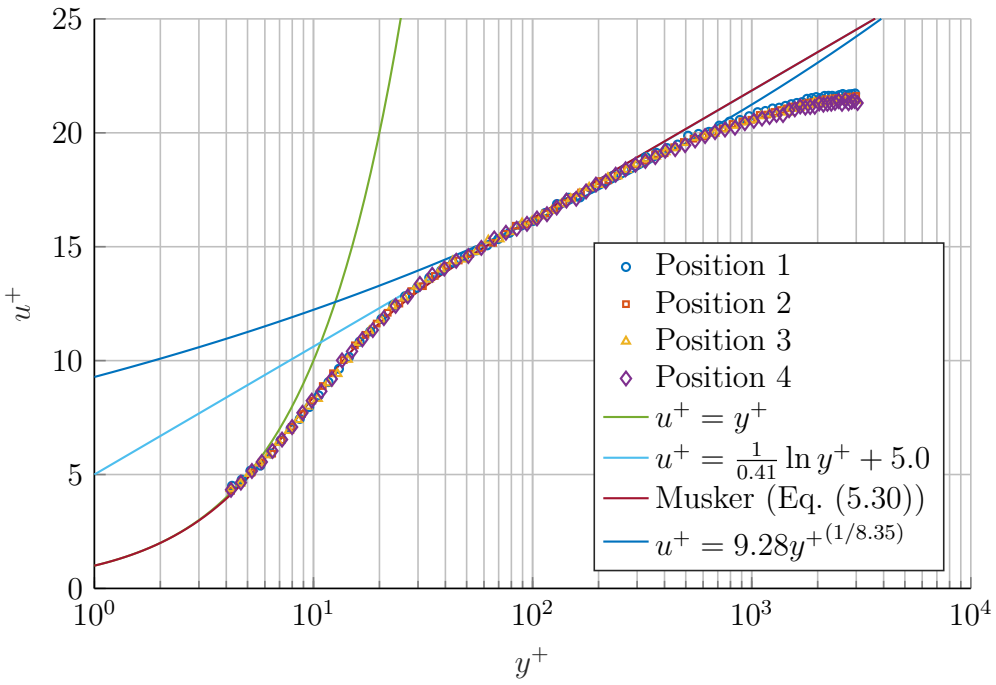

Figure 5.20: Turbulent Boundary Layer Profile

1.3 for turbulent boundary layers (Pope, 2011). Here, it was measured to be 1.24 for each measured position.

Determining the Virtual Origin of the Boundary Layer

The virtual origin is the apparent origin of the turbulent boundary layer in the absence of a laminar to turbulent transition. As an approximation for the turbulent boundary layer profile, a power-law profile in the following form is usually a good description for most of the boundary layer:

$$\frac{\overline{u}}{\overline{u}_\infty} = \left(\frac{y}{\delta}\right)^{1/n} \tag{5.34}$$

where δ is the boundary layer thickness at which the velocity is equal to the freestream velocity. The n in the power-law is expected to depend on the Reynolds number. From the definitions for the displacement thickness and the momentum thickness combined with the power-law profile, the following ratios between the boundary layer

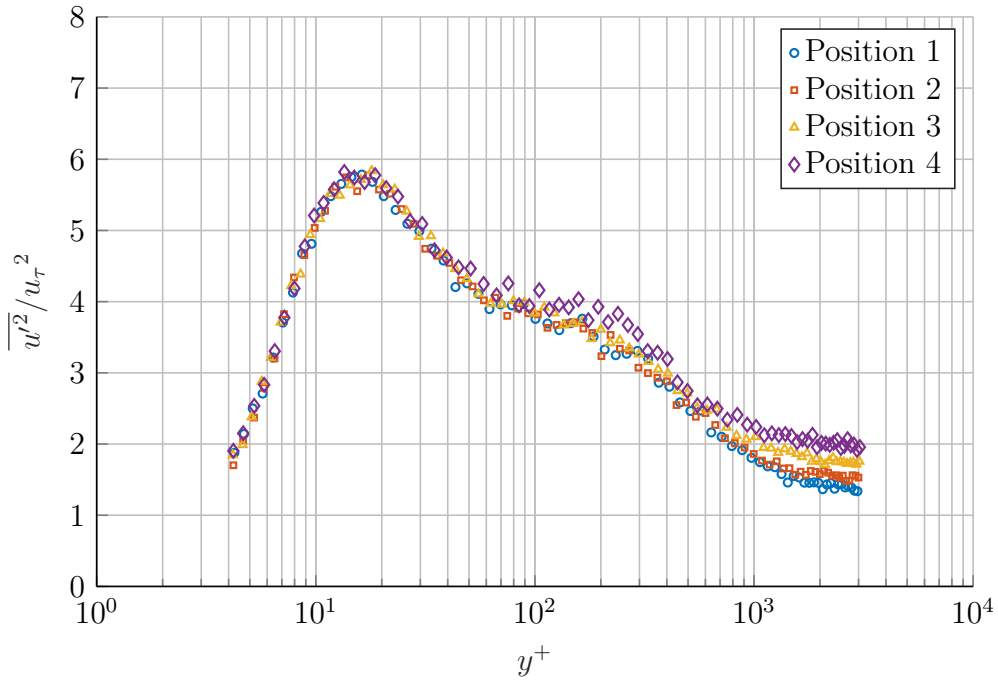

Figure 5.21: Variation of Non-dimensional Streamwise Kinetic Energy

thicknesses are found:

$$\frac{\delta_1}{\delta} = \frac{1}{n+1} \tag{5.35}$$

$$\frac{\delta_2}{\delta} = \frac{n}{(n+1)(n+2)} \tag{5.36}$$

Then, combining these two equations, the shape factor is found to be

$$H = 1 + \frac{2}{n} \tag{5.37}$$

which no longer depends on the boundary layer thickness δ, which is helpful since δ is an ill-defined quantity for external flow boundary layers (or developing internal flow boundary layers). Now, since H is available, the value for n is determined by inversing Eq. (5.37) to solve for n, where it was found to be $n = 8.35$. As an alternative to this approach, the best fit for n can be found by fitting the power-law curve $u^+ = ky^{+(1/n)}$ using a subset of the data in the boundary layer where the power-law is most accurate. If the data between $y^+ = 30$ and $y/\delta_{99} = 0.2$ is chosen, the value for n was found to be $n = 7.11$. However, since the power-law worked only moderately well to describe the

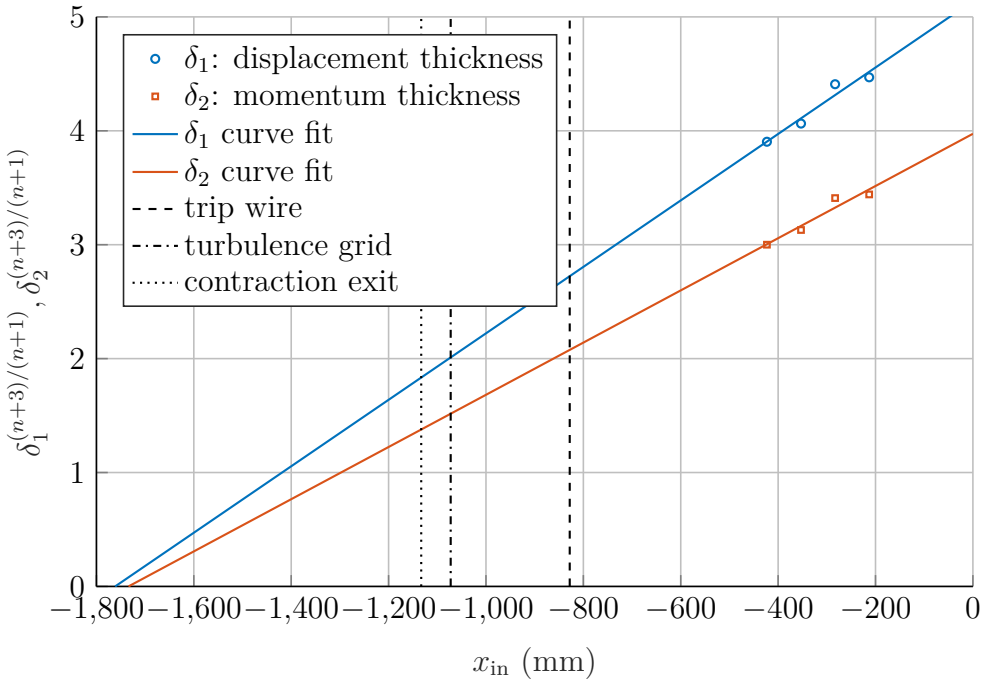

Figure 5.22: Determination of the Boundary Layer Virtual Origin

measured boundary layer profile in this work, the final result for n was quite sensitive to the subset of data that was used for the calculation. Therefore, the author prefers the first approach described, which is not dependent on the data subset selected, so the value of $n = 8.35$ was used here.

Furthermore, it is shown by Schlichting and Gersten (2016) that turbulent boundary layer thicknesses, including the displacement and momentum thicknesses, are expected to grow in the streamwise direction proportionally to $x^{(n+1)/(n+3)}$, where x is measured from the virtual origin and n is from the power-law fit result. Therefore, by plotting $\delta_1^{(n+3)/(n+1)}$ and $\delta_2^{(n+3)/(n+1)}$ vs. x and performing a linear fit, the virtual origin can be identified. The average of the virtual origin results for the momentum and displacement thicknesses best fit was found to be at $x_{\text{in}} = -1748\,\text{mm}$, as shown in Figs. 5.22 and 5.23.

Determination of Cascade Inlet Turbulence Intensity

The turbulence intensity is expected to decay in the streamwise direction as the flow exits the turbulence grid and moves toward the cascade inlet. Mohamed and Larue

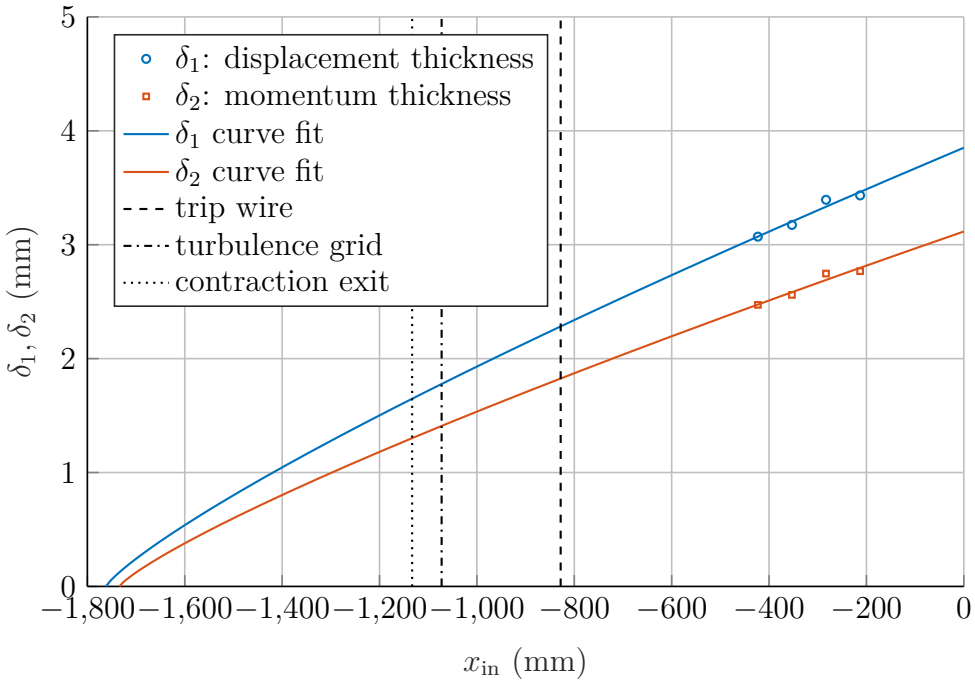

Figure 5.23: Displacement and Momentum Thicknesses

(1990) found that a decay law for the turbulent kinetic energy is expected to exhibit the following behavior downstream of a turbulence grid:

$$\frac{k}{\overline{u}^2} \propto (x - x_{\text{grid}})^{-n} \tag{5.38}$$

where n is near 1.3 and the definition for the turbulent kinetic energy k is

$$k = \frac{1}{2}\left(\overline{u'^2} + \overline{v'^2} + \overline{w'^2}\right) = \frac{3}{2}v_{\text{RMS}}^2 \tag{5.39}$$

Using the data from the four measured positions in the freestream, the value for n was found to equal 1.49, as shown in Fig. 5.24. Meanwhile, the turbulence intensity decays at half the decay rate of the turbulent kinetic energy, as shown in Fig. 5.25. Taking the result evaluated at $x_{\text{in}} = 0$, the turbulence intensity at the cascade inlet conditions was found to be $Tu_{\text{in}} = 4.6\,\%$.

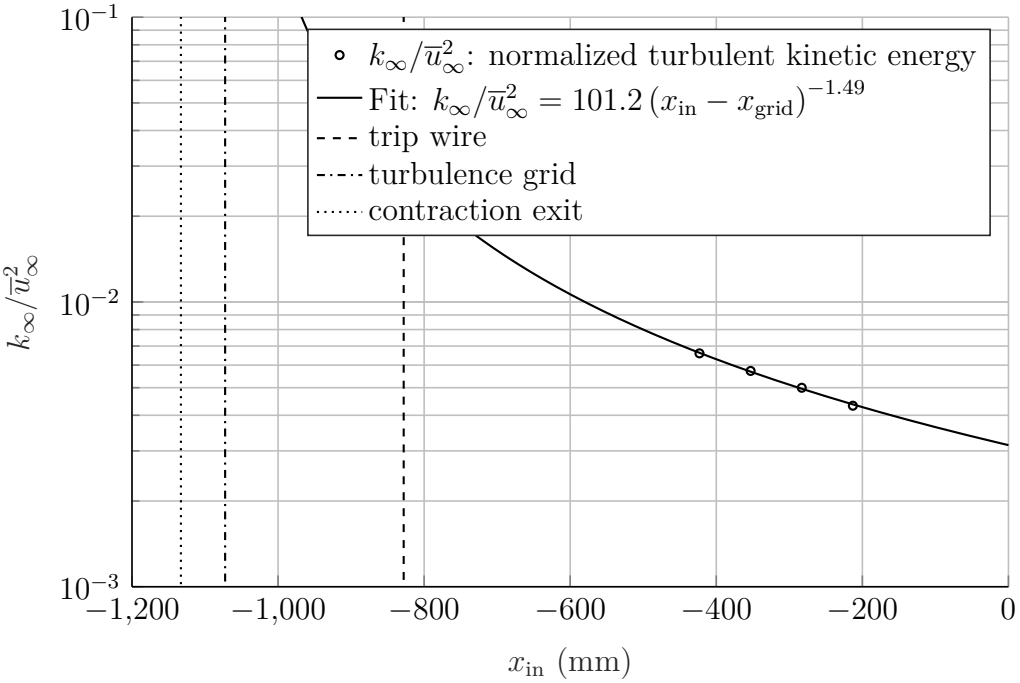

Figure 5.24: Freestream Turbulent Kinetic Energy Decay

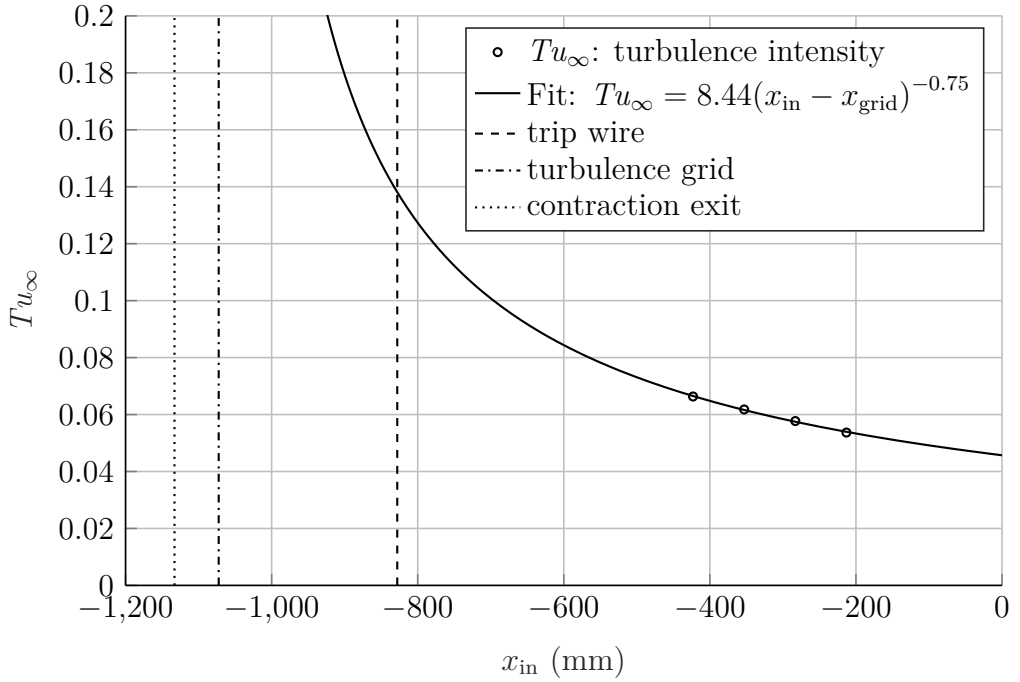

Figure 5.25: Freestream Turbulence Decay

5.5.2 Freestream Measurements

The hot-wire probe was positioned 66 mm away from the bottom wall at Position 4 to characterize the freestream turbulence: measuring turbulent flow length scales, dissipation levels, and the power spectral density. Hot-wire measurements were made at four different sampling frequencies: 5 kHz, 10 kHz, 25 kHz, and 50 kHz with an analog low-pass filter set to 2 kHz, 4 kHz, 10 kHz, and 20 kHz, respectively. These low pass filter levels were chosen to meet the Nyquist sampling criterion to prevent aliasing of high-frequency components with lower frequencies. For each sampling frequency, 50 000 velocity measurements were made.

Turbulence Length Scales and Dissipation

This section describes the calculations and results for the turbulent length scales and the dissipation levels present in the test section. Pope (2011) and Romano et al. (2007) discuss various theory and derivations for the calculations which are included in the following section. To determine the turbulence length scales present in the flow field, the autocorrelation coefficient of the spatial or temporal velocity is a useful quantity to determine first. In this case, the hot-wire probe was stationary, so the temporal autocorrelation coefficient was measured. For n discrete measurements, the kth autocorrelation coefficient for a set of fluctuating velocity measurements can be determined using

$$\rho_{u'^2}(k) = \frac{1}{(n-k)\overline{u'^2}} \sum_{i=1}^{n-k} u'_i u'_{i+k} \tag{5.40}$$

Since the maximum precision is desired near temporal time scales close to zero, only the 50 kHz sampling frequency data is used, which corresponds to a sampling period $T = 20\,\mu s$. Then, the autocorrelation result as a function of time lag τ can be achieved by plotting $\rho_{u'^2}(k)$ against $\tau = kT$. Additionally, by using Taylor's frozen turbulence hypothesis, the temporal autocorrelation can be converted to a spatial autocorrelation, in distance r, by merely multiplying the time lag τ by the local convective velocity $\overline{u}$:

$$r = \tau\overline{u} = kT\overline{u} \tag{5.41}$$

Specifically, this is a longitudinal spatial autocorrelation (opposed to a transverse or vertical autocorrelation) since the fluctuating measurement u' is in alignment with

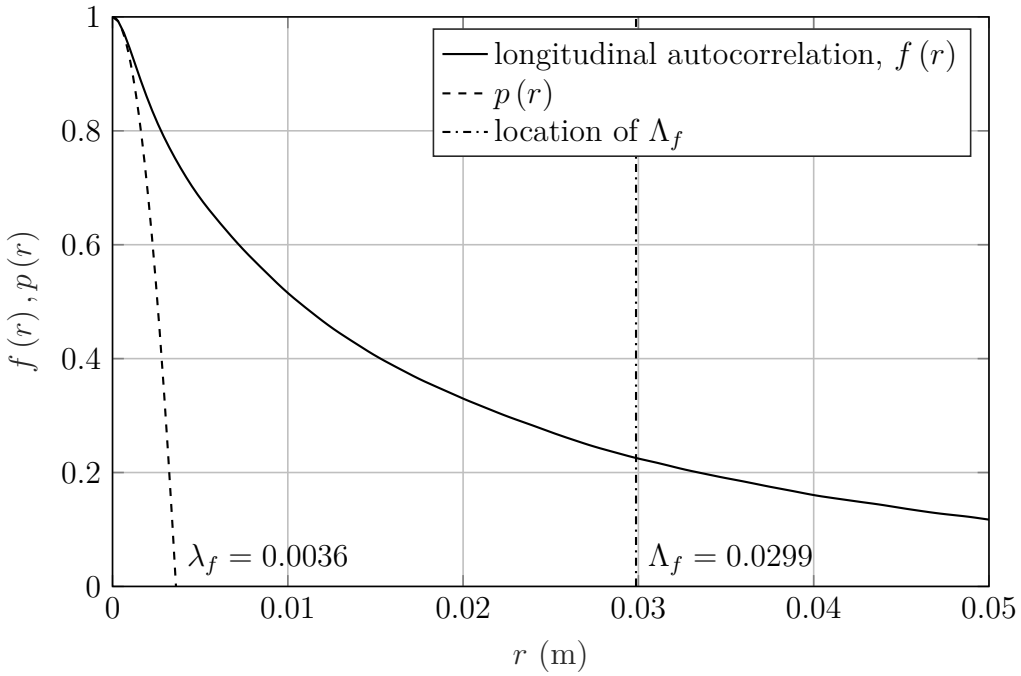

Figure 5.26: Turbulent Length Scales

the main flow direction, $\overline{u}$. The results for the longitudinal spatial autocorrelation are displayed in Fig. 5.26, where the longitudinal autocorrelation coefficient is labeled as $f(r)$.

The spatial autocorrelation can be processed to determine the Taylor microscale, which is representative of medium eddy sizes in the inertial subrange. The length scale is related to the second derivative of the spatial autocorrelation coefficient, and can visually be understood to be the r-intercept for a downward parabola that matches the second derivative at $r = 0$. This parabola is labeled as $p(r)$ in Fig. 5.26. The longitudinal and transverse Taylor microscales, λ_f and λ_g, respectively, are determined as follows:

$$\lambda_f = \left(-.5 \frac{\partial^2 f}{\partial r^2} \right)^{-.5} \tag{5.42}$$

$$\lambda_g = \frac{\lambda_f}{\sqrt{2}} \tag{5.43}$$

A central finite difference for the second derivative was estimated by using a nine coefficient, eighth-order accuracy calculation. Note that a central difference estimate can be used since the autocorrelation is an even function (symmetric about the y-axis).

The turbulence Reynolds number can then be calculated based on the transverse Taylor length scale as follows:

$$Re_\lambda = \frac{v_{\mathrm{RMS}}\lambda_g}{\nu} \tag{5.44}$$

Next, the spatial autocorrelation can be processed in a different manner to determine the integral length scale, which represents the largest eddies in the flow within the energy-containing scales. The longitudinal and transverse integral length scales, Λ_f and Λ_g, respectively, are found as follows:

$$\Lambda_f = \int_0^\infty f\left(r\right)\,\mathrm{d}r \tag{5.45}$$

$$\Lambda_g = \frac{\Lambda_f}{2} \tag{5.46}$$

For discrete measurements of an autocorrelation, as performed here, the estimate for $f(r)$ function becomes very noisy at high r since $n-k$, in Eq. (5.40), becomes small. Meanwhile, for turbulent flow, $f(r)$ must approach zero at high r (specifically as r grows large compared with the largest length scales). There are various options to deal with the noise issue. The most straightforward strategy, which was employed here, is to integrate using the trapezoid rule until the autocorrelation function first crosses zero (when the correlation first goes negative), as this was found to be consistent and robust with the datasets collected.

The dissipation rate in the turbulent flow can be determined in the following way for isotropic turbulent flow:

$$\varepsilon = 15\nu\overline{\left(\frac{\partial u'}{\partial x}\right)^2} \tag{5.47}$$

This can be related conveniently to the transverse Taylor microscale:

$$\varepsilon = \frac{15\nu\overline{u'^2}}{\lambda_g^2} \tag{5.48}$$

Another approach for estimating the dissipation is based on the streamwise derivative of the turbulent kinetic measurements in a decaying turbulence field downstream of a turbulence grid (Fig. 5.24):

$$\varepsilon_{\mathrm{dec}} = -\overline{u}\frac{\partial k}{\partial x} \tag{5.49}$$

Table 5.1: Turbulent Flow Measurement Quantities (Position 4)

Blade Reynolds Number, Re	5.12×10^5
Taylor Microscale Reynolds Number, Re_λ	161
Longitudinal Integral Length Scale, Λ_f	0.0299 m
Transverse Integral Length Scale, Λ_g	0.0149 m
Longitudinal Taylor Length Scale, λ_f	0.0036 m
Transverse Taylor Length Scale, λ_g	0.0026 m
Kolmogorov Length Scale, η	1.02×10^{-4} m
Dissipation, ε	$36.2\,\mathrm{m}^2/\mathrm{s}^3$
Dissipation, $\varepsilon_{\mathrm{dec}}$	$61.1\,\mathrm{m}^2/\mathrm{s}^3$

Next, the Kolmogorov length scale can be determined, which represents the scale of the smallest eddies in the flow (within the dissipation range):

$$\eta = \left(\frac{\nu^3}{\varepsilon}\right)^{1/4} \tag{5.50}$$

All of the results described in the proceeding section are summarized in Table 5.1.

Power Spectral Density

A power spectral density estimate of the velocity spectra was performed using Welch's method. The estimate was performed using Matlab's `pwelch` function for each measurement set, which results in an estimate for $E_{11}(f)$, which is the power spectral density estimate for u'. A Hann filter was used with a window size of 128 with overlap size equal to half the window size. Digital low-pass filtering was applied (in addition to the analog filtering) on the power spectral estimate results at 1 kHz, 2 kHz, 5 kHz, and 10 kHz, respectively, in order to remove the effect of the analog filter. For each measurement frequency, the test was performed four times in total. The results for each measurement frequency were then averaged in the frequency domain. Then, the segments for 0.001 kHz to 1 kHz, 1 kHz to 2 kHz, 2 kHz to 5 kHz, and 5 kHz to 10 kHz, corresponding to the four sampling frequencies, were stitched together, which results in the power density spectrum over the range from 0.001 kHz to 10 kHz. In total, 800 000 data points were used during this process. These results are shown in Fig. 5.27. Small discontinuities are observed where these results were stitched together: at 1 kHz,

2 kHz, and 5 kHz.

It is often convenient to restate the power spectral density results in the wavenumber domain rather than the frequency domain. The wavenumber κ_1 is defined as

$$\kappa_1 = \frac{2\pi f}{\overline{u}} \tag{5.51}$$

A $-5/3$ power-law behavior is expected to occur in the inertial subrange, which is in agreement with the data measured, as shown in Fig. 5.28. Also, if the results in the wavenumber domain are non-dimensionalized using the Kolmogorov scales (shown in Fig. 5.29), the power spectral density is expected to collapse onto a universal curve near the dissipation range: $\kappa_1\eta \approx 1$. This collapsing behavior is confirmed by comparing the results here with the data available in (Pope, 2011). Additionally, the value for the non-dimensional E_{11} within the energy-containing range (at low $\kappa_1\eta$ values) is expected to be a function of Re_λ primarily. The data available indicates that a value between 4×10^3 to 1×10^4 is expected based on the Re_λ present in this work. Here, a value near 6×10^3 was found, demonstrating alignment with literature turbulence measurements.

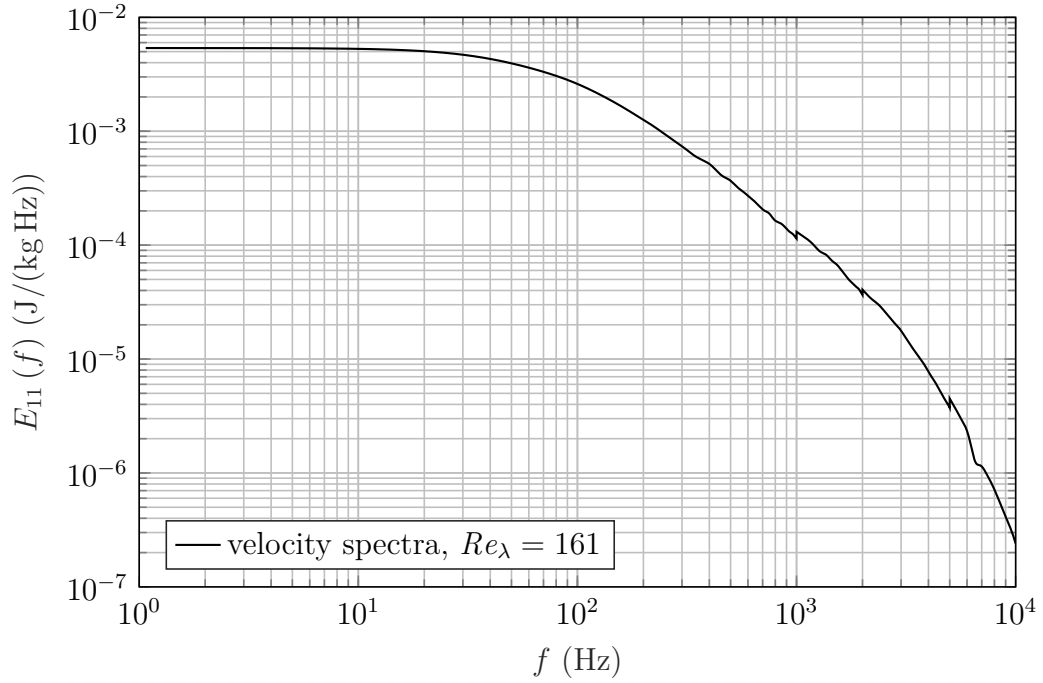

Figure 5.27: Velocity Spectra—Frequency Domain

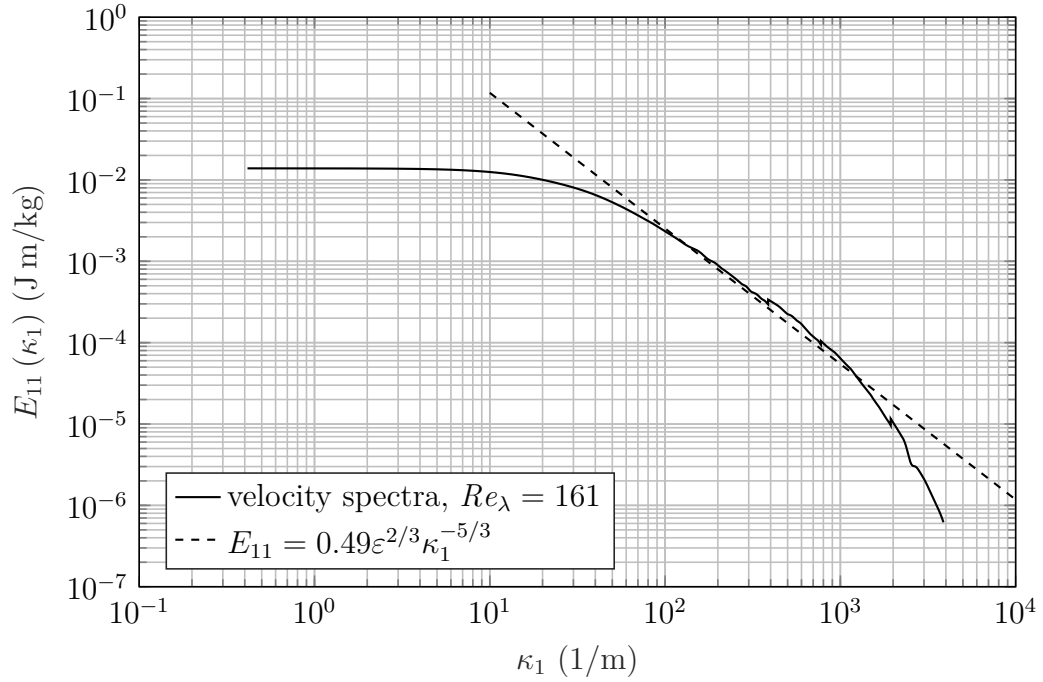

Figure 5.28: Velocity Spectra—Wavenumber Domain

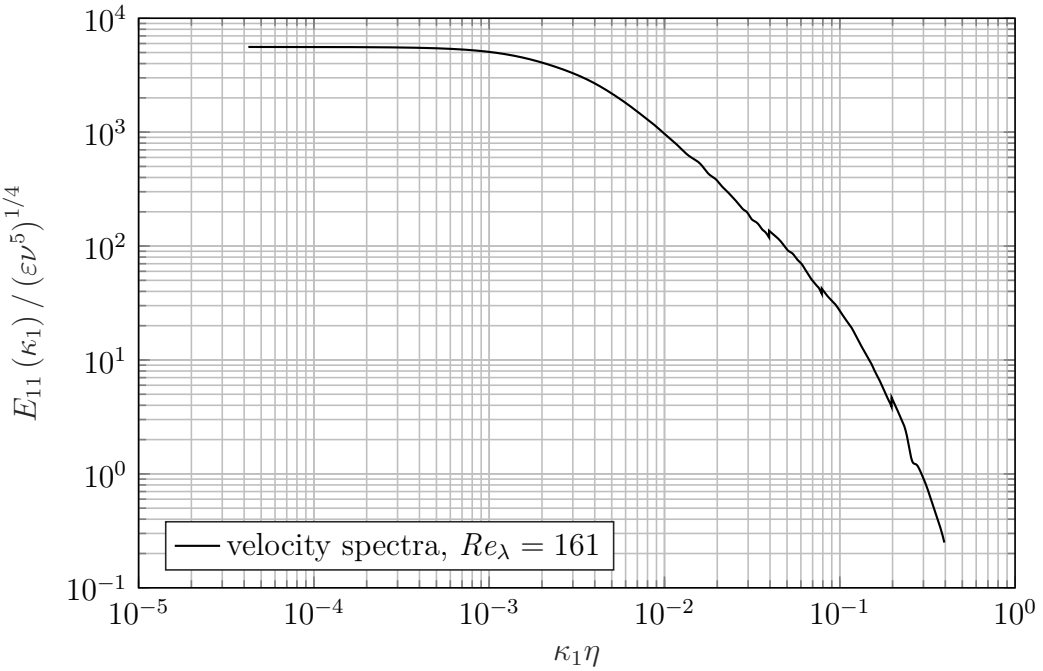

Figure 5.29: Kolmogorov Scaled Velocity Spectra

Chapter 6

Results

The experimental results for the four major experimental cases are reported in this chapter. For each case, the experimental design is presented, followed by the experimental results. The results include endwall contour and pitchwise-averaged results for the Sherwood number and film cooling effectiveness. Additionally, area-averaged summary results are tabulated. The significance of the findings is discussed. Lastly, the uncertainties in the reported results are given and discussed.

6.1 Case 1: Straight Slot

The straight slot experiment is designed to determine the effect of the blowing ratio and swirl angle on endwall mass transfer and film cooling for a simplified injection geometry. The experimental design for the straight slot experimental case is listed in Table 6.1, which includes the design conditions and the number of experimental replicates (labeled as "Rep."). The experimental design is a two-level factorial design with center point in variables M_s and θ. This type of design was chosen because it is an economical way to experiment over a full design space and determine the main effects and their interactions. Additionally, one case with $M_s = 0$ was performed, which was required to make the net heat flux reduction ($NHFR$) calculation. Lastly, a low Reynolds number test was performed to determine the effect of Reynolds number on mass transfer and film cooling. The results described in this section have been published in (Stinson et al., 2014).

The key results for the mass transfer, film cooling effectiveness, and the net heat flux reduction are presented in Figs. 6.1 to 6.21. The mass transfer and film cooling results

Table 6.1: Straight Slot Experimental Case Listing

Exp.	Rep.	M_s	θ	Saturated	Re	Tu
1a	1	0.5	0°	no	6×10^5	5 %
1b	1	0.5	0°	yes	6×10^5	5 %
2a	1	1.5	0°	no	6×10^5	5 %
2b	1	1.5	0°	yes	6×10^5	5 %
3a	1	0.5	60°	no	6×10^5	5 %
3b	1	0.5	60°	yes	6×10^5	5 %
4a	1	1.5	60°	no	6×10^5	5 %
4b	1	1.5	60°	yes	6×10^5	5 %
5a	1	1	30°	no	6×10^5	5 %
5b	1	1	30°	yes	6×10^5	5 %
6a	1	1	30°	no	3×10^5	5 %
6b	1	1	30°	yes	3×10^5	5 %
7	1	0	—	—	6×10^5	5 %

are summarized in Table 6.2. In the summary table, various quantities are calculated over the endwall surface: the area-averaged Sherwood number, the area-averaged film cooling effectiveness, and the area-averaged net heat flux reduction. The area averaging is performed for all the passage data such that $x/C_{ax} \leq 1$. Additionally, the axial penetration is reported, which indicates how far downstream in the axial direction that the coolant still provides significant film cooling coverage. The axial penetration calculation is done in this work by fitting a straight line to the pitchwise-averaged film cooling effectiveness results up until the point where the effectiveness first drops below 0.1. Then, the axial position at which that best fit line equals 0.2 is defined and reported as the axial penetration.

6.1.1 Mass Transfer

The Sherwood number results indicated a substantial enhancement in the mass transfer as the blowing ratio increased. Figure 6.8 shows the enhancement is primarily near the entrance closest to the injection slot, with the results nearly collapsing for $x/C_{ax} \geq 0.5$.

Meanwhile, the effect of the swirl on the endwall mass transfer was weakly positive at the low blowing rate cases (cases 1 and 3) as explained by the higher absolute slot velocity. The effect of the purge flow swirl was mixed for the high blowing rate

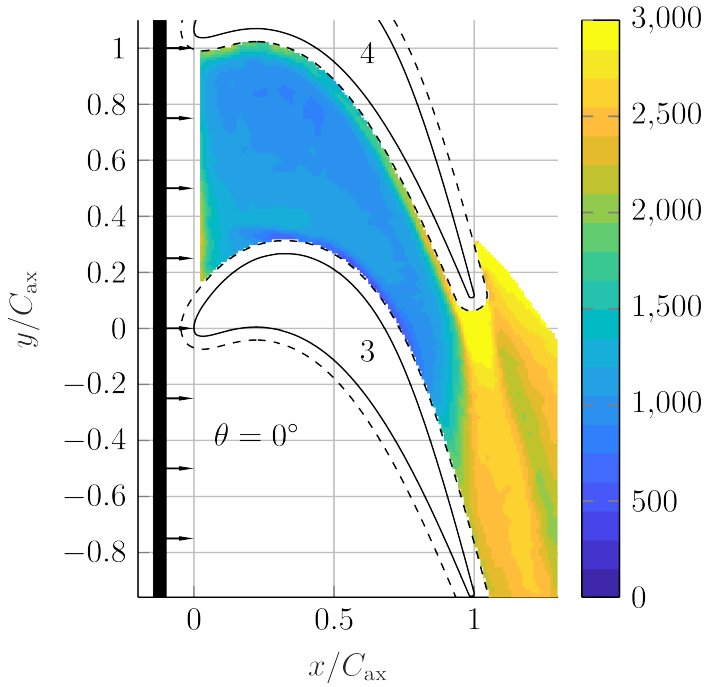

Figure 6.1: Sherwood Number—Straight Slot Case 1 ($M_{\text{s}} = 0.5$, $\theta = 0°$)

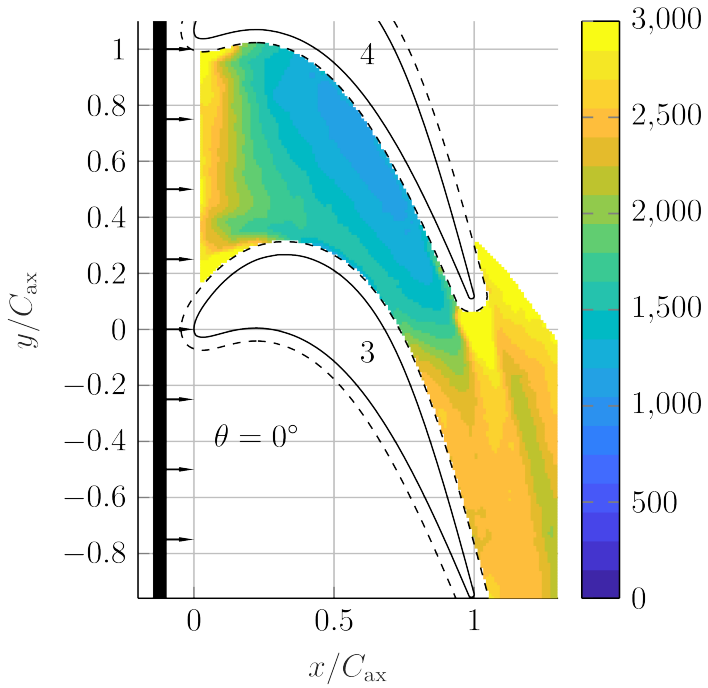

Figure 6.2: Sherwood Number—Straight Slot Case 2 ($M_{\text{s}} = 1.5$, $\theta = 0°$)

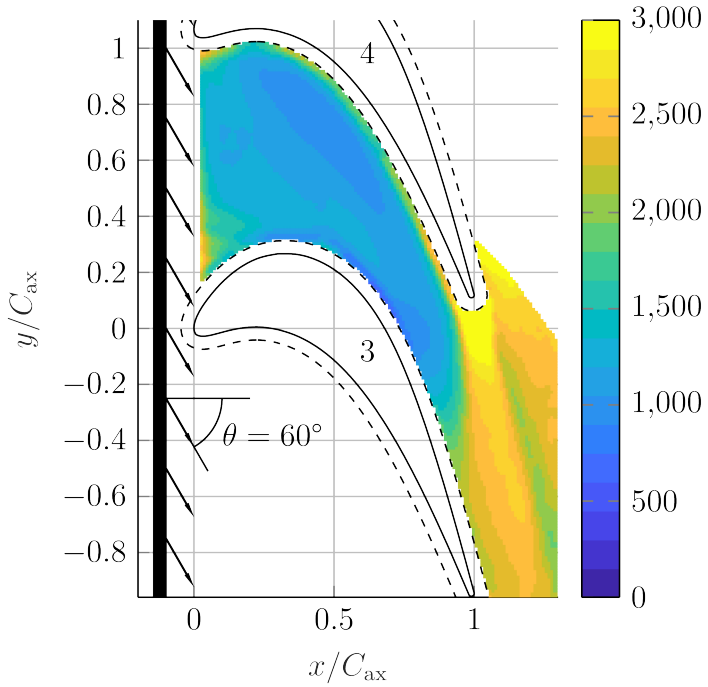

Figure 6.3: Sherwood Number—Straight Slot Case 3 ($M_s = 0.5$, $\theta = 60°$)

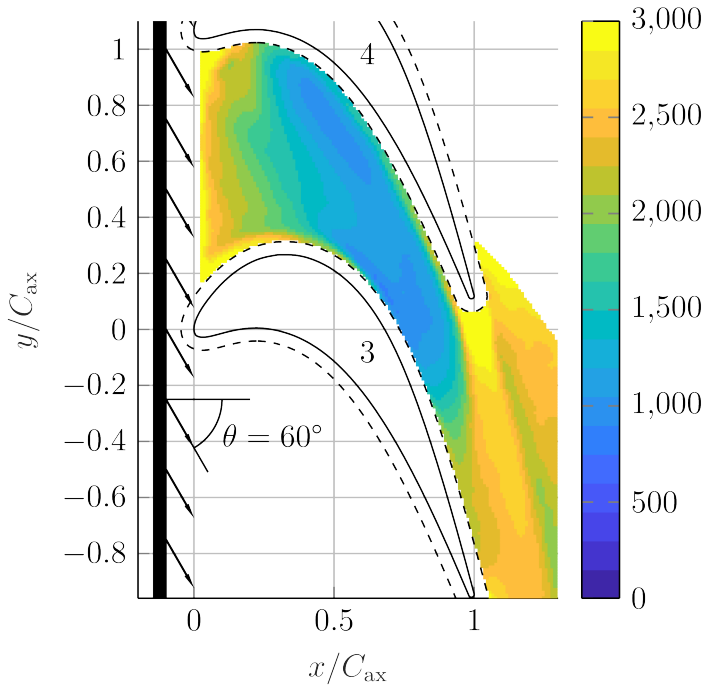

Figure 6.4: Sherwood Number—Straight Slot Case 4 ($M_s = 1.5$, $\theta = 60°$)

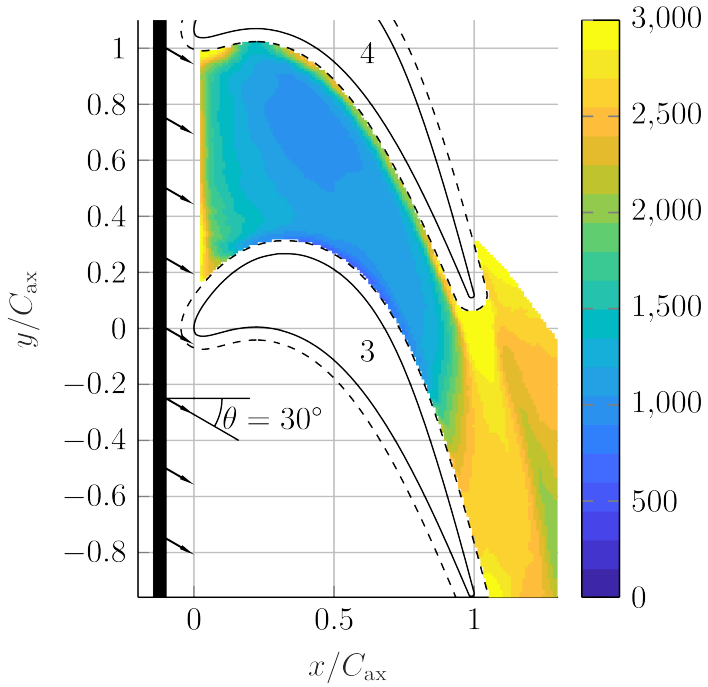

Figure 6.5: Sherwood Number—Straight Slot Case 5 ($M_{\text{s}} = 1$, $\theta = 30°$)

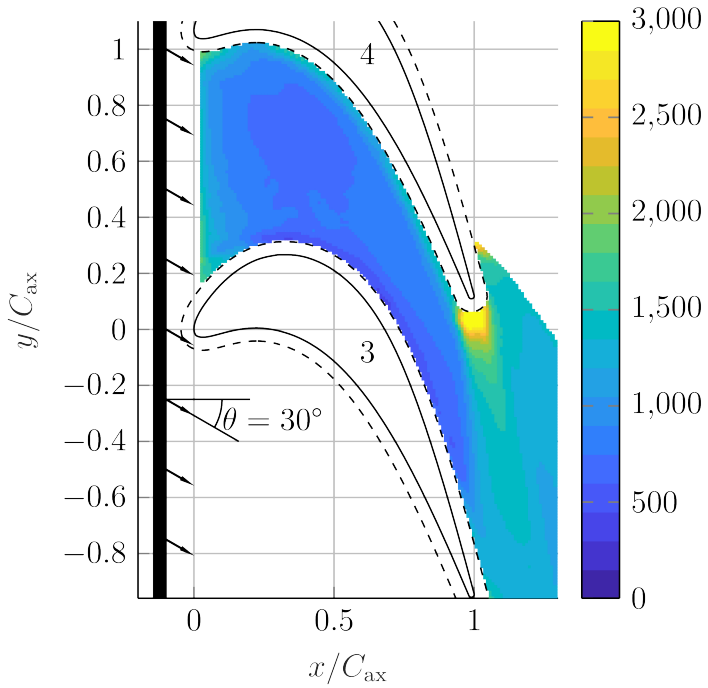

Figure 6.6: Sherwood Number—Straight Slot Case 6 ($M_{\text{s}} = 1$, $\theta = 30°$)

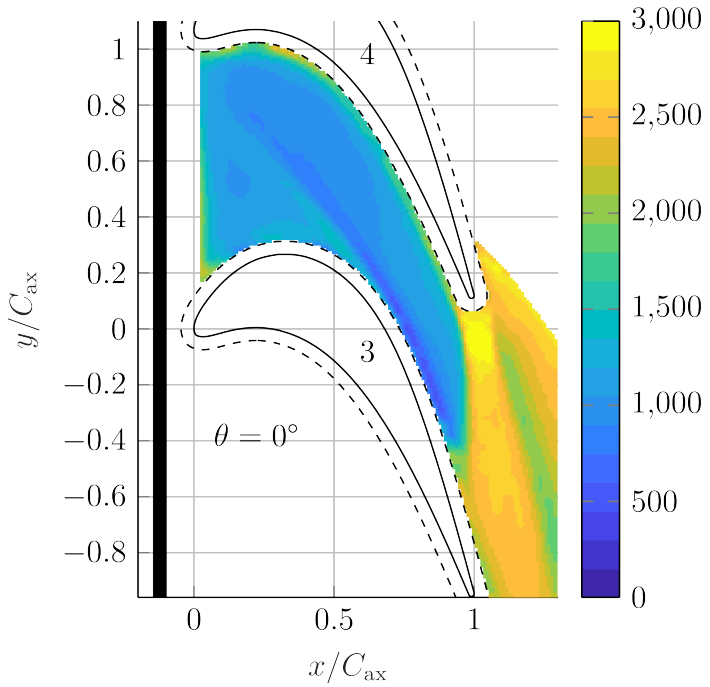

Figure 6.7: Sherwood Number—Straight Slot Case 7 ($M_{\mathrm{s}} = 0$, $\theta = 0°$)

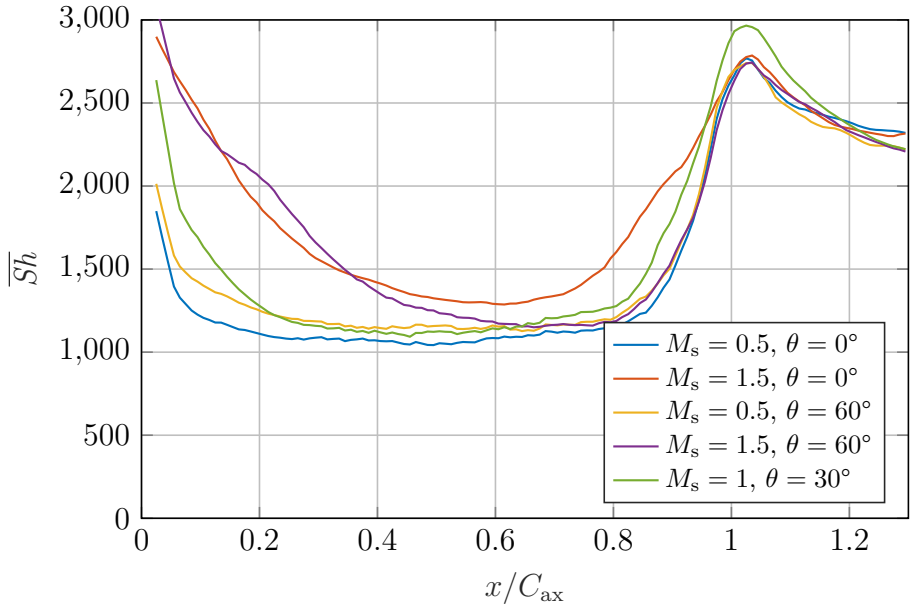

Figure 6.8: Pitchwise-Averaged Sherwood Number—Straight Slot

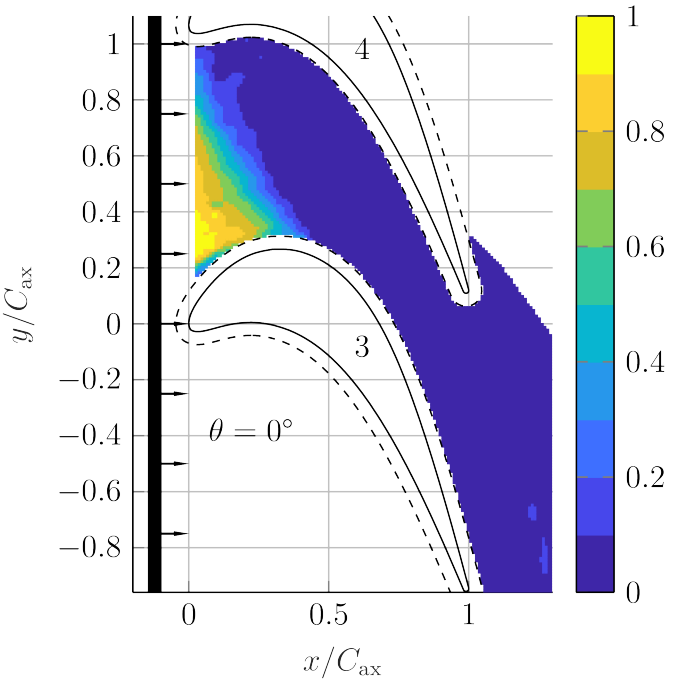

Figure 6.9: Film Cooling Effectiveness—Straight Slot Case 1 ($M_{\text{s}} = 0.5$, $\theta = 0°$)

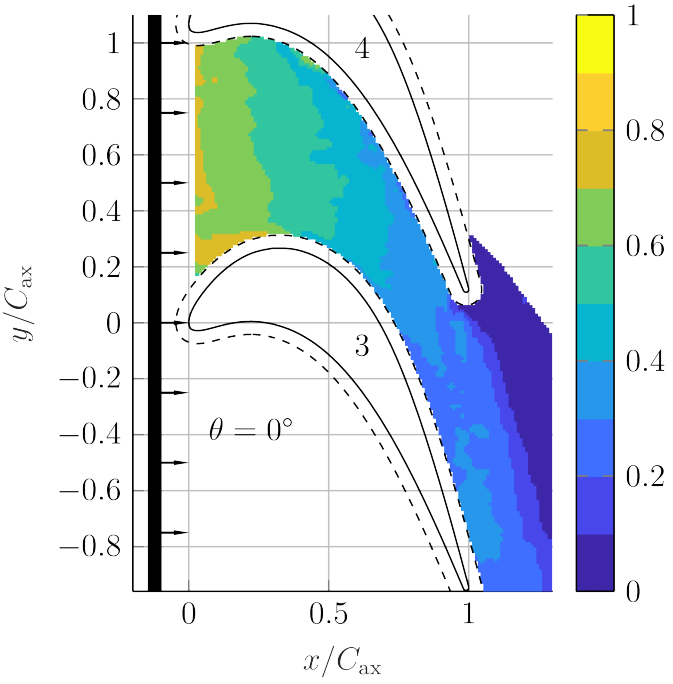

Figure 6.10: Film Cooling Effectiveness—Straight Slot Case 2 ($M_{\text{s}} = 1.5$, $\theta = 0°$)

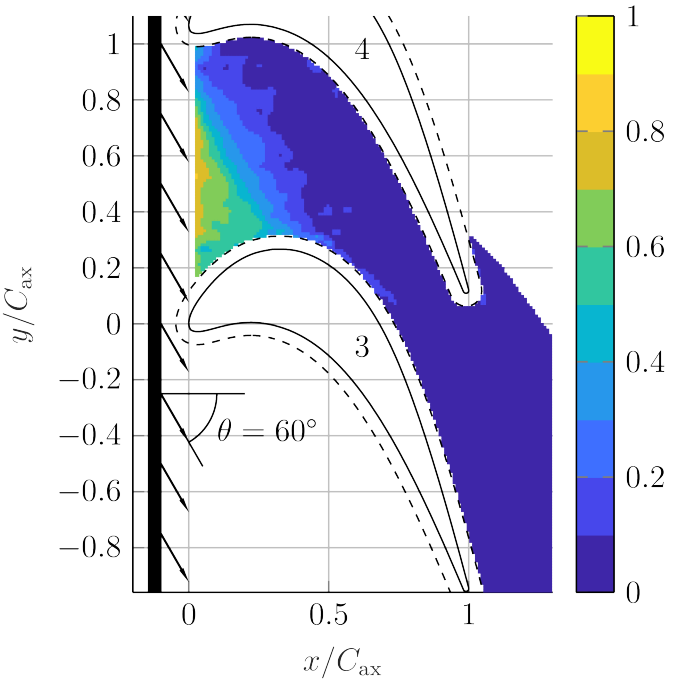

Figure 6.11: Film Cooling Effectiveness—Straight Slot Case 3 ($M_{\text{s}} = 0.5$, $\theta = 60°$)

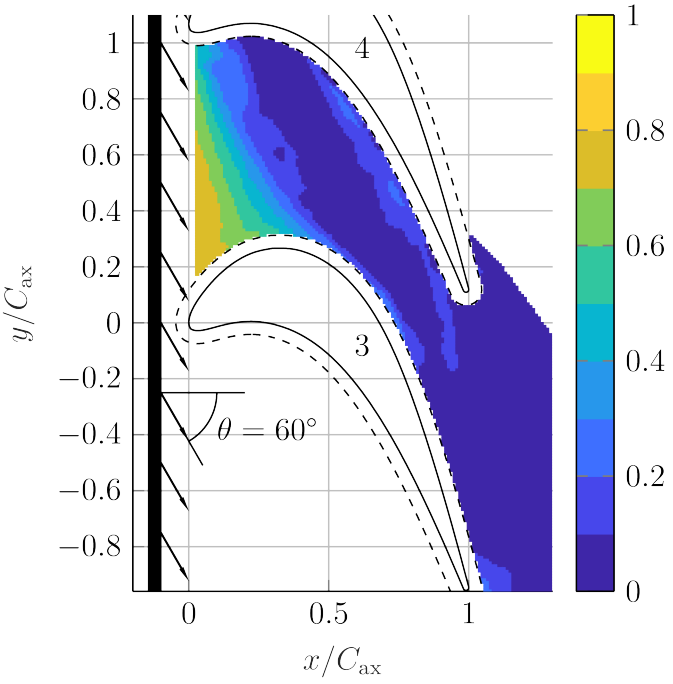

Figure 6.12: Film Cooling Effectiveness—Straight Slot Case 4 ($M_{\text{s}} = 1.5$, $\theta = 60°$)

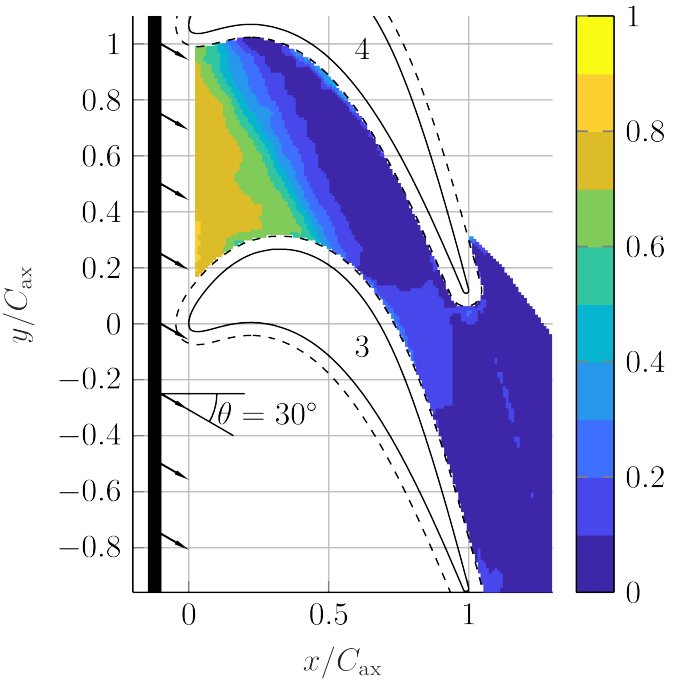

Figure 6.13: Film Cooling Effectiveness—Straight Slot Case 5 ($M_{\text{s}} = 1$, $\theta = 30°$)

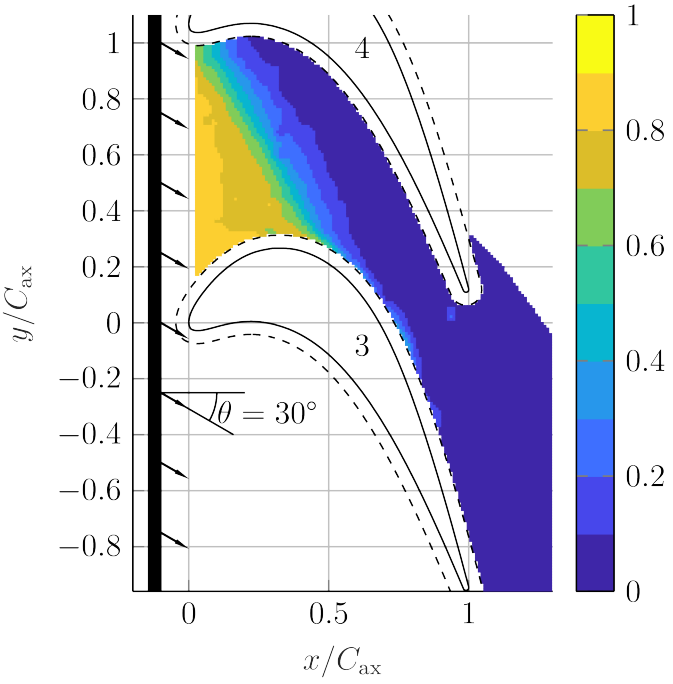

Figure 6.14: Film Cooling Effectiveness—Straight Slot Case 6 ($M_{\text{s}} = 1$, $\theta = 30°$)

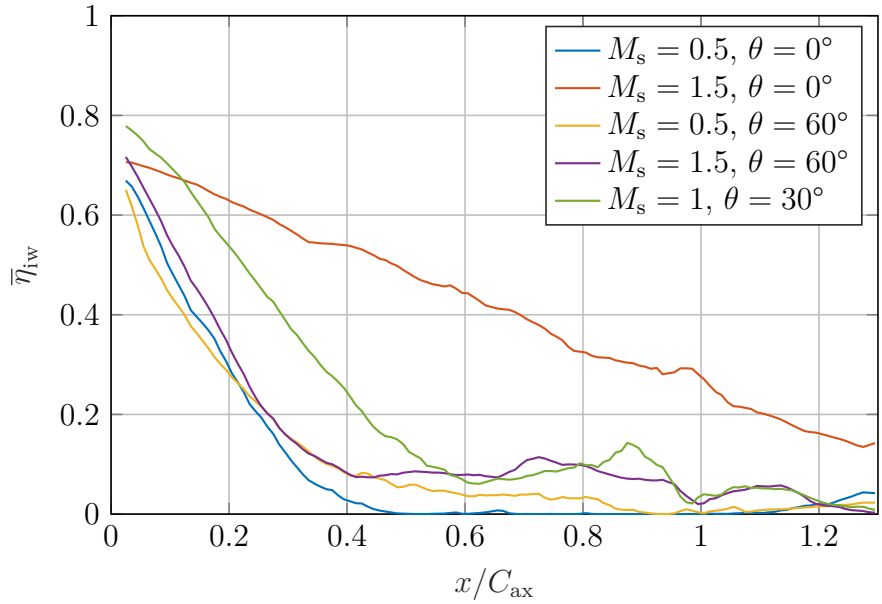

Figure 6.15: Pitchwise-Averaged Film Cooling Effectiveness—Straight Slot

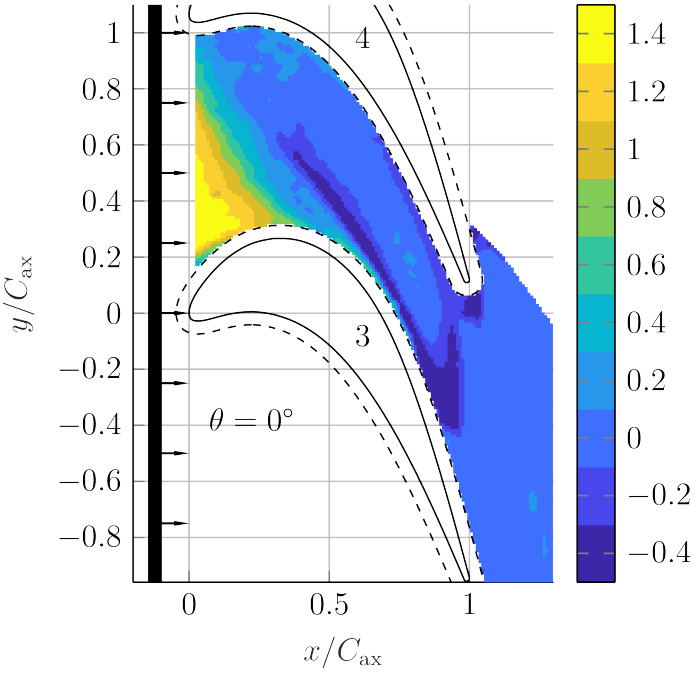

Figure 6.16: Net Heat Flux Reduction—Straight Slot Case 1 ($M_s = 0.5$, $\theta = 0°$)

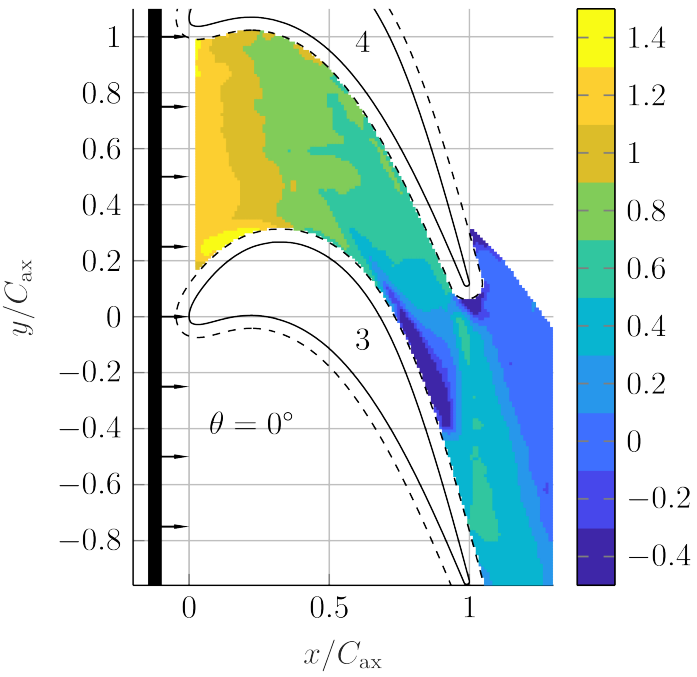

Figure 6.17: Net Heat Flux Reduction—Straight Slot Case 2 ($M_{\text{s}} = 1.5$, $\theta = 0°$)

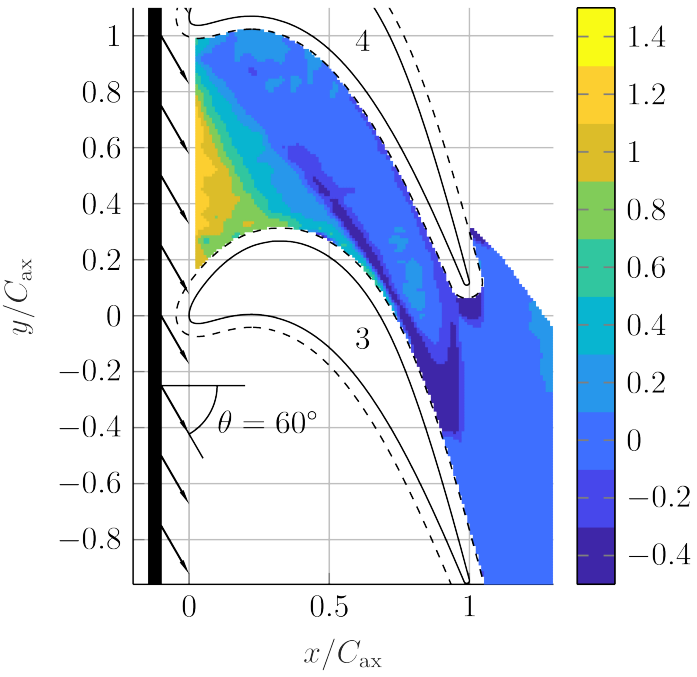

Figure 6.18: Net Heat Flux Reduction—Straight Slot Case 3 ($M_{\text{s}} = 0.5$, $\theta = 60°$)

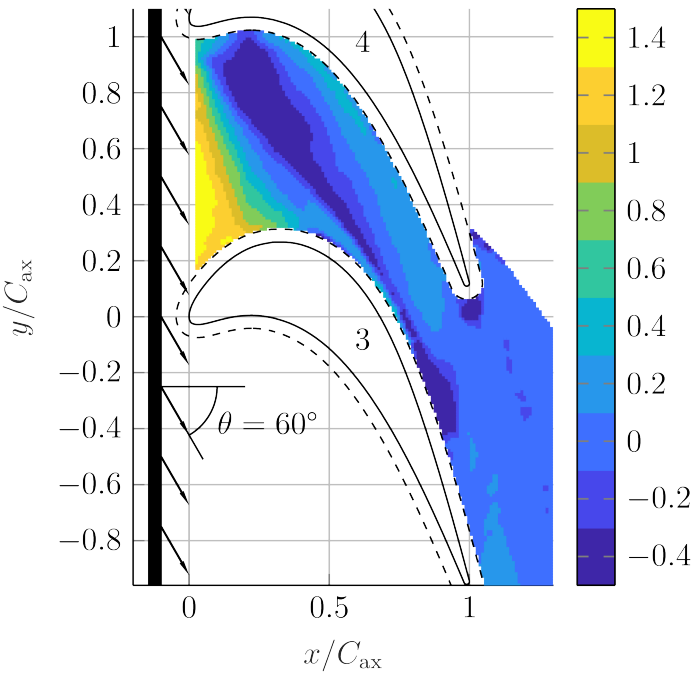

Figure 6.19: Net Heat Flux Reduction—Straight Slot Case 4 ($M_{\text{s}} = 1.5$, $\theta = 60°$)

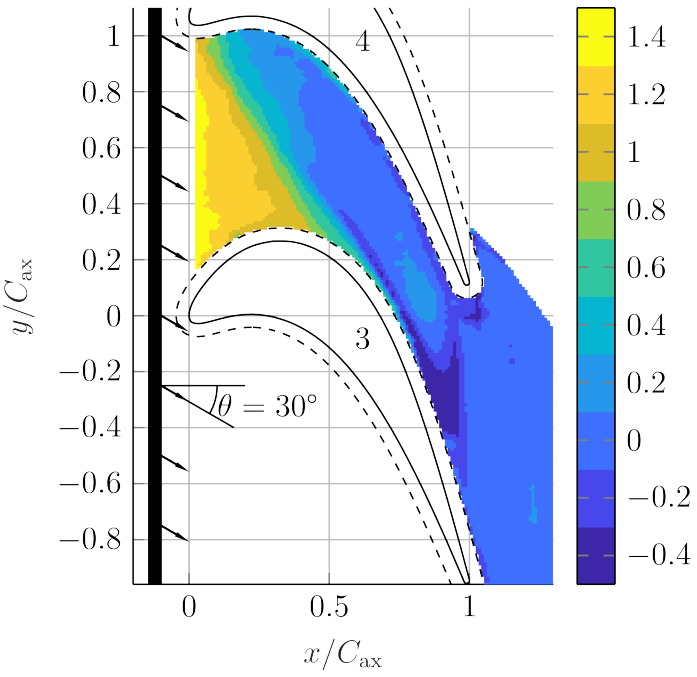

Figure 6.20: Net Heat Flux Reduction—Straight Slot Case 5 ($M_{\text{s}} = 1$, $\theta = 30°$)

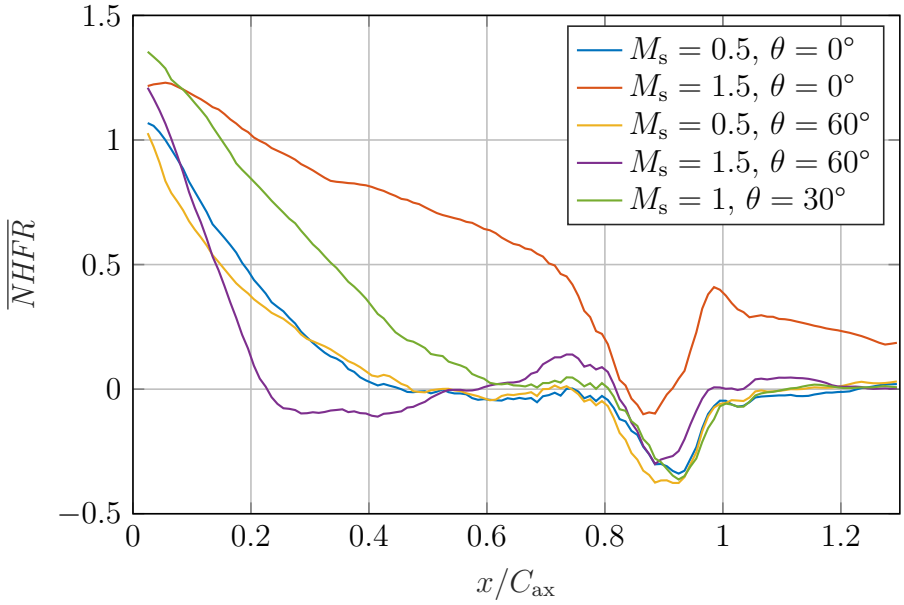

Figure 6.21: Pitchwise-Averaged Net Heat Flux Reduction—Straight Slot

Table 6.2: Straight Slot Result Summary

Exp.	M_{s}	θ	Re	$\overline{\overline{Sh}}$	$\overline{\overline{\eta}}_{\text{iw}}$	Axial Pen.	$\overline{\overline{NHFR}}$
1	0.5	0°	6×10^5	1.25×10^3	0.14	0.25	0.17
2	1.5	0°	6×10^5	1.78×10^3	0.49	1.12	0.69
3	0.5	60°	6×10^5	1.35×10^3	0.15	0.27	0.14
4	1.5	60°	6×10^5	1.68×10^3	0.20	0.28	0.12
5	1	30°	6×10^5	1.44×10^3	0.29	0.44	0.37
6	1	30°	3×10^5	8.85×10^2	0.29	0.44	—
7	0	—	6×10^5	1.21×10^3	—	—	—

cases (cases 2 and 4). Figure 6.8 shows that increased swirl led to some mass transfer enhancement in the front half of the passage while it led to a decrease in the mass transfer in the back half of the passage. For the high blowing rate combined with low swirl angle (case 2), the flow pattern was substantially different compared to the other cases as indicated by the apparent flow separation effect starting near $x/C_{\mathrm{ax}} \approx 0.75$ close to the blade suction surface. This finding indicates that the swirl significantly impacts the passage flow structures for high blowing.

6.1.2 Film Cooling

The results show an enhancement in the film cooling effectiveness as the blowing ratio increases. Meanwhile, at high blowing rates, the effect of increasing swirl led to diminished film cooling effectiveness, while at low blowing rates, the effect of the swirl was weak. This effect indicates that there is a strong interaction between blowing and swirl effects and that the blowing rate strongly influences whether the coolant follows its initial trajectory exiting the slot or is carried along with the surrounding flow. This also indicates that increasing blowing is a very effective way to enhance endwall film cooling, but it must be directed (angled) appropriately.

The film coolant penetrated around only a quarter of the way through the passage when either the blowing rate was low or when the swirl angle was high. For the combination of reduced swirl and increased blowing rate, the axial penetration significantly increased (cases 2 and 5). For case 2, when swirl was 0° and blowing ratio was 1.5, the coolant penetrated through the passage completely, confirming that the flow pattern was changed as the mass transfer results indicated. This extreme result shows that under special conditions the crossflow effect can be overcome.

The results from this straight slot case are found to be in alignment with the other recent literature that studied the effect of purge flow swirl: namely, that increased swirl reduces endwall film cooling, and this effect is more significant at higher blowing rates.

6.1.3 Net Heat Flux Reduction

The net heat flux reduction rewards enhanced film cooling effectiveness (compared to zero film cooling effectiveness) and penalizes enhanced mass transfer (compared to

the case without purge flow injection: case 7 here). Generally, it was found that the net heat flux reduction trends and averages correlated strongly with the film cooling effectiveness results. Additionally, it was generally demonstrated that the film cooling effect overpowered the mass transfer effect leading to significantly positive net heat flux reductions.

However, there were two instances when the net heat flux reduction was below zero (heat flux enhancement): (1) near $x/C_{\text{ax}} \approx 0.9$ since the presence of the purge flow significantly reduced the passage vortex strength, and (2) for the high blowing, high swirl case where the mass transfer was enhanced due to the high blowing but there was inadequate film cooling coverage due to the high swirl angle.

6.1.4 Reynolds Number Effects

Mass Transfer

Convective heat/mass transfer theory indicates that an increased Reynolds number should generally lead to enhanced mass transfer. Furthermore, it is expected that the boundary layer mass transfer coefficient will roughly scale proportionally to Re^m, where m should be in the range from 0.5 to 0.8 (corresponding from laminar to turbulent boundary layers). This expectation can be tested by comparing Figs. 6.5 and 6.6. A contour plot of $\log\left(Sh_{\text{Case 5}}/Sh_{\text{Case 6}}\right)/\log\left(600/300\right)$ was generated and is shown in Fig. 6.22, which indicates the exponent value for m applicable over the endwall surface. Three regions are observed: the portion where the coolant covers the endwall where m is approximately between 0.65 to 0.7, the portion where there is no coolant but significant endwall crossflow where m is approximately between 0.45 to 0.55, and the wake region where m is approximately between 0.8 to 1. Given these results, the Reynolds number corrections performed in this work used a value of 0.65 since it was most representative where the film coolant is primarily present, and it was near the mean value over the entire surface. The pitchwise-averaged Sherwood number result comparison between the two Reynolds numbers is plotted in Fig. 6.23. The plot indicates similar behavior trends throughout the passage. Note that it was observed that the trailing edge wake size was significantly enhanced at the higher Reynolds number, indicating that wake area flow pattern and cooling strategies are Reynolds number dependent.

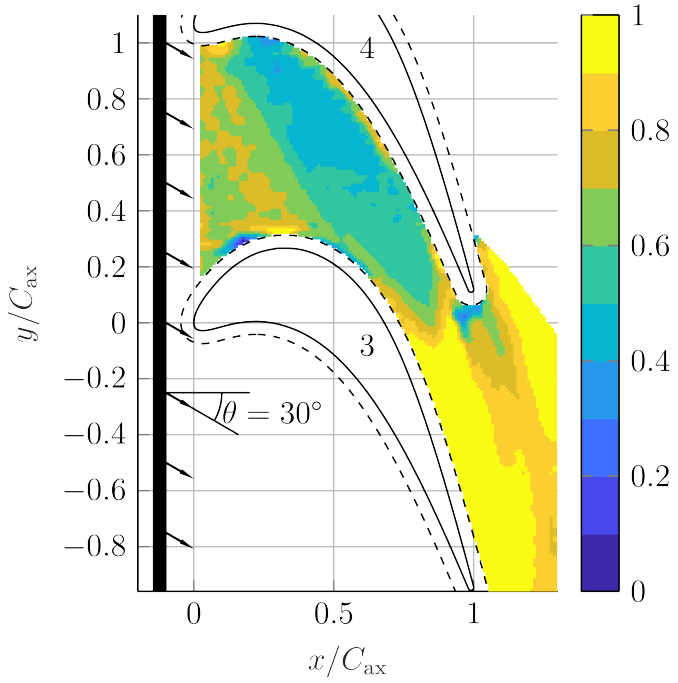

Figure 6.22: Contour of Reynolds Number to Sherwood Number Power Scaling: $\log\left(Sh_{\text{Case 5}}/Sh_{\text{Case 6}}\right)/\log\left(600/300\right)$

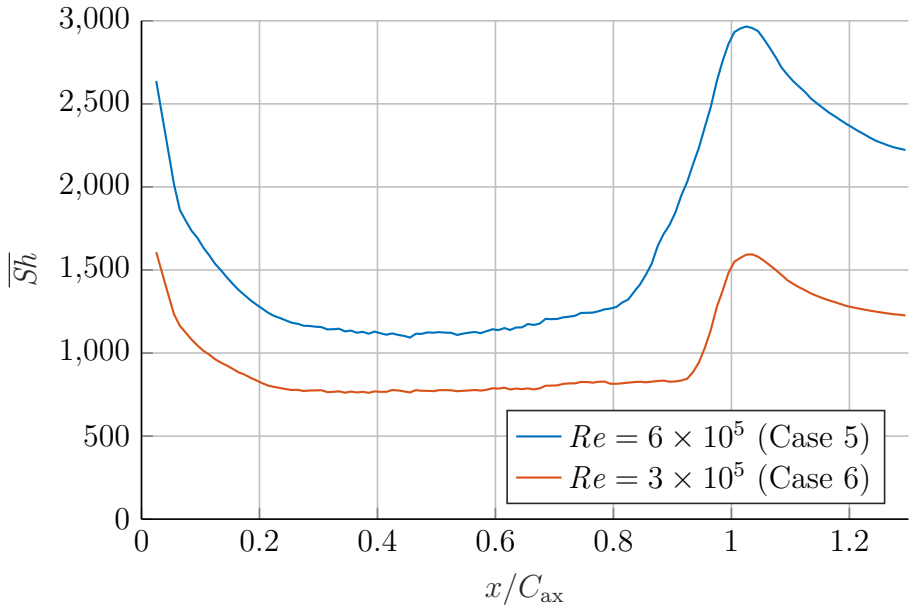

Figure 6.23: Pitchwise-Averaged Reynolds Number Effect on Sherwood Number

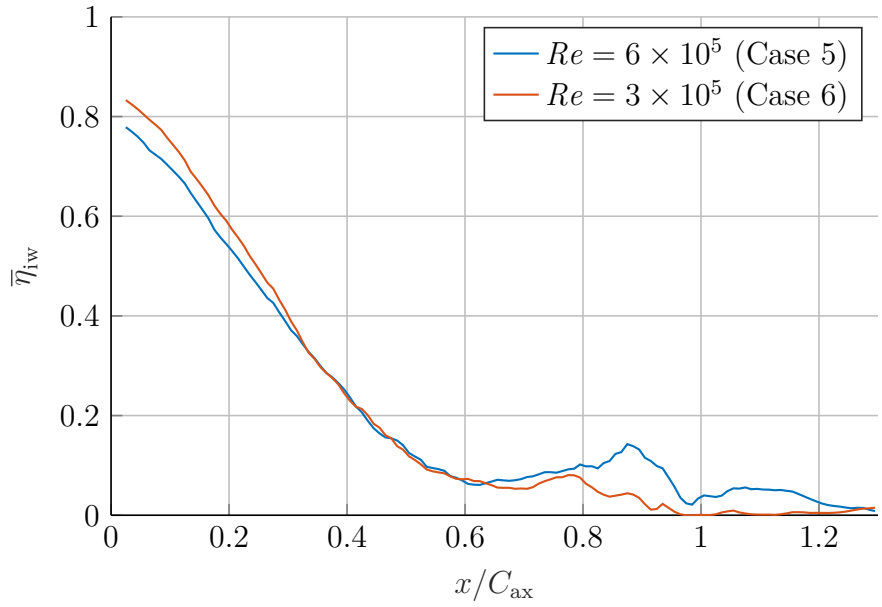

Figure 6.24: Pitchwise-Averaged Reynolds Number Effect on Effectiveness

Film Cooling

The streamlines and film cooling effectiveness values are expected to be largely Reynolds number independent for linear cascades. This expectation is demonstrated to be nearly the case based on the film cooling effectiveness contour results, the area-averaged results, and the pitchwise-averaged results. The Reynolds number independence is exemplified most clearly in the pitchwise-averaged results plotted in Fig. 6.24, which show that the contour and pitchwise-averaged results nearly overlap for the two Reynolds numbers tested. Additionally, the axial penetration and area-averaged film cooling effectiveness were equal, as reported to two significant figures.

6.1.5 Theoretical Comparisons

Mass Transfer

The laminar and turbulent integral solutions from Chapter 5 are compared in Fig. 6.25 at four different blowing levels: 0, 0.5, 1, and 1.5. Since the integral solutions do not account for the swirl, the lowest swirl angles were utilized in the comparison, as applicable. It was found that in the first half of the passage that there was an excellent

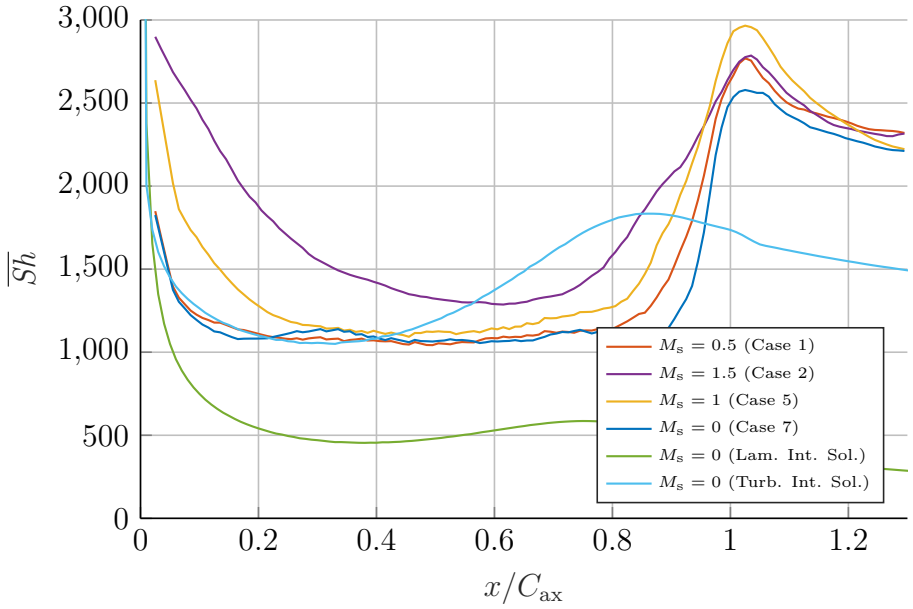

Figure 6.25: Pitchwise-Averaged Blowing Effect—Sherwood Number Theory

agreement with the turbulent integral solution for the low blowing cases (0 and 0.5). The turbulent integral solution is known to overestimate the mass transfer when there is strong acceleration where relaminarization is expected to occur, as applicable in the second half of the passage here. While the laminar integral solution presented for comparison is not very useful from an absolute prediction perspective, it does exhibit reasonable relative behavior trends for accelerating flow, indicating that a relaminarization effect is likely happening.

Film Cooling

The integral solutions for the film cooling effectiveness are compared in Fig. 6.26 at three blowing levels: 0.5, 1, and 1.5. The integral solution does not account for the swirl, so the lowest swirl angles were chosen for the comparison, as applicable. Since the crossflow effect is known to reduce the film cooling effectiveness significantly and the theoretical integral solutions do not account for crossflow, there is not expected to be a strong agreement between the experimental results and the integral solution. The results are found to support this expectation, indicating that the integral solution has limited predictive power in the presence of crossflow. However, for the $M_{\mathrm{s}} = 1.5$ case,

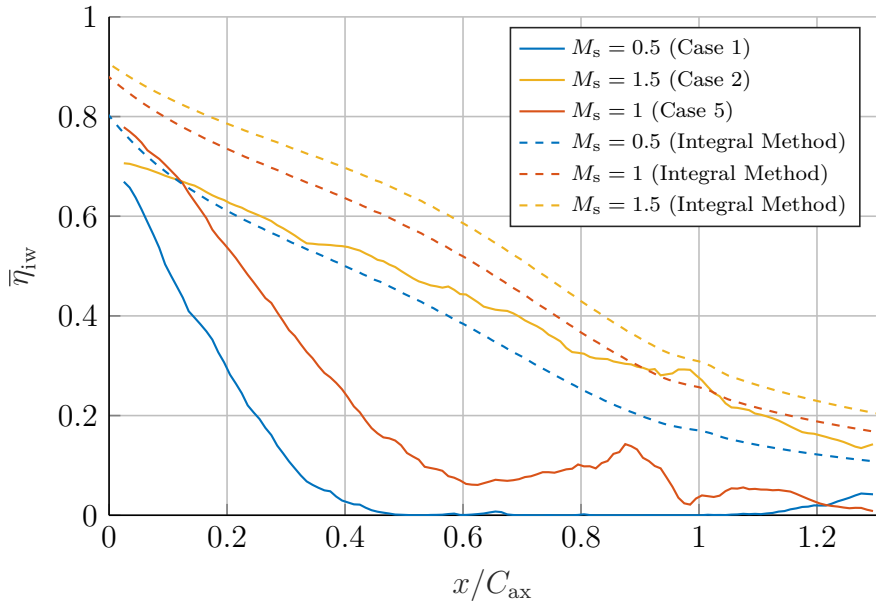

Figure 6.26: Pitchwise-Averaged Blowing Effect—Effectiveness Theory

the high blowing rate overpowered the crossflow effect, so the comparison becomes more valid. The results were found to differ by a factor near 0.75 throughout the passage, where the integral results were higher, indicating that the integral solutions are too idealized.

6.2 Case 2: Realistic Slot

The realistic slot case was set up to be similar to the straight slot case, but with a more realistic injection slot geometry (see Fig. 3.7). Instead of the straight ramp at 45° that was used for the straight slot case, a more realistic contoured ramp leading up to the endwall was used. The coolant mass flow rate per unit pitch was designed to be nearly the same as the straight slot case, but with a larger slot width, meaning a reduced injection velocity or blowing ratio. The experimental cases are listed in Table 6.3.

The results for the mass transfer and film cooling effectiveness are shown in Figs. 6.27 to 6.38. The mass transfer and film cooling results are summarized in Table 6.4, with all quantities calculated using the same approaches as the straight slot case.

Table 6.3: Realistic Slot Experimental Case Listing

Exp.	Rep.	M_s	θ	Saturated	Re	Tu
1a	3	0.215	0°	no	6×10^5	5 %
1b	3	0.215	0°	yes	6×10^5	5 %
2a	3	0.645	0°	no	6×10^5	5 %
2b	3	0.645	0°	yes	6×10^5	5 %
3a	2	0.215	45°	no	6×10^5	5 %
3b	2	0.215	45°	yes	6×10^5	5 %
4a	2	0.645	45°	no	6×10^5	5 %
4b	2	0.645	45°	yes	6×10^5	5 %
5a	2	0.430	22.5°	no	6×10^5	5 %
5b	2	0.430	22.5°	yes	6×10^5	5 %

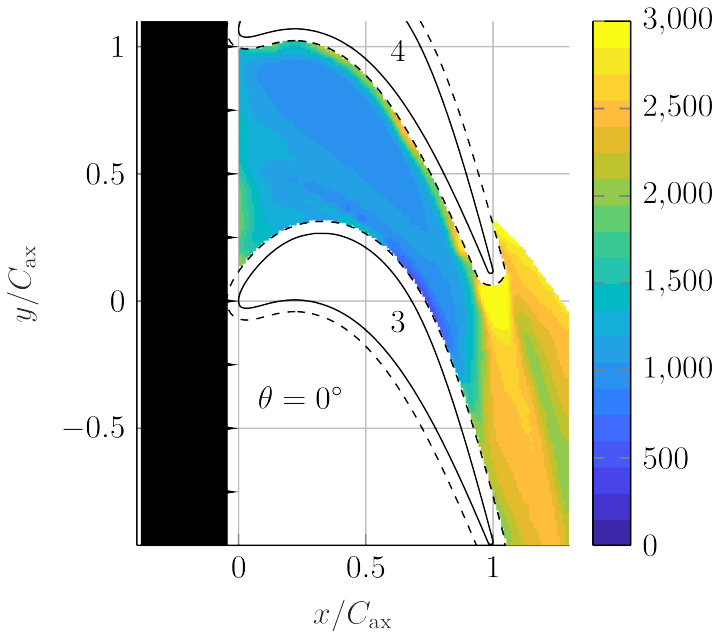

Figure 6.27: Sherwood Number—Realistic Slot Case 1 ($M_s = 0.215$, $\theta = 0°$)

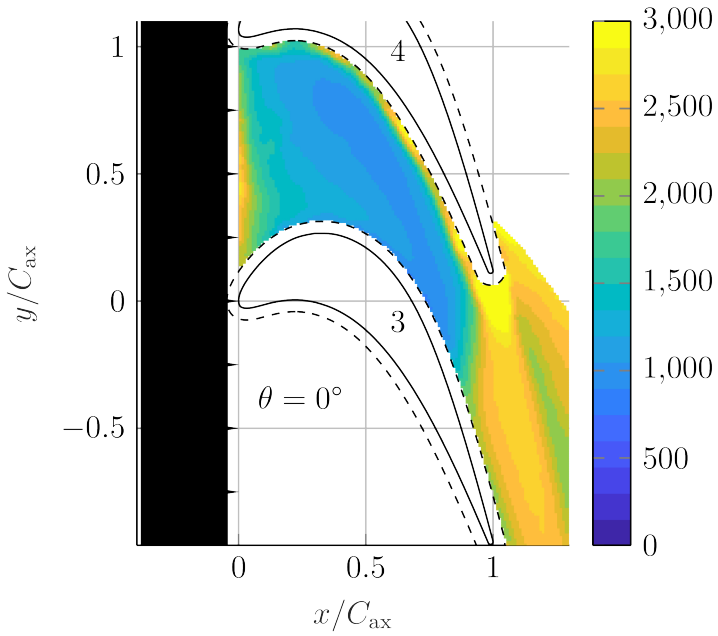

Figure 6.28: Sherwood Number—Realistic Slot Case 2 ($M_{\text{s}} = 0.645$, $\theta = 0°$)

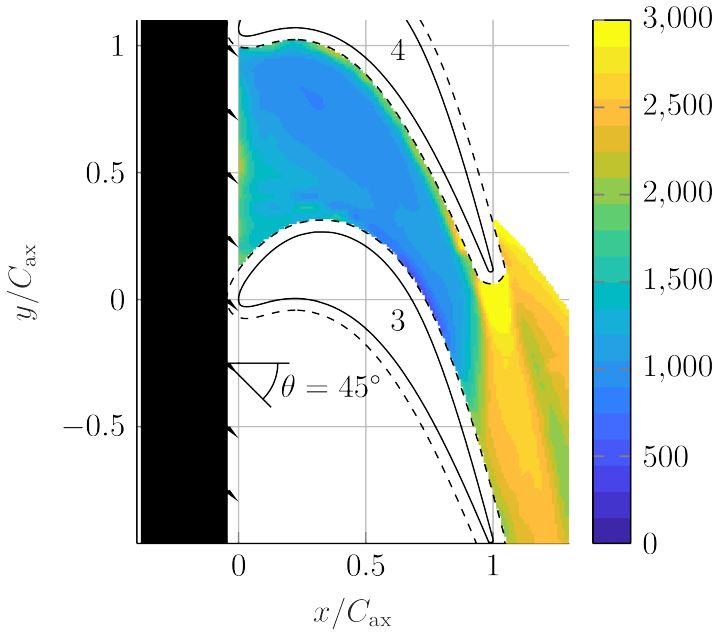

Figure 6.29: Sherwood Number—Realistic Slot Case 3 ($M_{\text{s}} = 0.215$, $\theta = 45°$)

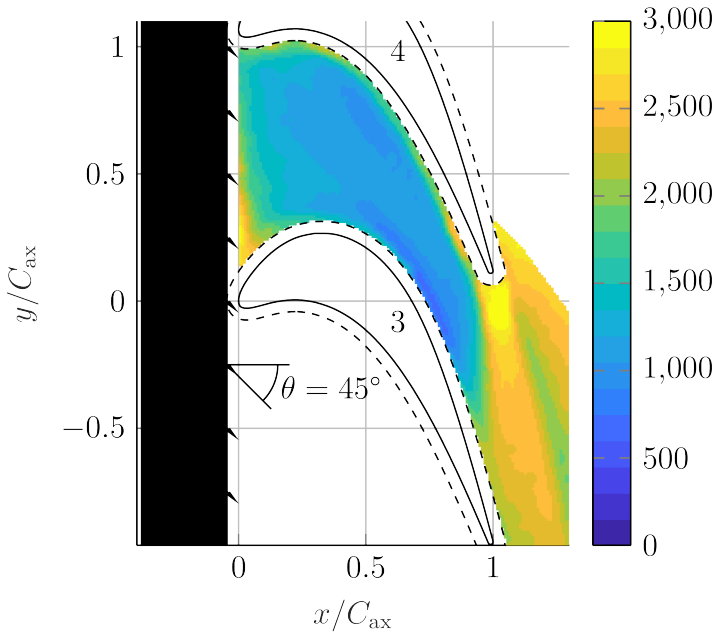

Figure 6.30: Sherwood Number—Realistic Slot Case 4 ($M_{\text{s}} = 0.645$, $\theta = 45°$)

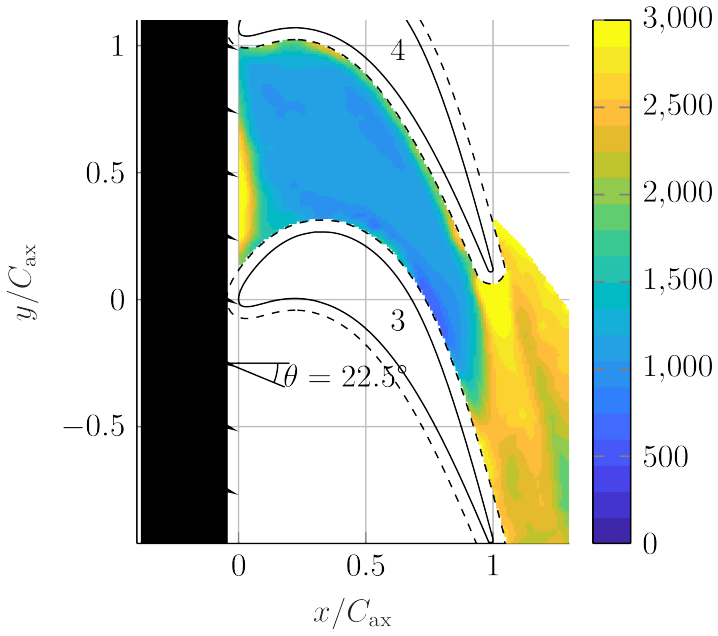

Figure 6.31: Sherwood Number—Realistic Slot Case 5 ($M_{\text{s}} = 0.430$, $\theta = 22.5°$)

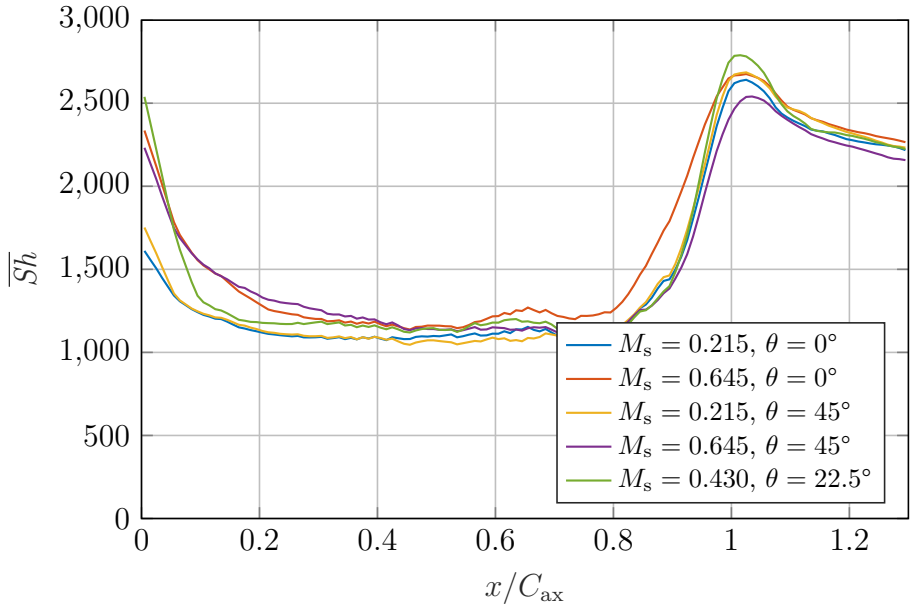

Figure 6.32: Pitchwise-Averaged Sherwood Number—Realistic Slot

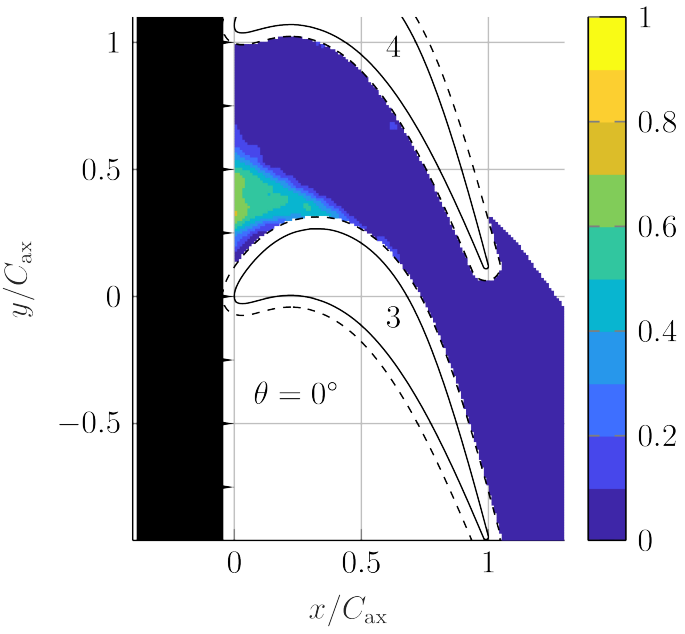

Figure 6.33: Film Cooling Effectiveness—Realistic Slot Case 1 ($M_{\text{s}} = 0.215$, $\theta = 0°$)

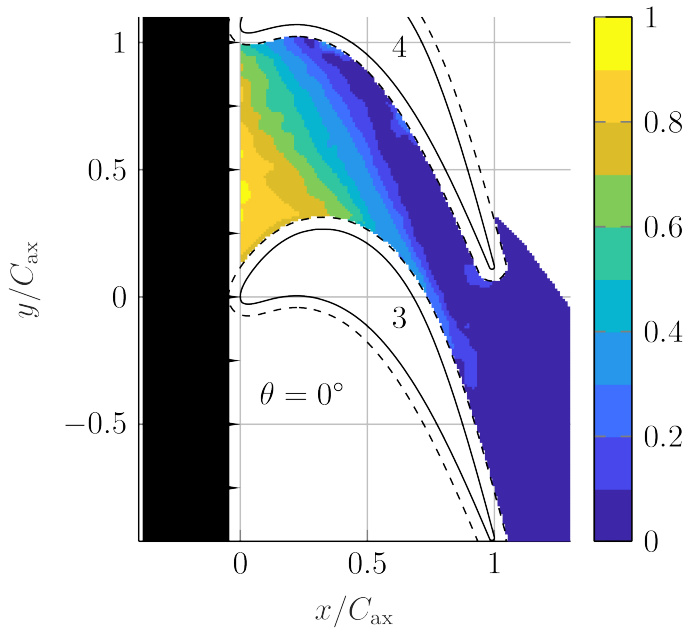

Figure 6.34: Film Cooling Effectiveness—Realistic Slot Case 2 ($M_{\text{s}} = 0.645$, $\theta = 0°$)

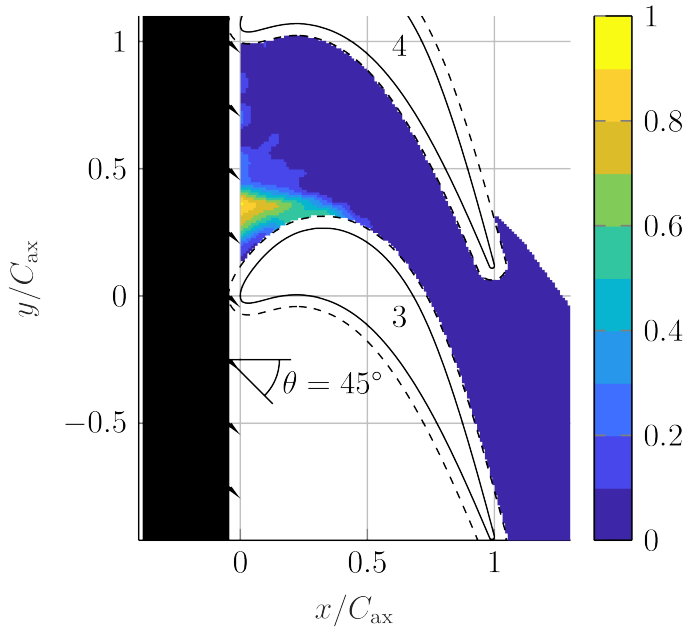

Figure 6.35: Film Cooling Effectiveness—Realistic Slot Case 3 ($M_{\text{s}} = 0.215$, $\theta = 45°$)

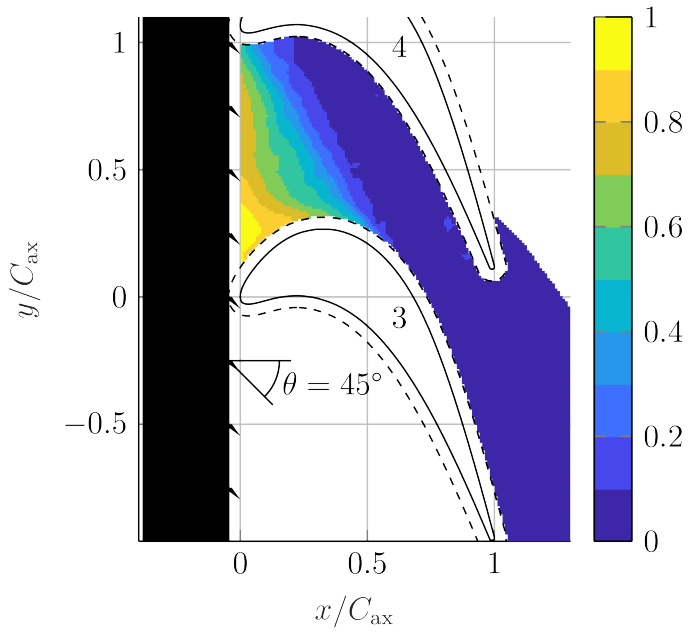

Figure 6.36: Film Cooling Effectiveness—Realistic Slot Case 4 ($M_{\text{s}} = 0.645$, $\theta = 45°$)

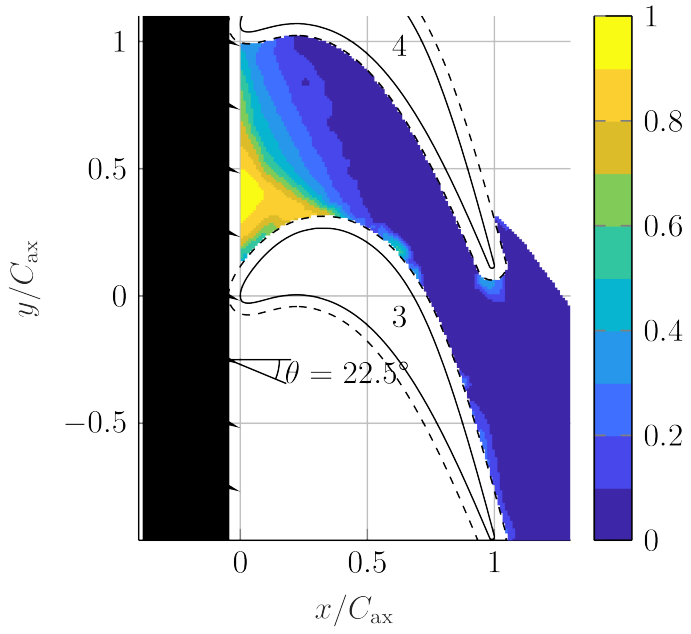

Figure 6.37: Film Cooling Effectiveness—Realistic Slot Case 5 ($M_{\text{s}} = 0.430$, $\theta = 22.5°$)

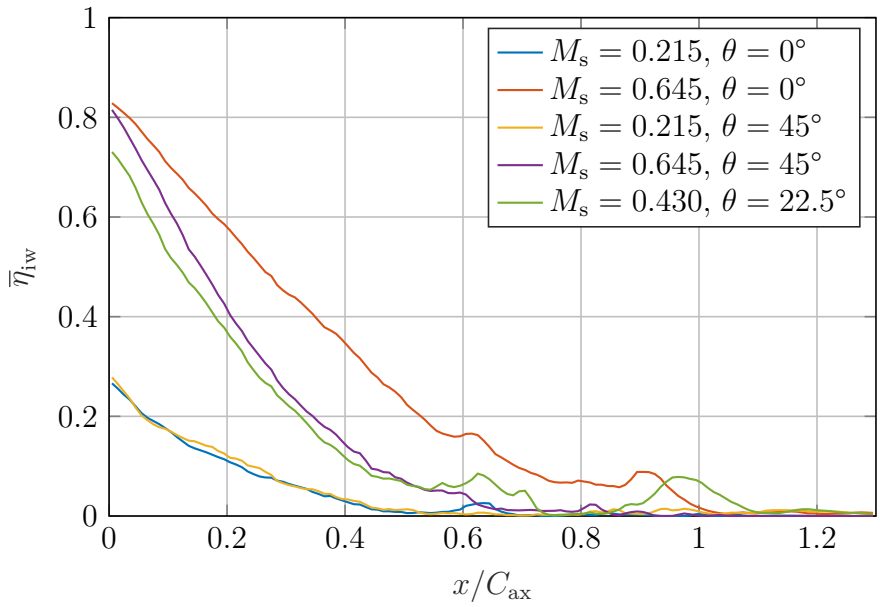

Figure 6.38: Pitchwise-Averaged Film Cooling Effectiveness—Realistic Slot

Table 6.4: Realistic Slot Result Summary

Exp.	M_s	θ	Re	$\overline{\overline{Sh}}$	$\overline{\overline{\eta}}_{iw}$	Axial Pen.
1	0.215	0°	6×10^5	1.26×10^3	0.06	0.07
2	0.645	0°	6×10^5	1.46×10^3	0.34	0.55
3	0.215	45°	6×10^5	1.27×10^3	0.06	0.08
4	0.645	45°	6×10^5	1.38×10^3	0.22	0.35
5	0.430	22.5°	6×10^5	1.37×10^3	0.21	0.33

6.2.1 Mass Transfer

The mass transfer results were found to nearly collapse in the back half of the passage while exhibiting a weak mass transfer enhancement effect for increased blowing in the front half of the passage. The effect of the swirl was found to be minor overall. Compared to the straight slot cases, the mass transfer coefficients were significantly decreased in the front half of the passage due to the decreased blowing ratio.

6.2.2 Film Cooling

The film cooling results exhibited trends consistent with the straight slot case. Increased blowing was found to enhance the film cooling effectiveness significantly. The effect of the swirl was negligible at low blowing rates and was found to decrease the film cooling effectiveness at high blowing rates significantly. The lower blowing rates combined with the farther-upstream slot location led to reduced endwall film cooling coverage overall as compared with the straight slot case. This finding is despite the preferable shape of the realistic slot, which should reduce mixing and prevent any blowing through the boundary layer.

While these results added limited insight beyond what was found for the straight slot case, they do serve to demonstrate that the findings are robust across a range of conditions and geometries, especially considering that others in the literature made similar findings with different techniques and different geometries.

6.3 Case 3: Discrete Holes

The discrete hole plates feature 15 discrete holes arranged in two ways: (1) the 0° plate angles the holes roughly in the same direction of the local near-wall flow (taking into account crossflow) and (2) the 90° plate angles the holes 90° offset with respect to the 0° plate. The purpose of this was to determine the effect of discrete hole flow direction misalignment with the near-wall adjacent flow. For practical wall cooling schemes, there are often geometrical constraints, which place limits on the discrete hole flow direction that is manufacturable. By shifting the discrete hole injection direction 90°, the coolant was expected to mix more with the main flow and result in less endwall cooling. The experimental cases are listed in Table 6.5.

Table 6.5: Discrete Holes Experimental Case Listing

Exp.	Rep.	Plate	M_{h}	Saturated	Re	Tu
1a	1	0°	0.75	no	5×10^5	5 %
1b	1	0°	0.75	yes	5×10^5	5 %
2a	1	0°	1.5	no	5×10^5	5 %
2b	1	0°	1.5	yes	5×10^5	5 %
3a	1	0°	2.5	no	5×10^5	5 %
3b	2	0°	2.5	yes	5×10^5	5 %
4a	2	90°	0.75	no	5×10^5	5 %
4b	2	90°	0.75	yes	5×10^5	5 %
5a	3	90°	1.5	no	5×10^5	5 %
5b	3	90°	1.5	yes	5×10^5	5 %
6a	5	90°	2.5	no	5×10^5	5 %
6b	3	90°	2.5	yes	5×10^5	5 %

Table 6.6: Discrete Holes Result Summary

Exp.	Plate	M_{h}	Re	$\overline{\overline{Sh}}$	$\overline{\overline{\eta}}_{\mathrm{iw}}$
1	0°	0.75	5×10^5	1.28×10^3	0.09
2	0°	1.5	5×10^5	1.35×10^3	0.11
3	0°	2.5	5×10^5	1.44×10^3	0.09
4	90°	0.75	5×10^5	1.47×10^3	0.05
5	90°	1.5	5×10^5	1.60×10^3	0.08
6	90°	2.5	5×10^5	1.75×10^3	0.08

The results for the mass transfer and film cooling effectiveness are shown in Figs. 6.39 to 6.52. The mass transfer and film cooling results are summarized in Table 6.6.

6.3.1 Mass Transfer

The presence of the discrete holes led to local mass transfer enhancement downstream of each discrete hole injection location (relative to the surrounding mass transfer levels). The enhancement effect was found to be higher in magnitude and in size (wider wake) for the 90° plate compared to the 0° plate. This effect indicates that the flow misalignment leads to enhanced mixing, which is expected to also lead to decreased film cooling. Increased blowing rates were found to enhance the endwall

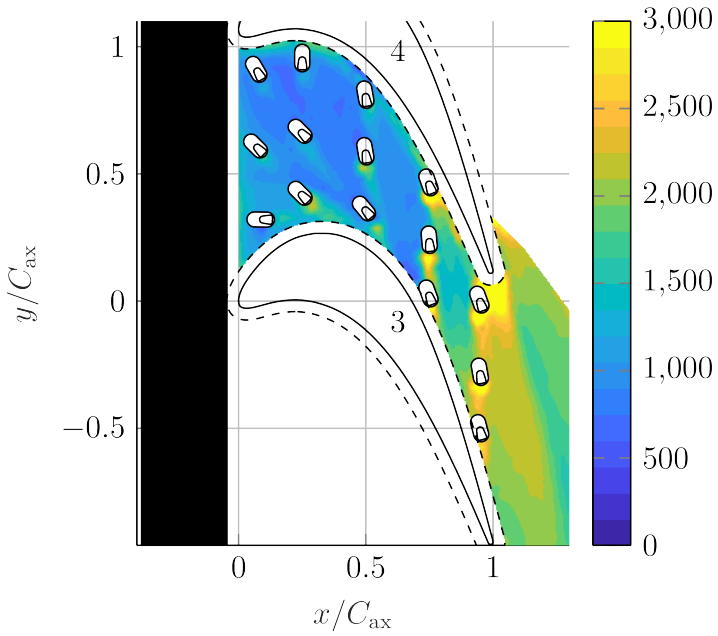

Figure 6.39: Sherwood Number—Discrete Holes Case 1 (0° Plate, $M_{\text{h}} = 0.75$)

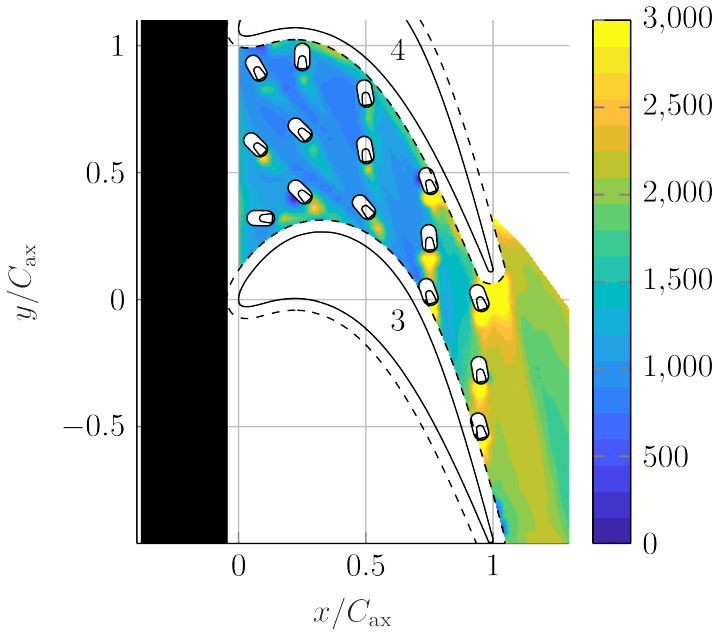

Figure 6.40: Sherwood Number—Discrete Holes Case 2 (0° Plate, $M_{\text{h}} = 1.5$)

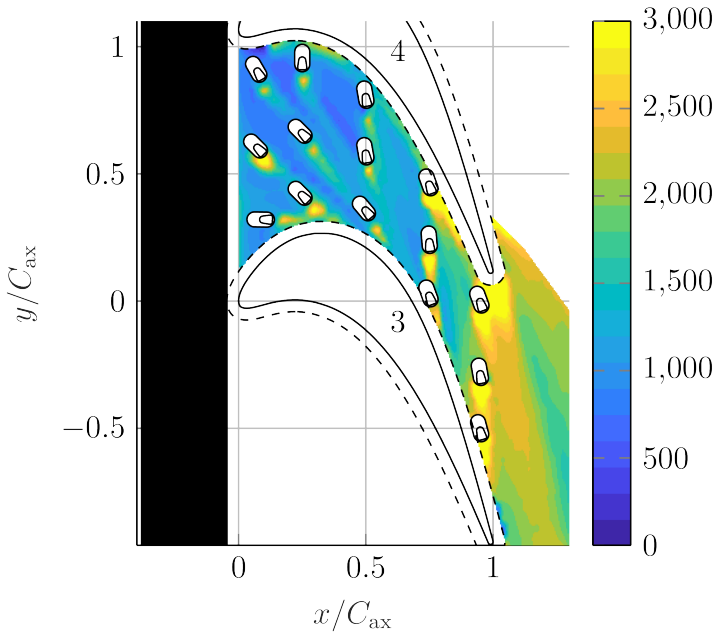

Figure 6.41: Sherwood Number—Discrete Holes Case 3 (0° Plate, $M_{\text{h}} = 2.5$)

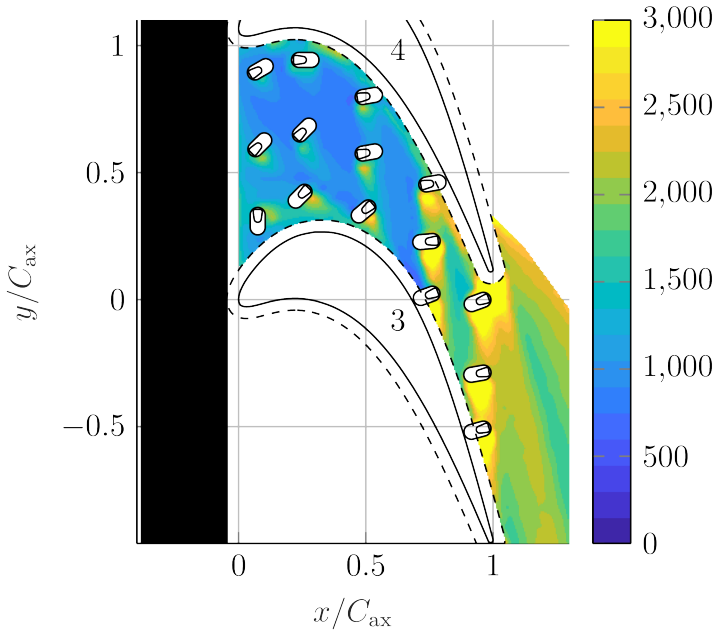

Figure 6.42: Sherwood Number—Discrete Holes Case 4 (90° Plate, $M_{\text{h}} = 0.75$)

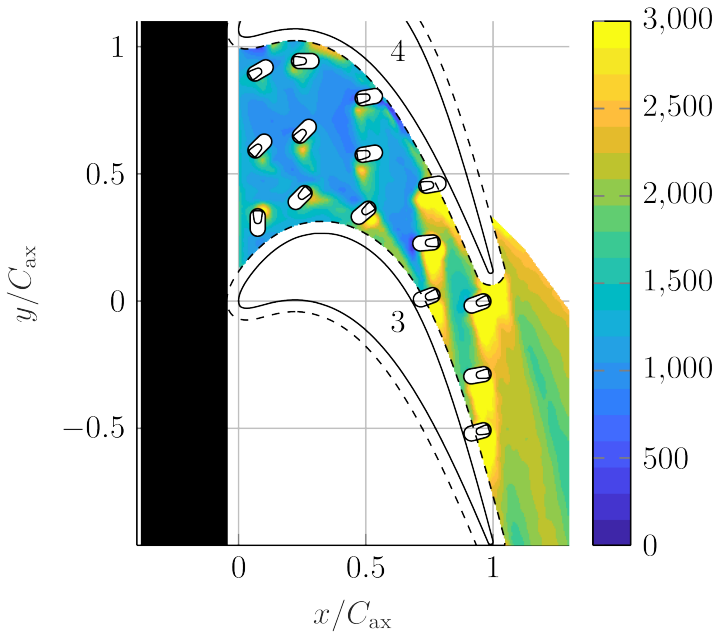

Figure 6.43: Sherwood Number—Discrete Holes Case 5 (90° Plate, $M_{\text{h}} = 1.5$)

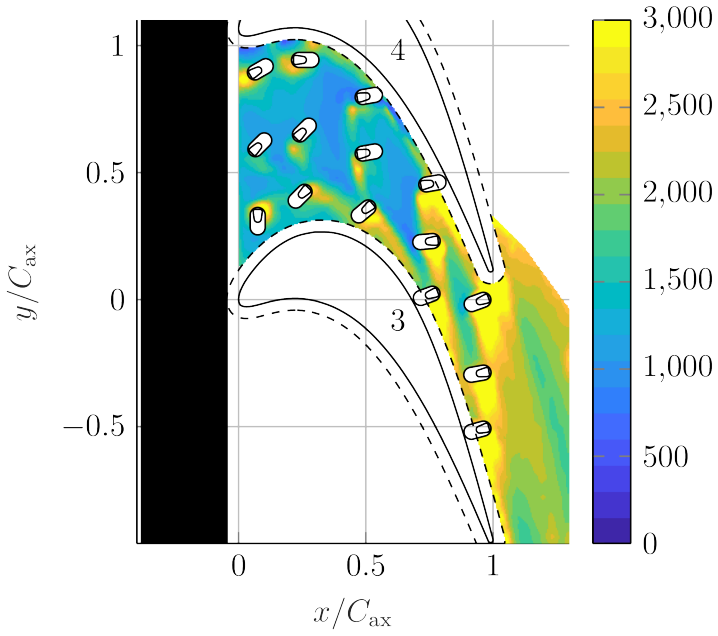

Figure 6.44: Sherwood Number—Discrete Holes Case 6 (90° Plate, $M_{\text{h}} = 2.5$)

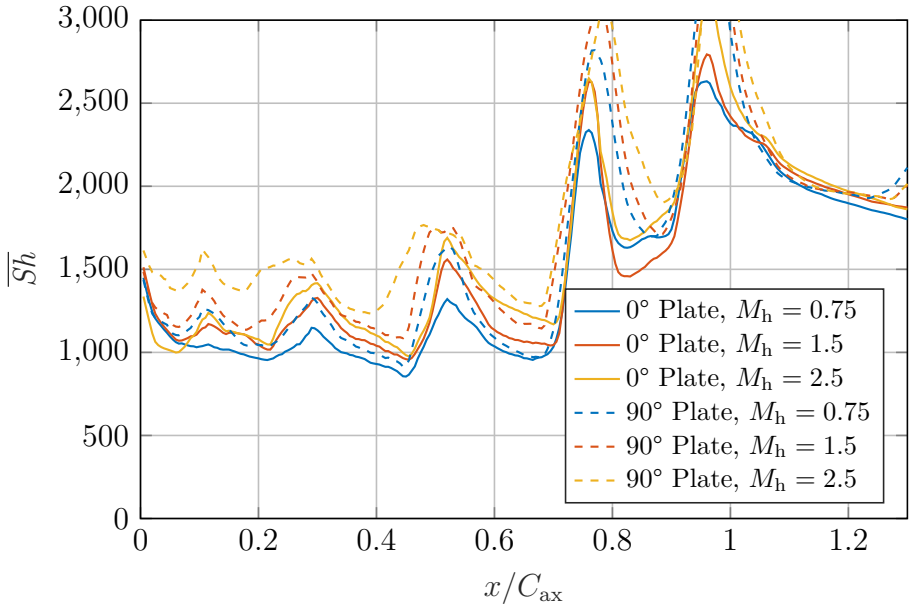

Figure 6.45: Pitchwise-Averaged Sherwood Number—Discrete Holes

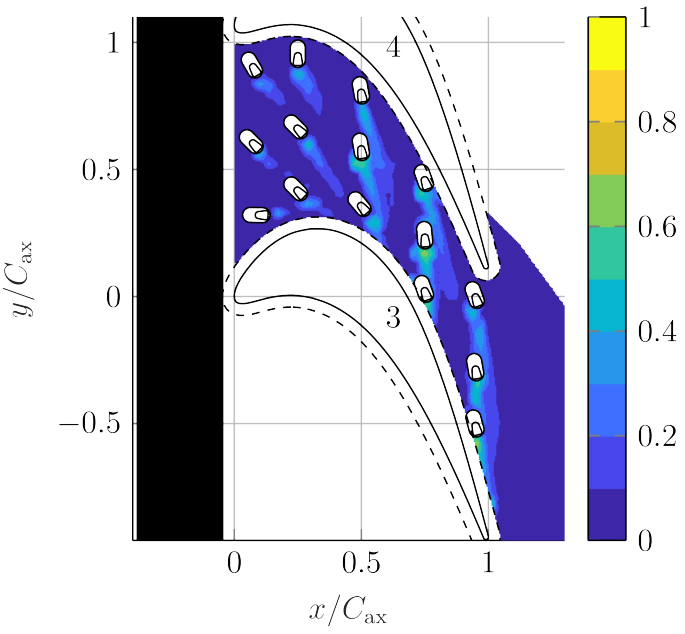

Figure 6.46: Film Cooling Effectiveness—Discrete Holes Case 1 (0° Plate, $M_{\mathrm{h}} = 0.75$)

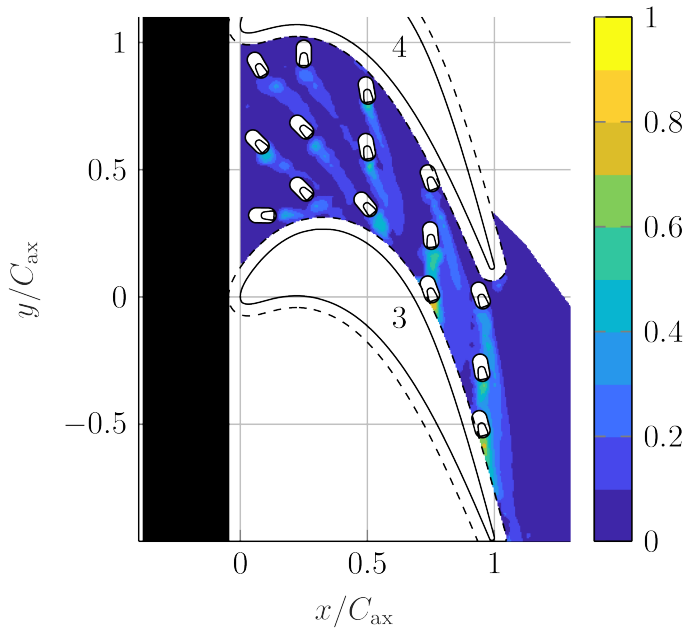

Figure 6.47: Film Cooling Effectiveness—Discrete Holes Case 2 (0° Plate, $M_{\text{h}} = 1.5$)

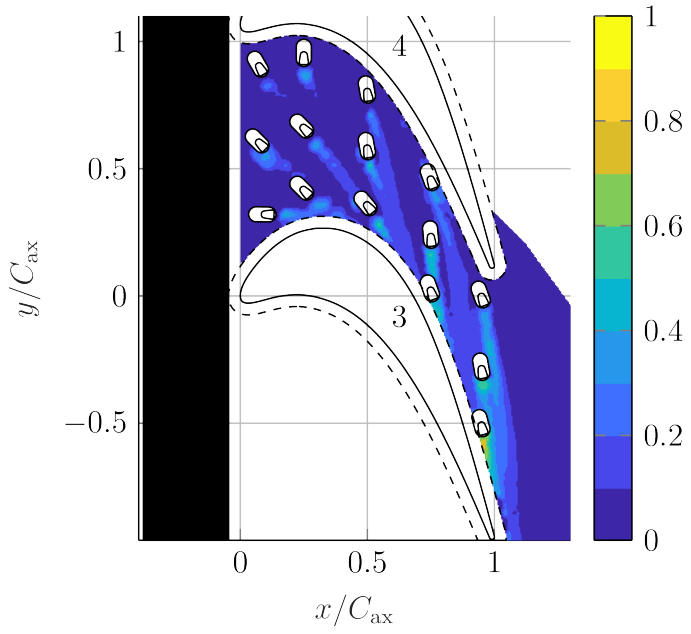

Figure 6.48: Film Cooling Effectiveness—Discrete Holes Case 3 (0° Plate, $M_{\text{h}} = 2.5$)

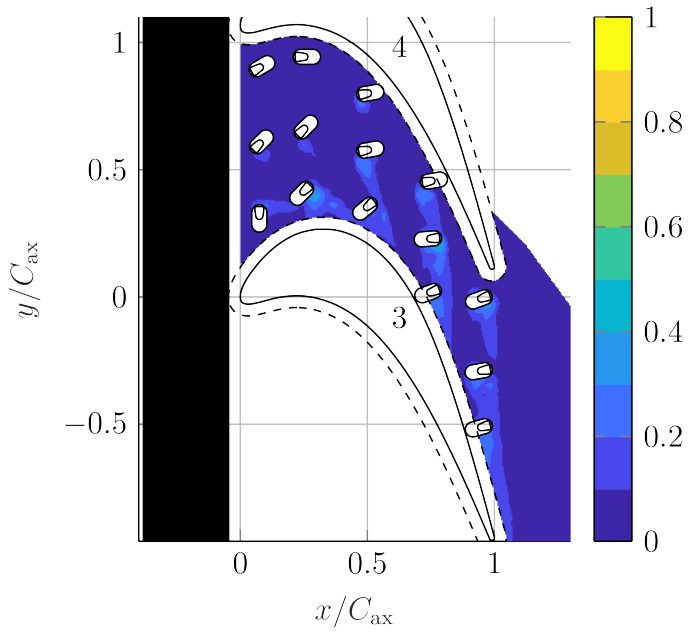

Figure 6.49: Film Cooling Effectiveness—Discrete Holes Case 4 (90° Plate, $M_{\text{h}} = 0.75$)

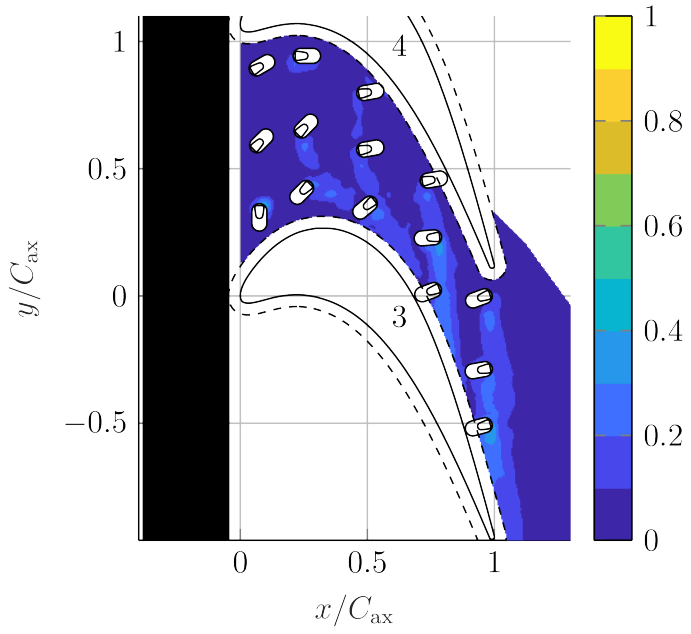

Figure 6.50: Film Cooling Effectiveness—Discrete Holes Case 5 (90° Plate, $M_{\text{h}} = 1.5$)

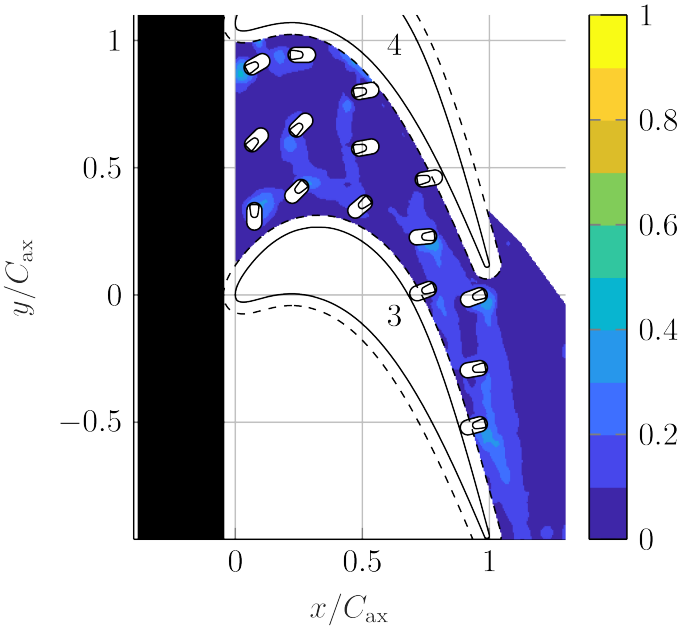

Figure 6.51: Film Cooling Effectiveness—Discrete Holes Case 6 (90° Plate, $M_{\mathrm{h}} = 2.5$)

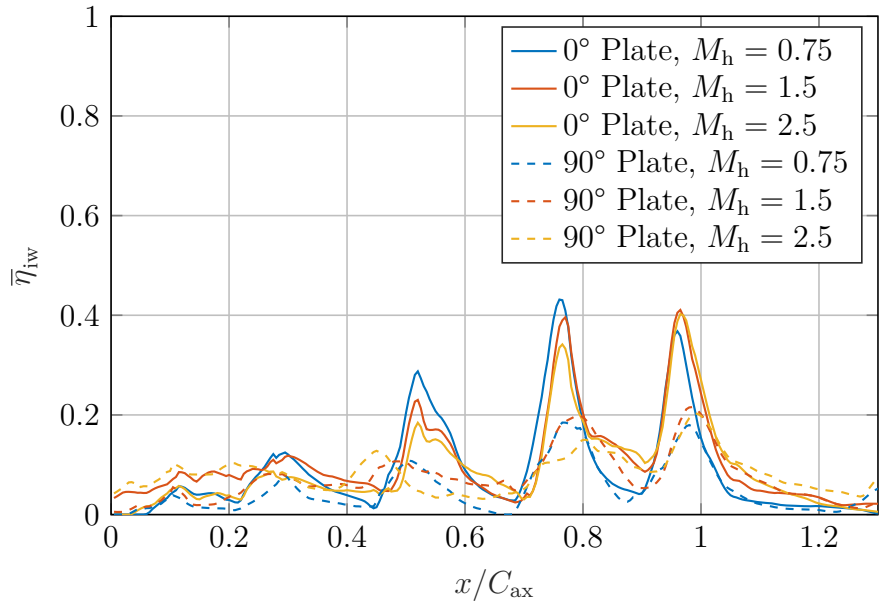

Figure 6.52: Pitchwise-Averaged Film Cooling Effectiveness—Discrete Holes

mass transfer for both plates. Compared to the straight slot and realistic slot cases (without the discrete holes), the endwall mass transfer was enhanced throughout the complete passage since the boundary layer was continuously reenergized and locally reset at the hole injection points.

6.3.2 Film Cooling

The discrete holes provided near-complete coverage over the back half of the passage, while providing only partial coverage over the front half of the passage. This result was expected since the back half of the passage receives more coolant by virtue of the freestream pressures being lower and also because there is more endwall area to cool over the front half of the passage. However, while there was measurable film cooling coverage, the absolute film cooling effectiveness was generally quite low and was only a weak function of blowing rate. Beyond $M_{\mathrm{h}} = 1.5$, there was a minimal apparent benefit to raising the blowing rate, indicating that for beyond $M_{\mathrm{h}} = 1.5$, a significant portion of the coolant blows through the boundary layer. Note that the mass transfer coefficients did continue to increase for beyond $M_{\mathrm{h}} = 1.5$. Therefore, an improved strategy compared to increasing the blowing beyond $M_{\mathrm{h}} = 1.5$ is to either enlarge the film cooling holes or to place more holes to enhance the endwall cooling (while maintaining the same blowing ratio). Immediately downstream of the holes for the 0° plate, the effectiveness reached near 40 % or so, while it reached only near 20 % for the 90° plate. This finding indicates that the 90° plate generally led to stronger mixing than the 0° plate, which significantly reduced its peak film cooling effectiveness levels. Despite the substantial differences in peak effectiveness, the overall differences over the full passage were more moderate (a factor closer to 1.4 rather than near 2 as the peak values might suggest). For the 90° plate, the coolant appears to disperse more widely, which helped to counteract the lower peak values. Nonetheless, for a denser grid of discrete holes, the 0° holes are expected to have the potential for nearly double the effectiveness compared to the 90° holes.

Table 6.7: Combined Injection Experimental Case Listing

Exp.	Rep.	Plate	M_s	θ	M_h	Saturated	Re	Tu
1a	2	0°	0.430	45°	0.75	no	5×10^5	5 %
1b	2	0°	0.430	45°	0.75	yes	5×10^5	5 %
2a	2	0°	0.430	45°	1.5	no	5×10^5	5 %
2b	3	0°	0.430	45°	1.5	yes	5×10^5	5 %
3a	1	0°	0.430	45°	2.5	no	5×10^5	5 %
3b	2	0°	0.430	45°	2.5	yes	5×10^5	5 %
4a	1	90°	0.430	45°	0.75	no	5×10^5	5 %
4b	1	90°	0.430	45°	0.75	yes	5×10^5	5 %
5a	2	90°	0.430	45°	1.5	no	5×10^5	5 %
5b	2	90°	0.430	45°	1.5	yes	5×10^5	5 %
6a	2	90°	0.430	45°	2.5	no	5×10^5	5 %
6b	2	90°	0.430	45°	2.5	yes	5×10^5	5 %

Table 6.8: Combined Injection Result Summary

Exp.	Plate	M_s	θ	M_h	Re	$\overline{\overline{Sh}}$	$\overline{\overline{\eta}}_{iw}$
1	0°	0.430	45°	0.75	5×10^5	1.41×10^3	0.25
2	0°	0.430	45°	1.5	5×10^5	1.43×10^3	0.29
3	0°	0.430	45°	2.5	5×10^5	1.52×10^3	0.26
4	90°	0.430	45°	0.75	5×10^5	1.54×10^3	0.23
5	90°	0.430	45°	1.5	5×10^5	1.66×10^3	0.22
6	90°	0.430	45°	2.5	5×10^5	1.73×10^3	0.23

6.4 Case 4: Combined Injection

This final case combined the realistic slot flow (for a fixed realistically large swirl angle) with discrete hole cooling. These conditions provide the most comprehensive cooling scheme and are most representative of the flow within an actual gas turbine blade passage. The experimental cases are listed in Table 6.7.

The results for the mass transfer and film cooling effectiveness are shown in Figs. 6.53 to 6.66. The mass transfer and film cooling results are summarized in Table 6.8.

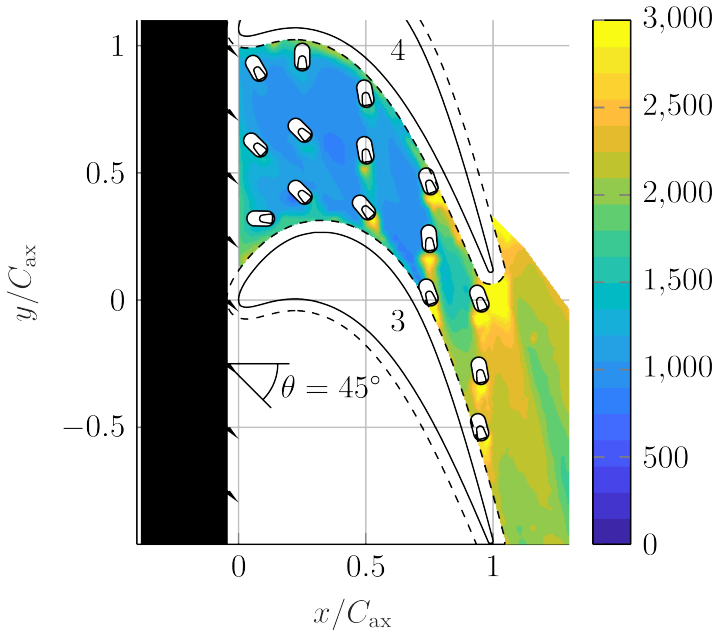

Figure 6.53: Sherwood Number—Combined Injection Case 1 (0° Plate, $M_{\text{s}} = 0.430$, $M_{\text{h}} = 0.75$)

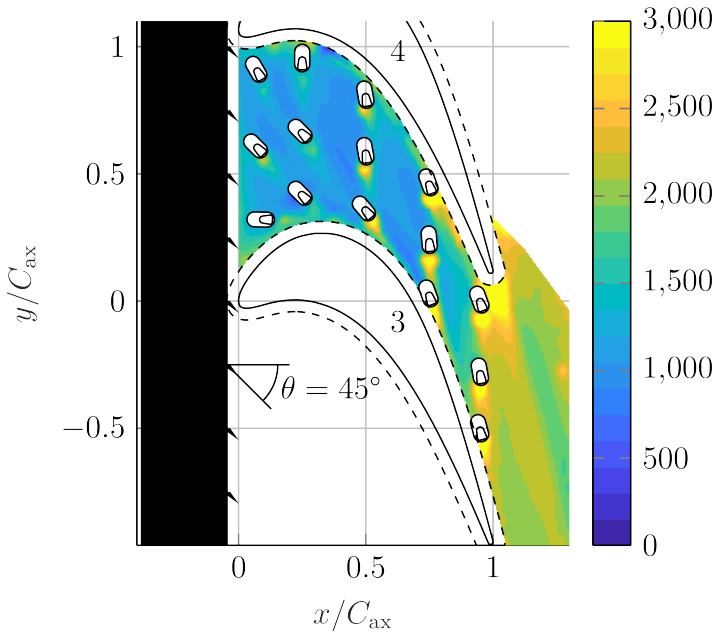

Figure 6.54: Sherwood Number—Combined Injection Case 2 (0° Plate, $M_{\text{s}} = 0.430$, $M_{\text{h}} = 1.5$)

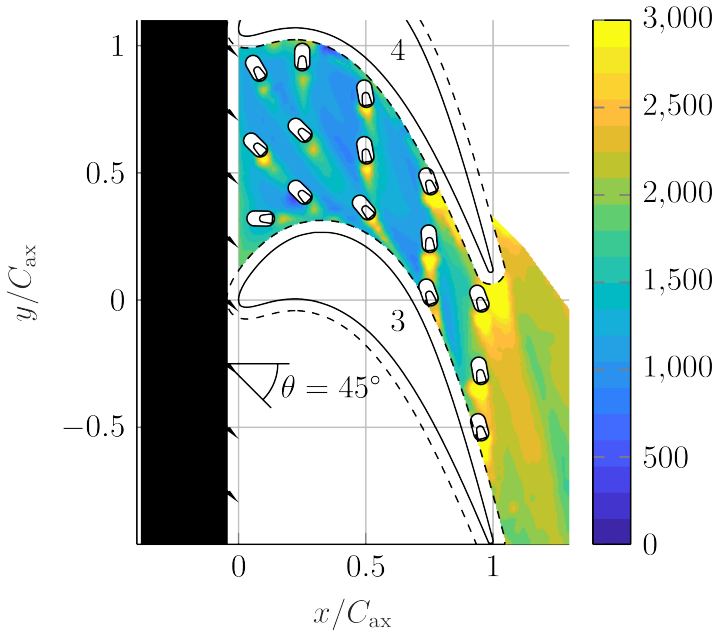

Figure 6.55: Sherwood Number—Combined Injection Case 3 (0° Plate, $M_{\text{s}} = 0.430$, $M_{\text{h}} = 2.5$)

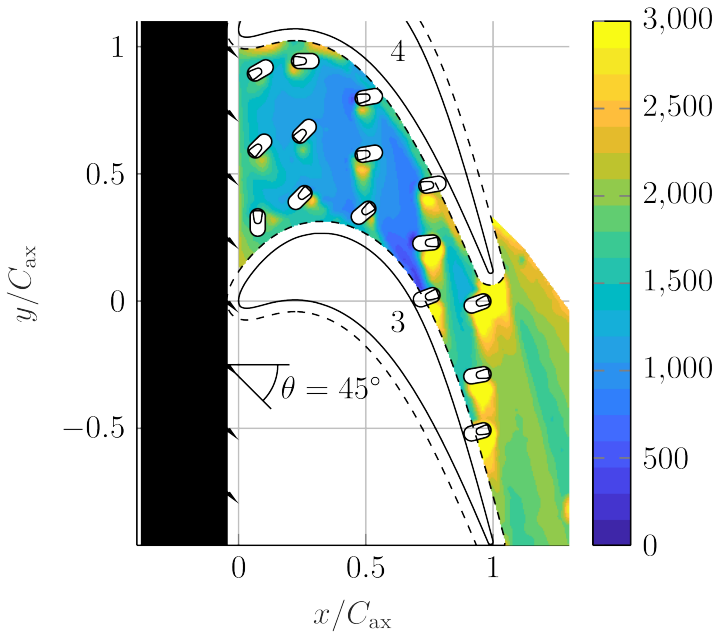

Figure 6.56: Sherwood Number—Combined Injection Case 4 (90° Plate, $M_{\text{s}} = 0.430$, $M_{\text{h}} = 0.75$)

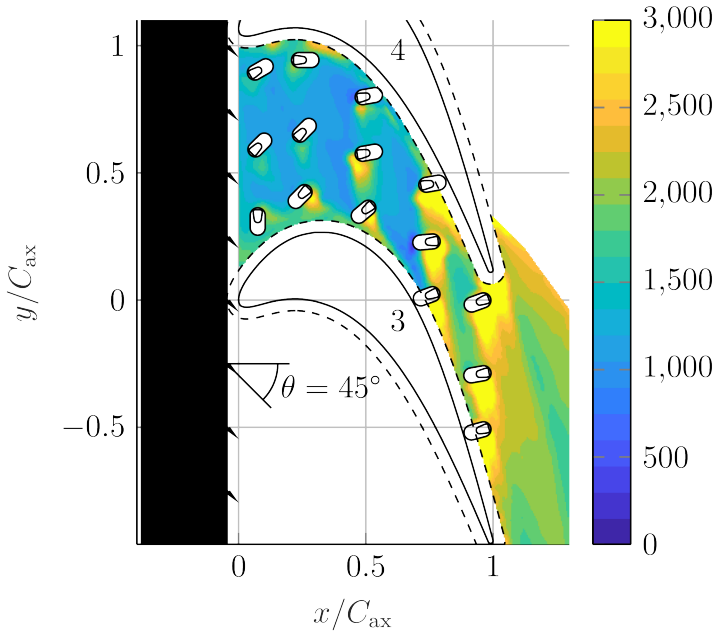

Figure 6.57: Sherwood Number—Combined Injection Case 5 (90° Plate, $M_{\text{s}} = 0.430$, $M_{\text{h}} = 1.5$)

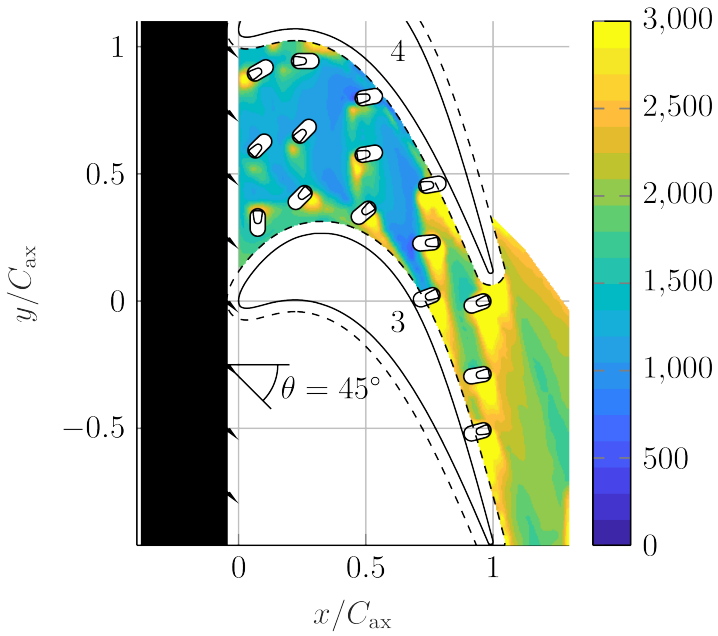

Figure 6.58: Sherwood Number—Combined Injection Case 6 (90° Plate, $M_{\text{s}} = 0.430$, $M_{\text{h}} = 2.5$)

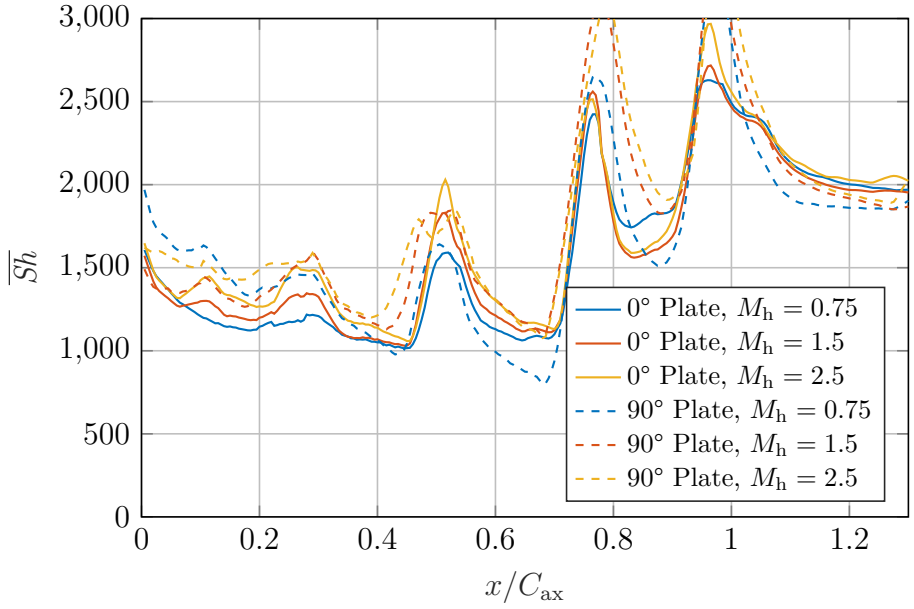

Figure 6.59: Pitchwise-Averaged Sherwood Number—Combined Injection

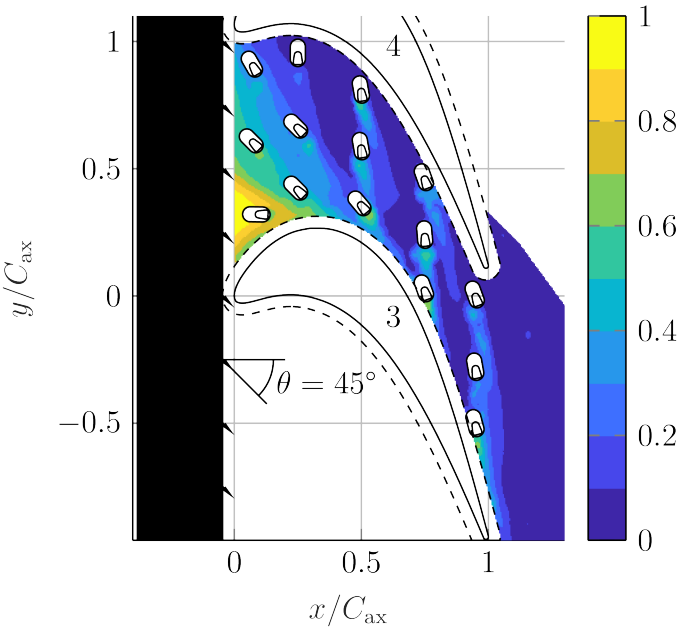

Figure 6.60: Film Cooling Effectiveness—Combined Injection Case 1 (0° Plate, $M_{\text{s}} = 0.430$, $M_{\text{h}} = 0.75$)

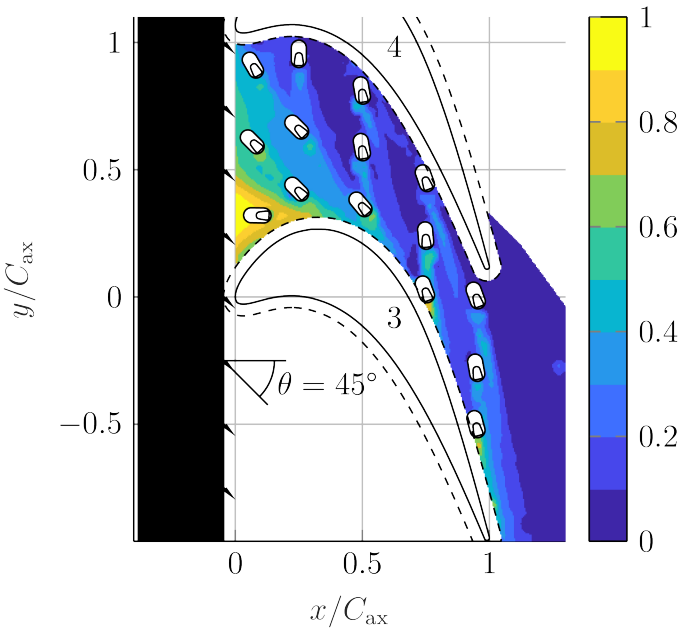

Figure 6.61: Film Cooling Effectiveness—Combined Injection Case 2 (0° Plate, $M_{\mathrm{s}} = 0.430$, $M_{\mathrm{h}} = 1.5$)

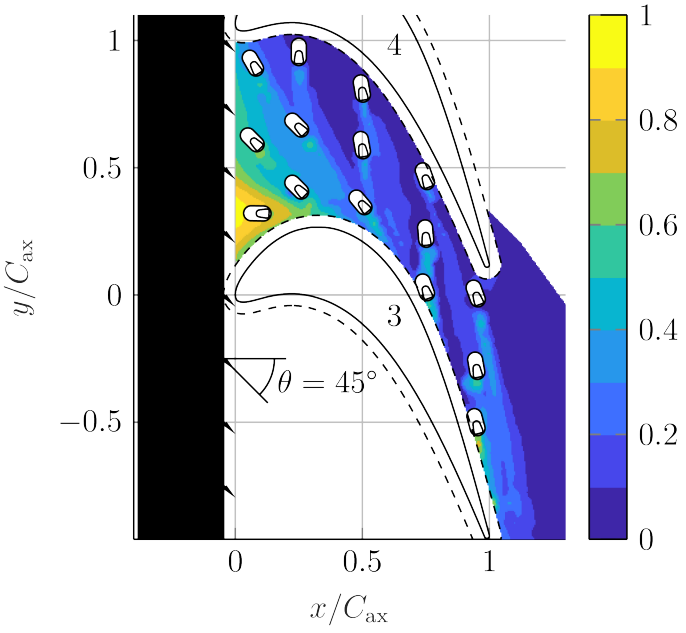

Figure 6.62: Film Cooling Effectiveness—Combined Injection Case 3 (0° Plate, $M_{\mathrm{s}} = 0.430$, $M_{\mathrm{h}} = 2.5$)

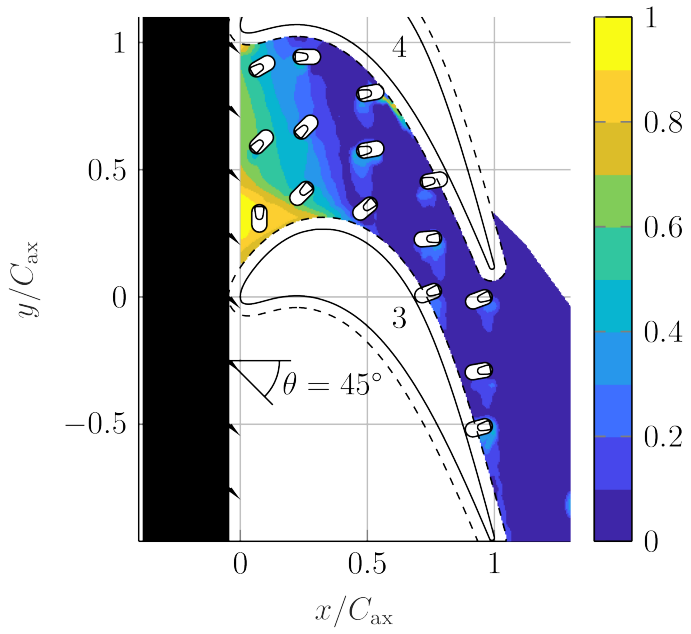

Figure 6.63: Film Cooling Effectiveness—Combined Injection Case 4 (90° Plate, $M_{\text{s}} = 0.430$, $M_{\text{h}} = 0.75$)

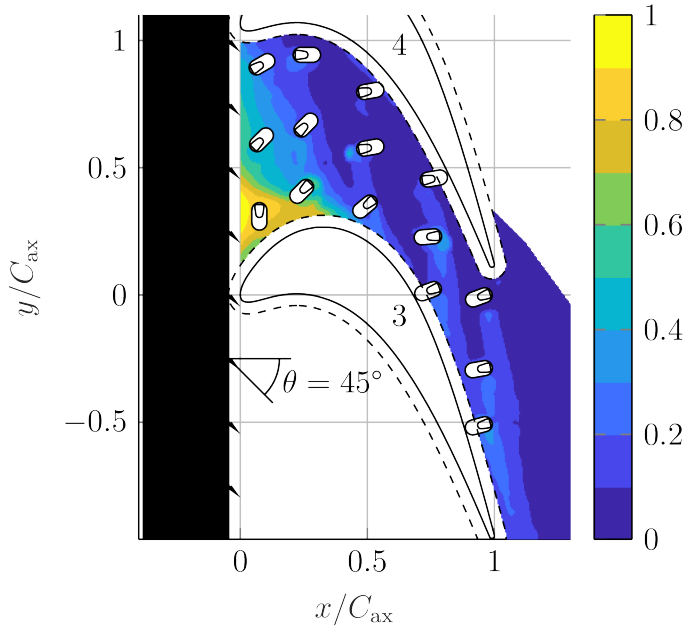

Figure 6.64: Film Cooling Effectiveness—Combined Injection Case 5 (90° Plate, $M_{\text{s}} = 0.430$, $M_{\text{h}} = 1.5$)

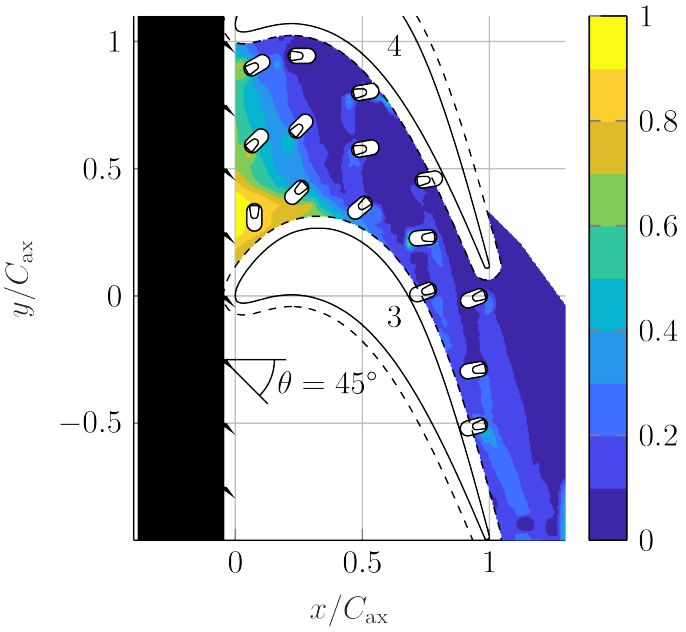

Figure 6.65: Film Cooling Effectiveness—Combined Injection Case 6 (90° Plate, $M_{\mathrm{s}} = 0.430$, $M_{\mathrm{h}} = 2.5$)

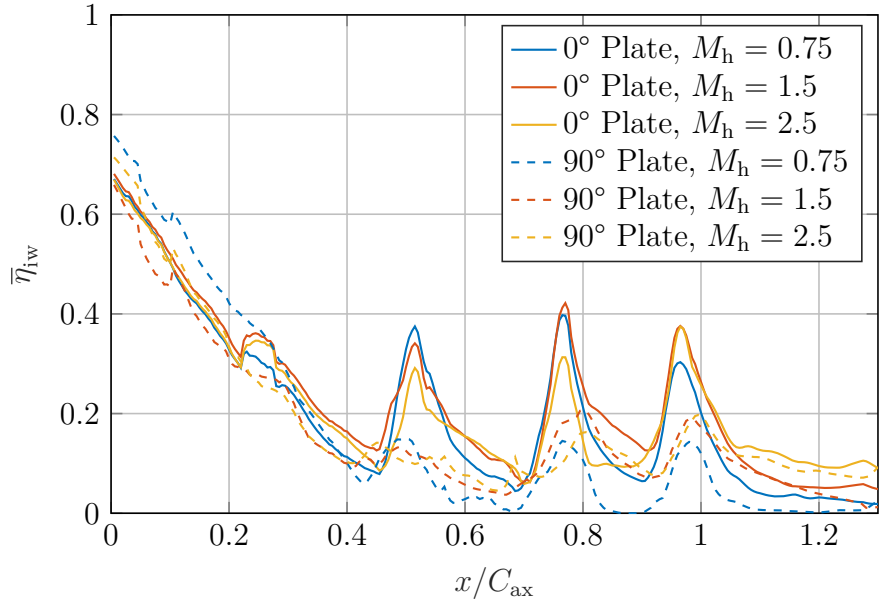

Figure 6.66: Pitchwise-Averaged Film Cooling Effectiveness—Combined Injection

6.4.1 Mass Transfer

The mass transfer trends and findings for the combined injection case are in good agreement with the discrete hole injection case, so the mass transfer commentary made in Section 6.3.1 still applies. However, note that the mass transfer results on the front part of the passage were enhanced for the combined injection case because the slot purge flow, meaning the overall mass transfer coefficients were more substantial as compared to the discrete injection case.

6.4.2 Film Cooling

At first indication, the results show that the combined injection film cooling effectiveness over the complete endwall can be estimated by taking the maximum of the film cooling effectiveness results from the individual sources. A closer look reveals a clear additive film cooling effectiveness result, especially observable near $x/C_{\text{ax}} = 0.25$ (2nd row of holes) and near $x/C_{\text{ax}} = 0.5$ (3rd row of holes). A simple addition of the two effectiveness values yields impossible results for high effectiveness sums (when the sum is beyond unity), so the author proposes a simple empirical model for the combined film cooling effectiveness that obeys the expected behavior at the limits and is in good alignment with the results in this work:

$$\eta_{\text{iw,combined}} = \eta_{\text{iw,s}} + \eta_{\text{iw,h}} - \eta_{\text{iw,s}}\eta_{\text{iw,h}} \tag{6.1}$$

The results show that for most of the combined injection cases, the coolant from the 1st and 2nd discrete hole rows is mostly wasted despite a small additive bonus apparent in the 2nd row. This highlights the need to consider the combined cooling effects when designing and endwall cooling scheme. These nearly wasted cooling holes would have been much better utilized elsewhere on the endwall.

Note that the area-averaged effectiveness value for case 4 (0.23) appears to be overestimated due to erroneously high effectiveness values for $x/C_{\text{ax}} \leq 0.3$ (see Fig. 6.66). If the effectiveness values for $x/C_{\text{ax}} \leq 0.3$ are corrected to the mean result from the other cases, then the corrected value for the area-averaged effectiveness is near 0.21, which is more consistent with the previous findings.

Table 6.9: Uncertainty Summary—Random Error Only

$\frac{U_{Sh}}{Sh}$	$\frac{U_{\overline{Sh}}}{\overline{Sh}}$	$\frac{U_{\overline{\overline{Sh}}}}{\overline{\overline{Sh}}}$	$U_{\eta_{\mathrm{iw}}}$	$U_{\overline{\eta}_{\mathrm{iw}}}$	$U_{\overline{\overline{\eta}}_{\mathrm{iw}}}$
6.6 %	6.5 %	5.9 %	$9.1\,\%\,(1-\eta_{\mathrm{iw}})$	$6.6\,\%\,(1-\overline{\eta}_{\mathrm{iw}})$	$6.3\,\%\left(1-\overline{\overline{\eta}}_{\mathrm{iw}}\right)$

6.5 Result Uncertainty

The majority of the experimental cases were run with replication. The replications were used to decrease the uncertainty of the mean result and to determine the uncertainty of the experimental method. Key results for the uncertainty in the Sherwood number and film cooling effectiveness are reported and examined.

The replication experiments were used to determine the random component of uncertainty statistically. The uncertainty in the Sherwood number and film cooling effectiveness were determined for discrete points, pitchwise-averaged quantities, and area-averaged quantities. The summary results for these different uncertainties are reported in Table 6.9. For the discrete point uncertainty estimate and the pitchwise-averaged uncertainty estimate, the figures represent typical (median) levels for the uncertainty since they may vary spatially within the turbine passage. Additional details for how the uncertainty estimates were calculated are given in Appendix B.3.

The results in Table 6.9 represent the uncertainties when no replications are performed ($n_0 = n_1 = 1$). To account for the reduction in uncertainty due to experimental replication, the following formulas can be used:

$$\frac{U_{Sh}}{Sh} = \frac{1}{\sqrt{n_0}} \left(\frac{U_{Sh}}{Sh} \right)_{n_0=1} \tag{6.2}$$

$$U_{\eta_{\mathrm{iw}}} = \frac{1}{\sqrt{2}} \left(\frac{1}{n_0} + \frac{1}{n_1} \right)^{1/2} \left(U_{\eta_{\mathrm{iw}}} \right)_{n_0=n_1=1} \tag{6.3}$$

where the number of replicated are given in the experimental case listing tables.

The uncertainty from the systematic sources can be added back in at this point. The uncertainty in the Sherwood number from systematic error sources was found to be 6.4 %. Since the systematic errors affect both the numerator and denominator in the film cooling effectiveness calculation to nearly the same extent, the uncertainty in the film cooling effectiveness due to systematic error sources effectively cancels out

and can be taken as 0 %.

6.5.1 Uncertainty Discussion

The uncertainty level in the Sherwood number is at an acceptable level to determine the main effects of interest in this work. However, the uncertainty level in the film cooling effectiveness is quite significant and partially obscures the film cooling effects of interest. This issue is especially apparent for the discrete hole experiments in which the uncertainty level of the film cooling effectiveness is the same order of magnitude as the film cooling effectiveness itself. Nonetheless, by using replicate experiments to reduce uncertainty in the mean result and by observing the results and trends in aggregate, the effects can be reasonably determined, and conclusions can be drawn.

Methods to Decrease Uncertainty In Future Work

Many suggestions are listed below to decrease the uncertainty level associated with the naphthalene mass transfer technique used in this work. While these methods will reduce uncertainty in both the Sherwood number and film cooling effectiveness, they are of most importance for the film cooling effectiveness given its more significant relative uncertainty level.

1. Perform at least 2 replicate experiments for both naphthalene-saturated and naphthalene-free experiments. Beyond, say, 4 replicates, the diminishing return effect becomes significant.

2. Setup automatic controllers for the following items that must otherwise be manually controlled. Design the controller's characteristic time constant to be on the order of a minute.
   - Blade Reynolds number
   - Slot and discrete injection blowing ratios
   - Injection flow tape heaters to equalize injection and main flow temperatures

3. Bring the tunnel and all settings to their steady-state experimental operating condition prior to installing the mass transfer plate and beginning the experiment in order to minimize the various transients after the plate is installed and the

experiment begins. Use a dummy mass transfer plate for this purpose so the wind tunnel can still operate.

4. Configure the wind tunnel such that the mass transfer plate (and dummy plate if applicable) can be installed and removed with minimal effort and time (say less than 1 minute).

5. Design the mass transfer plate such that there are minimal forces exerted on the naphthalene after secured into the tunnel. For example, the blade (with or without a fillet) should overhang onto the naphthalene minimally, say no more than 2.5 mm.

6. Design the mass transfer plate to be no larger than required (say only one flow passage for an endwall experiment). Smaller plates decrease the scan time and reduce the difficulty in ensuring the full plate is in the range of the LVDT probe. Smaller plates also help to produce more consistent naphthalene castings.

7. Within reason, run the wind tunnel portion of the experiment for the maximum amount of time while still ensuring that all of the points on the plate are within range of the LVDT probe. Take care to ensure the maximum sublimation depth is negligibly small compared to any characteristic length scales in the experiment.

Chapter 7

Conclusion

The main conclusions are summarized in this chapter. Additionally, suggestions for potential future work are given in Section 7.2.

7.1 Summary

In this study, detailed mass transfer measurements were conducted to determine the influence of purge flow swirl and discrete hole injection angle on endwall cooling in a blade passage. The naphthalene sublimation technique was used, which is a mass transfer technique that allows for high spatial resolution measurements and easily imposed boundary conditions. Two types of boundary conditions are utilized to measure both the mass transfer coefficient and the film cooling effectiveness distributions on the endwall. The mass transfer results can be used to estimate heat transfer using the heat/mass transfer analogy. Four complimentary experimental case configurations were executed for determining the influence of the purge flow swirl and discrete hole injection angle on endwall cooling:

1. Purge flow injection from a 45° straight slot
2. Purge flow injection from a realistically shaped slot
3. Discrete hole injection from 15 endwall holes
4. Combined injection from discrete holes and purge flow

The key findings from the four cases are synthesized and given in the following section.

7.1.1 Key Findings

Purge Flow Swirl

- For low blowing rates, the effect of purge flow swirl on the endwall cooling was found to be nearly negligible. Meanwhile, for higher blowing rates, the effect of purge flow swirl was found to reduce the coolant's axial penetration significantly and therefore the coolant's endwall film cooling potential.
- These results indicate that the blowing rate strongly influences to what degree the coolant follows the trajectory implied by the swirl angle
- The results indicate that for typical blowing rates with zero assumed swirl there is only mediocre film cooling coverage. The inclusion of swirl will only degrade the film cooling coverage further for real-world swirl levels. Purge flow coolant must be supplemented under practical circumstances to provide cooling to the complete endwall.
- The purge flow swirl effects are consistent between the straight slot and realistic slot within this work and are consistent with other literature that studied this effect, building confidence in the findings.

Discrete Hole Injection Angle

- When discrete holes were 90° misaligned with the near-wall flow direction, significant cooling penalties occurred in both the mass transfer (enhanced) and the film cooling effectiveness (diminished), indicating that the discrete hole injection misalignment penalty should be actively avoided if possible.
- While misaligned discrete hole injection led to substantially decreased peak film cooling effectiveness values, the coolant dispersed more widely, leading to a larger downstream film cooling area. Therefore, only a moderate reduction in averaged film cooling effectiveness was found overall.
- The results indicate that the angle misalignment effect leads to enhanced mixing and coolant blowing through the boundary layer, which explains the findings in the mass transfer and film cooling results.

7.1.2 Conclusions

The influence of both purge flow swirl and discrete hole injection angle are shown to significantly determine the coolant's potential for adequately cooling the endwall. The inclusion of the swirl effect leads to significant reductions in axial coolant penetration and therefore ignoring it would overestimate the cooling effectiveness from the purge flow. Similarly, the effect of angling the discrete holes away from their ideal orientation, potentially due to manufacturing constraints, promotes mixing, which enhances mass transfer and reduces film cooling effectiveness. Therefore, to design an effective endwall cooling scheme, which both provides adequate cooling coverage and minimizes wasted coolant, the effects of purge flow swirl and discrete hole injection angle should be taken into account.

7.2 Future Work

While the findings in this demonstrate the importance of considering purge flow swirl and discrete hole injection angle, there is much opportunity to study some additional aspects of these effects. Various potential ideas and considerations are given in the following paragraphs.

For typical endwall flow conditions in a blade passage, significant purge flow swirl is present, and most of the endwall coolant is swept away from the endwall and towards the suction surface. This situation indicates that the purge flow coolant is making its way onto the blade suction surface. It may be expected that the swirl effect enhances the blade suction surface cooling. By studying this effect, the swirled purge flow coolant could be maximally utilized, so any unnecessary coolant applied to the blade suction surface could be reduced.

The film cooling results in this work demonstrate significant difficulty in cooling the pressure side of the endwall, since the coolant, whether sourced from the purge flow or discrete cooling holes, is rapidly swept towards the suction surface. Therefore, improved coolant delivery strategies for the pressure side of the endwall should be proposed and studied. For example, a potential endwall cooling scheme is to inject coolant from the blade pressure surface along its perimeter nearest the endwall, since that coolant will immediately be swept off the blade and onto the endwall surface.

The effect of purge flow swirl is found to be detrimental at significantly high

blowing rates. Strategies to directly reduce the swirl, potentially via vanes within the wheelspace cavity may be of interest, especially if practically achievable in a real gas turbine.

While this work's focus was on endwall cooling, the effects of purge flow swirl and discrete hole injection angle will also influence the aerodynamics within the blade stage. An optimal cooling strategy does not imply optimal aerodynamics and vice versa. Therefore, a future study could analyze the effects on the aerodynamics and the tradeoffs.

Another research opportunity is to perform an equivalent computational study to match the experimental conditions present in this work. This computational study would help to build confidence in the findings made here and may provide a more straightforward starting point for studying some of the other proposed ideas.

In this work, the effect of the discrete hole injection angle was measured only for two extremes: aligned with the near endwall flow and 90° misalignment. A more comprehensive and granular study may be of interest to understand how much misalignment is acceptable before significant mixing and reduction in cooling occur. Additionally, since manufacturing constraints may ultimately limit the designer from angling the discrete holes as desired, it may be of interest to investigate new shaped hole designs that minimize mixing even for significant flow misalignment.

Bibliography

Ambrose, D., I. Lawrenson, and C. Spark (1975). "The Vapor Pressure of Naphthalene". *J. Chem. Thermodynamics* 7, pp. 1137–1176.

Barigozzi, G. et al. (2014). "Influence of Purge Flow Injection Angle on the Aerothermal Performance of a Rotor Blade Cascade". *Journal of Turbomachinery* 136.4, p. 041012.

Bedford, R. E. et al. (1996). "Recommended values of temperature on the International Temperature Scale of 1990 for a selected set of secondary reference points". *Metrologia* 33.2, p. 133.

Blair, M. F. (1974). "An experimental study of heat transfer and film cooling on large-scale turbine endwalls". *J. Heat Transfer* November, pp. 524–529.

Burd, S. W. and T. W. Simon (2000a). "Effects of slot bleed injection over a contoured endwall on nozzle guide vane cooling performance: Part I: Flow field measurements". *ASME Paper Number 199-GT-2000*.

Burd, S. W. and T. W. Simon (2000b). "Effects of slot bleed injection over a contoured endwall on nozzle guide vane cooling performance: Part II: Thermal measurements". *ASME Paper Number 200-GT-2000*.

Chen, P.-H. and P.-H. Wung (1989). "Diffusion coefficient of naphthalene in air". *J. of The Chin. I. Chem. E* 21.3, pp. 161–166.

Childs, P. R. N. (2010). *Rotating flow*. Elsevier.

Cho, K. (1989). "Measurement of the Diffusion Coefficient of Naphthalene into Air". PhD thesis. Stony Brook University.

Coleman, H. W. and W. G. Steele (2009). *Experimentation, validation, and uncertainty analysis for engineers*. John Wiley & Sons.

Constants, G. (1963). "Impossibility of linearizing a hot-wire anemometer for measurements in turbulent flows". *AIAA Journal* 1.5.

Cumpsty, N. A. (1968). *Crossflow in turbulent boundary layers*. Aeronautical Research Council Current Papers 1067. Cambridge University Engineering Department.

Dean, J. A. (1999). *Lange's handbook of chemistry*. New york; London: McGraw-Hill, Inc.

Deming, W. E. (1943). *Statistical adjustment of data.* Wiley.

Denton, J. D. (1993). "Loss Mechanisms in Turbomachines". *ASME 1993 International Gas Turbine and Aeroengine Congress and Exposition*. American Society of Mechanical Engineers, V002T14A001–V002T14A001.

Eckert, E. R. G. (1984). "Analysis of film cooling and full-coverage film cooling of gas turbine blades". *Journal of Engineering for Gas Turbines and Power* 106.1, pp. 206–213.

Eckert, E. R. G. and R. M. Drake Jr (1987). *Analysis of heat and mass transfer*. McGraw Hill.

Flow of fluids through valves, fittings, and pipe (1978). 410. Crane Company. Crane Company.

Friedrichs, S. (1997). "Endwall film-cooling in axial flow turbines". PhD thesis. University of Cambridge.

Gersten, K. and H. Herwig (1992). *Strömungsmechanik: Grundlagen der Impuls-, Wärme- und Stoffübertragung aus asymptotischer Sicht ; mit 58 Tabellen*. Fundamentals and advances in the engineering sciences. Vieweg. ISBN: 9783528064723.

Ghosh, K. (2009). "Effect of wall motion on a two-dimensional turbulent boundary layer". PhD thesis. University of Minnesota.

Goldstein, R. J. and H. H. Cho (1995). "A Review of Mass Transfer Measurements Using Naphthalene Sublimation". *Experimental Thermal and Fluid Science* 10, pp. 416–434.

Goldstein, R. J. and R. A. Spores (1988). "Turbulent transport on the endwall in the region between adjacent turbine blades". *Journal of Heat Transfer* 110.4a, pp. 862–869.

Goldstein, R. J. (1971). "Film cooling". *Advances in heat transfer*. Vol. 7. Elsevier, pp. 321–379.

Granser, D. and T. Schulenberg (1990). "Prediction and measurement of film cooling effectiveness for a first-stage turbine vane shroud". *ASME 1990 International Gas Turbine and Aeroengine Congress and Exposition*. American Society of Mechanical Engineers.

Graziani, R. A. et al. (1980). "An experimental study of endwall and airfoil surface heat transfer in a large scale turbine blade cascade". *Journal of Engineering for Power* 102.2, pp. 257–267.

Han, S. and R. J. Goldstein (2006). "Influence of blade leading edge geometry on turbine endwall heat (mass) transfer". *Journal of turbomachinery* 128.4, pp. 798–813.

Haynes, W. M. (2014). *CRC handbook of chemistry and physics*. CRC press.

Hinze, J. (1987). *Turbulence*. McGraw-Hill.

Jabbari, M. Y. et al. (1996). "Film cooling of the gas turbine endwall by discrete-hole injection". *Journal of Turbomachinery* 118.2, pp. 278–284.

Johnston, J. P. (1960). "On the three-dimensional turbulent boundary layer generated by secondary flow". *Journal of Basic Engineering* 82.1, pp. 233–246.

Kays, W. M. (2012). *Convective heat and mass transfer*. Tata McGraw-Hill Education.

Kohavi, R. et al. (1995). "A study of cross-validation and bootstrap for accuracy estimation and model selection". *IJCAI*. Vol. 14. 2. Stanford, CA, pp. 1137–1145.

Langston, L. S. (1980). "Crossflows in a turbine cascade passage". *Journal of engineering for power* 102.4, pp. 866–874.

Lee, S. W. et al. (2004). "Effects of combustor-level high inlet turbulence on the endwall flow and heat/mass transfer of a high-turning turbine rotor cascade". *KSME international journal* 18.8, pp. 1435–1450.

Leontiev, A. I. (1999). "Heat and mass transfer problems for film cooling". *Journal of heat transfer* 121.3, pp. 509–527.

Li, S.-J. et al. (2016). "Turbine platform cooling and blade suction surface phantom cooling from simulated swirl purge flow". *Journal of Turbomachinery* 138.8, p. 081004.

Mager, A. (1952). *Generalization of boundary-layer momentum-integral equations to three-dimensional flows including those of rotating system*. Tech. rep. 1067.

Measurement of Fluid Flow in Pipes Using Orifice, Nozzle, and Venturi (2007). ASME MFC-3Ma. American Society of Mechanical Engineers.

Mohamed, M. S. and J. C. Larue (1990). "The decay power law in grid-generated turbulence". *Journal of Fluid Mechanics* 219, pp. 195–214.

Mughal, B. H. (1992). "A calculation method for the three-dimensional boundary-layer equations in integral form". MA thesis. Massachusetts Institute of Technology.

Mughal, B. and M. Drela (1993). "A calculation method for the three-dimensional boundary-layer equations in integral form". *31st Aerospace Sciences Meeting*, p. 786.

Musker, A. J. (1979). "Explicit Expression for the Smooth Wall Velocity Distribution in a Turbulent Boundary Layer". *AIAA J.* 17, pp. 655–657.

Nicklas, M. (2001). "Film-cooled turbine endwall in a transonic flow field: Part ii—heat transfer and film-cooling effectiveness". *Journal of Turbomachinery* 123.4, pp. 720–729.

Oke, R. A., T. W. Simon, S. W. Burd, et al. (2000). "Measurements in a turbine cascade over a contoured endwall: discrete hole injection of bleed flow". *ASME Paper Number 214-GT-2000*.

Oke, R. A., T. W. Simon, T. Shih, et al. (2001). "Measurements over a Film-Cooled, Contoured Endwall with Various Coolant Rates". *ASME Paper Number 140-GT-2001*.

Ong, J., R. J. Miller, and S. Uchida (2012). "The effect of coolant injection on the endwall flow of a high pressure turbine". *Journal of Turbomachinery* 134.5.

Owen, J. M. and R. H. Rogers (1989). *Flow and heat transfer in rotating-disc systems*. New York, NY (USA): John Wiley and Sons Inc.

Pan, W. (2001). "Akaike's information criterion in generalized estimating equations". *Biometrics* 57.1, pp. 120–125.

Papa, M. (2006). "Influence of blade leading edge geometry and upstream blowing on the heat/mass transfer in a turbine cascade". PhD thesis. University of Minnesota.

Pohl, J. et al. (2017). "Structural Deflection's Impact in Turbine Stator Well Heat Transfer". *Journal of Engineering for Gas Turbines and Power* 139.4, p. 041901.

Pope, S. B. (2011). *Turbulent flows*. Cambridge Univ. Press.

Preston-Thomas, H. (1990a). "Supplementary information for the international temperature scale of 1990". *Bureau International des Poids et Mesures*.

Preston-Thomas, H. (1990b). "The international temperature scale of 1990 (ITS-90)". *metrologia* 27.1, p. 3.

Radomsky, R. W. and K. A. Thole (2000). "High Freestream Turbulence Effects on Endwall Heat Transfer for a Gas Turbine Stator Vane". *ASME Turbo Expo 2000: Power for Land, Sea, and Air*. American Society of Mechanical Engineers.

Rolls Royce (1986). *The Jet Engine*. John Wiley & Sons.

Romano, G. et al. (2007). "Measurements of turbulent flows". *Springer Handbook of Experimental Fluid Mechanics*. Springer, pp. 745–855.

Roy, R. P. et al. (2000). "Flow and Heat Transfer at the Hub Endwall of Inlet Vane Passages—Experiments and Simulations". *ASME Turbo Expo 2000: Power for Land, Sea, and Air*. American Society of Mechanical Engineers.

Schlichting, H. and K. Gersten (2016). *Boundary-layer theory*. Springer.

Schmidt, D. L., B. Sen, and D. G. Bogard (1996). "Film cooling with compound angle holes: adiabatic effectiveness". *Journal of Turbomachinery* 118.4, pp. 807–813.

Sen, B., D. L. Schmidt, and D. G. Bogard (1996). "Film cooling with compound angle holes: heat transfer". *Journal of Turbomachinery* 118.4, pp. 800–806.

Simon, T. W. and J. Piggush (2008). "Hot gas path heat transfer characteristics/active cooling of turbine components". *Thermal Engineering in Power Systems*. WIT Press. Chap. 22, p. 231.

Smith, P. D. (1972). *An integral prediction method for three-dimensional compressible turbulent boundary layers*. R & M 3739. Aeronautical Research Council.

Southwell, W. (1976). "Fitting data to nonlinear functions with uncertainties in all measurement variables". *The Computer Journal* 19.1, pp. 69–73.

Stinson, M. et al. (2014). "Effect of Swirled Leakage Flow on Endwall Film-Cooling". *International Heat Transfer Conference Digital Library*. Begel House Inc.

Stopwatch and Timer Calibrations (2009). National Institute of Standards and Technology.

Suryanarayanan, A. et al. (2010). "Film-cooling effectiveness on a rotating turbine platform using pressure sensitive paint technique". *Journal of Turbomachinery* 132.4, p. 041001.

Test Uncertainty (2013). ASME PTC 19.1. American Society of Mechanical Engineers.

The MathWorks, Inc. (2019). *MATLAB*. Version 2019a.

Thole, K. A. and D. G. Knost (2005). "Heat transfer and film-cooling for the endwall of a first stage turbine blade". *International Journal of Heat and Mass Transfer* 48, pp. 5255–5269.

Uncertainty of measurement – Part 3: Guide to the expression of uncertainty in measurement (GUM:1995) (2008). ISO 98-3:2008. International Organization for Standardization.

Wang, H.-P. et al. (1995). "Flow visualization in a linear turbine cascade of high performance turbine blades". *ASME 1995 International Gas Turbine and Aeroengine Congress and Exposition*. American Society of Mechanical Engineers.

White, D. R. et al. (2007). "Uncertainties in the realization of the SPRT sub-ranges of the ITS-90". *International journal of thermophysics* 28.6, pp. 1868–1881.

White, F. M. (1988). *Heat and Mass Transfer. 1988*. New York: Addison-Wesley Publishing Co.

Wilson, D. J. (1970). "An experimental investigation of the mean velocity, temperature and turbulence fields in plane and curved two-dimensional wall jets: Coanda effect." PhD thesis. Univ. of Minnesota.

York, D. et al. (2004). "Unified equations for the slope, intercept, and standard errors of the best straight line". *American Journal of Physics* 72.3, pp. 367–375.

Zhang, K. et al. (2019). "Effects of simulated swirl purge flow and mid-passage gap leakage on turbine blade platform cooling and suction surface phantom cooling performance". *International Journal of Heat and Mass Transfer* 129, pp. 618–634.

Zhang, L. J. and R. S. Jaiswal (2001). "Turbine nozzle endwall film cooling study using pressure-sensitive paint". *Journal of Turbomachinery* 123.4, pp. 730–738.

Zhang, L. and H. K. Moon (2003). "Turbine nozzle endwall inlet film cooling: The effect of a back-facing step". *ASME Turbo Expo 2003, collocated with the 2003 International Joint Power Generation Conference*. American Society of Mechanical Engineers, pp. 203–211.

Appendix A

Sample Calculations

Sample calculations are described in this chapter to demonstrate how the calculations for properties, flows, and mass transfer were performed in this work.

A.1 Calculation of Properties

A.1.1 Air Properties

Sample air properties within the wind tunnel are described here.

Temperature

The air temperature was determined by measuring the E-type thermocouple voltage and using the relation from Fig. 4.14:

$$T = 0.0159E_{\mathrm{TC}}^3 - 0.3061E_{\mathrm{TC}}^2 + 17.2359E_{\mathrm{TC}} \tag{A.1}$$

For $E_{\mathrm{TC}} = 1.6025\,\mathrm{mV}$, $T = 26.90\,^{\circ}\mathrm{C} = 300.05\,\mathrm{K}$.

Pressure

The atmospheric pressure p_{atm} was measured directly using the `pressure` terminal command to call the SETRACERAM™ sensor. In the following examples, it is taken as 97 589 Pa. The pressure differential between the test section and the ambient was measured using the pressure transducer number 4 with a calibration slope of

0.3838 kPa/mV (see Table 4.1). For $E_{\mathrm{PT}} = 2.550\,\mathrm{mV}$, the pressure differential is found as

$$\Delta p = 0.3838\,\mathrm{kPa/mV} \cdot 2.550\,\mathrm{mV} = 979\,\mathrm{Pa}$$

Then, the tunnel pressure equals

$$p = p_{\mathrm{atm}} + \Delta p = 97\,589\,\mathrm{Pa} + 979\,\mathrm{Pa} = 98\,568\,\mathrm{Pa}$$

Density

Density is calculated using ideal gas law. First, the specific gas constant for air is determined from $R_{\mathrm{air}} = \overline{R}/M_{\mathrm{air}}$:

$$R_{\mathrm{air}} = \frac{8314.4621\,\mathrm{J/(K\,kmol)}}{28.9644\,\mathrm{kg/kmol}} = 287.06\,\mathrm{J/(kg\,K)}$$

Then ideal gas law is used to calculate the density as

$$\rho = \frac{p}{R_{\mathrm{air}} T} \tag{A.2}$$

For the previously stated pressures and temperatures, the density is calculated as

$$\rho = \frac{98\,568\,\mathrm{Pa}}{287.06\,\mathrm{J/(kg\,K)} \cdot 300.05\,\mathrm{K}} = 1.144\,\mathrm{kg/m^3}$$

Viscosity

Air dynamic viscosities were taken from the CRC Handbook (Haynes, 2014) as a function of temperature. The viscosity was fit from a lookup table from 260 K to 380 K using a 2nd order polynomial:

$$\mu = -3.1548 \times 10^{-5} T^2 + 6.7226 \times 10^{-2} T + 1.207 \tag{A.3}$$

where viscosity μ is in micropascal per second and T is in kelvin. For $T = 300.05\,\mathrm{K}$, the viscosity μ is found to be $1.8538 \times 10^{-5}\,\mathrm{kg/(m\,s)}$. The kinematic viscosity is then calculated from $\nu = \mu/\rho$:

$$\nu = \frac{1.8538 \times 10^{-5}\,\mathrm{kg/(m\,s)}}{1.144\,\mathrm{kg/m^3}} = 1.6199 \times 10^{-5}\,\mathrm{m^2/s}$$

A.1.2 Naphthalene Properties

Sample naphthalene properties at the wall and in the mass transfer convective layer are described here.

Naphthalene Vapor Pressure

Naphthalene vapor pressure at the wall is calculated according to Ambrose et al. (1975) as a function of temperature. First, the variable ζ is calculated as follows:

$$\zeta = (2T - 574)/114 \tag{A.4}$$

where T is in kelvin. Then the vapor pressure p_{v} (in pascal) is calculated from

$$T \log_{10} p_{\mathrm{v}} = \frac{301.6247}{2} + 791.4937\zeta - 8.2536\left(2\zeta^2 - 1\right) + 0.4043\left(4\zeta^3 - 3\zeta\right) \tag{A.5}$$

For example, for $T_w = 26.25\,^{\circ}\mathrm{C} = 299.40\,\mathrm{K}$, $\zeta = 0.2175$, $T_{\mathrm{w}} \log_{10} p_{\mathrm{v,w}} = 330.22$, and $p_{\mathrm{v,w}} = 10^{330.22/299.40} = 12.67\,\mathrm{Pa}$.

Naphthalene Vapor Density

Naphthalene vapor density at the wall is calculated according to ideal gas law:

$$\rho_{\mathrm{v,w}} = \frac{p_{\mathrm{v,w}}}{R_{\mathrm{naph}} T_{\mathrm{w}}} \tag{A.6}$$

The specific gas constant for naphthalene is calculated first using the molar mass of naphthalene equal to 128.17 kg/kmol (Dean, 1999):

$$\begin{aligned} R_{\mathrm{naph}} &= \frac{\overline{R}}{M_{\mathrm{naph}}} \\ &= \frac{8314.4621\,\mathrm{J/(K\,kmol)}}{128.17\,\mathrm{kg/kmol}} \\ &= 64.87\,\mathrm{J/(kg\,K)} \end{aligned}$$

Then, for the previously stated wall vapor pressure and temperature, the naphthalene vapor density at the wall is calculated as

$$\rho_{\mathrm{v,w}} = \frac{12.67\,\mathrm{Pa}}{64.87\,\mathrm{J/(kg\,K)} \cdot 299.40\,\mathrm{K}} = 6.523 \times 10^{-4}\,\mathrm{kg/m^3}$$

Diffusion Coefficient

The binary diffusion coefficient for naphthalene in air is calculated according to Goldstein and H. H. Cho (1995):

$$D_{\mathrm{naph}} = D_{\mathrm{ref}} \left(\frac{T}{T_{\mathrm{ref}}} \right)^{1.93} \left(\frac{p_{\mathrm{ref}}}{p} \right) \tag{A.7}$$

where $D_{\mathrm{ref}} = 6.81 \times 10^{-6}\,\mathrm{m^2/s}$, $T_{\mathrm{ref}} = 298.16\,\mathrm{K}$, and $p_{\mathrm{ref}} = 1.013 \times 10^5\,\mathrm{Pa}$. The temperature used for the diffusion coefficient calculations is the film temperature:

$$T_{\mathrm{film}} = \frac{T_{\mathrm{w}} + T_{\infty}}{2} \tag{A.8}$$

Here, $T_{\mathrm{film}} = 26.58\,^{\circ}\mathrm{C} = 299.73\,\mathrm{K}$ using the previously stated tunnel and wall temperatures. Then, $D_{\mathrm{naph}} = 7.070 \times 10^{-6}\,\mathrm{m^2/s}$ using the film temperature and the tunnel pressure previously calculated.

Schmidt Number

The Schmidt number is calculated according to its definition:

$$Sc = \frac{\nu}{D_{\mathrm{naph}}} \tag{A.9}$$

Like the diffusion coefficient, it is calculated at the film temperature. Both the kinematic viscosity and the binary diffusion coefficient are inversely proportional to the pressure, so the pressure dependency drops out, and the resulting dependency is on the temperature only. The kinematic viscosity at the film temperature and tunnel pressure is found to be $1.6168 \times 10^{-5}\,\mathrm{m^2/s}$. Then, the Schmidt number is found to be 2.287 for the given film temperature.

A.2 Flow Calculations

Flow Speed

The dynamic pressure in the tunnel was measured using the pitot-static probe and Pressure Transducer 2 as 144.26 Pa. The dynamic pressure can be related to the velocity from Eq. (4.13):

$$V = \sqrt{\frac{2 \cdot 144.25\,\mathrm{Pa}}{1.144\,\mathrm{kg/m^3}}} = 15.88\,\mathrm{m/s}$$

This velocity measurement was corrected due to the error from the 5 % freestream turbulence intensity level using Eq. (4.14):

$$V_{\mathrm{corrected}} = \sqrt{\frac{(15.88\,\mathrm{m/s})^2}{1 + 0.05^2}} = 15.86\,\mathrm{m/s}$$

Reynolds Number

Then the Reynolds number is calculated using the characteristic length and velocity for the cascade:

$$\begin{aligned} Re &= \frac{\rho V_{\mathrm{ex}} C}{\mu} \\ &= \frac{\rho\,(AR \cdot V_{\mathrm{in}})\,C}{\mu} \\ &= \frac{1.144\,\mathrm{kg/m^3}\,(2.724 \cdot 15.86\,\mathrm{m/s})\,0.184\,15\,\mathrm{m}}{1.8538 \times 10^{-5}\,\mathrm{kg/(m\,s)}} \\ &= 490\,959 \end{aligned}$$

Orifice Mass Flow Rate

Orifice meters were used for upstream slot and discrete hole injection mass flow rate measurements. Pressures upstream and downstream of the orifice were measured using pressure transducers, and the temperature is measured downstream using an E-type thermocouple. An example for calculating the upstream slot mass flow rate is given here. The procedure for the discrete holes injection flow path is the same. For an upstream tap pressure of 100 184 Pa, downstream tap pressure of 98 658 Pa, and

downstream temperature of 26.33 °C (299.48 K), the upstream orifice density and the expansibility factor can be calculated. First the upstream orifice density is calculated with the assumption of minimal temperature change over the orifice:

$$\rho = \frac{100\,184\,\text{Pa}}{287.06\,\text{J/(kg K)} \cdot 299.48\,\text{K}} = 1.165\,\text{kg/m}^3$$

Next, the expansibility factor is calculated using the two pressure measurements, the ratio of specific heats $\gamma = 1.4$ for air, and the orifice geometry factor $\beta = 0.5925$. The expansibility factor is calculated as $Y = 0.9957$ by plugging into Eq. (4.12). To solve for the mass flow rate, the following iterative procedure is used:

1. Make initial guess for the discharge coefficient: $C = 0.606$.
2. Calculate $\dot{m}$ from Eq. (4.10).
3. Calculate the orifice pipe Reynolds number, Re_D, based on upstream conditions and the pipe diameter $D = 0.052\,725\,\text{m}$.
4. Calculate the discharge coefficient C from Eq. (4.11).
5. Check for convergence. If not converged, go back to step 2.

In practice, a more optimized procedure (with detail in *Measurement of Fluid Flow in Pipes Using Orifice, Nozzle, and Venturi* (2007)) iterates directly between the pipe Reynolds number and discharge coefficient. For that procedure, the mass flow rate can be post-processed from the converged Reynolds number. Either procedure will ultimately give the same result once converged. For the conditions described, the following results are found: $Re_D = 3.908 \times 10^4$, $\dot{m} = 0.029\,95\,\text{kg/s}$, and $C = 0.6162$.

Blowing Ratio

The slot blowing ratio M_s is calculated from its definition, knowledge of the coolant slot injection flow area, and previously calculated flow quantities. In this case, for the realistic slot, the width is 10 mm and the slot length is 39.46 cm resulting in a slot

area of $0.003\,946\,\mathrm{m}^2$. The value for M_s is then calculated as follows:

$$\begin{aligned} M_\mathrm{s} &= \frac{\rho_\mathrm{s} V_\mathrm{s,ax}}{\rho_\mathrm{in} V_\mathrm{in}} \\ &= \frac{\dot{m}_\mathrm{s}/A_\mathrm{s}}{\rho_\mathrm{in} V_\mathrm{in}} \\ &= \frac{(0.029\,95\,\mathrm{kg/s}) \,/\, \left(0.003\,946\,\mathrm{m}^2\right)}{1.144\,\mathrm{kg/m}^3 \cdot 15.86\,\mathrm{m/s}} \\ &= 0.4184 \end{aligned}$$

Note that the same approach is taken for the straight slot, but with modified values for the slot width and length of 4 mm and 42.44 cm, respectively. Also note that the calculation for the discrete hole blowing ratio, M_h, is similar, with the main differences that the total coolant area is the sum of the 15 hole areas and the denominator has the area ratio correction term.

Hot-wire Velocity

For ambient pressure equal to 98 630 Pa, ambient temperature equal to 26.04 °C, and a measured instantaneous voltage measurement of 0.6506 V, the instantaneous velocity can be calculated. First, the hot-wire voltage is calculated by accounting for the gain and offset of 10 and 1 V, respectively, that are applied on the IFA-100 readings:

$$\begin{aligned} E_\mathrm{hw} &= \frac{E_\mathrm{IFA100}}{\mathrm{IFA100}_\mathrm{gain}} + \mathrm{IFA100}_\mathrm{offset} \\ &= 0.6506\,/10 + 1\,\mathrm{V} \\ &= 1.065\,\mathrm{V} \end{aligned}$$

Then the reference hot-wire voltage is calculated as follows:

$$\begin{aligned} E_\mathrm{hw,ref} &= E_\mathrm{hw}\sqrt{\frac{T_\mathrm{wire} - T_\mathrm{ref}}{T_\mathrm{wire} - T_\infty}} \\ &= 1.065\,\mathrm{V}\sqrt{\frac{250\,^\circ\mathrm{C} - 25\,^\circ\mathrm{C}}{250\,^\circ\mathrm{C} - 26.04\,^\circ\mathrm{C}}} \\ &= 1.068\,\mathrm{V} \end{aligned}$$

Then the reference hot-wire voltage is used to calculate the reference hot-wire velocity by inversing the calibration ($E_{\text{ref}}^2 = 0.433 + 0.342V_{\text{ref}}^{0.415}$):

$$\begin{aligned} V_{\text{ref}} &= \left(\frac{E_{\text{ref}}^2 - 0.433}{0.342}\right)^{1/0.415} \\ &= \left(\frac{1.068^2 - 0.433}{0.342}\right)^{1/0.415} \\ &= 5.766\,\text{m/s} \end{aligned}$$

Lastly, the actual velocity is determined by inversing the V_{ref} definition:

$$\begin{aligned} V &= V_{\text{ref}}\frac{p_{\text{ref}}}{p} \\ &= 5.766\,\text{m/s}\frac{101\,325\,\text{Pa}}{98\,630\,\text{Pa}} \\ &= 5.924\,\text{m/s} \end{aligned}$$

A.3 Mass Transfer Calculations

Mass transfer measurements are made by scanning the surface using an LVDT probe. The LVDT and plate are positioned so that typical measurements fall between $\pm 12\,\text{V}$. As an example, for a voltage measurement of $-4.274\,\text{V}$ for the initial scan and $2.378\,\text{V}$ for the final scan at a given location, the depth is calculated as:

$$\begin{aligned} \delta z &= b\,(E_{\text{LVDT,f}} - E_{\text{LVDT,i}}) \\ &= \frac{1}{0.052\,365\,\text{V/µm}}\,(2.378\,\text{V} - -4.274\,\text{V}) \\ &= 127.0\,\text{µm} \end{aligned}$$

Then the mass flux is determined given the experimental time and naphthalene solid density. Here the time is taken as $3452\,\text{s}$ and the solid density is $1162\,\text{kg/m}^3$ (Dean, 1999). For this example calculation, the natural sublimation depth will be treated as

zero for simplicity:

$$\begin{aligned}\dot{m}'' &= \rho_{\mathrm{s}} \frac{\delta z - \delta z_{\mathrm{natural}}}{\delta t} \\ &= 1162\,\mathrm{kg/m^3} \frac{127.0\,\mu\mathrm{m} - 0\,\mu\mathrm{m}}{3452\,\mathrm{s}} \\ &= 4.275 \times 10^{-5}\,\mathrm{kg/(s\,m^2)}\end{aligned}$$

Next, the mass transfer coefficient is calculated. For the case when the freestream naphthalene concentration is zero, $\rho_{\mathrm{v},\infty} = \rho_{\mathrm{v,iw}} = 0$, the mass transfer coefficient is calculated as follows:

$$\begin{aligned}h'_{\mathrm{m}} = h_{\mathrm{m}} &= \frac{\dot{m}''}{\rho_{\mathrm{v,w}} - 0} \\ &= \frac{4.275 \times 10^{-5}\,\mathrm{kg/(s\,m^2)}}{6.523 \times 10^{-4}\,\mathrm{kg/m^3}} \\ &= 0.065\,54\,\mathrm{m/s}\end{aligned}$$

Finally, the mass transfer coefficient is non-dimensionalized as a Sherwood number:

$$Sh = \frac{h_{\mathrm{m}} C}{D_{\mathrm{naph}}} = \frac{0.065\,54\,\mathrm{m/s} \cdot 0.184\,15\,\mathrm{m}}{7.070 \times 10^{-6}\,\mathrm{m^2/s}} = 1707$$

Appendix B

Uncertainty Analysis

The uncertainty estimates in this investigation are calculated using the methods described in the ISO guide for measurement uncertainty (*Uncertainty of measurement – Part 3: Guide to the expression of uncertainty in measurement (GUM:1995)* 2008) and the corresponding ASME guide (*Test Uncertainty* 2013). The textbook on the subject by Coleman and Steele (2009) is also referenced here for its detailed explanations and insight on the subject, including many practical examples. The estimates are made at a 95 % level of confidence. An overview of the uncertainty analysis approach taken is given followed some specific uncertainty calculations that are of importance for this work.

B.1 Uncertainty of a Measurement

Every measurement has error, which is defined as the difference between the measured value and the true value. It is the goal of uncertainty analysis to estimate the limits of this error at a specified level of confidence. The total error can be classified into two broad categories: random error and systematic error. When the nature of the measurement error causes scatter in the test data, then the error contributes to the random error. When the nature of the measurement error is fixed, then the error contributes to systematic error. Random uncertainty and systematic uncertainty are the estimates of the random error and systematic error, respectively. Note that this classification of uncertainty is based on the effects of the errors. Another uncertainty classification that could be used is instead based on how the uncertainty is estimated. If the uncertainty is estimated using repeated observations and involves calculating a

standard deviation, then this may be called a Type A uncertainty. Conversely, if the uncertainty is estimated without repeated observations and using scientific judgment and information such as previous measurement data, manufacturer's specifications, etc., then this may be called Type B uncertainty. While Type A uncertainty tends to relate to random error and Type B uncertainty tends to relate to systematic error, this is not absolutely the case. Together these two different ways of classifying uncertainty lead to four independent uncertainty classifications. These classification alternatives are explained for completeness; however, in this work uncertainty will only be classified as random uncertainty and systematic uncertainty.

B.1.1 Random Standard Uncertainty of a Measurement

The process for estimating the random standard uncertainty associated with the measurement of quantity X is discussed. By taking a finite number of measurements, the sample mean and sample standard deviations can be calculated. The sample mean, $\overline{X}$, can be calculated as follows:

$$\overline{X} = \frac{\sum_{k=1}^{n} X_k}{n} \tag{B.1}$$

where X_k is an individual measurement of the total n sampled measurements. Then the sample standard deviation, s_X, can be calculated:

$$s_X = \sqrt{\frac{\sum_{k=1}^{n} \left(X_k - \overline{X}\right)^2}{n-1}} \tag{B.2}$$

Furthermore, the sample standard deviation of the mean, $s_{\overline{X}}$, can be calculated as follows:

$$s_{\overline{X}} = \frac{s_X}{\sqrt{n}} \tag{B.3}$$

In practice, it is not required to perform multiple measurements to estimate s_X every time X is measured. Instead, the estimate for s_X could be made at another time (before or after) or even multiple times. If s_X is estimated multiple times, and the true population standard deviation is expected to come from the same underlying distribution, a pooled sample standard deviation, s_{X_p}, for X can be calculated and

used:

$$s_{X\,\mathrm{p}} = \sqrt{\frac{\sum_{k=1}^{K}(n_k - 1)\, s_{Xk}^2}{\sum_{k=1}^{K}(n_k - 1)}} \tag{B.4}$$

where K is the number of measurement sets, and n_k and s_{Xk} are the number of measurements and the sample standard deviation for each set, respectively.

Finally, the random standard uncertainty associated with the measurement of X can be taken as either s_X or $s_{\overline{X}}$ depending on if a single or multitude of measurements for X are taken, respectively. Moving forward, s_X will be written, implying only 1 measurement was taken, however this need not be the case and s_X should be replaced with $s_{\overline{X}}$ as appropriate.

B.1.2 Systematic Standard Uncertainty of a Measurement

Next, the process for estimating the systematic standard uncertainty b_X, is explained. To begin, all of the elemental sources for the systematic error are to be identified, which requires a thorough understanding of the test objectives and test process. Then the distribution shape and magnitude of these elemental sources of systematic error are estimated or calculated, as appropriate. These values usually come from engineering judgments or manufacturer information, including instrument calibrations. Typical assumptions for the distributions of these systematic errors include normal distributions, uniform distributions, or triangular distributions. For uniform distributions, where there is reason to expect the systematic error is bounded by $\pm a$ with equal chance of error anywhere in that range, then $b_{Xk} = \frac{a}{\sqrt{3}}$. For triangular distributions, where there is reason to expect the systematic error is bounded by $\pm a$ and the error is more likely to be zero than $\pm a$, then $b_{Xk} = \frac{a}{\sqrt{6}}$. Alternatively, if the distribution of systematic error is approximately normal with a 95 % confidence interval of $\pm a$, then $b_{Xk} = \frac{a}{2}$ where the denominator 2 comes from rounding the 1.96 factor corresponding to 95 % confidence interval from the normal distribution. The normal distribution assumption is the approach generally taken here, unless there is specific reason to expect the uniform or triangular distributions are more likely. Note that the systematic standard uncertainty of the mean, $b_{\overline{X}k}$, is equal to the systematic standard uncertainty, b_{Xk}, since systematic error is the same regardless of if a single value or a mean value is taken and the averaging process does not affect systematic uncertainties as it does random uncertainties.

Finally, once each elemental systematic error source is estimated, they can be combined as follows to estimate the total systematic standard uncertainty of a measurement:

$$b_X = \sqrt{\sum_{k=1}^{M} b_{X_k}^2} \tag{B.5}$$

where M is the number of elemental sources for the systematic uncertainty of the measurement.

B.1.3 Combined Standard Uncertainty of a Measurement

The combined standard uncertainty of a measurement can be calculated simply as follows:

$$u_X = \sqrt{s_X^2 + b_X^2} \tag{B.6}$$

which estimates the total standard uncertainty of the measurement including random and systematic effects.

B.1.4 Expanded Uncertainty of a Measurement

Starting from the combined standard uncertainty of a measurement for X, the expanded uncertainty of a measurement can be calculated as follows:

$$U_X = k u_X \tag{B.7}$$

where the coverage factor k is to be chosen based on the desired level of confidence for the true estimate for result X. Ideally, k is to evaluated from the t-distribution as a function of the desired level of confidence and the degrees of freedom of u_X. There does not exist an exact analytical expression for the degrees of freedom for u_X for the general case of when u_X depends on two or more variance components. However, an effective degrees of freedom may be approximated using the Welch-Satterthwaite formula:

$$\nu_X = \frac{\left(s_X^2 + \sum_{k=1}^{M} b_{X\,k}^2\right)^2}{s_X^4/\nu_{s_X} + \sum_{k=1}^{M} b_{X\,k}^4/\nu_{b_{X\,k}}} \tag{B.8}$$

where ν_X is the effective degrees of freedom for u_X, ν_{S_X} is the degrees of freedom for s_X, and $\nu_{b_{Xk}}$ is the degrees of freedom for b_{Xk}. Note that ν_{s_X} is normally equal to $(n-1)$ except in the case where a pooled standard deviation is calculated: in which case it is equal to the denominator within the square root in Eq. (B.4). The degrees of freedom associated with the elemental systematic error sources, $\nu_{b_{Xk}}$, can be estimated using

$$\nu_{b_{Xk}} \approx \frac{1}{2}\left(\frac{\Delta b_{Xk}}{b_{Xk}}\right)^{-2} \tag{B.9}$$

where the term in parentheses represents the relative uncertainty in b_{Xk}, which usually comes from engineering judgment. As an example, if the relative uncertainty in b_{Xk} is 25 %, then the estimated degrees of freedom is 8. Note that if uniform or triangular distributions with known limits are assumed for the elemental systematic error source, this would imply no uncertainty in b_{Xk}, in which case $\nu_{b_{Xk}} = \infty$.

Generally, for real-world engineering applications, it is appropriate to use approximate values for the coverage factor since the effective degrees of freedom are usually appropriately large (greater than 10). It is recommended to use a value of $k = 2$ to define an interval having a level of confidence of approximately 95 %, or, for more critical applications, $k = 3$ can be used to define an interval having a level of confidence of approximately 99 %. When the effective degrees of freedom is known to be small or the particular application requires especially careful uncertainty estimates, then it may be best to carefully calculate the effective degrees of freedom and to obtain the coverage factor from the t-distribution. In this work, a coverage factor of $k = 2$ is adopted to represent 95 % confidence intervals, except where noted. Once the coverage factor is calculated or chosen, the combined standard uncertainty can be calculated and the true value for X can then be stated to fall into the following interval at the level of confidence associated with k:

$$X \pm U_X \tag{B.10}$$

B.2 Uncertainty of a Result

The general data reduction equation for result R as a function of N measured X_i variables is

$$R = R\left(X_1, X_2, \ldots, X_N\right) \tag{B.11}$$

Note that each input quantity could also represent an intermediate result in this context. The uncertainties in each quantity X_i input will propagate and contribute to an uncertainty in the calculated result.

B.2.1 Random Standard Uncertainty of a Result

The standard random uncertainty of a result can be calculated in two ways: by propagating the uncertainties in measurements X_i into uncertainty in R or by estimating the standard random uncertainty directly using repeat measurements of the result. These two methods may both be used at different phases in the experimental process and can be compared to determine whether or not the random uncertainties in X were accurately estimated. Ultimately, the direct estimate of the random uncertainty of R may be preferred and reported if it is available since it is a direct measurement rather than an estimate for the standard random uncertainty of a result.

Random Standard Uncertainty of a Result Calculated by Propagation

The random standard uncertainty of a result can be calculated by propagation as follows:

$$s_R = \sqrt{\sum_{i=1}^{N} \left(\frac{\partial R}{\partial X_i}\right)^2 s_{X_i}^2 + 2\sum_{i=1}^{N-1}\sum_{j=i+1}^{N} \frac{\partial R}{\partial X_i}\frac{\partial R}{\partial X_j} s_{X_i X_j}} \tag{B.12}$$

where the $s_{X_i X_j}$ is the covariance of the random errors between X_i and X_j. In general, this covariance term could be found by sampling X_i and X_j, however it is generally assumed to be negligible and set to zero.

Random Standard Uncertainty of a Result Calculated Directly

The random standard uncertainty of a result, s_R, can be calculated using the same approach for the random standard uncertainty of a measurement using Eqs. (B.1)

and (B.2) and replacing X_i with R_i and $\overline{X}$ with $\overline{R}$. Furthermore, $s_{\overline{R}}$ can be estimated using Eq. (B.3) with similar modifications. The direct measurement of s_R will automatically include the effect of covariance between the input measurements, so if it was a poor assumption to ignore the covariance terms when calculating s_R via propagation in Eq. (B.12), then that may be one reason for a disagreement between the methods.

B.2.2 Systematic Standard Uncertainty of a Result

The systematic standard uncertainty of a result can be calculated by propagation as follows:

$$b_R = \sqrt{\sum_{i=1}^{N} \left(\frac{\partial R}{\partial X_i} \right)^2 b_{X_i}^2 + 2 \sum_{i=1}^{N-1} \sum_{j=i+1}^{N} \frac{\partial R}{\partial X_i} \frac{\partial R}{\partial X_j} b_{X_i X_j}} \tag{B.13}$$

where $b_{X_i X_j}$ is the covariance of the systematic error between X_i and X_j. In the case where the correlation between all elements of the systematic error between X_i and X_j is zero, then $b_{X_i X_j}$ is set to zero. In the case where there is correlation between some elements of the systematic error between X_i and X_j, then

$$b_{X_i X_j} = \sum_{l=1}^{L} b_{X_i l} b_{X_j l} \tag{B.14}$$

where L is the number of correlated elemental sources of systematic error. This effect can be important in various situations: such at measuring temperature differences when systematic error between temperature probes is correlated; or, in the case of calibrations where the same equipment is used to measure the independent variable in a calibration curve and is also used for new measurements that feed into that calibration curve. This latter case is discussed further in Appendix C.

B.2.3 Combined Standard Uncertainty of a Result

Beginning with the random and systematic standard uncertainties of a result, the combined standard uncertainty of a result can be calculated simply as follows:

$$u_R = \sqrt{s_R^2 + b_R^2} \tag{B.15}$$

which estimates the total standard uncertainty of the result including random and systematic effects.

The above approach estimated random and systematic uncertainties of a result first before calculating the combined uncertainty of the result. If it were not required to estimate the random and systematic uncertainties of the result as intermediate results, then the combined standard uncertainty of a measurement can be calculated more directly by using

$$u_R = \sqrt{\sum_{i=1}^{N} \left(\frac{\partial R}{\partial X_i} \right)^2 u_{X_i}^2} \tag{B.16}$$

which is correct when the random and systematic covariance terms are negligible, as is often the case. For the situation when the covariance is not negligible, the following term would be added inside the square root term within Eq. (B.16):

$$2 \sum_{i=1}^{N-1} \sum_{j=i+1}^{N} \frac{\partial R}{\partial X_i} \frac{\partial R}{\partial X_j} \left(s_{X_i X_j} + b_{X_i X_j} \right) \tag{B.17}$$

A special case occurs when the relationship between the output and input variables is linearly proportional and in the following form:

$$R = X_1^{p_1} X_2^{p_2} \cdots X_N^{p_N} \tag{B.18}$$

In this case, the relative combined standard uncertainty of output R, u_R/R, is given by

$$\frac{u_R}{R} = \sqrt{\sum_{i=1}^{N} \left(p_i \frac{u_{X_i}}{X_i} \right)^2} \tag{B.19}$$

which is correct for the case when when covariance terms are negligible. If the covariance terms needed to be considered, then the following would be added inside the square root term within Eq. (B.19):

$$2 \sum_{i=1}^{N-1} \sum_{j=i+1}^{N} p_i p_j \frac{s_{X_i X_j} + b_{X_i X_j}}{X_i X_j} \tag{B.20}$$

B.2.4 Expanded Uncertainty of a Result

Starting from the combined standard uncertainty of a result R, the expanded uncertainty of a result can be calculated as follows:

$$U_R = k u_R \tag{B.21}$$

where the coverage factor k is chosen based on the desired level of confidence for the true estimate for result R. The process for picking k is the same as described in Appendix B.1.4. The primary exception is that the Welch-Satterthwaite formula is slightly modified to accommodate error propagation:

$$\nu_R = \frac{u_R^4}{\sum_{i=1}^{N} \frac{\left(\frac{\partial R}{\partial X_i}\right)^4 u_{X_i}^4}{\nu_{X_i}}} \tag{B.22}$$

As recommended previously, a coverage factor of $k = 2$ is adopted to represent a 95 % confidence interval, except where noted. Then the expanded uncertainty for R can be calculated and the true value for R can be stated to fall into the following interval at the level of confidence associated with k:

$$R \pm U_R \tag{B.23}$$

Additionally, it is worth noting that when the large degree of freedom assumption or treatment is taken (see Appendix B.1.4), all of the uncertainty propagation relations can be propagated with the expanded uncertainty directly instead of the standard uncertainty, which may be more convenient. By doing so, the degrees of freedom for any elemental terms are not factored in directly; rather, the chosen coverage factor can be multiplied by the standard uncertainties prior to propagating.

B.3 Uncertainty Calculations

B.3.1 Mass Transfer Coefficient

The uncertainty level for h_{m} is estimated by identifying and propagating the elemental uncertainties in the mass transfer coefficient calculation:

$$h_{\mathrm{m}} = \frac{\rho_{\mathrm{s}} \delta z / \delta t}{\rho_{\mathrm{v,w}}} \tag{B.24}$$

From Eq. (B.19), the expanded uncertainty in h_{m} can be expressed at

$$\frac{U_{h_{\mathrm{m}}}}{h_{\mathrm{m}}} = \left[\left(\frac{U_{\rho_{\mathrm{s}}}}{\rho_{\mathrm{s}}} \right)^2 + \left(\frac{U_{\rho_{\mathrm{v,w}}}}{\rho_{\mathrm{v,w}}} \right)^2 + \left(\frac{U_{\delta z}}{\delta z} \right)^2 + \left(\frac{U_{\delta t}}{t} \right)^2 \right]^{1/2} \tag{B.25}$$

The expanded uncertainty in the solid naphthalene is taken to be 1.1 % (Goldstein and H. H. Cho, 1995). The naphthalene vapor density at the wall is calculated from ideal gas law:

$$\rho_{\mathrm{v,w}} = \frac{p_{\mathrm{v,w}}}{R_{\mathrm{naph}} T_{\mathrm{w}}}$$

for which the expanded uncertainty is

$$\frac{U_{\rho_{\mathrm{v,w}}}}{\rho_{\mathrm{v,w}}} = \left[\left(\frac{U_{p_{\mathrm{v,w}}}}{p_{\mathrm{v,w}}} \right)^2 + \left(\frac{U_{R_{\mathrm{naph}}}}{R_{\mathrm{naph}}} \right)^2 + \left(\frac{U_{T_{\mathrm{w}}}}{T_{\mathrm{w}}} \right)^2 \right]^{1/2} \tag{B.26}$$

The uncertainty in the specific gas constant for naphthalene is negligible. The uncertainty in the temperature measurement comes from the calibration uncertainty, the spatial distribution uncertainty, and the uncertainty related to a new voltage measurement:

$$\begin{aligned}
\frac{U_{T_{\mathrm{w}}}}{T_{\mathrm{w}}} &= \left[\left(\frac{U_{T_{\mathrm{w}}}}{T_{\mathrm{w}}} \right)_{\mathrm{cal}}^2 + \left(\frac{U_{T_{\mathrm{w}}}}{T_{\mathrm{w}}} \right)_{\text{plate-spatial}}^2 + \left(\frac{\partial T}{\partial E_{\mathrm{TC}}} \frac{U_{E_{\mathrm{TC}}}}{T_{\mathrm{w}}} \right)^2 \right]^{1/2} \\
&= \left[\left(\frac{0.012}{298.15} \right)^2 + \left(\frac{0.05}{298.15} \right)^2 + \left(14 \times 10^3 \frac{7.2 \times 10^{-7}}{298.15} \right)^2 \right]^{1/2} \\
&= 0.018\,\%
\end{aligned}$$

Similarly, the uncertainty for the naphthalene vapor pressure comes from its correlation uncertainty of 3.8 % (Ambrose et al., 1975) and its uncertainty related to a new temperature measurement:

$$\begin{aligned}\frac{U_{p_{\mathrm{v,w}}}}{p_{\mathrm{v,w}}} &= \left[\left(\frac{U_{p_{\mathrm{v,w}}}}{p_{\mathrm{v,w}}}\right)^2_{\mathrm{corr}} + \left(\frac{\partial p_{\mathrm{v,w}}}{\partial T_{\mathrm{w}}}\frac{U_{T_{\mathrm{w}}}}{p_{\mathrm{v,w}}}\right)^2\right]^{1/2} \\ &= \left[(0.038)^2 + \left(1.1\frac{0.054}{11}\right)^2\right]^{1/2} \\ &= 3.8\,\%\end{aligned}$$

Then, the expanded relative uncertainty for the naphthalene vapor density is also 3.8 %. The expanded uncertainty from δz is found to be

$$\begin{aligned}\frac{U_{\delta z}}{\delta z} &= \left[\left(\frac{U_b}{b}\right)^2 + \left(\frac{U_{\Delta E_{\mathrm{LVDT}}}}{\Delta E_{\mathrm{LVDT}}}\right)^2 + \left(\frac{U_{\delta z}}{\delta z}\right)^2_{\mathrm{natural}}\right]^{1/2} \\ &= \left[\left(\frac{0.000070}{0.052365}\right)^2 + \left(\frac{420\times10^{-9}}{80\times10^{-6}}\right)^2 + (0.010)^2\right]^{1/2} \\ &= 1.1\,\%\end{aligned} \tag{B.27}$$

where b is the LVDT calibration constant and $U_{\Delta E_{\mathrm{LVDT}}}$ is found via the mock sublimation test. Lastly, the time uncertainty is due to the natural limitation of a quartz timer and the ability to start and stop time precisely when the intended:

$$\begin{aligned}\frac{U_{\delta t}}{t} &= \left[\left(\frac{U_t}{t}\right)^2_{\mathrm{quartz}} + \left(\frac{U_t}{t}\right)^2_{\mathrm{timer}}\right]^{1/2} \\ &= \left[(0.0001)^2 + \left(\frac{20}{3600}\right)^2\right]^{1/2} \\ &= 0.56\,\%\end{aligned} \tag{B.28}$$

Then the mass transfer coefficient relative expanded uncertainty can be calculated as:

$$\begin{aligned}\frac{U_{h_\mathrm{m}}}{h_\mathrm{m}} &= \left[(0.011)^2 + (0.038)^2 + (0.011)^2 + (0.0056)^2\right]^{1/2} \\ &= 4.1\,\%\end{aligned}$$

B.3.2 Sherwood Number

After the mass transfer coefficient uncertainty is computed, the Sherwood number uncertainty can be computed. From the definition of the Sherwood number, the uncertainty in the Sherwood number is found to be

$$\frac{U_{Sh}}{Sh} = \left[\left(\frac{U_{h_\mathrm{m}}}{h_\mathrm{m}}\right)^2 + \left(\frac{U_C}{C}\right)^2 + \left(\frac{U_{D_\mathrm{naph}}}{D_\mathrm{naph}}\right)^2\right]^{1/2} \tag{B.29}$$

The chord length uncertainty is negligible so it can be treated as zero and the uncertainty in the mass transfer coefficient is known from the previous section. The uncertainty in the diffusion coefficient is estimated from the uncertainties claimed by K. Cho (1989) (3 %) and Chen and Wung (1989) (4.1 %):

$$\frac{U_{D_\mathrm{naph}}}{D_\mathrm{naph}} = \left[0.03^2 + 0.041^2\right]^{1/2} = 5.1\,\%$$

Then the combined expanded relative uncertainty for Sh is calculated to be 6.5 %. Note that if the uncertainty due to systematic sources and random sources were separated, the random uncertainty is found to be 1.2 % and the systematic uncertainty is found to be 6.4 %. While the 1.2 % figure indicates that the mass flow rate can be measured precisely, it is however not a good estimate for the experimental repeatability since the flow parameters are not precisely fixed at their steady-state design values. In this particular experiment, there are five quantities that are controlled: blade Reynolds number, slot blowing ratio, discrete hole blowing ratio, slot injection temperature, and discrete hole injection temperature. The 95 % prediction intervals for the Reynolds number and blowing parameters was nearly 3 % across all experiments. Meanwhile, the 95 % prediction interval for the temperature difference between injected flow and main flow was nearly 0.8 K. Of these issues, the temperature effect may be the most problematic, especially in areas with high film cooling effectiveness due to the strong

temperature dependence on saturated naphthalene vapor density. Other factors such as naphthalene casting inconsistencies, imperfect naphthalene saturation in saturation chambers, presence of naphthalene vapor in main flow due to recirculation, and denting of naphthalene from clamping forces while installing the plate into the test section all may factor in as well. Given these considerations, the uncertainty for the Sherwood may be best realized via a direct end to end calculation rather than from propagation of elemental uncertainty sources. This will also automatically account for correlated uncertainties, which may have been ignored via propagation.

Direct Calculation of Sherwood Number Uncertainty

Following the methods in Appendix B.2, the uncertainty for the Sherwood number can be calculated directly via the replication experiments. Both the absolute uncertainty and the relative uncertainty in the Sherwood number were calculated. Note that the treatment for the Sherwood number uncertainty both with and without saturated naphthalene injection were treated the same. For the mass transfer measurement cases with replications, the mass transfer variance can be estimated spatially over the full mass transfer surface. It was observed that spatial variance for the relative uncertainty on a given mass transfer plate tends to be uniform in nature, but with patches of atypically larger relative uncertainty. Therefore, for each set of replicate mass transfer experiments, two values for the relative uncertainty are calculated: (1) a value indicative of the median relative uncertainty, and (2) a value indicative of the mean relative uncertainty. These values were pooled together using a pooled variance calculation to compute summary statistics (1) and (2). The pooled variance is calculated with weighting factors equal to the number of replication experiments minus one (the degrees of freedom). Finally, the square root of that result is taken to calculate the uncertainty estimate for methods (1) and (2). The resulting uncertainty for U_{Sh} was equal to 1.0×10^2 and 2.4×10^2 for options (1) and (2), respectively. Similarly, the uncertainty for (U_{Sh}/Sh) was equal to 6.6 % and 14 % for options (1) and (2), respectively. Since there was a significant difference between methods (1) and (2), it indicates non-uniformity and non-normal distribution in uncertainty over the mass transfer plate. Additionally, the ratio between methods (1) and (2) was less for the relative uncertainty rather than the absolute uncertainty, indicating that the Sherwood number uncertainty is best modeled as a relative uncertainty, which

Table B.1: Sherwood Number—Random Uncertainty Summary

Calculation Method	$\frac{U_{Sh}}{Sh}$	$\frac{U_{\overline{Sh}}}{\overline{Sh}}$	$\frac{U_{\overline{\overline{Sh}}}}{\overline{\overline{Sh}}}$
Spatial Median	6.6 %	6.5 %	—
Spatial RMS	14 %	8.6 %	5.9 %

indicates the uncertainty is nearly proportional to mass flux, which is intuitively appealing. Note that neither uncertainty assumption is perfect, but the constant relative uncertainty was preferred here and will be assumed.

The above approach was also followed to estimate the uncertainty in the reported values for the pitchwise-averaged Sherwood number and the area-averaged Sherwood number. The calculated values for each of these uncertainties for methods (1) and (2) are summarized in Table B.1.

For the general case when the experimental conditions were replicated, the random uncertainty in the averaged Sherwood number is related to the uncertainty without replication as follows:

$$\frac{U_{Sh}}{Sh} = \frac{1}{\sqrt{n_0}} \left(\frac{U_{Sh}}{Sh} \right)_{n_0=1} \tag{B.30}$$

where n_0 is the number of naphthalene-free experiments. This same approach can be equally applied for $\left(U_{\overline{Sh}}/\overline{Sh}\right)$ and $\left(U_{\overline{\overline{Sh}}}/\overline{\overline{Sh}}\right)$.

When performing a direct estimate for the error, only the random error is considered. Therefore, the systematic error from the previous discussion can be added back in at this point. As an example, the combined expanded relative uncertainty for (U_{Sh}/Sh) is equal to 9.2 % and 15 % for options (1) and (2), respectively when $n_0 = 1$.

B.3.3 Film Cooling Uncertainty

The film cooling is calculated from two Sherwood numbers inputs (for $\phi_1 = 1$):

$$\eta_{\text{iw}} = \frac{Sh - Sh'_1}{Sh} \tag{B.31}$$

By propagating the uncertainty and assuming $U_{Sh}/Sh = U_{Sh'_1}/Sh'_1$, the following result is found:

$$U_{\eta_{\mathrm{iw}}} = \sqrt{2}\left(\frac{U_{Sh}}{Sh}\right)(1-\eta_{\mathrm{iw}}) \tag{B.32}$$

Note that this understates the uncertainty if $\phi_1 \neq 1$: when the naphthalene-saturated air is not fully saturated. Here, note that only the random uncertainty needs to be used from Appendix B.3.2 rather than the combined uncertainty since the systematic uncertainty in Sh is correlated with Sh'_1, so the systematic effect should nearly cancel out.

Next, the effect of experimental replication can be factored in in the following way:

$$U_{\eta_{\mathrm{iw}}} = \left(\frac{1}{n_0}+\frac{1}{n_1}\right)^{1/2}\left(\frac{U_{Sh}}{Sh}\right)_{n_0=n_1=1}(1-\eta_{\mathrm{iw}}) \tag{B.33}$$

where n_0 is the number of naphthalene-free experiments and n_1 is the number of naphthalene-saturated experiments. For example, for $U_{Sh}/Sh = 6.6\,\%$, $\eta_{\mathrm{iw}} = 20\,\%$, and for the case when two replicates are performed, the uncertainty in the film cooling coefficient is $U_{\eta_{\mathrm{iw}}} = 5.3\,\%$, or $(U_{\eta_{\mathrm{iw}}}/\eta_{\mathrm{iw}}) = 26\,\%$.

The above approach underestimates the uncertainty near $\eta_{\mathrm{iw}} = 1$, since the constant relative uncertainty assumption implies that $U_{Sh'_1} = 0$ for $Sh'_1 = 0$. This highlights a situation where a constant relative uncertainty assumption is poor. Since there is limited data near $Sh' = 0$, the best estimate is via the propagation of uncertainty, as in Appendix B.3.2, which estimates

$$U_{\eta_{\mathrm{iw}}}(\eta = 1) = \left.\frac{U_{Sh'_1}}{Sh}\right|_{Sh'_1=0} \approx 1.2\,\% \tag{B.34}$$

Therefore, this uncertainty term estimate can be combined with Eq. (B.33) to estimate uncertainty across the full effectiveness range:

$$U_{\eta_{\mathrm{iw}}} = \left[\left(\frac{1}{n_0}+\frac{1}{n_1}\right)\left(\frac{U_{Sh}}{Sh}\right)^2_{n_0=n_1=1}(1-\eta_{\mathrm{iw}})^2 + \left(\frac{1}{n_1}\right)\left(\frac{U_{Sh'_1}}{Sh}\right)^2_{Sh'_1=0}\right]^{1/2} \tag{B.35}$$

Table B.2: Film Cooling Uncertainty Summary

Calculation Method	$U_{\eta_{\mathrm{iw}}}$	$U_{\overline{\eta}_{\mathrm{iw}}}$	$U_{\overline{\overline{\eta}}_{\mathrm{iw}}}$
Spatial Median	$9.1\,\%\,(1-\eta_{\mathrm{iw}})$	$6.6\,\%\,(1-\overline{\eta}_{\mathrm{iw}})$	—
Spatial RMS	$19\,\%\,(1-\eta_{\mathrm{iw}})$	$8.6\,\%\,(1-\overline{\eta}_{\mathrm{iw}})$	$6.3\,\%\,\left(1-\overline{\overline{\eta}}_{\mathrm{iw}}\right)$

Direct Calculation of Film Cooling Uncertainty

The film cooling uncertainty can also be found by direct calculation from replicated experimental results. Taking a cue from the propagated results, the film cooling uncertainty can be assumed to be proportional to $(1-\eta_{\mathrm{iw}})$ (or either the pitchwise-averaged or area-averaged equivalents). The results are reported in Table B.2. The results in Table B.2 are expected to be proportional to Table B.1 with a $\sqrt{2}\,(1-\eta_{\mathrm{iw}})$ factor difference based on the finding in Eq. (B.33). This was found to be nearly the case for $U_{\eta_{\mathrm{iw}}}$ compared with (U_{Sh}/Sh). For the pitchwise and area-averaged quantities, the factor was near unity rather than $\sqrt{2}$.

To use the directly calculated uncertainty results for the case of replicates, the following approach can be used:

$$U_{\eta_{\mathrm{iw}}} = \frac{1}{\sqrt{2}}\left(\frac{1}{n_0}+\frac{1}{n_1}\right)^{1/2}\left(U_{\eta_{\mathrm{iw}}}\right)_{n_0=n_1=1} \tag{B.36}$$

This same method can be applied for $U_{\overline{\eta}_{\mathrm{iw}}}$ and $U_{\overline{\overline{\eta}}_{\mathrm{iw}}}$. Additionally, when $\eta_{\mathrm{iw}} \approx 1$, the estimation approach included in Eq. (B.35) can be applied here.

Appendix C

Regression Analysis

Regression analysis is used to estimate relationships among variables. In this work, regression was used for calibrating measurement equipment and for extracting pertinent parameters or trends in measured data. In classical regression approaches, the error is assumed to be concentrated in the dependent variable only. When the independent variables and dependent variable are both measured variables, this assumption is always violated due to inherent measurement error involved with any measurement. Assuming all measurement error is in the dependent variable can systematically affect the fit coefficients and the uncertainties for the fit. For example, in the case of linear regression, if there were measurement error in the independent and dependent variables and classical regression were used instead of errors-in-variables regression, the slope estimate would be attenuated away from its true value towards zero. The degree of importance for accounting for error in the independent variables can be judged by calculating the coefficient of determination (R^2). When R^2 is less than 0.95, the effect of error in the independent variables becomes significant, and when the effect is greater than 0.99, the effect of error in the independent variables becomes negligible. In this work, special care is taken to properly account for both independent and dependent variable error as appropriate for each regression case. The specific methods to perform the regression analysis will depend on the nature of the regression equation.

C.1 Overview of Regression Analysis

Regression analysis estimates the true relationship between the dependent variable Y and the independent variables X_i:

$$Y^* = f(X_1^*, X_2^*, \ldots, X_N^*, \beta_1, \beta_2, \ldots, \beta_P) \tag{C.1}$$

where the $*$ superscript denotes the true values (ignoring the effect of systematic error here) for the variables, N is the number of independent variables, and P is the number of β_p parameters to be fit. The form of function f must be specified, and it is usually chosen based on engineering knowledge about the relationship between the independent and dependent variables. The primary outcome of the regression process is the best fit for the β_p parameters.

To solve for the β_p parameters, n measurements are taken for the independent and dependent variables. The number of measurements n must be greater than or equal to the number of parameters P, ideally significantly greater. It is assumed that the measured data $X_{1k}, X_{2k}, \ldots, X_{Nk}$, and Y_k are measured observations of the true values $X_{1k}^*, X_{2k}^*, \ldots, X_{Nk}^*$, and Y_k^*:

$$\begin{aligned} Y_k &= Y_k^* + \epsilon_k \\ X_{1k} &= X_{1k}^* + \eta_{1k} \\ \vdots &\qquad \vdots \\ X_{Nk} &= X_{Nk}^* + \eta_{Nk} \end{aligned} \tag{C.2}$$

where ϵ_k and η_{ik} are the kth measurement errors in the dependent and independent variables, respectively. Then, given the known or estimated variances for ϵ_k and η_{ik}, $\sigma_{\epsilon_k}^2$ and $\sigma_{\eta_{ik}}^2$, respectively, the following weighted sum of the squared residuals (SSR) is minimized for error-in-variables regression with any number of independent variables:

$$\text{SSR} = \sum_{k=1}^{n} \left(\frac{\epsilon_k^2}{\sigma_{\epsilon_k}^2} + \frac{\eta_{1k}^2}{\sigma_{\eta_{1k}}^2} + \cdots + \frac{\eta_{Nk}^2}{\sigma_{\eta_{Nk}}^2} \right) \tag{C.3}$$

The variance term can be estimated using the methods discussed in Appendix B, where the estimate for σ_{Xi} is equal to the random standard uncertainty s_{Xi}. Note

that if all of the variance terms were equal then Eq. (C.3) is the special case of orthogonal regression. For the case of where the error is assumed to be negligible in the independent variables, then Eq. (C.3) simplifies to inverse-variance weighted least-squares regression:

$$\text{SSR} = \sum_{k=1}^{n} \frac{\epsilon_k^2}{\sigma_{\epsilon_k}^2} \tag{C.4}$$

Finally, for the case when the inverse variances (or weights) are the same, Eq. (C.4) simplifies to least-squares regression:

$$\text{SSR} = \sum_{k=1}^{n} \epsilon_k^2 \tag{C.5}$$

C.2 Regression Minimization Problem

Regardless of which form of SSR is used, the goal is to minimize SSR by solving for the optimal values for the β_p parameters and for the true independent variables X_{ik}^*. The sum of the squared residuals (SSR) is a function of the following unknowns: $\text{SSR} = SSR(\beta_p, X_{ik}^*)$. At the point where the SSR is minimized, the set of derivatives with respect to β_p and X_{ik}^* are equal to zero:

$$\frac{\partial \text{SSR}}{\partial \beta_p} = 0 \tag{C.6}$$

$$\frac{\partial \text{SSR}}{\partial X_{ik}^*} = 0 \tag{C.7}$$

In total, these equations lead to a system of $P + nN$ equations and unknowns. One option is to solve all of these equations simultaneously; however, this tends to be a difficult system of equations to solve. A better option is to eliminate the dependency of SSR on X_{ik}^* by first solving Eq. (C.7), and then substituting into Eq. (C.6), as suggested by Southwell (1976). When this approach is taken, the final large system of equations only includes a total of P equations and unknowns. Note that when the error in the independent variables is treated as zero, then $\text{SSR} = SSR(\beta_p)$ only since $X_{ik}^* = X_{ik}$, and equations Eq. (C.7) need not be considered.

C.2.1 Notes on Specific Cases

The specific process for solving the minimization problem will depend on the form of the function f (linear or nonlinear, etc.) and whether or not the error in the independent variables is treated as negligible or not. Some cases lead to explicit solutions, and others are implicit in form and require iteration. Some of the cases are briefly discussed below.

Linear and Multiple Linear Regression

For the cases of linear regression or multiple linear regression with no error present in the independent variables, then the optimal β_p parameter values can be explicitly solved for by inverting the linear matrix system that results from Eq. (C.6). This can be readily handled by any standard regression software.

Errors-in-Variables Linear Regression

For the cases of linear regression with errors in independent and dependent variables, and the uncertainties in independent and dependent are treated as constant, then the optimal β_p can be solved for explicitly by manipulating the results of Eqs. (C.6) and (C.7). The final result of this case has a special name: Deming regression (Deming, 1943).

For the case where the uncertainties in the individual X_k and Y_k quantities are not equal to each other can be solved for using an iterative procedure: York regression (York et al., 2004).

Nonlinear Regression

For the case of nonlinear regression, a nonlinear least-squares approach must usually be utilized to solve Eq. (C.6). Usually, a Gauss-Newton type of method is prevalent here. Regression software typically have dedicated nonlinear regression routines readily available for this purpose.

Errors-in-Variables Nonlinear Regression

For the case of errors-in-variables nonlinear regression, a general nonlinear system of equation solver must be utilized to solve Eqs. (C.6) and (C.7). The approach detailed by Southwell (1976) can be critical to successfully solving the system of equations.

Note that since this approach is the most general, it can also be used to handle linear and multiple linear regression cases, with or without errors in variables. For Errors-in-Variables Multiple Linear Regression, this approach is taken in this work. Generally, nonlinear least squares can successfully solve linear systems of equations very easily, but it may be unneeded if a dedicated explicit approach is available.

Linearization of Nonlinear Regression Problem

Often a nonlinear function can be transformed into a linear problem. For example, for a heat transfer problem where $St = cRe^n Pr^m$, this equation can be transformed into $\ln St = \ln c + n \ln Re + m \ln Pr$. This system can then be solved by a multiple linear regression approach. Note that when performing transformations, it is important to transform the uncertainty in the variables as well. Note that in some cases the uncertainties may be constant before the transformation, but not afterward, or vice versa.

C.3 Uncertainty of Regression

It can be said that the fit parameters β_p is a function of the input data:

$$\beta_p = \beta_p \left(X_{11}, \ldots, X_{1n}, \ldots, X_{N1}, \ldots, X_{Nn}, Y_1, \ldots, Y_n \right) \tag{C.8}$$

Therefore, the combined standard uncertainty in the parameters can be found using standard propagation of uncertainty methods:

$$u_{\beta_p} = \sqrt{\sum_{i=1}^{N} \sum_{k=1}^{n} \left(\frac{\partial \beta_p}{\partial X_{ik}} \right)^2 u_{X_{ik}}^2 + \sum_{k=1}^{n} \left(\frac{\partial \beta_p}{\partial Y_k} \right)^2 u_{Y_k}^2} \tag{C.9}$$

Following the logic above, the uncertainty in $Y_{\text{regression}}$ can be stated as

$$u_{Y_{\text{regression}}} = \sqrt{\sum_{i=1}^{N}\sum_{k=1}^{n}\left(\frac{\partial Y}{\partial X_{ik}}\right)^2 u_{X_{ik}}^2 + \sum_{k=1}^{n}\left(\frac{\partial Y}{\partial Y_k}\right)^2 u_{Y_k}^2} \tag{C.10}$$

where Y is the value from the curve for a given independent variable set $(X_1, \ldots, X_N)$. Later, when a new measurements X_{new} is made and the regression fit is used, the uncertainty in Y is as follows:

$$u_Y = \sqrt{u_{Y_{\text{regression}}}^2 + \sum_{i=1}^{N}\left(\frac{\partial Y}{\partial X_{\text{new}}}\right)^2 u_{X_{\text{new}}}^2} \tag{C.11}$$

The above uncertainty equations do not consider any correlation effects. If the correlation is important, the approaches detailed in Appendix B can be used. In the special case where the systematic uncertainty b_{X_i} is correlated with $b_{X_{\text{new}}}$ (if the same equipment used in calibration is also used to measure X_{new}), then the effect of the systematic uncertainties in X_i and X_{new} on b_Y is negated and can be ignored. This can be understood because the calibration includes the systematic error in the variables. Therefore, if the new input includes the same systematic error, then the effect of the error is negated.